

申 报	系列：教师系列教学科研并重型
	专业：木材科学与技术
	职称：副教授

业绩成果材料

（申报人的业绩成果材料包括论文、科研项目、获奖以及其他成果等）

单 位（二级单位） 材料与能源学院

姓 名 周海洋

材料核对人：

单位盖章：

核对时间：

华南农业大学制

目 录（模板）

一、教学研究业绩

1. 教学研究项目：关于《基于“国际交流”和“智能制造”背景下的木材科学与工程专业师资培训与课程建设》项目的立项通知（合同）及有关佐证材料 5

二、科研项目

1. 主持：关于《木塑复合材料界面动力学相容性的作用机制》项目的立项通知（合同）及有关佐证材料..... 6
2. 主持：关于《生物基建材制造过程中的合成改性及加工关键技术研究》项目的立项通知（合同）及有关佐证材料. 14
3. 主持：关于《基于复杂木质纤维结构的超高含量木质纤维-聚烯烃界面作用机制》项目的立项通知（合同）及有关佐证材料 16
4. 主参：关于《超高木质纤维含量木塑复合材料动态界面流变机理》项目的立项通知（合同）及有关佐证材料..... 27
5. 主参：关于《超高木质纤维含量木塑复合材料非热力学界面作用机制》项目的立项通知（合同）及有关佐证材料.. 39

三、论文、著作等

1. 检索证明 49
2. 以第一作者发表本专业论文情况
 - 2.1. Nanostructured multifunctional wood hybrids fabricated via in situ mineralization of zinc borate in hierarchical wood structures 55
 - 2.2. Recycling end-of-life WPC products into ultrahigh-filled, high performance wood

fiber/polyethylene composites: A sustainable strategy for clean and cyclic processing in the WPC industry	71
2.3. Conductive and fire-retardant wood/polyethylene composites based on a continuous honeycomb-like nanoscale carbon black network	85
2.4. Effects of fiber geometry and orientation distribution on the anisotropy of mechanical properties, creep behavior, and thermal expansion of natural fiber/HDPE composites	93
2.5. Comparative study on the effects of silica size and dispersion mode on the fire retardancy of extruded wood fiber/HDPE composites	102
2.6. Mechanical Properties and Fire Retardancy of Wood Flour/High-Density Polyethylene Composites Reinforced with Continuous Honeycomb-like nano-SiO ₂ Network and Fire Retardant	115
3. 以通讯作者发表本专业论文情况	
3.1. Simultaneously strengthening and toughening reprocessable basswood through reactive waterborne acrylic resin impregnation	129
3.2. Preparation of waterborne intumescent flame-retardant coatings using adenosine-based phosphonates for wood surfaces	140
3.3. Phenol liquefaction of waste sawdust pretreated by sodium hydroxide: Optimization of parameters using response surface methodology	152

四、科研成果

1. 科技奖励证书	168
2. 知识产权	
2.1. 专利授权证书：一种含有三维网络结构天然纤维复合材料的制造方法	170
2.2. 专利授权证书：一种超高木质纤维含量木塑粒料及复合材料的制造方法	172
2.3. 专利授权证书：一种胶合夹芯结构木塑复合材料、制品及其制造方法.	174
3. 起草标准：木材产品碳足迹核算技术规范.....	175

五、其他业绩

1. 指导学生学科竞赛	
1.1. 广东省第十届大学生材料创新大赛高分子材料分赛二等奖“基于硼酸锌原位矿化的木材多功能化研究”.....	220
1.2. 广东省第十届大学生材料创新大赛总决赛三等奖“基于硼酸锌原位矿化的木材多功能化研究”.....	221
1.3. 第九届中国大学生高分子材料创新创业大赛三等奖“基于硼酸锌原位矿化的木材多功能化研究”.....	222

【佐证材料切记与目录页所列页码对应，不要用图片格式的材料进行打印。】

教育部产学合作协同育人项目
立项证书



项目编号：230800367163816

项目名称：基于“国际交流”和“智能制造”背景下的木材科学与工程专业师资培训与课程建设

项目负责人：周海洋

学校名称：华南农业大学

企业名称：河南讯林科技有限公司

该项目入选教育部产学合作协同育人项目2023年批次立项项目，特发此证。



教育部产学合作协同育人项目
cxhz.hep.com.cn

教育部产学合作协同育人项目专家组

2023年12月



项目批准号	32201494
申请代码	C1603
归口管理部门	
依托单位代码	51064208A0499-0932



322014941001774

国家自然科学基金 资助项目计划书 (包干制项目)

资助类别: 青年科学基金项目

亚类说明:

附注说明:

项目名称: 木塑复合材料界面动力学相容性的作用机制

资助经费: 30万元 执行年限: 2023.01-2025.12

负责人: 周海洋

通讯地址: 广东省广州市天河区五山路483号

邮政编码: 510642 电话: 13936330340

电子邮件: hyzhou@scau.edu.cn

依托单位: 华南农业大学

联系人: 唐家林 电话: 020-85280070

填表日期: 2022年09月20日

国家自然科学基金委员会制



国家自然科学基金资助项目计划书填报说明 （包干制项目）

- 一、项目负责人收到《国家自然科学基金资助项目批准通知》（以下简称《批准通知》）后，请认真阅读本填报说明，参照国家自然科学基金相关项目管理办法和新修订的《国家自然科学基金资助项目资金管理办法》（以下简称《资金管理办法》，请查阅国家自然科学基金委员会官方网站首页“政策法规”栏目），按《批准通知》的要求认真填写和提交《国家自然科学基金资助项目计划书》（以下简称《计划书》）。
- 二、填写《计划书》时要科学严谨、实事求是、表述清晰、准确。《计划书》经国家自然科学基金委员会相关项目管理部门审核批准后，将作为项目研究计划执行、检查和验收的依据。
- 三、《计划书》各部分填写要求如下：
 - （一）简表：由系统自动生成。
 - （二）摘要及关键词：各类获资助项目都应当填写中、英文摘要及关键词。
 - （三）正文：
 1. 青年科学基金项目：如果《批准通知》所附“项目评审意见及修改意见表”中“修改意见”栏目没有修改要求的，只需选择“研究内容和研究目标按照申请书执行”即可；如果《批准通知》中上述栏目明确要求调整研究期限或研究内容等的，须选择“根据研究方案修改意见更改”并填报相关修改内容。
 2. 国家杰出青年科学基金项目和优秀青年科学基金项目按下列提纲撰写：
 - （1）研究方向；
 - （2）结合国内外研究现状，说明研究工作的学术思想和科学意义（限两个页面）；
 - （3）研究内容、研究方案及预期目标（限两个页面）；
 - （4）年度研究计划；
 3. 科技管理专项项目按下列提纲撰写：
 - （1）科技战略研究领域方向；
 - （2）结合该领域国内外研究现状及发展趋势，分析科学基金资助战略与政策（限两个页面）；
 - （3）研究内容、研究方案及预期目标（限两个页面）；
 - （4）年度研究与实践计划。
- 四、资助经费相关要求：
 1. 资助经费批准时不再区分直接费用和间接费用。
 2. 项目负责人在提交计划书时需签署承诺书，承诺尊重科研规律，弘扬科学家精神，遵守科研伦理道德和作风学风诚信要求，认真开展科学研究工作；承诺项目经费全部用于与本项目研究工作相关的支出，不得用于与本项目研究无关的支出。
 3. 项目负责人提交计划书时，无需编制项目预算。项目资金由项目负责人自主决



定使用，按照《资金管理办法》第九条规定的开支范围列支。有关管理费用的补助支出，由依托单位根据实际需要，在充分征求项目负责人意见基础上合理确定。绩效支出由项目负责人根据实际科研需要和相关薪酬标准自主确定，依托单位按照工资制度进行管理。其余用途经费无额度限制，由项目负责人根据实际需要自主决定使用。

4. 项目结题时，项目负责人根据实际使用情况编制项目经费决算，经依托单位财务、科研管理部门审核后，报自然科学基金委。依托单位应当在单位内部公开非涉密项目立项、主要研究人员、资金使用（重点是间接费用、外拨资金、结余资金使用等）、决算、大型仪器设备购置以及项目研究成果等情况，接受内部监督。
5. 自然科学基金委结合项目管理，对经费使用情况和依托单位管理情况定期开展抽查。



简表

项目负责人信息	姓 名	周海洋	性 别	女	出生年月	1994年10月	民 族	汉族
	学 位	博士			职称	无		
	是否在站博士后	是		电子邮件	hyzhou@scau.edu.cn			
	电 话	13936330340		个人网页				
	工 作 单 位	华南农业大学						
	所 在 院 系 所	材料与能源学院						
依托单位信息	名 称	华南农业大学					代码	51064208A0499
	联 系 人	唐家林		电子邮件	kyc.jhk@scau.edu.cn			
	电 话	020-85280070		网站地址	http://kjc.scau.edu.cn/			
合作单位信息	单 位 名 称							
项目基本信息	项 目 名 称	木塑复合材料界面动力学相容性的作用机制						
	资 助 类 别	青年科学基金项目			亚 类 说 明			
	附 注 说 明							
	申 请 代 码	C1603:木材物理学						
	基 地 类 别							
	执 行 年 限	2023.01-2025.12						
	资 助 经 费	30万元						



项目摘要

中文摘要:

由于极性木质纤维与非极性聚合物不相容,木塑复合材料(木塑)熔融加工过程中异质两相在复杂作用下被强制分散并复合在一起,各相自动析出或凝聚的现象很难产生并长期处于动力学稳定状态。针对木塑界面问题虽然已展开众多的研究,但主要借鉴聚合物共混的溶解度参数理论,即将木质纤维去极性化或聚合物极性化处理以达到两相极性相近的目的,木塑界面已经严重偏离传统界面热力学相容范畴,彻底揭示木塑界面机理任重道远。本项目通过定量表征复杂环境下木质纤维/聚合物不相容两相表面自由能,研究其对木塑体系界面动力学相容性的影响机制。基于多级结构木质纤维表面自由能的不均匀和复杂性,及典型表面处理后木质纤维和聚合物表面自由能的变化,研究高温高压复杂环境下聚合物熔体对木质纤维表面动态浸润机理,定量解析木塑界面张力,建立界面模型,揭示木塑不相容两相表面自由能-动力学界面-宏观性能的相互关系和响应机制,推进木塑动力学界面基础理论研究。

Abstract:

The heterogeneous two phases of wood plastic composites (WPC) are forcibly dispersed and combined at complex action during the melting process due to the incompatibility between the polar wood fiber and nonpolar polymer, and the phenomenon of automatic precipitation or condensation of each phase is difficult and it is in a stable state of kinetics for a long time. Although many studies have been focused on the wood-plastic interface, it was primarily draw lessons from the similar compatibility theory of polymer, that is, reducing the polarity of wood fiber or increasing the polarity of polymer to achieve the similar polarity between the two phases. However, the interface of WPC has seriously deviated from the category of thermodynamic compatibility and there is a long way to go to thoroughly reveal the mechanism of wood-plastic interface. This project investigates the influence mechanism on the interfacial dynamic compatibility of WPC systems by quantitatively characterizing the surface free energy of wood fibers/polymers in a complex environment. Based on the inhomogeneity and complexity of the surface energy of the multistage wood fiber and the change of the surface free energy of wood fiber and polymer after typical surface treatment, the dynamic wetting mechanism of the polymer melt on wood fibers at high temperature and high pressure and the quantitative analysis of interfacial tension of WPC were studied to establish the interfacial model and reveal the interrelationships and response mechanisms among the surface free energy, interfacial dynamics and macro-properties, which promote the basic theoretical research of interfacial dynamics of WPC.

关键词(用分号分开): 木塑复合; 界面特性; 表面自由能; 动力学

Keywords(用分号分开): wood plastic composites; interfacial characteristics; surface free energy; dynamics



报告正文

研究内容和研究目标按照申请书执行。



国家自然科学基金项目负责人、依托单位承诺书

国家自然科学基金项目负责人承诺书

本人郑重承诺：我接受国家自然科学基金的资助，严格遵守中共中央办公厅、国务院办公厅《关于进一步加强科研诚信建设的若干意见》《关于进一步弘扬科学家精神加强作风和学风建设的意见》《关于加强科技伦理治理的意见》等规定，及国家自然科学基金委员会关于资助项目管理、项目资金管理等各项规章，在《计划书》填写及项目执行过程中：

（一）按照《批准通知》《国家自然科学基金资助项目计划书填报说明》的要求填写《计划书》，未自行降低、更改目标任务或约定要求，或缩减研究（研制）内容；

（二）树立“红线”意识，严格履行科研合同义务，按照《计划书》负责实施本项目（批准号：32201494），切实保证研究工作时间，按时报送有关材料，及时报告重大情况变动，不违规将科研任务转包、分包他人，不以项目实施周期外或不相关成果充抵交差；

（三）遵守科研诚信、科技伦理规范和学术道德，认真开展研究工作，对资助项目发表的论著和取得的科研成果按规定进行标注，不在非本项目资助的成果或其他无关成果上标注本项目批准号，反对无实质学术贡献者“挂名”，不在成果署名、知识产权归属等方面侵占他人合法权益，并如实报告本人及项目组成员发生的违背科研诚信要求的任何行为；

（四）尊重科研规律，弘扬科学家精神，严谨求实，追求卓越，反对浮夸浮躁、投机取巧，不人为夸大学术或技术价值，不传播未经科学验证的现象和观点；

（五）将项目资金全部用于与本项目研究工作相关的支出，并结合科研活动需要，科学合理安排项目资金支出进度；

（六）做好项目组成员的教育和管理，确保遵守以上相关要求。

如违背上述承诺，本人愿接受国家自然科学基金委员会和相关部门做出的各项处理决定。

项目负责人（签字）：

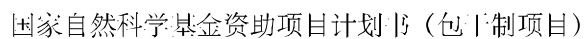
年 月 日

国家自然科学基金项目依托单位承诺书

我单位同意承担上述国家自然科学基金项目，将保证项目负责人及其研究队伍的稳定和研究项目实施所需的条件，严格遵守国家自然科学基金委员会有关资助项目管理、项目资金管理、科研诚信管理和科技伦理管理等各项规定，并督促实施。

依托单位（公章）

年 月 日



本栏目由自然科学基金委填写

负责人（签章）：
年 月 日

负责人（签章）：
年 月 日

南京工业大学——华南农业大学

“村镇生物基建筑材料关键技术研究与应用”项目合作协议书

乙方：南京工业大学

丙方：华南农业大学

本着强强联合、优势互补、协作发展的原则，经平等协商，乙丙双方同意共同承担国家十三五重点研发计划专项“绿色宜居村镇技术创新”中项目“村镇生物基建筑材料关键技术研究与应用”的研发工作，并就任务分工、考核指标、经费分配、研究成果的知识产权等达成如下协议，由合作双方共同遵守：

一、乙丙双方承诺遵守《国家重点研发计划管理暂行办法》、《国家重点研发计划资金管理办法》及其他相关法规制度的要求。

二、任务分工：乙方作为项目主持单位，负责项目的总体组织、任务分工、经费分配、研究进展监督、总结上报及整体协调；

丙方为项目合作单位，负责课题四“生物基建材制造过程中的合成改性及加工关键技术研究”中部分任务的具体实施，详细研究任务分工和考核指标如下表：

单位	研究任务分工	考核指标
华南农业大学	课题四下设“任务 3：生物基建材的热塑化加工与物理复合成型关键技术研究”中如下研究内容： (1)生物基建材流变学行为及热塑化加工关键技术研究：研究生物基纤维层次结构等因素对生物基建材熔体黏度、剪切/拉伸应力应变行为等的影响，揭示微观-介观-宏观多尺度流变机理。	(1)发表 SCI/EI 论文 2 篇； (2)培养硕士研究生 2 名。

三、丙方获得肆拾肆万伍仟元（¥44.50 万元）国拨经费用于相应任务研究，具体划拨经费将根据科技部最终批复经费进行调整。项目实施过程，丙方严格按照预算支出经费，独立核算并专款专用。

四、丙方积极配合项目组的安排，按要求完成项目任务。如丙方在课题执行过程中，出现研究进展严重滞后、研究方案的重大更改、经费不合理支出等方面的情况，应及时上报课题及项目主持单位，以便及时采取应对措施。

五、各方合作研究产生的科研成果和知识产权归本项目所有。双方承诺本课题产生的所有科学数据无条件、按期递交到科技部指定的平台，在专项约定的条件下对专项各承担单位，乃至今后面向所有的科技工作者和公众开放共享。

六、乙方按照项目要求组织开展研究工作，丙方将遵守国家有关规定配合相关检查工作，及时按照要求上报相关研究材料、提供相关财务资料。

七、本协议一式6份。

八、该协议在课题执行期间有效，未尽事宜双方协商解决。

项目承担单位（乙方）：

南京工业大学（盖章）

法定代表人：

项目负责人（签字）：

2019年11月19日

研究任务参加单位（丙方）：

华南农业大学（盖章）

法定代表人：

研究任务负责人（签字）：

2019年11月18日



受理编号：SL2024A04J02053

广州市科技计划项目 申报书

项目名称：	基于复杂显微结构的超高含量木质纤维-聚烯烃界面作用机制
申报单位：	华南农业大学
项目负责人：	周海洋
计划类别：	基础研究计划
专题名称：	2025年度基础与应用基础研究专题
支持方向：	青年博士“启航”项目
组织单位：	华南农业大学
起止时间：	2025-01-01 至 2026-12-31
主管处室：	引进智力管理处（科技人才处）

广州市科学技术局制

二〇二四年

填写说明

一、请申报单位认真阅读指南，所申报的项目研究内容须对应指南、符合指南的要求。

二、项目名称应清晰、准确反映研究内容，项目名称不宜宽泛，只能由中文、英文字符组成，不超过50中文字。

三、本申报书通过“广州科技大脑”在线填写、报送，不需要线下提交纸质材料。

四、申报书中的单位名称，请按规范全称填写，并与单位公章一致。

五、涉密项目请在“广州科技大脑”下载申报书的电子版模板，按保密要求离线填写、报送。

六、本申报书中凡是无需填写的内容，应在空白处划“/”，或用“无”表示。

七、申报书内容须按照项目申报书据实填写，要遵循实事求是原则，无需凑够字数。

一、基本信息

项目 基本 信息	项目名称	基于复杂显微结构的超高含量木质纤维-聚烯烃界面作用机制		
	学科领域1	生命综合处-林学-木材物理学-人工复合木材		
	学科领域2	工材综合处-有机高分子材料- 高分子材料的加工与成型- 加工与成型中的化学与物理问题		
	指南发布日	2024年4月15日		
	申请市级财政 金额	5万元	研究期限	2025年1月1日- 2026年12月31日
项目 摘要	<p>基于木质纤维复杂显微结构呈现多尺度不均一特性，直接影响其几何状态、比表面积等表面特性，导致超高木质纤维含量（85wt.%以上）木塑复合材料（UH-WPCs）在复合过程中表现出尤为复杂的界面作用机制，现有的热力学界面作用机制和高分子溶解度参数理论已不适用该体系。通过揭示基于复杂显微结构的UH-WPCs界面作用机制，可以为UH-WPCs的创新设计和定向制备提供科学依据，实现理论和技术原理的源头创新。</p>			

二、申报单位情况

项目承担单位	单位名称	华南农业大学	统一社会信用代码	124400004554165634
	注册时间	1952-01-01	单位类型	高等院校
	注册地址	广东省广州市天河区五山路483号		
	办公地址	广东省广州市天河区五山路483号		
	联系人	姓名	倪慧群	
		手机号码	13711345768	
		电子邮箱	kjcgxk@scau.edu.cn	
	开户银行	广东广州工行五山支行		
	开户户名	华南农业大学		
银行账号	3602002609000310520			

三、项目负责人信息

姓名	周海洋	证件类型	身份证
证件号码	232321199410191529	性别	女
出生年月	1994-10-19	民族	汉族
国籍	中国	学历	博士研究生
学位	博士	学位授予国家 (或地区)	中国
职务	无	职称	中级
所学专业	林业工程	手机号码	13936330340
办公电话	020-82580319	电子邮箱	hyzhou@scau.edu.cn

四、项目经费信息

本项目总投入：¥（5）万元，其中，市财政科技经费：¥（5）万元，自筹经费：¥（0）万元。

1. 经费下达计划			
资金来源	小计	市财政科技经费	自筹经费
2025	5	5	0
总计	5	5	0

（单位：万元）

注：本专题纳入“包干制”，市财政科技经费按市科技计划项目经费“包干制”相关规定执行。

审核通过

五、预期代表性成果

项目负责人在项目实施期内，以该项目作为资助项目获得以下5种情形之一且经费使用符合规定的，由组织单位审核后通过验收。

（一）项目实施期内，以第一作者/通讯作者发表论文1篇或以上（须标注资助项目编号）；

（二）项目实施期内，以第一完成人申请或授权专利、软件著作权1项或以上；

（三）项目实施期内，获省级以上科技计划项目或人才项目支持1项或以上；

（四）项目实施期内，获省级以上科技奖励（含列入获奖团队成员名单）1项或以上；

（五）项目实施期内，获得职称晋升。

审核通过

六、承诺函

申请人:	周海洋
承担申报单位:	华南农业大学
项目名称:	基于复杂显微结构的超高含量木质纤维-聚烯烃界面作用机制
专题方向:	2025年度基础与应用基础研究专题-青年博士“启航”项目

申请人承诺:

本人根据项目申报指南的要求自愿提交项目(课题)申报书,在此郑重承诺:严格遵守《关于进一步加强科研诚信建设的若干意见》《关于进一步弘扬科学家精神 加强作风和学风建设的意见》等有关规定,杜绝《科学技术活动违规行为处理暂行规定》(科学技术部令第19号)所列违规行为,所申报材料和相关内容真实有效,不存在违背科研诚信要求的行为;已按要求落实了科研作风学风和科研诚信主体责任;不得以任何形式实施请托行为,申报材料符合《中华人民共和国保守国家秘密法》和《科学技术保密规定》等相关法律法规,符合指南各项申报要求;在参与广州市科技计划项目申报、评审和实施全过程中,恪守职业规范和科学道德,遵守评审规则和工作纪律,杜绝以下行为:

- (一) 抄袭、剽窃他人科研成果或者伪造、篡改研究数据、研究结论或实施其他侵犯他人知识产权的行为;
- (二) 购买、代写、代投论文,虚构同行评议专家及评议意见;
- (三) 违反论文署名规范,擅自标注或虚假标注获得科技计划等资助;
- (四) 违反科研伦理规范;
- (五) 弄虚作假,骗取科技计划项目、科研经费以及奖励、荣誉等;
- (六) 在申报书中以高指标通过评审,在任务书签订时故意篡改降低任务书中相应指标;
- (七) 以任何形式探听尚未公布的评审专家名单及其他评审过程中的保密信息;
- (八) 本人或委托他人通过各种方式及各种途径联系有关专家进行请托、游说,违规到评审会议驻地游说评审专家和工作人员、询问评审或尚未正

式向社会公布的信息等干扰评审或可能影响评审公正性的活动；

（九）向评审工作人员、评审专家等提供任何形式的礼品、礼金、有价证券、支付凭证、商业预付卡、电子红包，或提供宴请、旅游、娱乐健身等任何可能影响评审公正性的活动；

（十）其它违反财经纪律和相关管理规定的行为。

如有违反，本人愿接受项目管理机构和相关管理部门做出的各项处理决定，包括但不限于取消项目（课题）承担资格，追回项目（课题）经费，向社会通报违规情况，取消一定期限广州市科技计划项目申报资格，记入科研诚信严重失信行为数据库以及接受相应的党纪政纪处理等。

签字：周海洋

日期：2024年07月06日

审核通过

承担单位承诺：

本单位根据项目申报指南的任务需求，严格履行承担单位职责，自愿审核提交申报书，在此郑重承诺：

严格遵守《关于进一步加强科研诚信建设的若干意见》《关于进一步弘扬科学家精神 加强作风和学风建设的意见》等有关规定和其它科研诚信要求的行为，已按要求落实了科研作风学风和科研诚信主体责任；不以任何形式实施请托行为，申报材料符合《中华人民共和国保守国家秘密法》和《科学技术保密规定》等相关法律法规，符合指南各项申报要求；在参与项目申报和评审活动全过程中，遵守有关评审规则和工作纪律，杜绝以下行为：

（一）采取贿赂或变相贿赂、造假、剽窃、故意重复申报等不正当手段获取科技计划项目承担资格；

（二）以任何形式探听未公开的评审专家名单及其他评审过程中的保密信息；

（三）组织或协助项目团队向评审工作人员、评审专家等提供任何形式的礼品、礼金、有价证券、支付凭证、商业预付卡、电子红包等；宴请评审组织者、评审专家，或向评审组织者、评审专家提供旅游、娱乐健身等可能影响评审公正性的活动；

（四）包庇、纵容项目团队虚假申报项目，甚至骗取国家科技计划项目；

（五）包庇、纵容项目团队，甚至帮助项目团队采取“打招呼”等方式，影响评审公正；

（六）在正式申报书中以高指标通过评审，在任务书签订时故意篡改降低任务书中相应指标；

（七）其它违反财经纪律和相关管理规定的行为。

如有违反，本单位愿接受项目管理机构和相关部门做出的各项处理决定，包括但不限于停拨或核减经费，追回项目（课题）经费，取消一定期限广州市科技计划项目申报资格，记入科研诚信严重失信行为数据库等。

承担单位：华南农业大学

日期：2024年07月06日

七、单位审核

承担单位意见：

审核通过

日期：2024年07月07日

组织单位意见：

通过

日期：2024年07月11日

审核通过



项目批准号	32471786
申请代码	C1603
归口管理部门	
依托单位代码	51064208A0499-0932



国家自然科学基金 资助项目计划书 (预算制项目)

资助类别: 面上项目

亚类说明:

附注说明:

项目名称: 超高木质纤维含量木塑复合材料动态界面流变机理

直接费用: 50万元 执行年限: 2025.01-2028.12

负责人: 郝笑龙 BRID: 06896.00.72968

通讯地址: 广州市天河区五山路483号

邮政编码: 510642 电 话: 18846080538

电子邮件: haoxiaolong@scau.edu.cn

依托单位: 华南农业大学

联系人: 唐家林 电 话: 020-85280070

填表日期: 2024年08月25日

国家自然科学基金委员会制



国家自然科学基金资助项目计划书填报说明 （预算制项目）

- 一、项目负责人收到《国家自然科学基金资助项目批准通知》（以下简称《批准通知》）后，请认真阅读本填报说明，参照国家自然科学基金相关项目管理办法和新修订的《国家自然科学基金资助项目资金管理办法》（以下简称《资金管理办法》，请查阅国家自然科学基金委员会官方网站首页“政策法规”栏目），按《批准通知》的要求认真填写和提交《国家自然科学基金资助项目计划书》（以下简称《计划书》）。
- 二、填写《计划书》时要科学严谨、实事求是、表述清晰、准确。《计划书》经国家自然科学基金委员会相关项目管理部门审核批准后，将作为项目研究计划执行、检查和验收的依据。
- 三、《计划书》各部分填写要求如下：
 - （一）简表：由系统自动生成。
 - （二）摘要及关键词：各类获资助项目都应当填写中、英文摘要及关键词。
 - （三）项目组主要成员：计划书中列出姓名的项目组主要成员由系统自动生成，与申请书原成员保持一致，不可随意调整。如果《批准通知》所附“项目评审意见及修改意见表”中“修改意见”栏目有调整项目组成员相关要求的，待项目开始执行后，按照项目成员变更程序另行办理。
 - （四）资金预算表：根据批准的项目资助额度，按规定调整项目预算，并按照《国家自然科学基金项目计划书预算表编制说明》填报资金预算表和预算说明书。
 - （五）正文：
 1. 面上项目、地区科学基金项目：如果《批准通知》所附“项目评审意见及修改意见表”中“修改意见”栏目没有修改要求的，只需选择“研究内容和研究目标按照申请书执行”即可；如果《批准通知》中上述栏目明确要求调整研究期限或研究内容等的，须选择“根据研究方案修改意见更改”并填报相关修改内容。
 2. 重点项目、重点国际（地区）合作研究项目、重大项目、重大研究计划重点支持项目、重大研究计划集成项目、国家重大科研仪器研制项目、联合基金项目、原创探索计划项目：须选择“根据研究方案修改意见更改”，根据《批准通知》的要求填写研究（研制）内容，不得自行降低、更改研究目标（或仪器研制的技术性能与主要技术指标、验收技术指标等）或缩减研究（研制）内容。此外，还要突出以下几点：
 - （1）研究的难点和在实施过程中可能遇到的问题（或仪器研制风险），拟采用的研究（研制）方案和技术路线；
 - （2）项目主要参与者分工，合作研究单位（如有）之间的关系与分工，重大项目还需说明课题之间的关联；
 - （3）详细的年度研究（研制）计划。
 3. 创新研究群体项目：须选择“根据研究方案修改意见更改”，按下列提纲撰写：



- (1) 研究方向；
 - (2) 结合国内外研究现状，说明研究工作的学术思想和科学意义（限两个页面）；
 - (3) 研究内容、研究方案及预期目标（限两个页面）；
 - (4) 年度研究计划；
 - (5) 研究队伍的组成情况。
4. 基础科学中心项目：须选择“根据研究方案修改意见更改”，根据《批准通知》的要求和现场考察专家组的意见和建议，进一步完善并细化研究计划，按下列提纲撰写：
 - (1) 五年拟开展的研究工作（包括主要研究方向、关键科学问题与研究内容）；
 - (2) 研究方案（包括骨干成员之间的分工及合作方式、学科交叉融合研究计划等）；
 - (3) 年度研究计划；
 - (4) 五年预期目标和可能取得的重大突破等；
 - (5) 研究队伍的组成情况。
 5. 数学天元基金项目：天元前沿重点专项项目和数学与其他学科交叉联合资助项目，参照重点项目的方式进行选择和填写；其他类型项目，参照面上项目的方式进行选择和填写。
 6. 对于其他类型项目，参照面上项目的方式进行选择和填写。



简表

项目负责人信息	姓 名	郝笑龙	性 别	男	出生年月	1990年04月	民 族	汉族
	学 位	博士			职称	副教授		
	是否在站博士后	否			电子邮件	haoxiaolong@scau.edu.cn		
	电 话	18846080538			个人网页	https://ibe.scau.edu.cn/2022/1017/c13910a327251/page.psp		
	工 作 单 位	华南农业大学						
	所 在 院 系 所	生物质工程研究院						
依托单位信息	名 称	华南农业大学					代码	51064208A0499
	联 系 人	唐家林			电子邮件	kycjkh@scau.edu.cn		
	电 话	020-85280070			网站地址	http://kjc.scau.edu.cn/		
合作单位信息	单 位 名 称							
项目基本信息	项 目 名 称	超高木质纤维含量木塑复合材料动态界面流变机理						
	资 助 类 别	面上项目				亚 类 说 明		
	附 注 说 明							
	申 请 代 码	C1603:木材物理学						
	基 地 类 别							
	执 行 年 限	2025.01-2028.12						
	直 接 费 用	50万元						



项目摘要

中文摘要:

大幅度提高木质纤维用量能够显著降低成本并为赋予木塑复合材料阻燃等功能创造条件, 备受产业和学术界关注。超高木质纤维含量(85wt.%以上)木塑复合材料(UH-WPCs), 尤其在成型加工过程中, 界面与流变极其复杂且相互作用强烈, 两者存在时间与空间维度的交叉和重叠, 呈现界面和态演变与加工流变动态耦合, 即动态界面流变机理。由于超高含量木质纤维的存在, UH-WPCs体系很难形成典型的聚合物连续相, 现有的热力学界面和基于平衡态的流变学理论已不适用于UH-WPCs体系, 其非典型界面作用机制与非线性流变行为的关联性尚不明确, 相关研究鲜有报道。界面和流变学始终是贯穿木塑结构-加工-性能的关键科学问题, 本项目拟通过研究UH-WPCs体系的非典型界面作用机制、非线性流变规律、界面与流变动态耦合, 揭示超高木质纤维含量木塑动态界面流变机理, 为UH-WPCs的设计和高效制备提供科学依据, 实现理论和技术原理的源头创新。

Abstract:

Significantly increasing the wood fiber content is an effective way to reduce the production cost of the wood-plastic composites and create conditions for giving them flame retardant and other functions, which has attracted much attentions of industrial and academic circles. The ultra-high filling (more than 85wt.%) wood-plastic composites (UH-WPCs) exhibit extremely complex and strongly interacting interface and rheological properties especially in the process of molding and processing, which occurs a crossover and overlap in both temporal and spatial dimensions. It presents the dynamic coupling between the interface phase evolution and processing rheology, namely the dynamic interface-rheology mechanism. It is difficult to form a typical continuous phase structure in UH-WPCs owing to the presence of ultra-high amount of wood fiber, which results in that the existing thermodynamic interface mechanism and rheological theory based on equilibrium state are not applicable to the UH-WPCs system. The relevance of the mechanism of atypical interface action to nonlinear rheological behavior is unclear, and the related studies are rarely reported. Interface and rheology are always the key scientific issues throughout the structure-processing-performance of the wood-plastic composites. This project intends to study the mechanism of atypical interface action, nonlinear rheological behavior and their dynamic coupling, which can reveal the dynamic interface-rheology mechanism of UH-WPCs. This study can provide scientific basis for the design and efficient preparation of UH-WPCs, and realize the source innovation of theory and technical principles.

关键词(用分号分开): 木塑复合; 流变学; 超高填充; 动态界面流变; 木质纤维

Keywords(用分号分开): Wood-plastic composites; Rheology; Ultra-high filling; Dynamic interface-rheology mechanism; Wood fiber



项目组主要成员

编号	姓名	出生年月	性别	职称	学位	单位名称	电话	证件号码	项目分工	每年工作 时间 (月)	
1	郝笑龙	1990.04	男	副教授	博士	华南农业大学	18816080538	130131199004190312	项目负责人	10	
2	王清文	1961.07	男	教授	博士	华南农业大学	18813966430	230107196107010410	理论与方向指导	6	
3	周海洋	1994.10	女	讲师	博士	华南农业大学	13936330340	232321199410191529	界面作用机制分析	10	
总人数		高级		中级		初级		博士后		博士生	硕士生
7		2		1		0		0		2	2



国家自然科学基金预算制项目预算表

项目批准号：32471786

项目负责人：郝笑龙

金额单位：万元

序号	科目名称	金额
1	一、科学基金资助项目直接费用合计	50.0000
2	1、设备费	0.0000
3	其中：设备购置费	0.0000
4	2、业务费	40.0000
5	3、劳务费	10.0000
6	二、其他来源资金	0.0000
7	三、合计	50.0000

注：请按照项目研究实际需要合理填写各科目预算金额。



预算说明书

一、科学基金资助项目直接费用

请按照《国家自然科学基金项目计划书预算编制说明》等有关要求，按照政策相符性、目标相关性和经济合理性原则，实事求是编制项目预算。填报时，直接费用应按设备费、业务费、劳务费三个科目填报，每个科目结合科研任务按支出用途进行说明。

1. 设备费（是指在项目实施过程中购置或试制专用仪器设备，对现有仪器设备进行升级改造，以及租赁外单位仪器设备而发生的费用。计算类仪器设备和软件工具可在设备费科目列支。填报时，应对设备费支出的必要性和测算的合理性等内容进行说明。单价大于50万元（含50万元）的设备需补充说明设备的主要性能指标、主要技术参数等内容；单价小于50万元的设备仅需按照设备购置费、试制改造费和租赁使用费分类进行说明即可。）

无。

2. 业务费（是指项目实施过程中消耗的各种材料、辅助材料等低值易耗品的采购、运输、装卸、整理等费用，发生的测试化验加工、燃料动力、出版/文献/信息传播/知识产权事务、会议/差旅/国际合作交流等费用，以及其他相关支出。）

2.1 材料费：16.00 万元，占总经费 32.00%

主要用于原材料购置、加工及运费，试剂购买等，其中：

- （1）竹子、木材、稻壳、秸秆等运输、粉碎、干燥处理，8 吨，费用 $8 \times 0.15 = 1.20$ 万元；
- （2）购置高密度聚乙烯（HDPE）树脂 4 吨，费用 $4 \times 1.20 = 4.80$ 万元；
- （3）购置聚丙烯（PP）树脂 4 吨，费用 $4 \times 1.10 = 4.40$ 万元；
- （4）购置偶联剂（MAPE、MAPP）0.6 吨，费用 $0.6 \times 2.00 = 1.20$ 万元；
- （5）购置木塑复合润滑剂 0.4 吨，费用 $0.4 \times 1.5 = 0.60$ 万元；
- （6）购置抗氧剂 1010、紫外光吸收剂、热稳定剂等助剂 0.1 吨，费用 $0.1 \times 10.00 = 1.00$ 万元；
- （7）购置木塑无机添加剂二氧化硅、滑石粉、钙粉等，费用 1.00 万元；
- （8）购置其他化学试剂、玻璃仪器、氧气、氮气、液氮、坩埚等耗材，费用 1.80 万元。

2.2 测试化验加工费：9.00 万元，占总经费的 18.00%

团队的设备免费测试只需购买耗材。如下测试费用用于在华南农业大学测试中心和外单位测试所发生费用，其中：

- （1）显微分析（TEM、SEM）： $50 \times 0.02 = 1.00$ 万元；
- （2）X 射线断层扫描分析（X- μ CT）： $50 \times 0.03 = 1.5$ 万元；
- （3）原位变温激光显微拉曼测试： $25 \times 0.04 = 1.00$ 万元；
- （4）原位变温红外光谱分析： $50 \times 0.03 = 1.50$ 万元；
- （5）原位变温固体核磁共振分析： $30 \times 0.05 = 1.50$ 万元；
- （6）原位变温 XRD： $50 \times 0.03 = 1.50$ 万元；
- （7）双料筒毛细管流变仪： $100 \times 0.005 = 0.50$ 万元；
- （8）高温凝胶渗透色谱仪： $50 \times 0.01 = 0.50$ 万元。

2.3 燃料动力费：无

2.4 出版/文献/信息传播/知识产权事务费：1.22 万元，占总经费 2.44%

文献资料检索费、科技查新费、打印复印费、快递费等：1.22 万元。

2.5 会议/差旅/国际合作交流费：13.78 万元，占总经费 27.56%



（1）主要用于项目组成员国内调研、学习、学术交流等，计 5.09 万元；

交通费（机票、火车票）：3 人·次×3000 元/人·次×4 年=3.60 万元；

住宿费：3 人·次×350 元/人·天×2 天/年×4 年=0.84 万元；

伙食及市内交通补助：3 人·次×3 天/年×180 元/人·天×4 年=0.65 万元。

（2）主要用于项目组成员参加国内学术会议等，计 8.69 万元；

会议注册费：3 人·次×3000 元/人·次×4 年=3.60 万元；

交通费（机票、火车票）：3 人·次×3000 元/人·次×4 年=3.60 万元；

住宿费：3 人·次×350 元/人·天×2 天/年×4 年=0.84 万元；

伙食及市内交通补助：3 人·次×3 天/年×180 元/人·天×4 年=0.65 万元。

3. 劳务费（是指在项目实施过程中支付给参与项目研究的研究生、博士后、访问学者以及项目聘用的研究人员、科研辅助人员等的劳务性费用，以及支付给临时聘请的咨询专家的费用等。填报时，应综合考量劳务费支出对象所承担研究任务的必要性、投入本项目的工作时长、费用标准的合理性等因素。）

劳务费：10.00 万元，占经费 20.00%

博士生 2 人，每人每月 1000 元，每人每年参与 8 个月；硕士生 2 人，每人每月 700 元，每人每年参与 8 个月。

劳务费：1000*2*8*4(年)+700*2*8*3(年)=97600 元；其他劳务费 0.24 万元，共计：10.00 万元。

二、其他来源资金

对其他来源资金的经费来源、主要用途、支出预算做简要说明。

无。

三、合作研究外拨资金

对合作研究单位承担研究任务及资金外拨情况进行必要说明。如存在多个合作研究单位，请逐一说明。如存在资金外拨的情况，还需对外拨资金的金额进行重点说明。

无。



报告正文

研究内容和研究目标按照申请书执行。



国家自然科学基金项目负责人、依托单位承诺书

国家自然科学基金项目负责人承诺书

本人郑重承诺：我接受国家自然科学基金的资助，严格遵守中共中央办公厅、国务院办公厅《关于进一步加强科研诚信建设的若干意见》《关于进一步弘扬科学家精神加强作风和学风建设的意见》《关于加强科技伦理治理的意见》《科技伦理审查办法（试行）》等规定，和国家自然科学基金委员会关于资助项目管理、项目资金管理等各项规章，在《计划书》填写及项目执行过程中：

（一）按照《批准通知》《国家自然科学基金资助项目计划书填报说明》的要求填写《计划书》，未自行降低、更改目标任务或约定要求，或缩减研究（研制）内容；

（二）树立“红线”意识，严格履行科研合同义务，按照《计划书》负责实施本项目（批准号：32471786），切实保证研究工作时间，按时报送有关材料，及时报告重大情况变动，不违规将科研任务转包、分包他人，不以项目实施周期外或不相关成果充抵交差；

（三）遵守科研诚信、科技伦理规范和学术道德，认真开展研究工作，对资助项目发表的论著和取得的研究成果按规定进行标注，不在非本项目资助的成果或其他无关成果上标注本项目批准号，反对无实质学术贡献者“挂名”，不在成果署名、知识产权归属等方面侵占他人合法权益，并如实报告本人及项目组成员发生的违背科研诚信要求的任何行为；

（四）尊重科研规律，弘扬科学家精神，严谨求实，追求卓越，反对浮夸浮躁、投机取巧，不人为夸大学术或技术价值，不传播未经科学验证的现象和观点；

（五）将项目资金全部用于与本项目研究工作相关的支出，并结合科研活动需要，科学合理安排项目资金支出进度；

（六）做好项目组成员的教育和管理，确保遵守以上相关要求。

如违背上述承诺，本人愿接受国家自然科学基金委员会和相关部门做出的各项处理决定。

项目负责人（签字）：

年 月 日

依托单位科研管理部门：

负责人（签章）：

年 月 日

依托单位财务管理部门：

负责人（签章）：

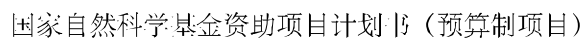
年 月 日

国家自然科学基金项目依托单位承诺书

我单位同意承担上述国家自然科学基金项目，将保证项目负责人及其研究队伍的稳定和研究项目实施所需的条件，严格遵守中共中央办公厅、国务院办公厅《关于进一步加强科研诚信建设的若干意见》《关于进一步弘扬科学家精神加强作风和学风建设的意见》《关于加强科技伦理治理的意见》《科技伦理审查办法（试行）》等规定，和国家自然科学基金委员会有关资助项目管理、项目资金管理、科研诚信管理和科技伦理管理等各项规定，并督促实施。

依托单位（公章）

年 月 日



本栏目由自然科学基金委填写

负责人（签章）：
年 月 日

负责人（签章）：
年 月 日

受理编号: c23140500002189

项目编号: 2023A1515012640

文件编号: 粤基金字(2023)2号

广东省基础与应用基础研究基金项目 任务书

项目名称: 超高木质纤维含量木塑复合材料非热力学界面作用机制

项目类别: 广东省自然科学基金-面上项目

项目起止时间: 2023-01-01 至 2025-12-31

管理单位(甲方): 广东省基础与应用基础研究基金委员会

依托单位(乙方): 华南农业大学

通讯地址: 广东省广州市天河区五山路483号

邮政编码: 510642

单位电话: 020-85283435

项目负责人: 郝笑龙

联系电话: 02085285596



(广东科技微信公众号)



(查看任务书信息)



(受理纸质材料二维码)

广东省基础与应用基础研究
基金委员会
二〇二〇年制

填写说明

一、项目任务书内容原则上要求与申报书相关内容保持一致，不得无故修改。

二、项目承担单位通过广东省科技业务管理阳光政务平台下载项目任务书，按要求完成签名盖章后扫描上传到广东省科技业务管理阳光政务平台。

三、签名盖章说明。请分别在单位工作分工及经费分配情况页、人员信息页、签约各方页等地方按要求签字或盖章，签章不合规或错漏将不予受理。其中，人员信息页要求所有参与人员本人亲笔签名，代签或印章无效，漏签将不予受理。

四、本任务书自签字并加盖公章之日起生效，各方均应负本任务书的法律责任，不应受机构、人事变动影响。

五、根据《广东省科学技术厅广东省财政厅关于深入推进省基础与应用基础研究基金项目经费使用“负面清单+包干制”改革试点工作的通知》（粤科规范字[2022]2号），2022年度及以后立项资助的全部省基金项目（包括省自然科学基金、省市联合基金、省企联合基金项目等）均适用“负面清单+包干制”，项目提交申请书和任务书时无需编制费用明细科目预算。

一、主要研究内容和要达到的目标

主要研究内容

本项目提出UH-WPCs异质不相容两相非热力学相容性界面作用机制问题，主要从以下几个方面展开系统研究：

（1）聚合物熔体对超高含量木质纤维动态塑化原理研究

UH-WPCs在熔融制备过程中，木质纤维在高温/压力/剪切交互作用下发生塑性变形和松弛过程（黏弹性行为），聚合物熔体主要对木质纤维进行表面浸润和细胞腔填充等作用。研究少量界面相容剂和润滑剂存在时，通过压力和温度的调控，采用流变学方法分析少量聚合物熔体对超高含量木质纤维动态塑化原理，重点包括聚合物熔体/木质纤维动态浸润及界面处扩散规律。

（2）超高含量木质纤维/聚合物微纳界面层动态演变与形成机制研究

超高木质纤维含量木塑复合材料体系在混合、流变加工过程中，聚合物由连续相变为分散相，在复杂加工流场中（高温、高压和剪切）表现出异于传统热塑性复合材料两相之间的界面相互作用，重点是UH-WPC加工制备过程中异质不相容两相多尺度、多阶段的微纳界面层动态演变与形成机制：1）木质纤维多尺度结构下的超高含量木质纤维/聚合物微纳界面层形成及耦合机制，包括界面形貌、界面物理等；2）聚合物熔体对超高含量木质纤维动态塑化过程中不同时间维度下的微纳界面层的动态演变机制，重点研究界面流变学规律。

（3）超高含量木质纤维/聚合物非热力学界面作用机制研究

基于超高木质纤维含量木塑体系的结构特点与加工特性，重点是从高温高压环境下动态塑化原理及异质不相容两相微纳界面层动态演变和形成过程入手，建立微纳界面模型，分析复杂加工流场下超高含量木质纤维/聚合物动态演变对UH-WPCs非热力学界面相容性的作用机制。

（4）UH-WPCs加工过程中不相容两相动态塑化-非热力学界面-宏观性能之间的联动机制

基于（1）（2）（3）的研究和综合分析，对UH-WPCs进行界面、流变、和宏观物理力学等性能测试，研究加工过程中复杂环境下不相容两相动态塑化、非热力学界面对UH-WPCs宏观性能的影响规律，构建异质不相容两相表界面性质与宏观性能之间的内在联系，揭示宏观性能变化的内在机制，为UH-WPCs界面的优化和设计、以及宏观性能的调控提供理论依据。

研究目标

（1）弄清在复杂加工流场下的少量聚合物熔体对超高含量木质纤维动态塑化机理；

（2）解析超高含量木质纤维/聚合物微纳界面层动态演变与形成机制，阐明UH-WPCs非热力学界面相容性的作用原理；

（3）揭示UH-WPCs加工过程中不相容两相动态塑化-非热力学界面-宏观性能之间的联动机制。

二、项目预期获得的科研成果及形式

论文及专著情况	国家统计局源刊物以上刊物 发表论文（篇）		3		科技报告（篇）		1	
	其中被SCI/EI/ISTP收录 论文数（篇）		2		培养人才（人）			
	专著（册）				引进人才（人）			
专利情况(项)	发明专利		实用新型专利		外观设计专利		国外专利	
	申请	授权	申请	授权	申请	授权	申请	授权

三、项目进度和阶段目标

(一) 项目起止时间: 2023-01-01 至 2025-12-31		
(二) 项目实施进度及阶段主要目标:		
开始日期	结束日期	主要工作内容
2023-01-01	2023-12-31	(1) 购买原材料, 制备不同基体和木质纤维种类的超高填充木塑复合材料; (2) 表征复杂加工流场下聚合物熔体对超高含量木质纤维动态塑化过程; (3) 撰写相关论文1篇。
2024-01-01	2024-12-31	(1) 表征不同基体和木质纤维种类的超高填充木塑复合材料界面及流变行为; (2) 分析超高含量木质纤维/聚合物微纳界面层动态演变与形成过程; (3) 撰写相关论文1篇。
2025-01-01	2025-12-31	(1) 揭示超高木质纤维含量木塑复合材料非热力学界面作用机制; (2) 撰写阶段性论文1篇; (3) 撰写项目结题报告1份。

四、项目总经费及省基金委经费预算

1. 省基金委经费下达总额： （大写）壹拾万圆整；（小写 ）10万元；					
2. 省基金委经费年度下达计划：					
年度	2023 年	年	年	年	年
经费(万元)	10.00				

五、人员信息

项目负责人								
姓名	证件号码	年龄	性别	职称	学历	在项目中承担的任务	所在单位	签名
郝笑龙	130431199004190312	33	男	助理研究员	博士研究生	项目负责人	华南农业大学	

项目组主要成员								
姓名	证件号码	年龄	性别	职称	学历	在项目中承担的任务	所在单位	签名
周海洋	232321199410191529	29	女	讲师	博士研究生	超高填充木塑制备及性能表征	华南农业大学	
欧荣贤	430419198407040011	39	男	副研究员	博士研究生	超高填充木塑非热力学行为研究	华南农业大学	
王清文	230107196107010410	62	男	教授	博士研究生	超高填充木塑界面理论指导	华南农业大学	
徐俊杰	421121199505054010	28	男	未取得	硕士研究生	超高填充木塑动态塑化研究	华南农业大学	
罗怡山	510105200008070526	23	女	未取得	本科	超高填充木塑界面流变学表征	华南农业大学	
韦妍慧	452731200009010040	23	女	未取得	本科	超高填充木塑物理力学表征	华南农业大学	

六、工作分工及财政经费分配

承担/参与单位名称 (盖章)	工作分工	省级财政科技资金分配 (万元)
华南农业大学	项目申报依托单位，负责项目管理，项目实施和完成过程中的场地，水、电、机制保障等。	10.00
	合计	10.00

七、任务书条款

第一条 甲方与乙方根据《中华人民共和国民法典》及国家有关法规和规定，按照《广东省科学技术厅关于广东省基础与应用基础研究基金（省自然科学基金、联合基金等）项目管理的实施细则（试行）》《广东省省级科技计划项目验收结题工作规程（试行）》等规定，为顺利完成（2023）年超高木质纤维含量木塑复合材料非热力学界面作用机制专项项目（文件编号：粤基金字（2023）2号）经协商一致，特订立本任务书，作为甲乙双方在项目实施管理过程中共同遵守的依据。

第二条 甲方的权利义务：

1. 按任务书规定进行经费核拨的有关工作协调。
2. 根据甲方需要，在不影响乙方工作的前提下，定期或不定期对乙方项目的实施情况和经费使用情况进行检查或抽查。
3. 根据《广东省科研诚信管理办法(试行)》等规定对乙方进行科技计划信用管理。

第三条 乙方的权利义务：

1. 确保落实自筹经费及有关保障条件。
2. 按任务书规定，对甲方核拨的经费实行专款专用，单独列账，并随时配合甲方进行监督检查。
3. 经费使用按照广东省级财政科研项目经费使用等有关规定进行管理。
4. 项目依托单位应制定经费使用“负面清单+包干制”内部管理制度并报甲方备案。
5. 使用财政资金采购设备、原材料等，按照《广东省实施〈中华人民共和国招标投标法〉办法》有关规定，符合招标条件的须进行招标。
6. 项目任务书任务完成后，或任务书规定的任务、指标及经费投入等提前完成的，乙方可提出验收结题申请，并按甲方要求做好项目验收结题工作。
7. 若项目发生需要终止结题的情况，乙方须提出终止结题申请，并按甲方要求做好项目终止结题工作。
8. 在每年规定时间内向甲方如实提交上年度工作情况报告，报告内容包含上年度项目进展情况、经费决算和取得的成果等。
9. 按照国家和省有关规定，提交科技报告及其他材料。
10. 利用甲方的经费获得的研究成果，项目负责人和参与者应当注明获得“广东省基础与应用基础研究基金（英文：Guangdong Basic and Applied Basic Research Foundation）（项目编号）”资助或作有关说明。
11. 乙方要恪守科学道德准则，遵守科研活动规范，践行科研诚信要求，不得抄袭、剽窃他人科研成果或者伪造、篡改研究数据、研究结论；不得购买、代写、代投论文，虚构同行评议专家及评议意见；不得违反论文署名规范，擅自标注或虚假标注获得科技计划（专项、基金等）等资助；不得弄虚作假，骗取科技计划（专项、基金等）项目、科研经费以及奖励、荣誉等；不得有其他违背科研诚信要求的行为。
12. 确保本项目开展的研究工作符合我国科技伦理管理相关规定。

第四条 在履行本任务书的过程中，如出现广东省相关政策法规重大改变等不可抗力情况，甲方有权对所核拨经费的数量和时间进行相应调整。

第五条 在履行本任务书的过程中，当事人一方发现可能导致项目整体或部分失败的情形时，应及时通知另一方，并采取适当措施减少损失，没有及时通知并采取适当措施，致使损失扩大的，应当就扩大的损失承担责任。

第六条 本项目技术成果的归属、转让和实施技术成果所产生的经济利益的分享，除双方另有约定外，按国家和广东省有关法规执行。

第七条 根据项目具体情况，经双方另行协商订立的附加条款，作为本任务书正式内容的一部分，与本任务书具有同等效力。

第八条 本任务书一式三份，各份具有同等效力。甲、乙方及项目负责人各执一份，三方签字、盖章后即生效，有效期至项目结题后一年内。各方均应负任务书的法律责任，不应受机构、人事变动的影响。

第九条 乙方必须接受甲方聘请的本项目任务书监理单位的监督和管理。监理单位按照甲方赋予的权利对本项目任务书的履行进行审核、进度调查，对项目任务书变更、经费使用情况进行监督管理及组织项目验收。

说明：1. 本任务书中，凡是当事人约定无需填写的内容，应在空白处划（/）。

2. 委托代理人签订本任务书的，应出具合法、有效的委托书。

检索证明

根据委托人提供的论文材料，委托人华南农业大学材料与能源学院 周海洋 17 篇论文收录情况如下表。

序号	论文名称	发表刊物及发表的年月卷期/页码等	作者排名	论文等级	作者文中单位	收录情况	影响因子	中科院大类分区
1	Nanostructured multifunctional wood hybrids fabricated via in situ mineralization of zinc borate in hierarchical wood structures	CHEMICAL ENGINEERING JOURNAL 出版年: 2023 出版日期: JAN 1 卷期: 451 页码: - 文献号: 138308 文献类型: Article	第一	T2 类	华南农业大学	SCI	IF2-year=13.4 IF5-year=13.2 (2023)	工程技术 1 区 Top 期刊: 是 (2023)
2	Recycling end-of-life WPC products into ultra-high filled, high-performance wood fiber/polyethylene composites: a sustainable strategy for clean and cyclic processing in the WPC industry	JOURNAL OF MATERIALS RESEARCH AND TECHNOLOGY-JMR&T 出版年: 2022 出版日期: MAY-JUN 卷期: 18 页码: 1-14 文献号: 091 文献类型: Article	第一	T2 类	华南农业大学	SCI	IF2-year=6.4 IF5-year=6.4 (2022)	材料科学 1 区 Top 期刊: 是 (2022)
3	Simultaneously strengthening and toughening reprocessable basswood through reactive waterborne acrylic	CHEMICAL ENGINEERING JOURNAL 出版年: 2024	共同通讯作者	T2 类	华南农业大学	SCI	IF2-year=13.2 IF5-year=13.5 (2024)	材料科学 1 区 Top 期刊: 是 (2025)

	resin impregnation	出版日期: JUN 1 卷期: 489 页码: - 文献号: 151313 文献类型: Article					
4	Conductive and fire-retardant wood/polyethylene composites based on a continuous honeycomb-like nanoscale carbon black network	CONSTRUCTION AND BUILDING MATERIALS 出版年: 2020 出版日期: FEB 10 卷期: 233 页码: - 文献号: 117369 文献类型: Article	第一	P2 类	华南农业大学	SCI	IF2-year=6.141 IF5-year=6.841 (2020) 工程技术 1 区 Top 期刊: 是 (2020)
5	Comparative study on the effects of silica size and dispersion mode on the fire retardancy of extruded wood fiber/HDPEcomposites	POLYMER COMPOSITES 出版年: 2020 出版日期: NOV 卷期: 41 11 页码: 4920-4932 文献类型: Article	第一	B 类	华南农业大学	SCI	IF2-year=3.171 IF5-year=2.877 (2020) 材料科学 3 区 Top 期刊: 否 (2020)
6	Mechanical Properties and Fire Retardancy of Wood Flour/High-Density Polyethylene Composites Reinforced with Continuous Honeycomb-Like Nano-SiO ₂ Network and Fire Retardant	JOURNAL OF RENEWABLE MATERIALS 出版年: 2020 卷期: 8 5 页码: 485-498 文献类型: Article	第一	B 类	华南农业大学	SCI	IF2-year=1.67 IF5-year=1.793 (2020) 材料科学 4 区 Top 期刊: 否 (2020)

7	Preparation of waterborne intumescent flame-retardant coatings using adenosine-based phosphonates for wood surfaces	PROGRESS IN ORGANIC COATINGS 出版年: 2024 出版日期: FEB 卷期: 187 页码: - 文献号: 108061 文献类型: Article	共同通讯 作者	A类	华南农业大学	SCI	IF2-year=7.3 IF5-year=7.0 (2024)	材料科学 2区 Top 期刊: 否 (2025)
8	Phenol Liquefaction of Waste Sawdust Pretreated by Sodium Hydroxide: Optimization of Parameters Using Response Surface Methodology	MOLECULES 出版年: 2022 出版日期: NOV 卷期: 27 22 页码: - 文献号: 7880 文献类型: Article	共同通讯 作者	A类	华南农业大学	SCI	IF2-year=4.6 IF5-year=4.9 (2022)	化学 2区 Top 期刊: 是 (2022)
9	Effects of fiber geometry and orientation distribution on the anisotropy of mechanical properties, creep behavior, and thermal expansion of natural fiber/HDPE composites	COMPOSITES PART B- ENGINEERING 出版年: 2020 出版日期: MAR 15 卷期: 185 页码: - 文献号: 107778 文献类型: Article	并列第一 作者	T2类	华南农业大学	SCI	IF2-year=9.078 IF5-year=8.234 (2020)	工程技术 1区 Top 期刊: 是 (2020)
10	Effects of SiO ₂ Filler in the Shell and Wood Fiber in the Core on the Thermal Expansion of Core- Shell Wood/Polyethylene Composites	POLYMERS 出版年: 2020 出版日期: NOV	第二	B类	华南农业大学	SCI	IF2-year=4.329 IF5-year=4.493 (2020)	工程技术 3区 Top 期刊: 否 (2020)

		卷期: 12 11 页码: - 文献号: 2570 文献类型: Article					
11	Interfacial adhesion mechanisms of ultra-highly filled wood fiber/polyethylene composites using maleic anhydride grafted polyethylene as a compatibilizer	MATERIALS & DESIGN 出版年: 2021 出版日期: DEC 15 卷期: 212 页码: - 文献号: 110182 文献类型: Article	第三	T2类	华南农业大	SCI	IF2-year=9.417 IF5-year=8.272 (2021) 材料科学 1区 Top 期刊: 是 (2021)
12	Constructing a rigid-flexible grid structure for simultaneously strengthening and toughening bamboo flour/plastic composites through the introduction of continuous carbon fabric meshes via multi-layer co-extrusion	COMPOSITES SCIENCE AND TECHNOLOGY 出版年: 2023 出版日期: SEP 29 卷期: 242 页码: - 文献号: 110204 文献类型: Article	第三	T2类	华南农业大	SCI	IF2-year=8.3 IF5-year=8.1 (2023) 材料科学 1区 Top 期刊: 是 (2023)
13	Rapid production of high-performance unilaterally surface-densified wood through integrating mechanical compression and thermochemical modification	CONSTRUCTION AND BUILDING MATERIALS 出版年: 2024 出版日期: NOV 29 卷期: 453 页码: - 文献号: 139014 文献类型: Article	第三	T2类	华南农业大	SCI	IF2-year=8.0 IF5-year=8.6 (2024) 工程技术 1区 Top 期刊: 是 (2025)

14	Efficient fractionation of lignin from <i>Camellia oleifera</i> shell by acidic deep eutectic solvent under mild conditions	JOURNAL OF INDUSTRIAL AND ENGINEERING CHEMISTRY 出版年: 2025 出版日期: JUN 25 卷期: 146 页码: 697-704 文献类型: Article	第四	B 类	华南农业大学	SCI	IF2-year=6.0 IF5-year=5.8 (2024)	工程技术 3 区 Top 期刊: 否 (2025)
15	Mechanical properties, morphology, and creep resistance of ultra-highly filled bamboo fiber/polypropylene composites: Effects of filler content and melt flow index of polypropylene	CONSTRUCTION AND BUILDING MATERIALS 出版年: 2021 出版日期: DEC 6 卷期: 310 页码: - 文献号: 125289 文献类型: Article	第四	A 类	华南农业大学	SCI	IF2-year=7.693 IF5-year=8.194 (2021)	工程技术 2 区 Top 期刊: 是 (2021)
16	Dimensional stability improvements of waste wood flour/HDPE composites via carbon black network embedding	CONSTRUCTION AND BUILDING MATERIALS 出版年: 2021 出版日期: SEP 13 卷期: 299 页码: - 文献号: 123955 文献类型: Article	第四	A 类	华南农业大学	SCI	IF2-year=7.693 IF5-year=8.194 (2021)	工程技术 2 区 Top 期刊: 是 (2021)
17	Optimizing the rheological and mechanical properties of ultra-highly filled wood	COMPOSITES SCIENCE AND TECHNOLOGY 出版年: 2024	第四	A 类	华南农业大学	SCI	IF2-year=9.8 IF5-year=9.3 (2024)	材料科学 2 区 Top 期刊: 是 (2025)

fiber/polyethylene composites through binary alloy matrix strategy	出版日期: SEP 29 卷期: 256 页码: - 文献号: 110740 文献类型: Article						
---	---	--	--	--	--	--	--

说明: 论文等级和中科院大类分区按《华南农业大学学位论文评价方案(试行)》划分。

报告免责声明: 如未盖章, 报告无效



华南农业大学图书馆SCA ULIB202518887



Nanostructured multifunctional wood hybrids fabricated *via in situ* mineralization of zinc borate in hierarchical wood structures

Haiyang Zhou^{a,b,c}, Dongxian Wen^b, Xiaolong Hao^{a,b,c}, Chuanfu Chen^{a,b,c}, Nianhan Zhao^{a,b}, Rongxian Ou^{a,b,c,*}, Qingwen Wang^{a,b,c}

^a Institute of Biomass Engineering, South China Agricultural University, Guangzhou 510642, China

^b Key Laboratory for Biobased Materials and Energy of Ministry of Education, College of Materials and Energy, South China Agricultural University, Guangzhou 510642, China

^c Guangdong Laboratory for Lingnan Modern Agricultural Science and Technology, Guangzhou 510642, China

ARTICLE INFO

Keywords:

Multifunctional wood
Mineralization
Zinc borate
Nanostructured

ABSTRACT

Developing feasible and eco-friendly methods to fabricate multifunctional wood remains an imperative yet challenging task. Prompted by biomineralization, this study proposes the fabrication of nanostructured wood hybrids with efficient flame retardancy, smoke suppression, mold resistance, and antitermite activity *via in situ* mineralization of nanosized zinc borate (ZnB) particles in a hierarchical void system of wood. ZnB was successfully deposited in the hierarchical nano/microporous cell wall structures, as confirmed by X-ray microtomography and energy-dispersive X-ray spectroscopy. The mineralized wood exhibited excellent heat insulation performance during combustion. The limiting oxygen index of the mineralized wood with 22.1 wt% ZnB (MW₂₂) increased from 22.6% of the untreated wood to 41.2%. Cone calorimetry testing revealed reductions of 51.4%, 89.0%, and 79.5% in average CO yields, total smoke production, and maximum smoke production ratio, respectively, in MW₂₂ relative to those in the untreated wood; the peak heat release rate and total heat release also decreased by 46.9% and 47.9%, respectively. A noncombustible film of molten ZnB covered and cross-linked the carbonaceous char layer, forming a cohesive and robust 3D residual skeleton, which endowed thermal insulation to the wood, delayed oxygen diffusion, reduced flammable gas release, and suppressed toxic smoke. Antitermite tests showed a mothproofing rating of 10 for MW₂₂, far higher than the rating of 4 for untreated wood. Moreover, MW₂₂ exhibited exceptional mold resistance, with an average infection of 0 and an average protective efficiency of 100%. Therefore, *in situ* mineralization of the wood cell wall architecture with ZnB provides a facile and feasible strategy to fabricate multifunctional integrated wood, which is suitable for scaling up and can be potentially used in modern green buildings.

1. Introduction

Natural wood has been applied for millennia in building and furniture industries, benefiting not only from its exceptional mechanics but also from its environmental characteristics, including bioregulation, carbon neutrality, and renewability, among others [1]. As a material intimately in contact with humans, wood is a potential fire hazard, in addition to its susceptibility to mold growth and termite attack, because of its intrinsic chemical structures. These deficiencies of natural wood lead to significant economic losses, endanger human health, and pose a threat to life safety. Therefore, eco-friendly fabrication strategies for multifunctional wood are urgently needed.

Prompted by biomineralization *via* living organisms that generate robust inorganic–organic hybrid composites under ambient conditions [2–4], biomimetic mineralization of wood has recently received increasing attention because of its functional tailoring, industrial potential, and eco-friendly features [5]. Mineralization of wood generally refers to the formation of silicates, phosphates, borate, and carbonates in hierarchical wood structures [6–9]. The size and distribution of the inorganic phase are crucial in the fabrication of functional mineralized wood. Nano-inorganics need to be uniformly distributed inside the hardly accessible nanoporous cell walls, instead of merely filling the lumens, to achieve functional efficiency [9]. Most extensive studies on wood mineralization have focused on calcification [10–13]. For

* Corresponding author at: Institute of Biomass Engineering, South China Agricultural University, Guangzhou 510642, China.

E-mail address: rongxian_ou@scau.edu.cn (R. Ou).

<https://doi.org/10.1016/j.cej.2022.138308>

Received 18 February 2022; Received in revised form 26 July 2022; Accepted 27 July 2022

Available online 6 August 2022

1385-8947/© 2022 Elsevier B.V. All rights reserved.

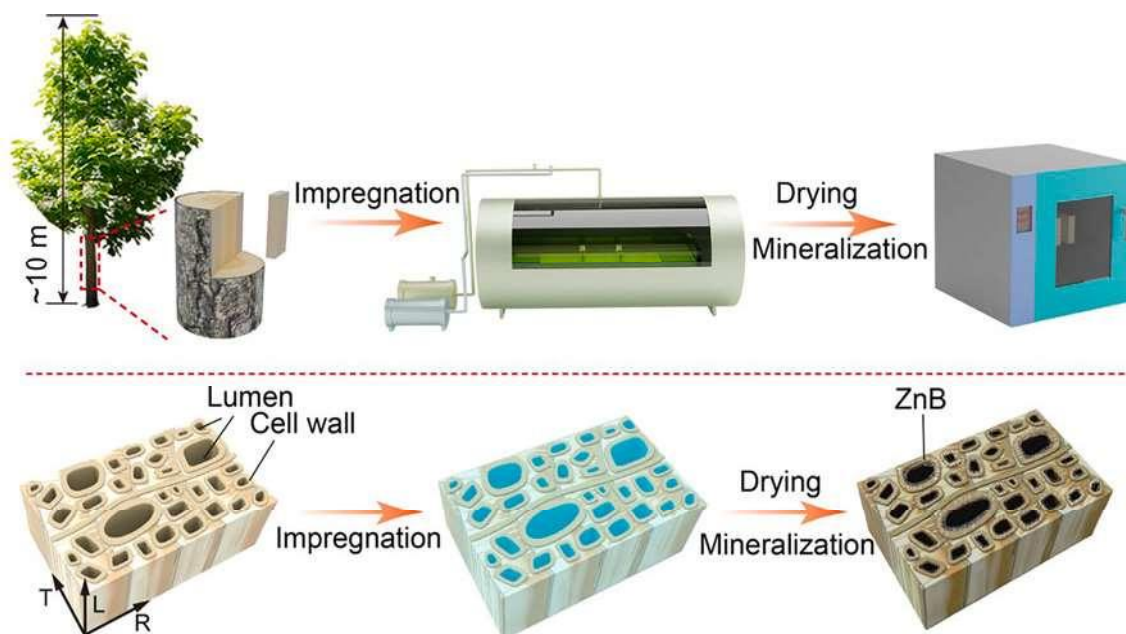


Fig. 1. Schematic for the fabrication of mineralized wood.

instance, in one study, dimethyl carbonate and CaCl_2 were dissolved in water and then diffused into bulk wood, and CaCO_3 was predominantly deposited in the nano- and submicron-sized pores of the wood cell wall structure [11]. The heat release of the resulting calcified wood was reduced to 32 %–37 % of the original value for the unmodified wood. However, the mineralized wood samples were more sensitive to moisture because of the residual sodium chloride. Furuno *et al.* impregnated disodium tetraborate decahydrate ($\text{Na}_2\text{B}_4\text{O}_7 \cdot 10\text{H}_2\text{O}$) into the cell wall of wood, yielding a 7 % mass loss and 100 % termite mortality after termite attack, relative to those of the untreated control with 39 % mass loss and 16 % termite mortality [14]. However, owing to the water-solubility of $\text{Na}_2\text{B}_4\text{O}_7 \cdot 10\text{H}_2\text{O}$, the treated wood was prone to moisture absorption, easily leaching $\text{Na}_2\text{B}_4\text{O}_7 \cdot 10\text{H}_2\text{O}$ from the wood, hence the weakening of its antitermite activity. The previously studied mineralized wood was capable of only a single function depending on the inorganic phase [7,9,15], substantially limiting its efficient utilization.

Zinc borate (ZnB) has been used to enhance the resistance of polymer composites against fire, fungi, and termites [16–19]. However, ZnB is water-insoluble, limiting its application in the wood industry; treatment of bulk wood using ZnB is thus rarely reported. Garba used $2 \text{ mol} \cdot \text{L}^{-1}$ of hydrochloric acid aqueous solution (HCl) to dissolve commercial ZnB (ZnB-to-HCl volume ratio = 2:1); the solution was impregnated into tropical wood to obtain ZnB mineralized wood after drying [20]. The ZnB-treated wood exhibited an extremely low flame propagation rate ($0.05 \text{ cm} \cdot \text{s}^{-1}$) with 16 wt% ZnB loading, and the limiting oxygen index increased by 48.6 % relative to that of the control wood. However, the excessive utilization of volatile and corrosive HCl did not conform with the health and environmental requirements. Mantanis *et al.* used an acrylic emulsion to fix ZnB in wood. The resultant treated wood slightly resisted the formation of mold but strongly inhibited termite feeding—that is, a 2.5 % mass loss was observed after a termite attack [21]. However, the introduction of an acrylic emulsion substantially increased the inflammability of wood [22]. A two-step process of first impregnating $\text{Na}_2\text{B}_4\text{O}_7 \cdot 10\text{H}_2\text{O}$ and then zinc sulfate heptahydrate ($\text{ZnSO}_4 \cdot 7\text{H}_2\text{O}$) was also used to synthesize ZnB in wood [14,23]. However, ZnB precipitation has been generated before $\text{ZnSO}_4 \cdot 7\text{H}_2\text{O}$ solution entered the wood cell wall due to the rapid reaction, resulting in a blocked synthesis of ZnB within the cell wall, thus reducing the functional effect of the treated wood. Therefore, the use of ZnB to fabricate multifunctional wood in a

scalable and eco-friendly way continues to present a challenge.

In the current study, a transparent $[\text{Zn}(\text{NH}_3)_4]^{2+}$ solution coexisting with borate ions was synthesized using $\text{Na}_2\text{B}_4\text{O}_7 \cdot 10\text{H}_2\text{O}$, $\text{ZnSO}_4 \cdot 7\text{H}_2\text{O}$, and ammonium water ($\text{NH}_3 \cdot \text{H}_2\text{O}$) as raw materials. The transparent solution was infiltrated into the hierarchical void system of poplar wood by using a facile vacuum/pressure impregnation method. Nanosized ZnB particles were *in situ* mineralized in the nano/microporous structure of wood after ammonia volatilization. The microstructure, flammability, mold resistance, and antitermite activity of the nanostructured wood hybrids were systemically examined. The current study is the first to demonstrate that ZnB-mineralized wood exhibits excellent flame retardancy, smoke suppression capability, mold resistance, antitermite activity, and scalability. This development alleviates the problem of traditional wood modifiers being limited to a single function.

2. Experimental

2.1. Materials

Fast-growing poplar wood (*Populus euramericana* cv. 'I-214') board originated from Luohe, Henan Province, China. They were stored in a chamber operated at a constant temperature (20°C) and humidity (65 %). Wood blocks were cut from defect-free sapwood with a density of $0.45\text{--}0.48 \text{ g} \cdot \text{cm}^{-3}$. $\text{Na}_2\text{B}_4\text{O}_7 \cdot 10\text{H}_2\text{O}$, $\text{ZnSO}_4 \cdot 7\text{H}_2\text{O}$, and analytical-grade $\text{NH}_3 \cdot \text{H}_2\text{O}$ (25 wt% NH_3 in H_2O) were purchased from Guangdong Guangshi Regent Technology Co., Ltd., China. Commercial zinc borate ($2\text{ZnO} \cdot 3\text{B}_2\text{O}_3 \cdot 3.5\text{H}_2\text{O}$, Model no. 2335) and $\text{Zn}(\text{OH})_2$ were purchased from Aladdin.

2.2. Methods

2.2.1. Preparation of the zinc borate mineralization solution

$\text{ZnSO}_4 \cdot 7\text{H}_2\text{O}$ was dissolved in deionized water at ambient temperature to form a clear solution with a mass concentration of 35.9 %. $\text{Na}_2\text{B}_4\text{O}_7 \cdot 10\text{H}_2\text{O}$ was dissolved in deionized water and magnetically stirred at 50°C to obtain a clear solution with a concentration of 19.1 wt %. The two aforementioned solutions were compounded and then stirred for 1 h to form a uniform and stable suspension. The suspension was centrifuged and then washed with deionized water to remove the

unreacted substances. Subsequently, the filter residue was immediately dissolved in 3.8 wt% dilute ammonia ($\text{NH}_3\cdot\text{H}_2\text{O}$) to obtain a clear and transparent $[\text{Zn}(\text{NH}_3)_4]^{2+}$ solution (named as the mineralized solution), which was used for wood impregnation. $\text{ZnSO}_4\cdot 7\text{H}_2\text{O}$, $\text{Na}_2\text{B}_4\text{O}_7\cdot 10\text{H}_2\text{O}$, and $\text{NH}_3\cdot\text{H}_2\text{O}$ were mixed in a molar ratio of 1:1:10. The reaction mechanism is described in Equations S1–S4 in a supplemental file.

2.2.2. Mineralized wood fabrication

Mineralized wood was fabricated via *in situ* synthesis of ZnB in hierarchical wood structures (Fig. 1). First, the wood samples measuring $300\text{ mm} \times 100\text{ mm} \times 30\text{ mm}$ ($L \times T \times R$) were placed in an impregnation tank and pumped to -0.08 MPa for 20 min. Second, the mineralized solution was siphoned into the tank by using a vacuum, and the tank was pressurized to 0.6 MPa for 30 min. Third, the mineralized solution was discharged, and the pressure was released. The wood samples were subsequently removed from the impregnation tank and carefully wiped with dust-free paper to remove the residual solution on the wood surface. Lastly, the resulting wood samples were initially air-dried for 12 h and then dried in a vacuum oven for 8 h at 45°C , 75°C , and 105°C , sequentially, to obtain ZnB-mineralized wood with insoluble ZnB. The aforementioned processes were repeated to obtain different values for weight percent gain (WPG) (Fig. S1). The ZnB-mineralized wood samples with average WPGs of 9.8 %, 15.7 %, and 22.1 % were labeled as MW_{10} , MW_{16} , and MW_{22} , respectively. The original mineralized solution was also dried in a vacuum oven by using the aforementioned parameters to obtain freestanding ZnB particles for characterization.

2.3. Measurements and characterization

The distribution of ZnB in mineralized wood was determined by X-ray microcomputed tomography ($\mu\text{-CT}$) (EasyTom 150 kV, RX Solutions, France). Samples measuring $5\text{ mm} \times 5\text{ mm} \times 5\text{ mm}$ ($L \times T \times R$) were tested. Three-dimensional (3D) tomographic volumes were reconstructed and analyzed using the software VG Studio. The working voltage was 50 kV, and the current was 200 μA . The voxel size was 5.0 μm .

Morphological analysis of ZnB, untreated wood (UW), and mineralized wood was conducted by scanning electronic microscopy (SEM) (FEI Quanta200, FEI Co., Hillsboro, OR, United States) with the accelerating voltage set to 12.5 kV. The cross-section from the middle layer of the samples was trimmed with an ultramicrotome (REM-710, YAMATO, Japan) and sputtered with a thin layer of gold before testing. The elemental distribution on the cross-section of the sample was tested by energy-dispersive spectroscopy (EDS).

Changes in the crystal structure of ZnB after heat treatment were analyzed by X-ray diffraction (Rigaku, MiniFlex 600, Tokyo, Japan) with an $\text{AlK}\alpha$ radiation source at 40 kV. The test was ramped from 5° to 50° with a step of 0.02° . ZnB was heat-treated using a tube furnace at 250°C , 350°C , 450°C , 600°C , 800°C , and 1000°C , respectively, for 5 min under N_2 atmosphere.

The leaching test was conducted according to the AWP A E11-97 standard. The mineralized wood samples ($19\text{ mm} \times 19\text{ mm} \times 19\text{ mm}$) were completely submerged in the deionized water and shaken in an orbital shaker. The deionized water was changed after 6, 24, 48 and thereafter at 72 h intervals, continuing leaching for 14 days. The mass of the wood samples before and after leaching was recorded to calculate the leaching rate of ZnB.

A synchronous thermal analyzer (SDT 650, TA Instruments Inc., United States) was used to characterize the mass and heat changes of the samples. The test was run under N_2 atmosphere with a heating rate of $10^\circ\text{C}\cdot\text{min}^{-1}$. The samples were dried in an oven at 103°C for 24 h before testing.

Inductively coupled plasma optical emission spectrometry (ICP-OES) (Agilent 720ES) with a radio frequency generator of 1200 W was used to analyze the Zn and B contents in ZB. Flow rates of argon as plasma,

auxiliary, and spray gases were 15, 1.5, and $0.75\text{ L}\cdot\text{min}^{-1}$, respectively. The mass of ZB was 0.05 g and fixed to $10\text{ }\mu\text{L}$ with nitric acid. Three-replicate measurements were conducted, and the average was determined.

A thermal infrared camera (Ti2009Hz, Fluke Company, Seattle WA, United States) was employed to record the thermal distribution field of the samples ($100\text{ mm} \times 100\text{ mm} \times 10\text{ mm}$) during combustion by using a propane blowtorch as a heat source (1200°C). The temperature distribution on the non-exposed side was recorded by video recording. The software SmartView 4.3 was used to analyze the video results.

The limiting oxygen index (LOI) of each wood sample measuring $100\text{ mm} \times 6.5\text{ mm} \times 3.2\text{ mm}$ ($L \times R \times T$) was determined using an oxygen index tester (JF-3, Jiangning Analytical Instrument Co., Ltd., Nanjing, China) in accordance with ASTM D2863-2017. The gas sources were O_2 and N_2 with a purity of 99.5 %.

A cone calorimeter (CONE) was used to evaluate the combustion behavior of wood samples measuring $100 \times 100 \times 10\text{ mm}$ ($L \times T \times R$) at a heat flux of $50\text{ kW}\cdot\text{m}^{-2}$ in accordance with ISO 5660-1(2002).

After heat treatment, the untreated and mineralized wood samples were analyzed using a Fourier transform infrared (FT-IR) spectrometer (iS10, Thermo Fisher Scientific, United States). Spectra were collected over the range of 500 to 4000 cm^{-1} at a resolution of 4 cm^{-1} and for 32 scans. Heat treatment was performed using a tube furnace at 300°C , 400°C , and 550°C , respectively, for 5 min under N_2 atmosphere.

X-ray photoelectron spectroscopy was conducted on a Thermo ESCALAB 250XI spectrometer (Thermo Fisher Scientific Co., Ltd. United States) equipped with an $\text{AlK}\alpha$ X-ray excitation source ($h\nu = 1486.8\text{ eV}$). Elemental changes in the untreated and mineralized wood samples and in their corresponding char residue were analyzed.

Thermogravimetry–Fourier transform infrared (TG-FTIR) analysis was performed using a TG209F3 Netzsch thermogravimetric analyzer connected to a Tensor27 Bruker FT-IR spectrophotometer. Samples of 8 mg were heated from 40°C to 700°C at a heating rate of $10^\circ\text{C}\cdot\text{min}^{-1}$ under N_2 atmosphere.

Pyrolysis and the separation and identification of the pyrolysis products were performed on a pyrolyzer (FrontierEGA/PY3030D, Frontier, Japan) along with a gas chromatography (TRACE1310, Thermo Fisher Scientific, United States) which was in conjunction with mass spectrometry (ISQ, Thermo Fisher Scientific, United States). Subsequently, 0.5 mg samples were used for pyrolysis at 350°C for 30 s at a heating rate of $20^\circ\text{C}\cdot\text{ms}^{-1}$ under helium. The chromatographic column used was the DB-5 quartz capillary column ($30\text{ m} \times 0.25\text{ mm} \times 0.25\text{ }\mu\text{m}$). The split ratio was 100:1, and the helium carrier gas was at a constant flow of $1.0\text{ mL}\cdot\text{min}^{-1}$. The mass spectrometry was recorded at electron ionization (70 eV) in the m/z range of 40 – 500 amu . The chromatographic peaks were identified by comparing the mass spectrometric results with the NIST mass spectrometric database and the data reported in the literature [24–26].

The dynamic water vapor sorption behavior of the wood samples was determined using a dynamic vapor sorption apparatus (DVS Intrinsic, Surface Measurement Systems Ltd, United Kingdom). Approximately 5 mg of block samples were used for testing. The relative humidity (RH) was preset to increase from 0 to 95 % at a 5 % interval. For each target RH, the wood reached the equilibrium moisture content until the rate of mass change was less than 0.002 % per min over a period of 10 min. Sorption techniques were run at 25°C over the full range of RH.

Anti-mold process and evaluation were conducted per GB/T18261-2013 [27]. Pre-dried and sterilized wood samples were incubated at 28°C and with 85 % RH for 4 weeks with *Aspergillus niger* v. Tiegh, *Penicillium citrinum* Thom, *Botryodiplodia theobromae* Pat., and *Trichoderma viride* Pers. ex Fr. Six duplicate samples were tested. After incubation, the infection values were determined by observing the infection area on the sample surfaces and then ranked on a scale from 0 to 4 (Table S2). Protective efficiency (E) was calculated as follows:

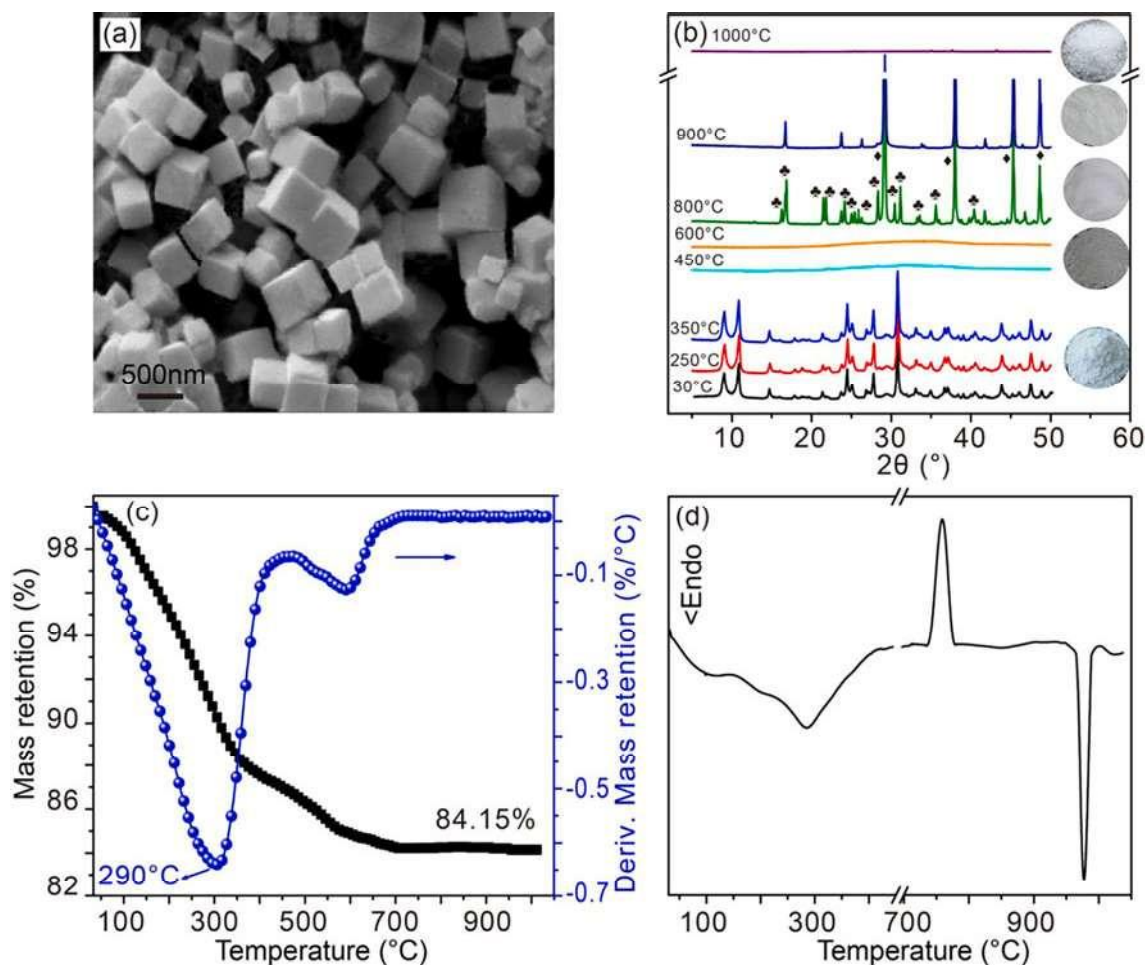


Fig. 2. SEM of the synthesized ZnB (a), XRD of ZnB at different temperatures (b) (“♦” and “◆” corresponds to the peaks from $\text{Zn}_4\text{B}_6\text{O}_{13}$ and ZnB_4O_7 , respectively), TG and DTG curves of ZnB (c), and DSC curve of ZnB (d).

$$E = \left(1 - \frac{D_1}{D_0}\right) \times 100\% \quad (1)$$

where D_1 and D_0 are the average infection values of MW_{22} and UW, respectively.

Laboratory termite tests were conducted in accordance with AWPA E1-2017 [28]. Pre-dried and weighed wood samples were placed in previously prepared containers with one sample in each for no-choice antitermite testing. A total of 360 workers and 40 soldiers of *Coptotermes formosanus* Shiraki were added to each container. All test containers were maintained at 28 °C with 75 % RH for 4 weeks. The samples were removed and dried after testing to determine the mass loss of each and visually assess the samples by using the rating system (Table S3). The number of live termites was determined to calculate the termite mortality after testing.

3. Results and discussion

3.1. Characterization of the synthesized ZB

The synthesized ZnB was a square with dimensions measuring 100–500 nm (Fig. 2a). Changes in the crystal structure of the ZnB heat-treated in a tube furnace (30 °C–1000 °C) and their corresponding appearance are shown in Fig. 2b. The changes were classified into four stages: (1) crystalline ZnB with a white appearance at 25 °C–350 °C; (2) an amorphous structure with a dark appearance at 450 °C–600 °C; (3) mixed crystals of anhydrous $\text{Zn}_4\text{B}_6\text{O}_{13}$ and ZnB_4O_7 resulting from

Table 1

Molar ratio of Zn to B and weight ratio of crystal water in the synthesized ZnB.

	Mass concentration (mg L^{-1})	Molality (mol kg^{-1})	Molar ratio	Crystal water (wt.%)
Zn	11.38	5.96	1	—
B	3.62	11.47	1.92	—
H_2O	—	—	—	15.85

structural rearrangement at 800 °C–900 °C; [29] and (4) amorphous ZnB with a transparent appearance at 1000 °C. The ZnB had a mass loss of about 16 % at 1000 °C caused by the release of crystalline water, and the maximum mass loss rate was observed at about 300 °C (Fig. 2c). Moreover, DSC results indicated that ZnB underwent an endothermic process of dehydration accompanied by melting (30 °C–450 °C), an exothermic process of crystallization (740 °C–780 °C), and an endothermic process of melting (950 °C–1000 °C) (Fig. 2d), which were consistent with the changes in the crystal structure for ZnB (Fig. 2b). Further, an appropriate amount of ammonia can react with zinc salt to form the desired $[\text{Zn}(\text{NH}_3)_4]^{2+}$ solution; with insufficient ammonia, $\text{Zn}(\text{OH})_2$ is formed. To confirm the absence of $\text{Zn}(\text{OH})_2$ in the synthesized ZnB, the auger electron spectra of Zn LMM from the synthesized ZnB (in the current study), commercial ZnB, and commercial $\text{Zn}(\text{OH})_2$ were collected (Fig. S2). The spectra of Zn LMM from the synthesized ZnB and commercial ZnB exhibited the same binding energy (499.8 KeV); meanwhile, a higher binding energy of 497.8 KeV was observed in $\text{Zn}(\text{OH})_2$, indicating that no $\text{Zn}(\text{OH})_2$ was doped in the synthesized ZnB.

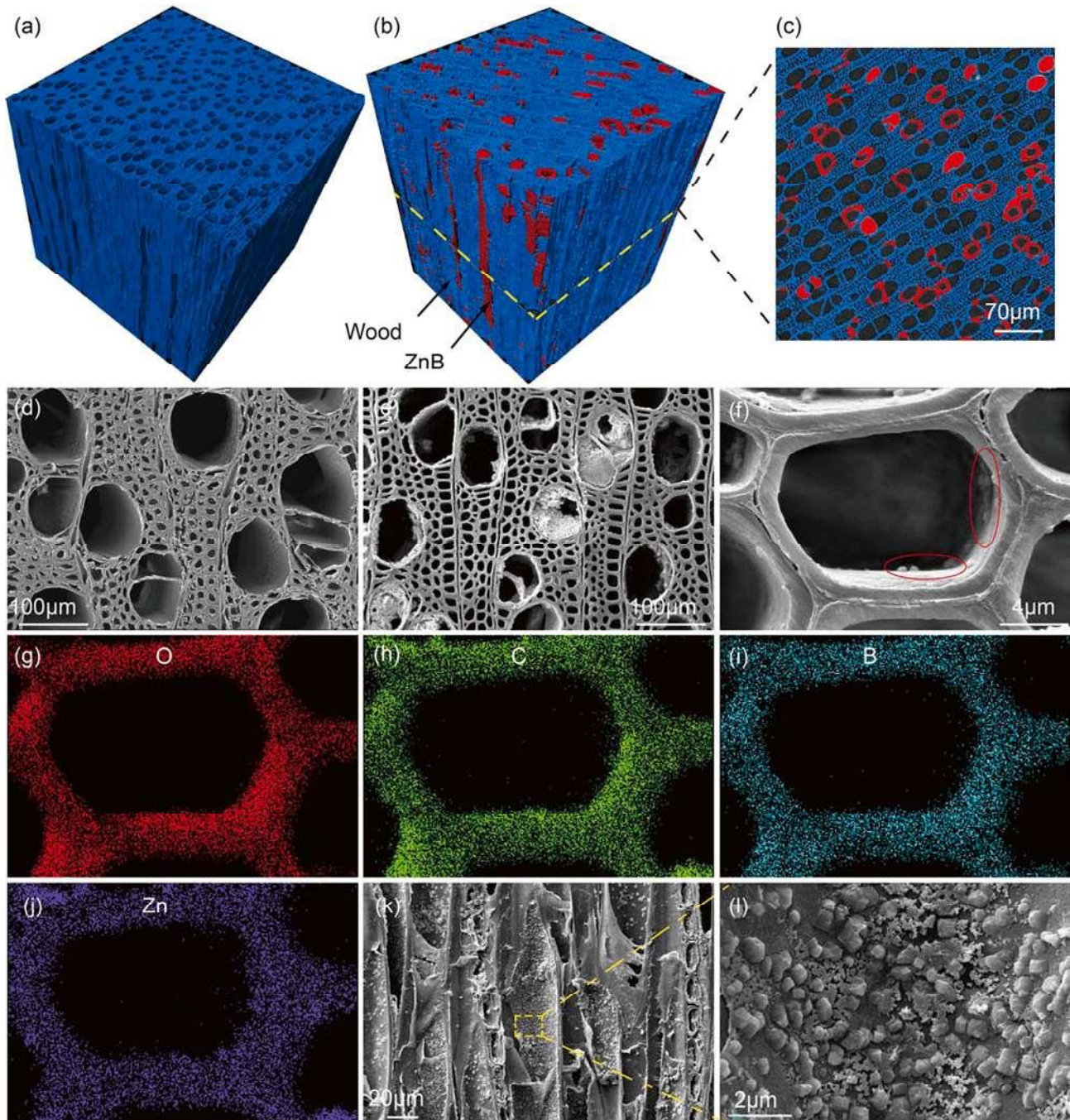


Fig. 3. 3D rendering of a small region-of-interest from the analyzed X-ray tomogram of untreated wood (a) and mineralized wood with 22.1 wt% ZB (b), with voxels assigned to ZnB particles rendered in red, whereas the wood cell wall is rendered in blue. Planar cross-section of the X-ray tomogram of the mineralized wood specimen (c). SEM of transverse section of the untreated wood (d) and mineralized wood (e). SEM image on the transverse section of mineralized wood fiber cell (f) together with EDS elements mapping of O (g), C (h), B (i), and Zn (j), respectively. Radial section of mineralized wood (k), and (l) is the magnification of the yellow box in (k).

The molar ratio of Zn to B in the synthesized ZnB was determined by ICP-OES, and the weight percentage of crystalline water in the synthesized ZnB was measured by TGA; the results are shown in Table 1. The molecular formula of ZnB was determined to be $2\text{ZnO} \cdot 2\text{B}_2\text{O}_3 \cdot 3\text{H}_2\text{O}$ (ZnO wt.% = 45.34 %, B_2O_3 wt.% = 38.81 %, H_2O wt.% = 15.85 %).

3.2. Characterization of mineralized wood

3.2.1. Micromorphological analysis

The 3D structures of the untreated and mineralized wood samples

were visualized by X-ray tomographic microscopy. The untreated wood exhibited hierarchical pore structures (Fig. 3a). After treatment, the ZnB particles appeared agglomerated mainly on the inner wall of the vessels (Fig. 3b and c), and the wood porosity was reduced by 6.6 %. The ZnB particles and their aggregates smaller than 5 μm could not be detected because of the resolution limitation of $\mu\text{-CT}$. To further analyze the distribution of ZnB in smaller scales, SEM-EDS was employed (Fig. 3d–i). The transverse section of the mineralized wood revealed the deposition of the ZnB particles on the inner wall of the vessels (Fig. 3e). A closer observation of a fiber cell showed that smaller ZnB particles

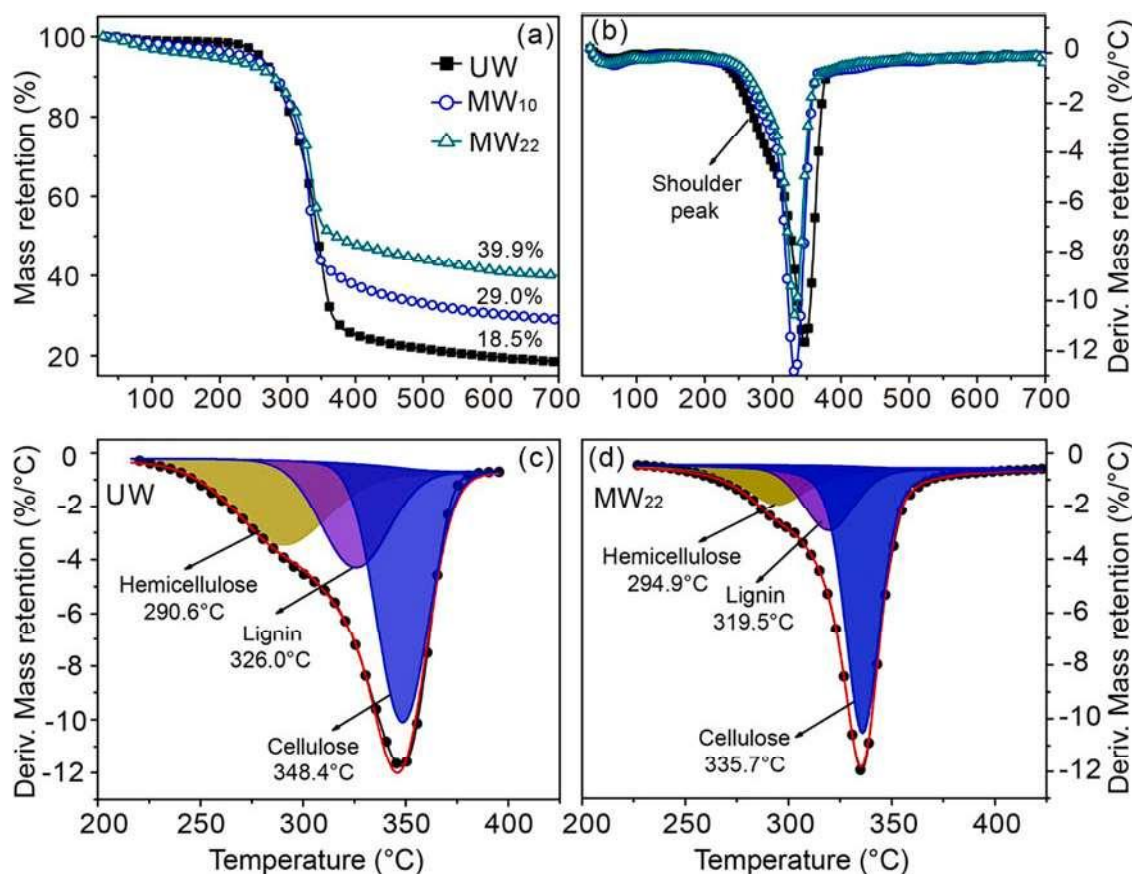


Fig. 4. TG (a) and DTG (b) curves of untreated (UW) and mineralized wood, the fitting curve of UW (c) and mineralized wood (d) based on the wood components.

were attached to the internal wall (Fig. 3f). EDS elemental mapping showed that C, O, B, and Zn were uniformly distributed on the transverse section of the wood cell wall (Fig. 3g–j), indicating the successful modification of the wood cell wall by ZnB. The radial section of the mineralized wood showed that the 100–500 nm ZnB particles were uniformly deposited onto the inner walls of the fiber cells, with most particles being square (Fig. 3k–l). These results indicate that the ZnB

particles successfully target the hardly accessible nanoporous cell wall structure rather than the micron-sized pores of the cell lumina.

3.2.2. Thermal properties

The thermal stability of the wood samples is presented in Fig. 4. The untreated wood retained a residual mass of 18.5 % at 700 °C (Fig. 4a). The shoulder peak on the differential thermogravimetry (DTG) curve for

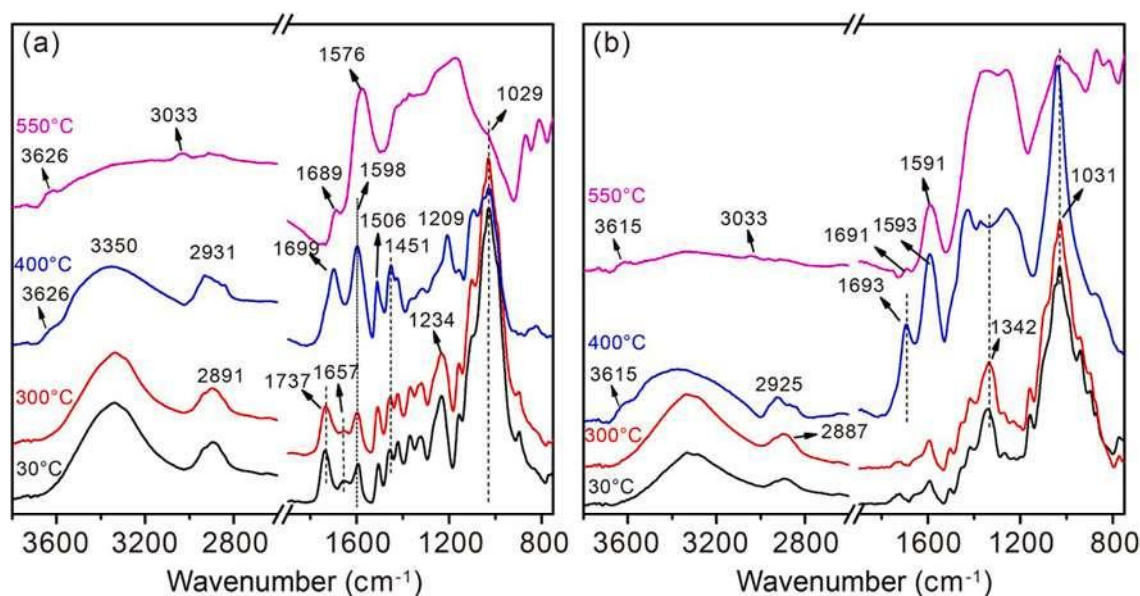


Fig. 5. FT-IR spectra of untreated wood (a) and mineralized wood (b) treated at different temperatures.

the untreated wood was primarily attributed to the degradation of hemicellulose, whereas the main peak at 348 °C was mainly assigned to the degradation of cellulose; moreover, both processes were accompanied by the degradation of lignin (Fig. 4b) [30]. For the mineralized wood, the residual mass increased with an increase in ZnB content (Fig. 4a), and their residual mass exceeded the sum of the masses of the dehydrated ZnB and untreated wood residue at 1000 °C; 2.2 % and 2.9 % supernumerary residues for MW₁₀ and MW₂₂, respectively, were observed. To further assess the effect of ZnB on the thermal degradation of wood, the DTG curves were fitted using the mixed Gaussian–Lorentzian function according to the degradation temperatures of wood components (Fig. 4c and d) [31,32]. The temperature at the maximum degradation rate (T_{max}) of hemicellulose was increased by 4.3 °C for MW₂₂ relative to that of the untreated wood. This increase is attributable to the endothermic reaction caused by the release of crystal water from ZnB within this temperature range (Fig. 3c). However, the T_{max} values of cellulose and lignin were decreased by 12.7 °C and 6.5 °C, respectively, which were the catalytic effect of the dehydrated ZnB that promoted the devolatilization reaction of cellulose and lignin [16]. The fitting curves also show that the maximum degradation rates (peak value) of hemicellulose and lignin were markedly decreased after mineralization, whereas the change in cellulose was not apparent. These results reveal that ZnB mineralization, particularly at high ZnB content, enhanced the thermal stability of the untreated wood, as determined from the reduced thermal degradation rate and the increased residual mass. The improvement in thermal stability resulted from the cooling of the crystal water released, the barrier provided by premature char layer formation, and the physical shielding of dehydrated ZnB, which reduced the thermal degradation dynamics [33].

The variation of the thermal degradation process of the wood samples with temperature under N₂ atmosphere was analyzed by FT-IR. For the untreated wood, the stretching vibration intensities of aliphatic C=O at 1737 cm⁻¹ and CO–OR at 1234 cm⁻¹ from hemicellulose, the aromatic C=O at 1657 cm⁻¹ from lignin [34], and the free and associated O–H at 3050–3670 cm⁻¹, slightly decreased after heat treatment at 300 °C (Fig. 5a), indicating the occurrence of deacetylation and dehydration. After heat treatment at 400 °C, the stretching vibration intensity of aliphatic C–OH at 1029 cm⁻¹ was considerably decreased, indicating the significant dehydration of cellulose and hemicellulose. The CO–OR at 1234 cm⁻¹ disappeared, and the phenolic hydroxyl (Ph–OH) at 1209 cm⁻¹ appeared, indicating the occurrence of deoxygenation and carbonization reactions. Meanwhile, the saturated aliphatic C=O stretching vibration (1737 cm⁻¹) shifted to a low frequency (1699 cm⁻¹), suggesting an increase in unsaturated carbonyl groups (C=C–C=O) [35]. The aromatic skeleton vibrations (1598, 1506, and 1451 cm⁻¹) were evidently enhanced, demonstrating apparent aromatization [36]. Moreover, the stretching vibration of free O–H at 3626 cm⁻¹ was increased, possibly owing to high temperatures that destroy the hydrogen bond between the hydroxyl groups. At 550 °C, the unsaturated carbonyl was further shifted to a lower frequency, producing aromatic C=O (1689 cm⁻¹), and the vibration intensity was significantly reduced due to the deoxygenation reaction. The stretching vibration strength of C–O (1209 cm⁻¹) was also markedly reduced, and the aliphatic C–H stretching vibration (near 2900 cm⁻¹) almost disappeared, indicating that further dehydrogenation and deoxygenation occurred. A new peak appeared at 3033 cm⁻¹, corresponding to the aromatic C–H stretching vibration, suggesting further aromatization [37]. The aromatic skeleton vibration shifted from 1598 cm⁻¹ to 1576 cm⁻¹, indicating the presence of sp²-hybridized carbon [38]—that is, the occurrence of graphitization. For MW₂₂, the peaks at 1342 and 1031 cm⁻¹ were assigned to the B–O–B in ZnB [39] and the stretching vibration of aliphatic C–OH from holocellulose, respectively (Fig. 5b). The changes in the characteristic groups of the mineralized wood treated at 300 °C were less significant compared with those of the untreated wood. However, heat treatment at 400 °C enhanced the aromatic skeleton vibration at 1593 cm⁻¹ and slightly weakened the C–OH

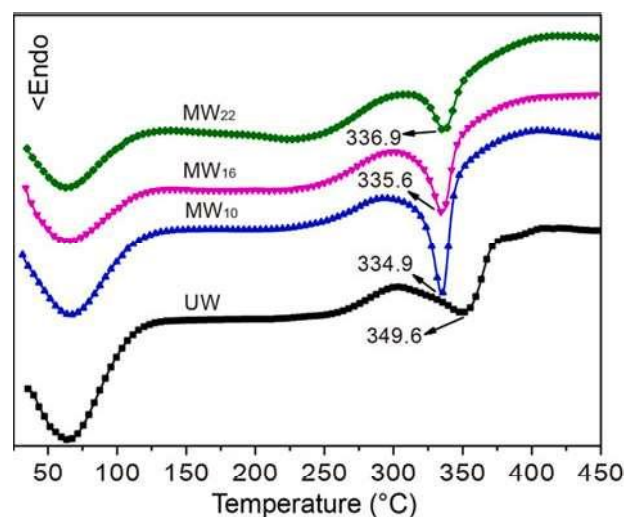


Fig. 6. DSC curves of untreated (UW) and mineralized wood.

stretching vibrations, indicating the occurrence of dehydration and aromatization. After heat treatment at 550 °C, the samples were further dehydrogenated and deoxidized, and the aliphatic C–H (2850–2950 cm⁻¹) disappeared. The vibration intensity of aromatic C–H (3033 cm⁻¹) was considerably weaker than that of the untreated wood, and the change in peak position of the aromatic skeleton was not apparent (from 1593 to 1591 cm⁻¹), indicating the weakening of aromatization and the absence of graphitization. These changes might be attributable to the physical protection conferred by the dehydrated ZnB and preformed charcoal, which inhibited the further thermal degradation of wood.

DSC was performed on the untreated and mineralized wood samples to analyze the thermal conversion (Fig. 6). The first endothermic peak (below 130 °C) of the untreated wood resulted from the release of bound water. The heat absorption (below 130 °C) of the mineralized wood weakened because a portion of bound water was lost during ZnB mineralization. The second endothermic peak appeared between 300 °C and 380 °C, corresponding to the maximum mass loss stage (Fig. 4b). Although considerable mass loss occurred at this stage, the heat absorption was low, suggesting the occurrence of polymerization reactions—that is, endothermic decomposition was accompanied by exothermic polymerization. Previous studies have confirmed that pyrolysis of cellulose is primarily a decomposition reaction, whereas pyrolysis of hemicellulose and lignin is accompanied by a significant polymerization reaction, ultimately oriented the total thermal effect toward endothermic reactions [40]. For the mineralized wood, this endothermic effect was decreased relative to that of the untreated wood, particularly with higher ZnB content, indicating that the ZnB particles inhibited wood decomposition and promoted a polymerization reaction toward charring [40].

Heat transfer in wood during exposure to a propane flame was recorded using an infrared thermal imager (Fig. 7a). The IR images show that the temperature of the untreated wood rapidly increased with exposure time, reaching 360 °C after 20 min (Fig. 7b). The untreated wood was then ignited and burned rapidly. Heat transfer in MW₁₀ was delayed, and after exposure for 45 min, the maximum temperature (360 °C) was reached. With a further increase in ZnB content to 22.1 %, heat transfer in MW₂₂ significantly slowed down, as confirmed by a slight change in temperature with exposure time. After exposure for 45 min, the maximum temperature (84 °C) was reached, indicating excellent heat insulation performance. The decrease in heat transfer in the mineralized wood may be attributed to the cooling effect of the release of crystalline water in ZnB and the thermal isolation after catalytic carbonization achieved by dehydrated ZnB.

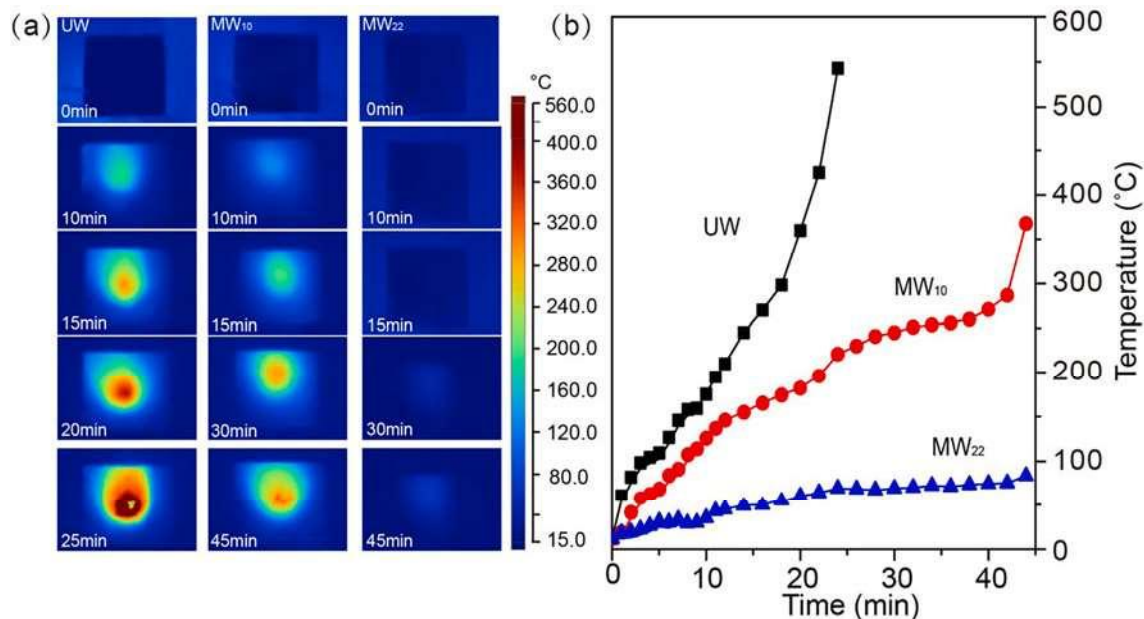


Fig. 7. The IR images of untreated (UW) and mineralized wood on the backside during combustion (a) and 45-minute continuous measurement of the maximum temperature points (b).

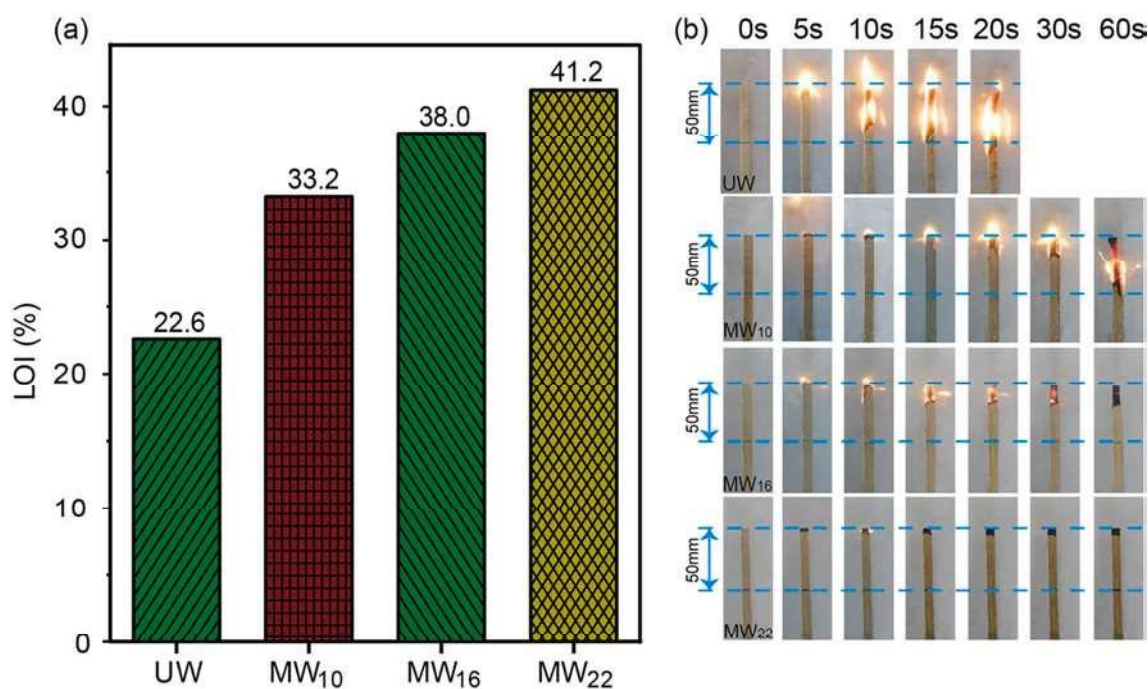


Fig. 8. The limiting oxygen index of untreated (UW) and mineralized wood (a), and their combustion phenomenon at 35 vol% O₂ concentration (b).

3.2.3. Combustibility

The limiting oxygen index (LOI) represented the minimum O₂ concentration that maintained material combustion [41]. The mineralized wood exhibited resistance to direct flame exposure, preventing ignition under the air atmosphere. The LOI of MW₂₂ was 41.2 %, which was about twice that of the untreated wood (Fig. 8a). The combustion processes of the untreated and mineralized wood at 35 vol% O₂ are presented in Fig. 8b. After direct exposure to the flame, the untreated wood was ignited in 2 s, with its burning length exceeding 50 mm within 20 s. The speed of fire propagation was markedly delayed in MW₁₀, and the burning length of the samples exceeded 50 mm at 60 s. MW₁₆ was self-extinguished after 30 s, and the burning length of the samples was less

than 50 mm. MW₂₂ was hardly ignited at 35 vol% O₂, indicating considerable flame resistance.

Cone calorimetry (CONE) is a powerful method for evaluating flame retardancy because the test is close to the real fire situation [42]. The untreated wood shows a typical heat release rate (HRR) curve of charring thermally thick polymer, presenting an HRR peak immediately after ignition (Fig. 9a). After 40 s, the HRR decreased with the carbonization of the superficial wood. Subsequently, the flammable volatiles were released from the inner wood because of the cracking of the char layer, resulting in a second HRR peak after 300 s. The mineralized wood also showed two HRR peaks, which were markedly decreased and delayed for the second peak by 80–100 s. The second peak of HRR for MW₂₂ was

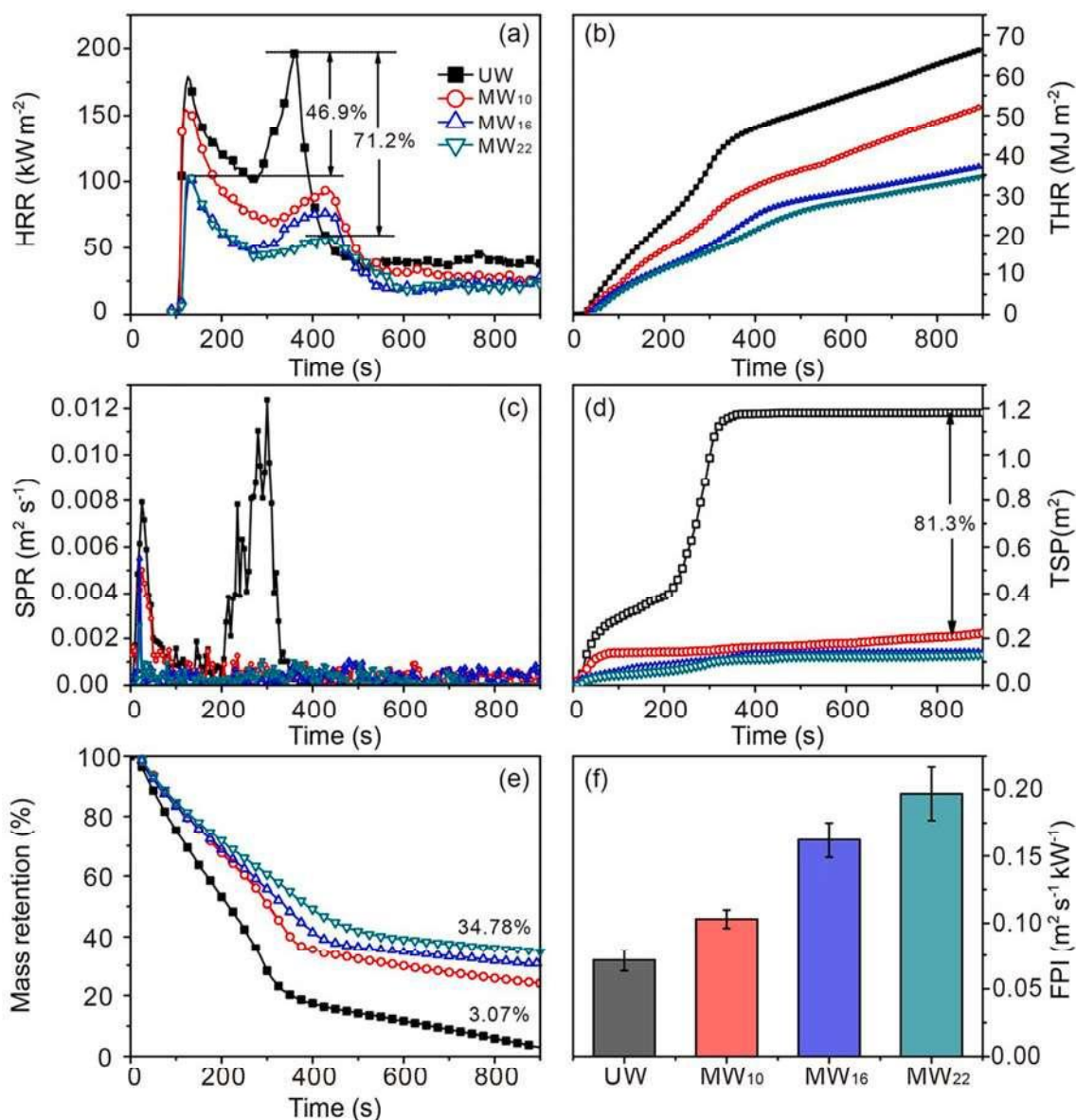


Fig. 9. Cone calorimeter measurement of untreated (UW) and mineralized wood: (a) Average heat release rate (HRR), (b) Total heat release, (c) Average smoke production rate (SPR), (d) Total smoke production (TSP), (e) Mass retention, and (f) Fire performance index (FPI).

reduced by 71.2 % compared to the untreated wood. The total heat release (THR) of the mineralized wood was significantly decreased, reaching a maximum reduction of 47.9 % with 22.1 % ZnB loading (Fig. 9b). Smoke release and carbon monoxide (CO) production are also crucial parameters in a fire disaster. The smoke released during wood combustion is primarily composed of suspended particles and gases. The smoke production rate (SPR) of the untreated wood was consistent with the HRR (Fig. 9c), reaching its maximum SPR of $0.0124 \text{ m}^2/\text{s}$ and a total smoke production (TSP) of 1.18 m^2 . The mineralized wood was almost smokeless during combustion, exhibiting superior smoke suppression (Fig. 9c and d), with reductions of 89.0 % in TSP and 79.5 % in the maximum SPR in MW₂₂ relative to those of the untreated wood. Relative to those of the untreated wood, the average CO yields of the mineralized wood were significantly reduced, with a maximum decrement of 51.4 % in MW₂₂ (Fig. S3). Another vital indicator of flame resistance is residual yield. With the assumption that no interaction occurs between ZnB and wood during combustion, the theoretical residual mass of MW₂₂ was expected to be 21.6 % (the sum mass of the dehydrated ZnB and untreated wood residue), and the actual value was 34.8 % (Fig. 9e),

indicating the strong catalytic charring effect of ZnB on wood [43]. The fire performance index (FPI) is a critical parameter for evaluating fire hazards and is calculated as the ratio of ignition time to the first peak of HRR [26,44]. Compared with the untreated wood, the mineralized wood showed a significantly higher FPI (Fig. 9f), indicating a considerably lower fire hazard. In addition, the flame retardancy of MW₂₂ after leaching (the leaching rate was 7.05 %) was also examined. The results showed that MW₂₂ after leaching still exhibited excellent flame retardancy (Fig. S4).

3.2.4. Condensed-phase analysis

The residual structures after CONE testing were analyzed to reveal flame retardant mechanisms. After burning for 500 s, the untreated wood was disintegrated into fragments (Fig. 10a), whereas the mineralized wood with 22.1 % ZnB had a compact and robust char residue with slight cracks on the surface (Fig. 10b). The surface of the MW₂₂ residue was relatively white, which was caused by the accumulation of dehydrated ZnB after the degradation and consequent volatilization of the surface wood. Both the aforementioned compact and robust char

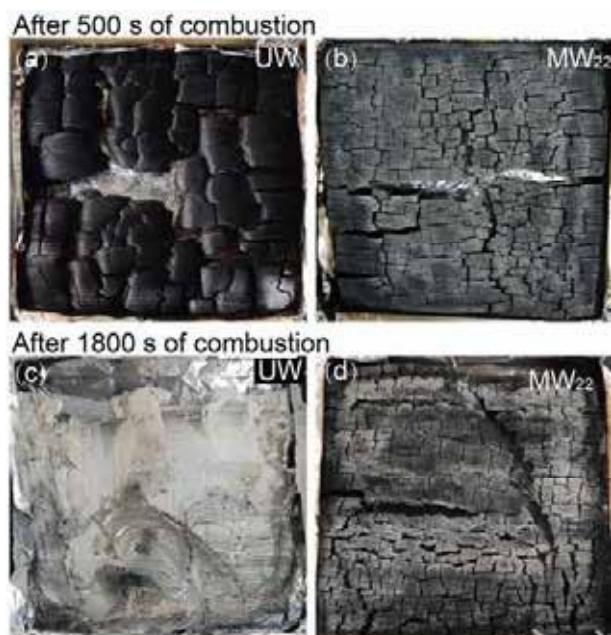


Fig. 10. Morphology of char residue: (a) untreated wood (UW) and (b) mineralized wood with 22.1 % ZnB (MW_{22}) after CONE test for 500 s, and (c) UW and (d) MW_{22} after CONE test for 1800 s.

residue and the accumulated dehydrated ZnB exerted physical isolation, including thermal resistance, oxygen insulation, and blocking of combustible volatiles. Moreover, the untreated wood was burned out after the testing time was extended to 1800 s (Fig. 10c), whereas the char residue of MW_{22} remained dense and exhibited good compressive strength (Fig. 10d), intuitively indicating the efficient flame retardancy of ZnB.

The microstructures of the char residue after CONE testing for 500 s were also characterized by SEM-EDS. The transverse section of the untreated wood residue retained the typical wood scaffold structure (Fig. 11a); meanwhile, the multitier wall structure, which was replaced by a smooth crystalline graphite structure, could not be distinguished (Fig. 11b). The dehydrated ZnB particles accumulated in the fiber cells and vessels of the mineralized wood (Fig. 11c) and were uniformly embedded in the nano- and submicron pores of the cell wall (Fig. 11d); this finding was confirmed by elemental mapping (Fig. 11e and 11f). This homogeneous distribution of ZnB particles inside the cell wall is crucial to the efficiency of flame retardancy. The microstructures of the radial section of the char residue were also observed. A clean residual surface of the untreated wood was found (Fig. 11g), whereas a layer of dehydrated ZnB in the mineralized wood accumulated on the residue surface (Fig. 11h), confirming that the dehydrated ZnB caused the whitish surface in Fig. 11b. The dehydrated ZnB particles at high magnification (Fig. 11i) were melted and wrapped on the residual surface. The glassy melt was attributed to the boron compounds, which promote the formation of a cohesive and robust residue, inhibiting the transfer of heat and mass between the gaseous and condensed phases [45].

To reveal the flame retardant mechanisms, the chemical structures of

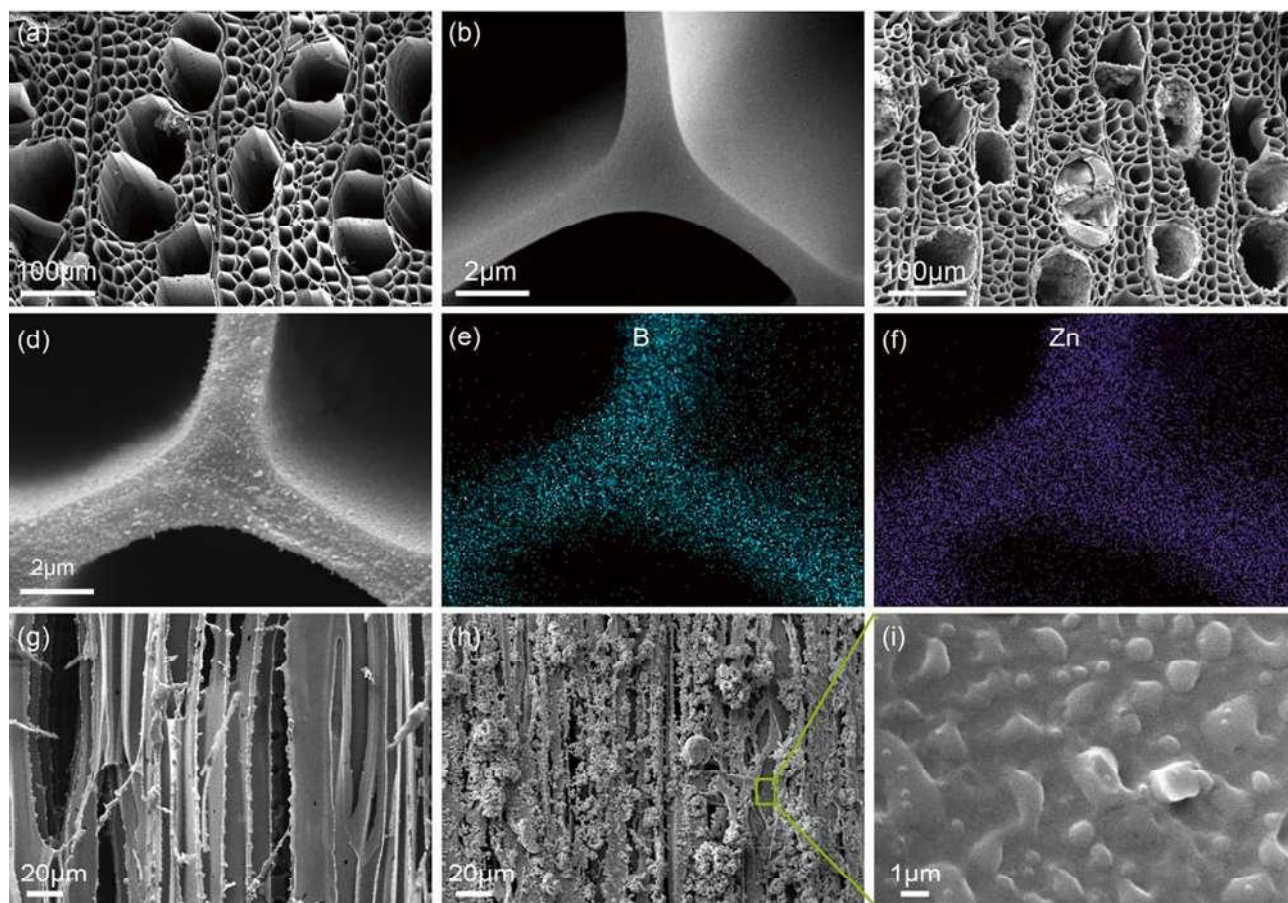


Fig. 11. Microstructure of the char residue after 500 s CONE tests: (a) transverse section and (b) cell corner of the untreated wood residue, (c) transverse section of the mineralized wood residue with 22.1 % ZnB (MW_{22}), (d-f) cell corner and element mapping of the MW_{22} residue, (g) radial section of the untreated wood residue, and (h) radial section of the MW_{22} residue and (i) its local magnification.

Table 2

Summary of XPS spectral parameters of the untreated wood (UW) and mineralized wood with 22.1% ZnB (MW₂₂) as well as their char residue.

Sample	O/C	sp ² C (%)	C-C/ C-H (%)	C-O (%)	C=O (%)	O-C=O (%)	π - π (%)
UW	0.904	—	54.00	36.87	6.74	2.39	—
Residue of UW	0.229	74.31	10.67	7.44	3.51	—	3.87
MW ₂₂	1.110	—	49.72	40.56	7.86	1.86	—
Residue of MW ₂₂	0.683	65.14	19.33	8.24	4.36	—	2.92

the untreated and mineralized wood before and after CONE testing were analyzed. The oxygen to carbon atomic ratio (O/C) of the untreated wood markedly decreased after combustion, whereas the decrease in MW₂₂ was less (Table 2). This finding suggests that large amounts of oxygen-containing compounds in the untreated wood were volatile during combustion. The fine spectra of C1s were also analyzed (Table 2 and Fig. 12) [28,46–48]. The residues of both the untreated wood and MW₂₂ presented sp² C, with the former containing a larger proportion, indicating that the former possessed a higher degree of graphitization (Fig. 12c and d). Moreover, the π - π content in the untreated wood residue was higher than that in the MW₂₂ residue, indicating a more pronounced aromatization of the untreated wood. The hydrogen- and oxygen-containing components of the MW₂₂ residues were also higher than those of the untreated wood. The aforementioned results indicate that ZnB slowed the chemical transformation of wood during combustion.

3.2.5. Gas-phase analysis

The gaseous products during thermal degradation were analyzed by

TG-FTIR. As shown in the 3D diagrams, the intensity of gas generated from the degradation of the untreated wood was much higher than that of the MW₂₂ (Fig. 13a). To further analyze the gaseous products, the FTIR spectra of the released gases were collated at the temperature with strong gas emissions (Fig. 13b), and the absorption bands were identified, with reference to the literature [43,49–52]. The absorption peaks at 3500–3800 cm⁻¹ corresponded to the stretching vibration of free O—H, related to H₂O, alcohols, and phenols. The peaks located at 2850–3200 cm⁻¹ indicated the presence of hydrocarbons, mainly methane. The absorption bands at 2000–2250 and 2250–2400 cm⁻¹ were ascribed to CO and CO₂, respectively. The peaks at 1600–1900 cm⁻¹ corresponded to the carbonyl from aldehydes, ketones, and acids. Further, the absorption bands at 1300–1600 cm⁻¹ were the combined frequency of O—H bending and aromatic ring skeleton vibration. The absorption band at 1000–1300 cm⁻¹ was associated with the C—O stretching vibrations in ether, phenols, or alcohols. Most groups in MW₂₂ significantly decreased relative to those in the untreated wood, suggesting a reduced gas release. The thermal degradation of wood is a competitive process between the volatilization of gaseous products and the formation of a stable carbon layer [5]. The formation of a stable carbon layer, rather than gaseous volatilization, facilitates wood flame retardancy; thus, owing to the reduction in gas release, MW₂₂ exhibited a higher flame resistance than that of the untreated wood. In addition, some small molecular gases, such as H₂O and CO₂, are generally the ultimate products for multiple pyrolysis of wood, and their yield affects the flame retardancy of wood. The FTIR spectra of four typical small molecular gases (H₂O, CO₂, CH₄, and CO) versus temperatures are presented in Fig. 13c. Two peaks for CH₄ release were observed during the thermal degradation of the untreated wood. The first peak at 306 °C primarily resulted from the cleavage of the weak methoxyl (—OCH₃) and the methylene (—CH₂—) from hemicellulose [40]. The second peak at 379 °C of CH₄ was mainly caused by the pyrolysis of cellulose and lignin,

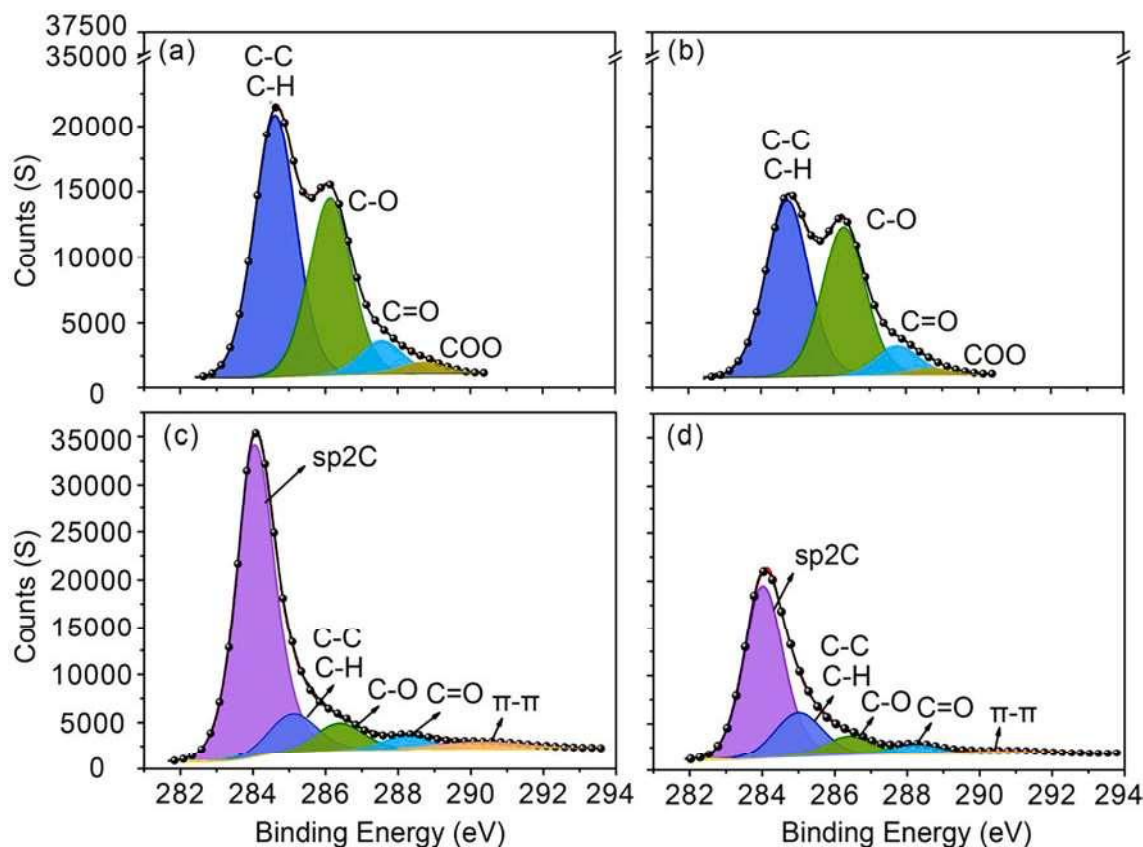


Fig. 12. High-resolution C1s spectra: (a) untreated wood (UW), (b) mineralized wood with 22.1 % ZnB (MW₂₂), (c) residue of UW, and (d) residue of MW₂₂.

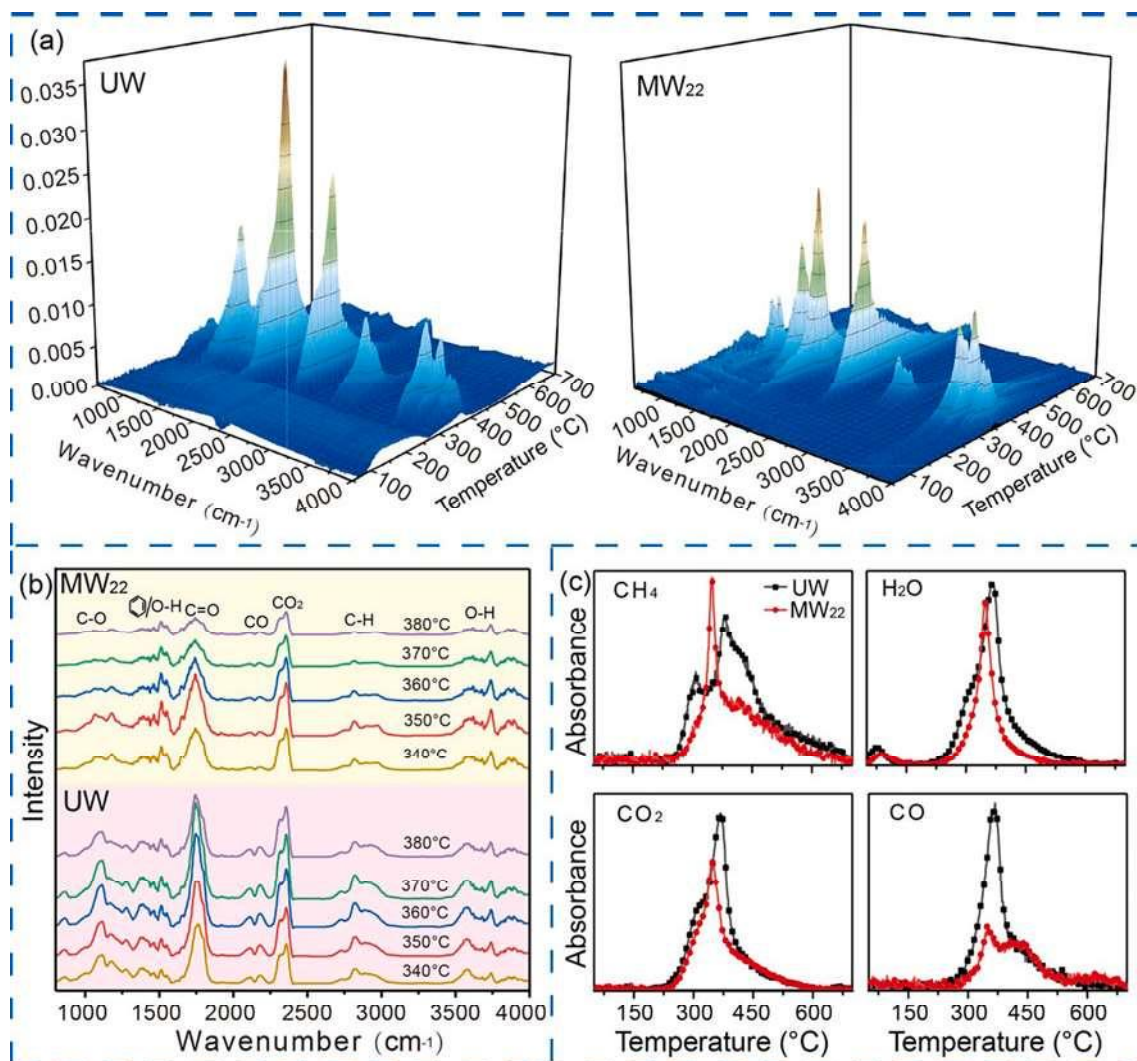


Fig. 13. (a) TG-FTIR 3D diagrams for untreated wood (UW) and mineralized wood with 22.1% ZnB (MW₂₂), (b) FTIR of the volatiles of UW and MW₂₂ at different degradation temperatures, and (c) FTIR of four typical gases (H₂O, CO₂, CH₄, and CO).

as well as the multiple pyrolysis of preformed organic volatiles [51]. The CH₄ profile merged into one sharp peak (346 °C) for MW₂₂, indicating that ZnB delayed the pyrolysis of hemicellulose and catalyzed the pyrolysis of cellulose and lignin, which is consistent with the TGA result. The yield of inflammable CH₄ in MW₂₂ decreased relative to that in the untreated wood, which is favorable for flame retardancy because of the decreased combustible source. The release of H₂O at 240 °C–600 °C in the untreated wood was attributed to the cleavage of aliphatic hydroxyl groups and the condensation of hydroxyl groups in the polysaccharide [50]. The H₂O yield in MW₂₂ decreased even though ZnB released a small amount of crystal water, indicating that ZnB inhibited the dehydration reaction of wood, particularly at elevated temperatures. In addition, the maximum H₂O release was reached earlier as the dehydrated ZnB catalyzed the degradation of wood at relatively lower temperatures. Both CO₂ and CO yields of MW₂₂ were lower than those of the untreated wood, indicating that most C and O remained in the condensed phase. The sharply reduced CO emission of MW₂₂ significantly decreased the fire hazard because CO is the primary gas causing suffocation and poisoning.

Pyrolysis-gas chromatography/mass spectrometry was employed to identify the volatile organic compounds (VOCs) released through wood pyrolysis. More than 200 species of VOC products emitted by the untreated wood were detected at 350 °C; the related total ion chromatogram is given in Fig. S5. The primary products are listed in Table S1,

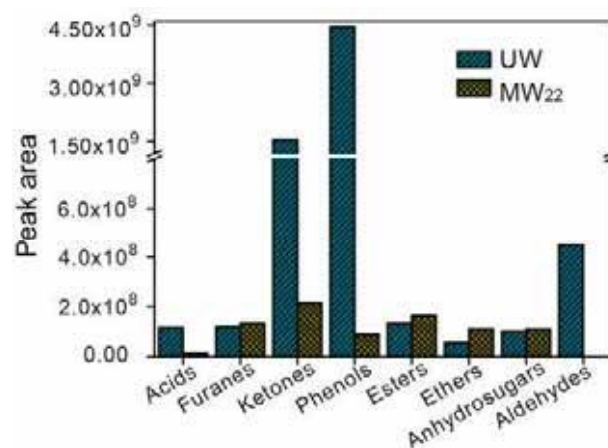


Fig. 14. Distribution of the pyrolysis products for untreated wood (UW) and mineralized wood with 22.1% ZnB (MW₂₂).

including several classes of oxy-containing compounds such as acids, aldehydes, ketones, furans, phenols, and so on (Fig. 14). Owing to their inflammability, the listed products are undesirable for wood flame

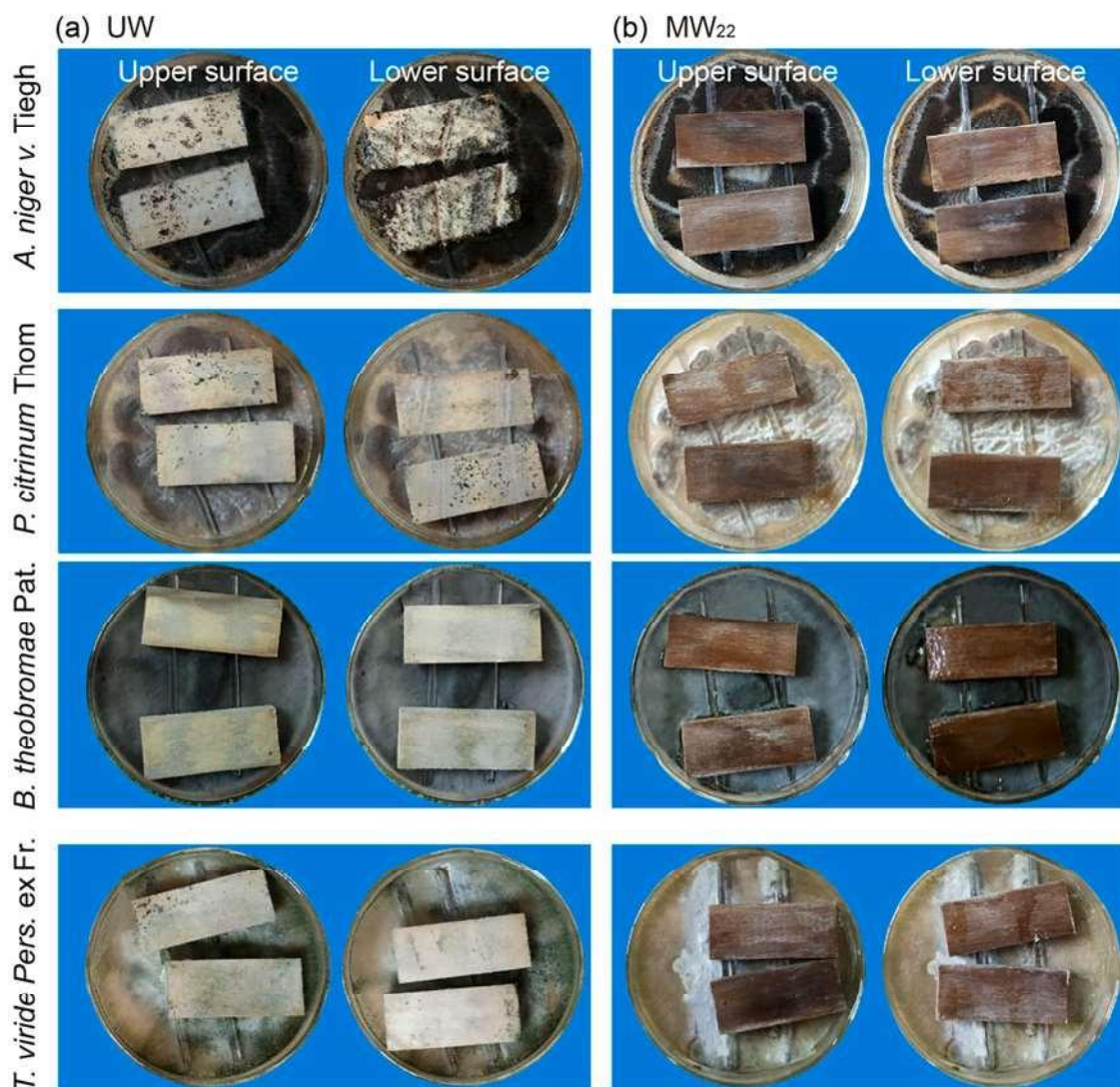


Fig. 15. Appearance of (a) untreated wood (UW) and (b) mineralized wood with 22.1% ZnB (MW₂₂) after anti-mold tests; top to bottom: *A. niger* v. Tiegh, *P. citrinum* Thom, *B. theobromae* Pat., and *T. viride* Pers. ex Fr.

retardant. Compared with the untreated wood, MW₂₂ released significantly fewer ketones and phenols, which are the main components of combustible wood tar [53]. However, the anhydro-sugars, primarily levoglucosan (Fig. S5 and Table S1), produced from MW₂₂ was an order of magnitude higher than that from the untreated wood. Levoglucosan was mainly generated from 1,4-glucosidic bonds cracking and the subsequent intramolecular rearrangement. The cleavage of the 1,4-glucosidic bonds was competed with the decomposition of glycan rings which directly produced small molecules such as alcohol and aldehyde [54]. The higher levoglucosan yield of MW₂₂ indicates that ZnB catalyzed the fracture of the 1, 4-glycosidic linkage rather than the glycan rings. Levoglucosan as an intermediate could be further degraded at high temperatures, and its pyrolysis could be prolonged to produce furans, alcohol, ketones, and so on. ZnB inhibited the further pyrolysis of levoglucosan, which is conducive to achieving efficient flame retardancy. In summary, incorporating ZnB changed the pyrolysis pathways of wood and reduced the total yield of inflammable volatiles, thus promoting wood flame retardancy.

3.2.6. Flame retardant mechanism

On the basis of the aforementioned analysis, the flame retardant mechanisms of ZnB on wood are summarized as follows. The cooling effect of crystalline water release in ZnB delays the thermal degradation

of hemicellulose. Subsequently, the dehydrated ZnB particles catalyze the devolatilization of cellulose and lignin toward carbonaceous char formation. The preformed thermal stabilized char layer serves as a barrier, protecting the interior wood. The most crucial process is the formation of a glass-like protective film by the ZnB particles at high temperatures, coating the wood. The incombustible ZnB film also prevents cellulose and lignin from further devolatilization, thus reducing the heat feedback to the wood substrate and consequently decreasing the kinetics of wood pyrolysis. In addition, the uniformly impregnated ZnB particles in the hierarchical pores of the cell wall melt at high temperatures, forming a cross-linking network. This formation improves the robustness of the residual skeleton and consequently delays the growth of cracks produced by the impulse of volatile gases and flame. The integrity of the residual skeleton hinders heat/mass transport between gaseous and condensed phases. Therefore, ZnB inhibits the three sufficient conditions (combustibles, ignition sources, and combustion improver) for wood combustion.

3.2.7. Mold resistance

The untreated wood and MW₂₂ were incubated with *A. niger* v. Tiegh, *P. citrinum* Thom, *B. theobromae* Pat., and *T. viride* Pers. ex Fr. The results showed that the upper and lower surfaces of the untreated wood were severely infected with mold (Fig. 15a), and the average infection value

Table 3

Mold resistance of the untreated wood (UW) and mineralized wood with 22.1% ZnB (MW₂₂).

Samples		A. niger v. Tiegh	P. citrinum Thom	B. theobromae Pat.	T. viride Pers. ex Fr.
UW	Average infection value	4	4	4	4
	Average protective efficiency (%)	–	–	–	–
MW ₂₂	Average infection value	0	0	0	0
	Average protective efficiency (%)	100	100	100	100

against four types of mold was 4 (Table 3). However, MW₂₂ showed exceptional mold resistance (Fig. 15b), with an average infection value of 0 and average protective efficiencies of 100 % to four types of mold (Table 3). The mold resistance of MW₂₂ after leaching was also detected. The results showed that MW₂₂ after leaching still had excellent mold resistance. (Fig. S6). The superior mold resistance of MW₂₂ is due to the destruction of mold by ZnB via the inhibition of cell wall synthesis, inhibition of metabolism by binding to enzymes, and disruption of cell membrane permeability [55]. The low hygroscopicity (Fig. S7) and loss of nutrients (glucose and starch) during mineralization also contribute to the mold resistance of MW₂₂ [56].

3.2.8. Antitermite properties

The untreated wood, which was severely attacked by termites (Fig. 16a), exhibited an average mass loss of 61.5 %, an average moth-proofing rating of 4.8, and average termite mortality of 50.8 % (Table 4). Meanwhile, MW₂₂ showed extremely superior termite resistance (Fig. 16b), with an average mass loss of 3.6 %, an average rating of 10, and average termite mortality of 100 % (Table 3). The reason was that when ingested *via* feeding, ZnB particles act as stomach poison to termites. Specifically, ZnB particles can kill the protozoa that secrete cellulase to digest lignocellulose in the gut of termite, thereby inhibiting cellulase secretion, leading to termite death from starvation [57]. The aforementioned effect is passed to other termites *via* trophallaxis, killing the termite population and protecting wood from termite attack [58]. The diagram illustrating the antitermite mechanism is presented in Fig. S8.

4. Conclusions

In this study, nanostructured wood with efficient flame retardancy, smoke suppression capability, mold resistance, and antitermite properties were fabricated by *in situ* synthesis of nano/microscale ZnB particles that were uniformly deposited in a hierarchical porous wood. *In situ* mineralization of insoluble ZnB inside the wood structure enables bulk treatment and retains the aesthetically pleasing appearance of untreated wood. The dominant factor affecting the flame retardancy of wood is the formation of a compact char layer, which is catalyzed by dehydrated ZnB deposited in a hierarchical wood structure. The dehydrated ZnB particles melt at high temperatures, forming a noncombustible film, which covers and cross-links the carbonaceous char layer and promotes



Fig. 16. Appearance of (a) untreated wood (UW) and (b) mineralized wood with 22.1% ZnB (MW₂₂) before and after termite attack.

Table 4

Evaluation of antitermite properties of the untreated wood (UW) and mineralized wood with 22.1% ZnB (MW₂₂).

Samples	Mass loss (%)	Termite mortality (%)	Rating
UW-1	64.9	52.2	4
UW-2	61.4	50.2	6
UW-3	68.4	58.2	4
UW-4	57.1	46.4	4
UW-5	55.5	45.8	6
Average value	61.5	50.6	4.8
MW ₂₂ -1	4.3	100	10
MW ₂₂ -2	4.6	100	10
MW ₂₂ -3	3.2	100	10
MW ₂₂ -4	4.2	100	10
MW ₂₂ -5	3.6	100	10
Average value	4.0	100	10

Note: Numbers behind UW and MW₂₂ represent the number of replicates.

the formation of a cohesive and robust 3D residual skeleton. The residual skeleton forms an insulation barrier, which is responsible for the retardation of oxygen diffusion, thermal insulation, reduction of the release of flammable gas, and the suppression of toxic smoke. The toxicity of ZnB against mold and termites endows mineralized wood with superior antitermite activity and mold resistance. Owing to its simple, cost-effective, and eco-friendly fabrication process, ZnB-mineralized wood is a promising candidate as a green building material in various fields of application.

Declaration of Competing Interest

The authors declare that they have no known competing financial interests or personal relationships that could have appeared to influence the work reported in this paper.

Data availability

No data was used for the research described in the article.

Acknowledgements

This work was supported by the Research and Development Program in Key Areas of Guangdong Province (2020B0202010008) and the National Key Research and Development Program of China (Grant No. 2019YFD1101203). The authors also express thanks to the supported by the National Natural Science Foundation of China (Grant Nos. 31901251 and 32071698).

Appendix A. Supplementary data

Supplementary data to this article can be found online at <https://doi.org/10.1016/j.cej.2022.138308>.

References

- [1] Q. Fu, Y. Chen, M. Sorieul, Wood-based flexible electronics, *ACS nano* 14 (2020) 3528–3538.
- [2] L.B. Mao, H.L. Gao, H.B. Yao, L. Liu, H. Colfen, G. Liu, S.M. Chen, S.K. Li, Y.X. Yan, Y.Y. Liu, Synthetic nacre by predesigned matrix-directed mineralization, *Science* 354 (2016) 107.
- [3] Y. Wang, T. Azas, M. Robin, A. Vallée, C. Catania, P. Legriel, G. Pehau-Arnaudet, F. Babonneau, M.M. Giraud-Guille, N. Nassif, The predominant role of collagenin the nucleation, growth, structure and orientation of bone apatite, *Nat. Mater.* 11 (2012) 724–733.
- [4] Y. Chen, J. Fu, B. Dang, Q. Sun, H. Li, T. Zhai, Artificial wooden nacre: a high specific strength engineering material, *ACS Nano* 14 (2020) 2036–2043.
- [5] Q. Fu, L. Medina, Y. Li, F. Carosio, A. Hajian, L.A. Berglund, Nanostructured wood hybrids for fire-retardancy prepared by clay impregnation into the cell wall, *ACS Appl. Mater. Interfaces* 9 (2017) 36154–36163.
- [6] L.J. Sweeney, K. Chin, J.C. Hower, D.A. Budd, D.G. Wolfe, Fossil wood from the middle Cretaceous Moreno Hill Formation: unique expressions of wood mineralization and implications for the processes of wood preservation, *Int. J. Coal Geol.* 79 (2009) 1–17.
- [7] H. Guo, M. Lukovic, M. Mendoza, C.M. Schlepütz, M. Griffa, B. Xu, S. Gaan, H. Herrmann, I. Burgert, Bioinspired struvite mineralization for fire-resistant wood, *ACS Appl. Mater. Interfaces* 11 (2019) 5427–5434.
- [8] Z. Xiao, J. Xu, C. Mai, H. Militz, Q. Wang, Y. Xie, Combustion behavior of Scots pine (*Pinus sylvestris* L.) sapwood treated with a dispersion of aluminum oxychloride-modified silica, *Holzforschung* 70 (2016) 1165–1173.
- [9] L.A. Berglund, I. Burgert, Bioinspired wood nanotechnology for functional materials, *Adv. Mater.* 30 (2018) 1704285–1704300.
- [10] V. Merk, M. Chanana, S. Gaan, I. Burgert, Mineralization of wood by calcium carbonate insertion for improved flame retardancy, *Holzforschung* 70 (2016) 867–876.
- [11] V. Merk, M. Chanana, T. Keplinger, S. Gaan, I. Burgert, Hybrid wood materials with improved fire retardance by bio-inspired mineralisation on the nano- and submicron level, *Green Chem.* 17 (2015) 1423–1428.
- [12] A. Pondelak, A.S. Skapin, N. Knez, F. Knez, T. Pazlar, Improving the flame retardancy of wood using an eco-friendly mineralisation process, *Green Chem.* 23 (2021) 1130–1135.
- [13] Y. Tao, P. Li, L. Cai, S.Q. Shi, Flammability and mechanical properties of composites fabricated with CaCO₃-filled pine flakes and phenol formaldehyde resin, *Compos. Part B: Eng.* 167 (2019) 1–6.
- [14] T. Furuno, F. Wada, S. Yusuf, Biological resistance of wood treated with zinc and copper metaborates, *Holzforschung* 60 (2006) 104–109.
- [15] V. Merk, M. Chanana, N. Gierlinger, A.M. Hirt, I. Burgert, Hybrid wood materials with magnetic anisotropy dictated by the hierarchical cell structure, *ACS Appl. Mater. Interfaces* 6 (2014) 9760–9767.
- [16] K. Shen, Kelvin, review of recent advances on the use of boron-based flame retardants, in: C.D. Papaspyrides, P. Kiliaris (Eds.), *Polymer Green Flame Retardants*, Elsevier, Amsterdam, 2014, pp. 367–389.
- [17] L.A. Savas, M. Dogan, Flame retardant effect of zinc borate in polyamide 6 containing aluminum hypophosphite, *Polym. Degrad. Stab.* 165 (2019) 101–109.
- [18] P. Khalili, X. Liu, K.Y. Tshai, C. Rudd, X. Yi, I. Kong, Development of fire retardancy of natural fiber composite encouraged by a synergy between zinc borate and ammonium polyphosphate, *Compos. Part B: Eng.* 159 (2019) 165–172.
- [19] C. Tascioglu, K. Umemura, T. Yoshimura, Seventh-year durability evaluation of zinc borate incorporated wood-plastic composites and particleboard, *Compos. Part B: Eng.* 137 (2018) 123–128.
- [20] B. Garba, Effect of zinc borate as flame retardant formulation on some tropical woods, *Polym. Degrad. Stab.* 64 (1999) 517–522.
- [21] G. Mantanis, E. Terzi, S.N. Kartal, A.N. Papadopoulos, Evaluation of mold, decay and termite resistance of pine wood treated with zinc- and copper-based nanocompounds, *Int. Biodeterior. Biodegrad.* 90 (2014) 140–144.
- [22] T.T. Nguyen, T.V.K. Nguyen, Z. Xiao, F. Wang, Z. Zheng, W. Che, Y. Xie, Combustion behavior of poplar (*Populus adenopoda* Maxim.) and radiata pine (*Pinus radiata* Don.) treated with a combination of styrene-acrylic copolymer and sodium silicate, *Eur. J. Wood Wood Prod.* 77 (2019) 439–452.
- [23] T. Furuno, L. Lin, S. Katoh, Leachability, decay, and termite resistance of wood treated with metaborates, *J. Wood Sci.* 49 (2003) 344–348.
- [24] J. Zhang, A. Koubaa, D. Xing, H. Wang, Y. Wang, W. Liu, Z. Zhang, X. Wang, Q. Wang, Conversion of lignocellulose into biochar and furfural through boron complexation and esterification reactions, *Bioresour. Technol.* 312 (2020), 123586.
- [25] X. Gu, X. Ma, L. Li, C. Liu, K. Cheng, Z. Li, Pyrolysis of poplar wood sawdust by TG-FTIR and Py-GC/MS, *J. Anal. Appl. Pyrolysis* 102 (2013) 16–23.
- [26] Y. Xie, J. Xu, H. Militz, F. Wang, Q. Wang, C. Mai, Z. Xiao, Thermo-oxidative decomposition and combustion behavior of Scots pine (*Pinus sylvestris* L.) sapwood modified with phenol- and melamine-formaldehyde resins, *Wood Sci. Technol.* 50 (2016) 1125–1143.
- [27] GB/T18261-2013, Test method for efficacy of mildew inhibitor against wood mould and discoloration fungus, Chinese National Committee for Standardization.
- [28] AWPA. E1-2017, Laboratory methods for evaluating the termite resistance of wood-based materials: choice and no-choice tests, American Wood Protection Association, 2017.
- [29] F. Samyn, S. Bourbigot, S. Duquesne, R. Delobel, Effect of zinc borate on the thermal degradation of ammonium polyphosphate, *Thermochim. Acta* 456 (2007) 134–144.
- [30] B. Guo, Y. Liu, Q. Zhang, F. Wang, Q. Wang, Y. Liu, J. Li, H. Yu, Efficient flame-retardant and smoke-suppression properties of Mg-Al-layered double-hydroxide nanostructures on wood substrate, *ACS Appl. Mater. Interfaces* 9 (2017) 23039–23047.
- [31] T. Orhan, N.A. Isitman, J. Hacaloglu, C. Kaynak, Thermal degradation mechanisms of aluminium phosphinate, melamine polyphosphate and zinc borate in poly (methyl methacrylate), *Polym. Degrad. Stab.* 96 (2011) 1780–1787.
- [32] L.M. Alvarenga, T.P. Xavier, M.A. Barrozo, M.S. Babelos, T.S. Lira, Determination of activation energy of pyrolysis of carton packaging wastes and its pure components using thermogravimetry, *Waste Manage.* 53 (2016) 68–75.
- [33] Q. Qin, R. Guo, E. Ren, X. Lai, C. Cui, H. Xiao, M. Zhou, G. Yao, S. Jiang, J. Lan, Waste cotton fabric/zinc borate composite aerogel with excellent flame retardancy, *ACS Sustain. Chem. Eng.* 8 (2020) 10335–10344.
- [34] Q. Xia, C. Chen, T. Li, S. He, J. Gao, X. Wang, L. Hu, Solar-assisted fabrication of large-scale, patternable transparent wood, *Sci. Adv.* 7 (2021) 7342–7369.
- [35] M.S. Akhter, J.R. Keifer, A.R. Chughtai, D.M. Smith, The absorption band at 1590cm⁻¹ in the infrared spectrum of carbons, *Carbon* 23 (1985) 589–591.

- [36] V. Emmanuel, B. Odile, R. Celine, FTIR spectroscopy of woods: a new approach to study the weathering of the carving face of a sculpture, *Spectrochim. Acta A* 136 (2015) 1255–1259.
- [37] T.T. Bartels, *The Sadtler Handbook of Infrared Spectra*, Bio-Rad Laboratories Inc, Informatics Division, 1978.
- [38] J. Wu, *Technique and Application of Modern Fourier Transform Infrared Photoacoustic Spectroscopy*, Science and Technology Document Press, Shanghai, 1994.
- [39] J. Li, S. Xia, S. Gao, FT-IR and Raman spectroscopic study of hydrated borates, *Spectrochim. Acta A* 51 (1995) 519–532.
- [40] H. Yang, R. Yan, H. Chen, D.H. Lee, C. Zheng, Characteristics of hemicellulose, cellulose and lignin pyrolysis, *Fuel* 86 (2007) 1781–1788.
- [41] B.R. Xu, C. Deng, Y.M. Li, P. Lu, P.P. Zhao, Y.Z. Wang, Novel amino glycerin decorated ammonium polyphosphate for the highly-efficient intumescent flame retardance of wood flour/polypropylene composite via simultaneous interfacial and bulk charring, *Compos. Part B: Eng.* 172 (2019) 636–648.
- [42] T. Liu, L. Sun, R. Ou, Q. Fan, L. Li, C. Guo, Z. Liu, Q. Wang, Flame retardant eugenol-based thiol-ene polymer networks with high mechanical strength and transparency, *Chem. Eng. J.* 368 (2019) 359–368.
- [43] A.N. Zhang, H.B. Zhao, J.B. Cheng, M.E. Li, S.L. Li, M. Cao, Y.Z. Wang, Construction of durable eco-friendly biomass-based flame-retardant coating for cotton fabrics, *Chem. Eng. J.* 410 (2021), 128361.
- [44] B. Tawiah, Y. Zhou, R.K.K. Yuen, J. Sun, B. Fei, Microporous boron based intumescent macrocycle flame retardant for poly(lactic acid) with excellent UV protection, *Chem. Eng. J.* 402 (2020), 126209.
- [45] X. Wang, H. Pang, W. Chen, Y. Lin, L. Zong, G. Ning, Controllable fabrication of zinc borate hierarchical nanostructure on brucite surface for enhanced mechanical properties and flame retardant behaviors, *ACS Appl. Mater. Interfaces* 6 (2014) 7223–7235.
- [46] J.F. Moulder, W.F. Stickle, P.E. Sobol, K.D. Bomben, *Handbook of x-ray photoelectron spectroscopy*, Muilenberg Perkin-Elmer Corp, Physical Electronics Division, Eden Prairie, Minnesota, USA, 1992.
- [47] G. Beamson, D. Briggs, *High Resolution XPS of Organic Polymers : The Scienta ESCA 300 database*, John Wiley & Sons, Hoboken, 1992.
- [48] Thermo scientific XPS simplified: Elements Table, Carbon. <https://xpssimplified.com/elements/carbon.php>, 2021 (accessed 24 June 2021).
- [49] T. Yang, M. Xia, S. Chen, M. Mu, G. Yuan, Enhancing the thermal stability of silica-mineralized wood via layer-by-layer self-assembly, *J. Therm. Anal. Calorim.* 14 (2020) 309–318.
- [50] P. Fu, S. Hu, J. Xiang, L. Sun, S. Su, S. An, Study on the gas evolution and char structural change during pyrolysis of cotton stalk, *J. Therm. Anal. Calorim.* 97 (2012) 130–136.
- [51] Q. Liu, S. Wang, Y. Zheng, Z. Luo, K. Cen, Mechanism study of wood lignin pyrolysis by using TG–FTIR analysis, *J. Anal. Appl. Pyrolysis* 82 (2008) 170–177.
- [52] G. Huang, W. Chen, T. Wu, H. Guo, P. Song, Multifunctional graphene-based nano-additives toward high-performance polymer nanocomposites with enhanced mechanical, thermal, flame retardancy and smoke suppressive properties, *Chem. Eng. J.* 410 (2020), 127590.
- [53] Y. Dong, B. Tian, F. Guo, S. Du, Y. Zhan, H. Zhou, L. Qian, Application of low-cost Fe-based catalysts in the microwave-assisted pyrolysis of macroalgae and lignocellulosic biomass for the upgradation of bio-oil, *Fuel* 300 (2021), 120944.
- [54] G. Lv, S. Wu, Analytical pyrolysis studies of corn stalk and its three main components by TG-MS and Py-GC/MS, *J. Anal. Appl. Pyrolysis* 97 (2012) 11–18.
- [55] D.N. Obanda, T.F. Shupe, H.M. Barnes, Reducing leaching of boron-based wood preservatives - a review of research, *Bioresour. Technol.* 99 (2008) 7312–7322.
- [56] W. Li, M. Liu, H. Zhai, H. Wang, Y. Yu, Preparing highly durable bamboo materials via bulk furfurylation, *Constr. Build. Mater.* 262 (2020), 120726.
- [57] C.E. Bernard, M.C. Harrass, M.J. Manning, Chapter 94 - Boric acid and inorganic borate pesticides, in: K. Robert (Ed.), *Hayes' Handbook of Pesticide Toxicology*, 3th ed., Academic Press, USA, 2010, pp. 2033–2053.
- [58] C.A. Clausen, N.S. Kartal, R.A. Arango, F. Green, The role of particle size of particulate nano-zinc oxide wood preservatives on termite mortality and leach resistance, *Nanoscale Res. Lett.* 6 (2011).

Available online at www.sciencedirect.com
jmr&t
 Journal of Materials Research and Technology
journal homepage: www.elsevier.com/locate/jmrt

Original Article

Recycling end-of-life WPC products into ultra-high-filled, high-performance wood fiber/polyethylene composites: a sustainable strategy for clean and cyclic processing in the WPC industry


 Haiyang Zhou ^{a,b,1}, Wenjuan Li ^{a,b,1}, Xiaolong Hao ^{a,b}, Guanggong Zong ^c,
 Xin Yi ^b, Junjie Xu ^{a,b}, Rongxian Ou ^{a,b,*}, Qingwen Wang ^{a,b}
^a Institute of Biomass Engineering, Key Laboratory of Energy Plants Resource and Utilization (Ministry of Agriculture and Rural Affairs), South China Agricultural University, 483 Wushan Road, Guangzhou 510642, China

^b Key Laboratory for Biobased Materials and Energy of Ministry of Education, College of Materials and Energy, South China Agricultural University, 483 Wushan Road, Guangzhou 510642, China

^c Art and Design Institute, Yangzhou University, 88 Daxue South Road, Yangzhou, 225009, China

ARTICLE INFO

Article history:

Received 27 January 2022

Accepted 18 February 2022

Available online 25 February 2022

Keywords:

Wood-plastic composites

Recycling

Ultra-highly filled

Sustainability

Circular utilization

ABSTRACT

As “green” composites, recycling end-of-life wood-plastic composites (WPCs) is crucial for sustainable and efficient resource utilization and carbon neutrality. In this study, waste WPC windows with 47.6 wt.% wood fiber (WF) were recycled as the polymer matrix and then reprocessed with waste WFs by extrusion into ultra-high-filled WF/polyethylene composites (UH-WPCs) using MAPE as a compatibilizer. The tensile and flexural moduli of all UH-WPCs with/without MAPE were higher than those of the waste WPCs. The MAPE-compatibilized UH-WPCs demonstrated improved water resistance, creep resistance, and dimensional stability. The tensile strength, tensile modulus, flexural strength, and flexural modulus of the UH-WPCs with 80 wt.% WF and 4 wt.% MAPE were 26.6%, 50.0%, 26.4%, and 87.9% higher than those of the waste WPCs, respectively. The presence of MAPE could improve the WF-matrix interfacial interaction and protect the WF from damage during reprocessing owing to the improved wettability and plasticization on WF. It is anticipated that the proposed strategy will provide a facile method to recycle end-of-life WPC products into high-performance composites at a low cost.

© 2022 The Author(s). Published by Elsevier B.V. This is an open access article under the CC BY-NC-ND license (<http://creativecommons.org/licenses/by-nc-nd/4.0/>).

* Corresponding author.

E-mail address: rongxian_ou@scau.edu.cn (R. Ou).

¹ These authors contributed equally to this work.

<https://doi.org/10.1016/j.jmrt.2022.02.091>

2238-7854/© 2022 The Author(s). Published by Elsevier B.V. This is an open access article under the CC BY-NC-ND license (<http://creativecommons.org/licenses/by-nc-nd/4.0/>).

1. Introduction

Wood-plastic composites (WPCs) are renewable and sustainable materials that are composed of natural fibers as fillers and a thermoplastic polymer matrix [1–4]. Natural fibers are derived either from agricultural and forest residues or from the processing residues of wood products, such as wood, bamboo, bast fibers, and crop straws [2,5–8]. Polyethylene (PE), polypropylene (PP), and polyvinyl chloride (PVC) are the most commonly used thermoplastic matrixes for WPCs as they are re-moldable, in contrast to thermosets, which permits the more efficient use of raw materials through recycling [1,5,9,10]. Deforestation and growing environmental concerns were the main driving forces for the launch of WPCs as a natural wood substitute over two decades ago [11]. Recently, WPCs have been extensively utilized in non-structural applications such as buildings, construction, furniture, packaging, and automotive products due to their water resistance, easy processing, recyclability, and environmental friendliness [1,12–14].

As the WPCs industry develops, there is a pressing need for dealing with end-of-life WPC products. Compared with landfills and incineration, recycling can prevent waste disposal and reduce environmental pollution by minimizing raw material consumption and storing carbon for a longer period [11,15–17]. As green composites, in addition to green sources of raw materials, WPCs are recyclable, which makes them a promising option for reducing production costs and enhancing resource reuse efficiency and cascade utilization [18]. Compared with virgin WPCs, recycled WPCs exhibit different physical and mechanical properties due to changes in the particle size, chemical composition, and dispersibility of natural fibers and the thermal degradation and crosslinking of thermoplastics [18,19]. The wide variability of WPC compositions in the waste stream, especially for end-of-life WPCs, complicates their recycling and determines whether they are suitable for use as a base for high-quality products.

Thermomechanical recycling, one of the most common methods for reprocessing WPCs, is predicted to be the most energy-efficient technique during the product lifecycle [20]; however, the mechanical, physical, and thermal properties of the regenerated WPCs are considerably lower after being recycled multiple times [16,21]. This is mainly due to fiber damage and thermo-oxidative degradation of matrixes [16,20] resulting from the high temperature and shear stress of extruder screws [21]. Moreover, the reprocessing of industrial WPCs scrap mixed with virgin WPCs in a specific ratio can help maintain their mechanical properties to some degree after being recycled multiple times [11]. Compared with flax or glass fiber-reinforced polypropylene composites, WPCs using medium-density fiberboard (MDF) fibers showed the best mechanical property retention after reprocessing due to the lowest reduction in the MDF fiber length after six cycles [22]. Rigid inorganic fibers are damaged once a critical stress is reached, while natural fibers break after being subjected to repeated deformation cycles and are more recyclable [20,22]. It has been reported that the effect of fiber breakage on the tensile properties of reprocessed WPCs is greater than that of using a coupling agent [23,24]. Despite the aforementioned

disadvantages, the fiber dispersion in a matrix was improved during reprocessing [25], and the water resistance increased by reducing the number of microvoids in WPCs [26]; however, the feasibility of WPCs reprocessing and their potential industrial applications have not been fully explored [27], and very few literatures are available on the recycling of WPC products into ultra-high-filled WPCs. This is a cost-effective approach to obtaining WPCs with high mechanical properties and satisfactory dimensional stability. Consequently, balancing recyclability and material performance is a determining factor for future applications of WPCs.

Ultra-high-filled (over 80 wt.%) wood fiber/polymer composites (UH-WPCs) have a broad application prospects, but its development is still in the initial stage due to its low mechanical performance, poor dimensional stability and other defects. Here, we report the reuse of end-of-life WPCs as the polymer matrix in bio-composites filled with sawdust to provide a sustainable cyclic processing strategy for WPCs. Low-cost, high-strength, high dimensional stability, and ultra-high-filled wood fiber/polyethylene composites (UH-WPCs) were prepared by reprocessing waste WPC window profiles with extra various recycled wood fiber contents. In order to investigate the plasticization and wettability of waste WPCs on WF without or with addition of MAPE during reprocessing, the effects of the wood fiber and maleic anhydride-grafted polyethylene (MAPE) contents on the dimensional stability, creep resistance, water uptake, and mechanical properties of the UH-WPCs were systematically investigated.

2. Experimental

2.1. Materials

Recycled wood fiber (WF, *Populus adenopoda*) was crushed in 40–80 mesh using sawdust as the raw material by a special crusher (FY600, Fuyang Machinery Co., Ltd., China). MAPE (HS3-008) with 1 wt.% MA grafting ratio was used as a compatibilizer (Hecheng Company, Guangzhou, China) and exhibited a melt flow index of $2.0 \text{ g } 10 \text{ min}^{-1}$ according to ASTM 1238. HDPE-based WPCs windows were fabricated and installed in our laboratory in August 2015. The formulation for the WPCs window profiles was WF: HDPE: MAPE: Lubricant = 50: 45: 5: 5, in which the WF (40–80 mesh) was also poplar wood as above. Stearic acid (#1801) and polyethylene wax (E19) were used as the lubricant, and both were purchased from Rizhisheng Company (Nantong, China). The end-of-life WPCs window profiles (waste WPCs) were smashed to granules for use.

2.2. Fabrication of the composites

Original WFs, waste WPCs granules, and MAPE were mixed in a specific ratio (Table 1) using a high-speed mixer for 10 min at 80 °C. They were then melt-blended using a conical twin-screw extruder (diameter of 31.8/20 mm) equipped with a strand pelletizer (HAAKE PolyLab OS Rheodrive 7 with Rheomex CTW100 OS extruding module, Thermo Fisher Scientific, Germany) at 165–185 °C. The total weight content of WF ranged from 60 wt.% to 85 wt.%. The UH-WPCs were extruded

Table 1 – Formulations of the UH-WPCs filled with various contents of WF and MAPE.

Samples ^a	Waste WPCs (wt.%)	WF (wt.%)	Total WF content (wt.%)	MAPE (wt.%)	Total MAPE (wt.%)	Total HDPE (wt.%)
W60	76.36	23.64	60	0	3.64	32.73
W65	66.82	33.18	65	0	3.18	28.64
W70	57.27	42.73	70	0	2.73	24.54
W75	47.73	52.27	75	0	2.27	20.46
W80	38.18	61.82	80	0	1.82	16.36
W85	28.64	71.36	85	0	1.36	12.27
WM60-1	74.45	24.55	60	1	4.55	31.91
WM65-1	64.91	34.09	65	1	4.09	27.82
WM70-1	55.36	43.64	70	1	3.64	23.73
WM75-1	45.82	53.18	75	1	3.18	19.64
WM80-1	36.27	62.73	80	1	2.73	15.54
WM80-2	34.36	63.64	80	2	3.64	14.73
WM80-4	30.55	65.45	80	4	5.45	13.09
WM85-1	26.73	72.27	85	1	2.27	11.46

^a W and M represent WF and MAPE, respectively, and the number behind M indicates the weight content of WF, and the number behind WM60-85 indicates the weight content of MAPE.

using the above pellets by the same extruder with sectional dimensions of 25 × 4 mm. The melt-blended and extrusion processing parameters for the waste WPCs and UH-WPCs are provided in [supplementary Table 1](#) and [Table 2](#), respectively.

2.3. Fiber size and morphology

The WFs in UH-WPCs were extracted using xylene solvent at 140 °C for 48 h to remove the polymer matrix components. Then, the mixture was filtered to isolate WF, and the separated WFs were further extracted using xylene for 24 h to remove the residual polymer matrix. The fiber size distribution was measured using a laser particle size analyzer (Mastersizer 3000, Malvern Instruments Ltd., UK) equipped with a wet dispersion system (Hydro 2000MU). After being sputter-coated with a thin gold layer, the morphology of the original and extracted WFs were analyzed with a tungsten filament scanning electron microscope (EVO18, Carl Zeiss, Oberkochen, Germany) at an accelerating voltage of 10 kV.

2.4. Characterizations of the composites

2.4.1. Morphological analysis

The extruded UH-WPCs samples were immediately broken vertical to the length direction after frozen in liquid nitrogen. The morphology of fractured surfaces were observed with a tungsten filament scanning electron microscope (EVO18, Carl Zeiss, Oberkochen, Germany) at an accelerating voltage of 10 kV after sputter-coated with a thin gold layer.

2.4.2. Mechanical tests

The classical dumbbell-shaped tensile specimens (type-I, 165 × 13 × 4 mm) were prepared using a special sampling machine (GT-7016-HA, Gotech Testing Machines Dong Guan Co., Ltd., China) and then tested at a speed of 5 mm min⁻¹ (ASTM D638) using a universal testing machine (AI 7000 MUT, Goodtechwill, Qingdao, China) with a 20 kN load cell. Three-point bending test (80 × 13 × 4 mm) was conducted at a speed of 2 mm min⁻¹ (ASTM D790) using the same machine. Un-notched cantilever impact test (80 × 10 × 4 mm) was

performed using an electronic impact tester (XJUD-5.5, Jinjian, Chengde, China) according to ASTM D6110. At least eight replicates were tested for each condition.

2.4.3. Creep behavior

The creep behavior of the UH-WPC specimens (35 × 12 × 4 mm) was performed using a dynamic thermol-mechanical analyzer (Q800, TA Instruments Inc., USA) equipped with the single-cantilever clamp. Isothermal 25 °C and a 2 MPa load were chose for the short-time creep tests, and the applying/releasing load time was 30 min [28,29].

2.4.4. Effect of heat and humidity on the dimensional stability

Before testing, the extruded UH-WPCs samples (100 × 25 × 4 mm) were placed at room temperature and indoor humidity (50–60%) for two months to reach an equilibrium moisture content. The specimens were then oven-dried in a drum wind oven at 80 °C for 10 days, and their size and mass were recorded to investigate the combined effects of heat and humidity on their dimensional stability. The dimensional changes of UH-WPCs were calculated in terms of their length, width, and thickness.

The linear coefficient of thermal expansion (LCTE) was analyzed from 25 °C to 80 °C. After the samples reached equilibrium mass after oven-drying at 80 °C for 7 days, they were naturally cooled to 25 °C in a desiccator, and their dimensions were recorded. The samples were conditioned in a drum wind oven at 80 °C for 24 h from an initial temperature of 25 °C, and the LCTE was also calculated in terms of their three-dimensional directions.

2.4.5. Water absorption and dimensional swelling testing

Before testing, the extruded UH-WPCs specimens (25 × 25 × 4 mm) were oven-dried at 80 °C for 24 h to reach an equilibrium moisture content. The samples with constant weight were then soaked in water at 25 °C for 50 days (ASTM D7031) to calculate the water absorption (WA, %). Moreover, the dimensional swelling (DS, %) of the UH-WPCs in the three-dimensional directions (LS, WS, and TS) were also calculated at specific times.

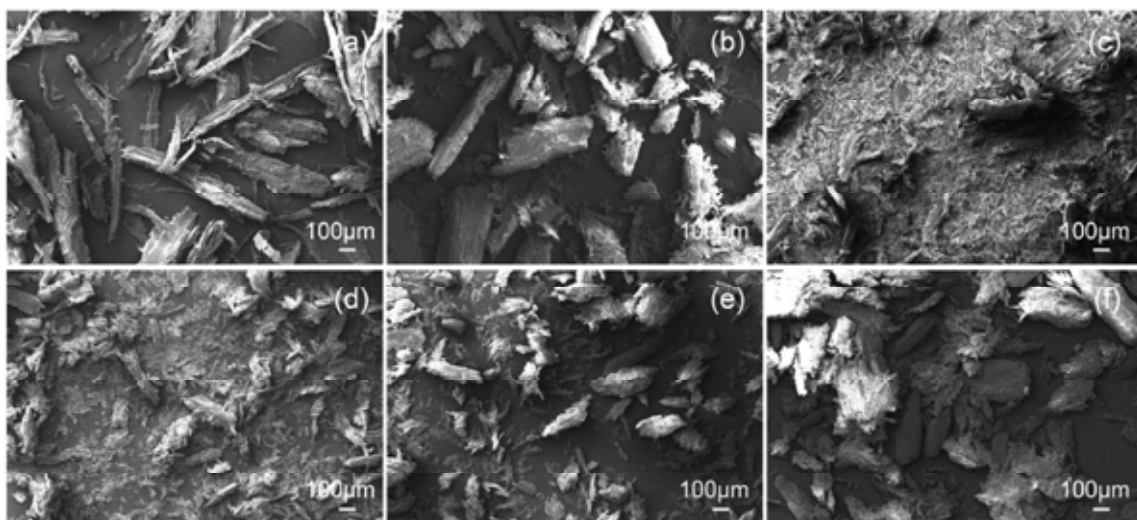


Fig. 1 — Micrographs of original WFs (a) and different WFs extracted from waste WPCs (b), W80 (c), WM80-1 (d), WM80-2 (e), and WM80-4 (f).

3. Results and discussion

3.1. Morphological analysis

The original WFs were rod-shaped with the largest aspect ratio (Fig. 1a). It has been shown that the geometric size and aspect ratio of the WFs greatly decrease after once melt blending/extrusion for the WPCs filled with 60 wt.% WF [29]. This was because WFs were considerably damaged (peeling, squeezing, and splitting) by the high pressure and shear forces during the extrusion process [13,29–31]. The WFs extracted from the waste WPCs showed the smallest decrease in their particle size among all extracted WFs (Fig. 1b–f) due to its highest polymer matrix content, which protected the WFs from damage during one melt blending/extrusion cycle. The WFs extracted from W80 were considerably damaged and exhibited the smallest size (Fig. 1c) due to the high melt pressure and shear forces during repeated melt blending/extrusion process. However, the fiber size of the WFs extracted from WM80-1 was considerably higher after adding 1 wt.% MAPE (Fig. 1d), and the number of large WFs increased upon increasing the MAPE content (Fig. 1e and f). The fiber-shaped original WFs were squeezed into plate-like particles in WM80-4 with destroying of the wood cell cavities and lumen. This results in a comparable size to that of the waste-WPCs processed only once (Fig. 1f). This result indicates that the ductility and flexibility of WFs extracted from WM80-4 were considerably enhanced owing to improved plasticization and wettability at higher MAPE contents. Moreover, the size distributions of the extracted WFs shifted to much smaller sizes after extrusion compared with the original WFs (Fig. 2). The particle size decreased in the order original WF > waste WPCs > WM80-4 > W80, which was in good agreement with the SEM results. The above results reveal that increasing the MAPE content helped maintain the WFs size during reprocessing due to improved plasticization and wettability, which

could act as a dominant factor that affected the different properties of the extruded WPCs.

The impact fracture surface of W60 exhibited noticeable gaps and boundaries between the WFs and polymer matrix (ellipse in Fig. 3a). This suggests insufficient wettability of the waste WPCs on the WF surface without MAPE after adding extra WFs. For W80, some traces are visible where the WFs were pulled-out and produced more gaps (Fig. 3b). After adding 1 wt.% MAPE, the boundary of WF-matrix became obscure, and the WFs were sufficiently covered by the matrix in WM60 and WM80 (Fig. 3c and d). The broken WFs were embedded in the polymer matrix without evident gaps at the interface, revealing stress transfer from the boundaries to WFs more effectively. This is attributed to the enhanced wettability of WFs by waste WPCs with MAPE and improved WF-matrix interfacial adhesion, which promoted the orientation and dispersion of WFs in the WM60 and WM80 matrix. The

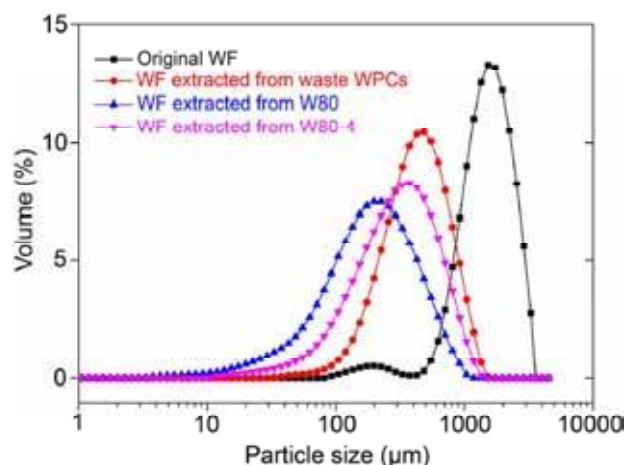


Fig. 2 — Particle size distributions of original and extracted WFs.

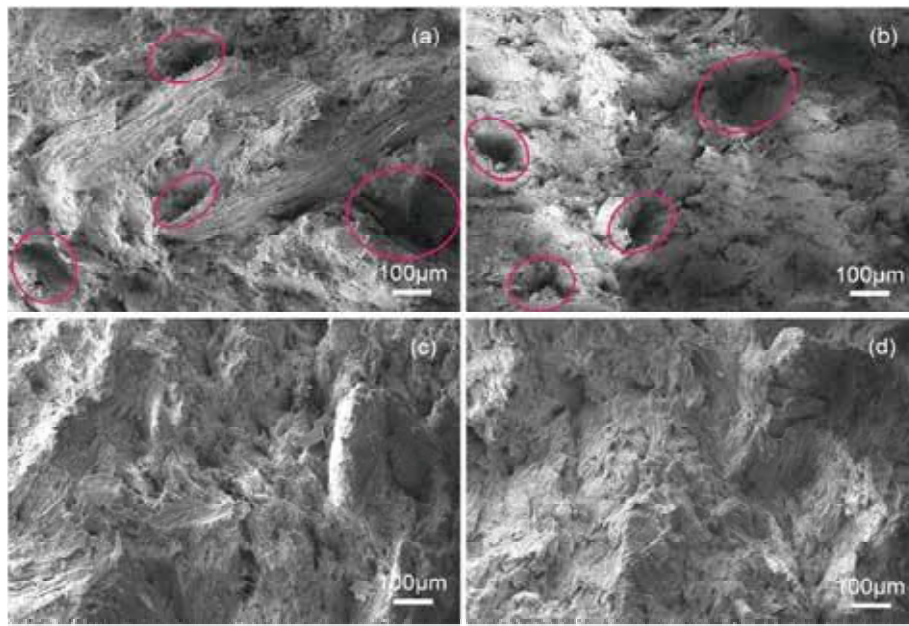


Fig. 3 – Micrographs of the fracture surface of UH-WPCs: (a) W60, (b) W80, (c) WM60-1, and (d) WM80-1.

improved WFs dispersion and WF-matrix interface will help enhance the durability of UH-WPCs such as dimensional stability, creep and water uptake resistance etc.

3.2. Mechanical properties of UH-WPCs

The effects of the MAPE and WF contents on the tensile and flexural properties of the UH-WPCs are shown in Fig. 4.

Without MAPE, both the tensile and flexural strengths of the UH-WPCs decreased upon increasing the WF content from 60 wt.% to 85 wt.% (Fig. 4a and b), and all values were lower than those of the waste WPCs. Specifically, the tensile and flexural strengths decreased from 31.5 MPa to 49.3 MPa for waste WPCs to 15.7 MPa and 30.7 MPa for the uncompatibilized UH-WPC with 85 wt.% WF (W85). This was attributed to the insufficient wettability of waste WPCs melt

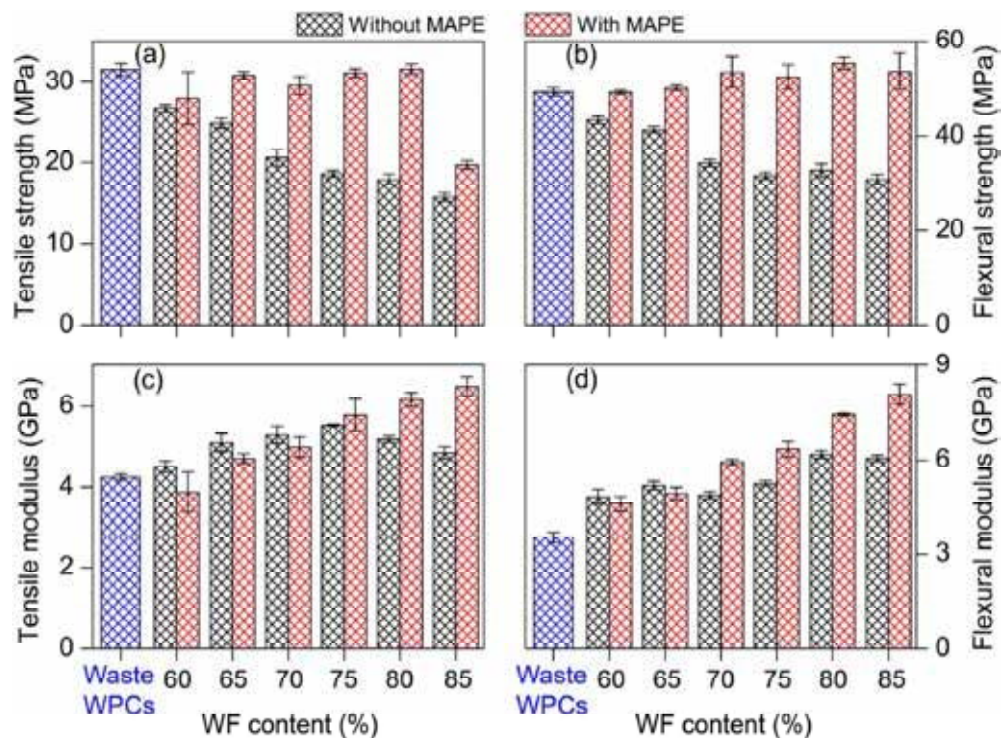


Fig. 4 – Mechanical properties of the UH-WPCs with different WF contents: (a) tensile strength, (b) flexural strength, (c) tensile modulus, and (d) flexural modulus.

on the additional WFs [30], which prevented the poorly-bonded WFs from serving as barriers against crack growth in UH-WPCs [32]. However, the tensile and flexural strengths dramatically increased after adding 1 wt.% MAPE as a compatibilizer compared with that of un-compatible counterparts, and the maximum increase in tensile and flexural strengths were 76.8% and 69.6% at 80 wt.% WF, respectively. The tensile strength of the MAPE-compatible UH-WPCs with 65–80 wt.% was comparable to that of the waste WPCs, while the flexural strength was higher. The improvement in the tensile and flexural strengths of the UH-WPCs with 1 wt.% MAPE was mostly attributed to the compatibilization of MAPE and the larger WFs particle size as demonstrated by SEM results (Figs. 1 and 3) [33–36]. It has been reported that MAPE acts as a toughness interphase that improves the WF-polymer matrixes interfacial adhesion, which results in stress transfer from the polymer matrix to WFs more efficiently [31,37].

The tensile and flexural moduli of the un-compatible UH-WPCs at various WFs content were all higher than those of the waste WPCs due to the higher stiffness of the WFs (Fig. 4c and d). Both the tensile and flexural moduli of the MAPE-compatible UH-WPCs continuously increased upon increasing the WFs content, and the UH-WPCs with 85 wt.% WF (WM85-1) exhibited the highest tensile and flexural moduli of 6.5 GPa and 8.1 GPa, respectively. This indicates that the rigidity of WFs was fully demonstrated in the presence of MAPE, especially at high WF contents. This may be because adding MAPE improved the interface interaction and protected the WFs from damage during reprocessing due to the improved plasticization and wettability on WFs. Compared with the un-compatible UH-WPCs, the MAPE-compatible UH-WPCs exhibited comparable tensile and flexural moduli at low WF contents but higher moduli at high WF contents. Generally, the tensile and flexural moduli are measured in the linear elastic regime range in low-stress rates, where the material has not broken for WPCs with appropriate amount of WFs (less than 70 wt.%) and is therefore less sensitive to the interfacial interaction. The moduli increase upon increasing the WF content in WPCs below the critical content (about 70 wt.%) due to the high rigidity of WFs [31]. However, the WF content was no longer the dominant factor determining the modulus of WPCs beyond the critical content [30]. Except for the WF content, matrix wettability and WF-matrix interface are also factors that greatly affect the modulus for highly-filled WPCs. Moreover, the SEM results (Fig. 1) revealed that WF breakage in the compatibilized UH-WPCs was minimized compared with that of un-compatible counterparts, and the large WFs resulting from the MAPE plasticization and wettability were believed to be the main factor responsible for the high modulus [30].

The impact strength of WPCs was dominated by WF breakage and the crack propagation energy between WFs-matrix interface [29]. Compared with the waste WPCs, the un-compatible UH-WPCs exhibited a lower un-notched impact strength that decreased upon increasing the WF content (Fig. 5). The maximum decrease was 78.3% for W85 compared with the waste WPCs. This was due to an increased stiffness after adding WFs and the insufficient interfacial adhesion between WFs and the matrix [38,39]. Incorporating MAPE as the compatibilizer resulted in a considerably higher

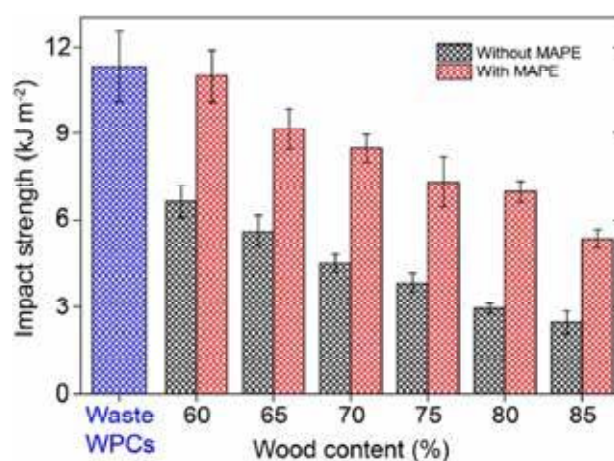


Fig. 5 – Impact strength of the UH-WPCs with different WF contents.

impact strength than the UH-WPCs without MAPE due to the improved WF-matrix interface and larger WF size. The maximum increase was 139.6% for WM80-1 compared with the W80. This indicates that more energy was dissipated for the compatibilized UH-WPCs when WFs were pulled-out from the matrix.

To investigate the effect of the MAPE content on the mechanical properties of UH-WPCs, various MAPE contents (1–4 wt.%) were added into the UH-WPCs filled with 80 wt.% WF. Compared with W80, the incorporation of MAPE greatly increased the tensile and flexural strengths, with maximum increases of 123.3% and 91.0%, respectively, for WM80-4 loaded with 4 wt.% MAPE (Fig. 6a and b). This is corresponding with previous reports, which showed that increasing the MAPE content improved the WF-matrix interfacial interactions, which helped stress transfer from the polymer matrix to WFs more efficiently [37]; therefore, a higher MAPE content within an appropriate range improved the mechanical strengths. In addition, with the increase of MAPE content, the damage of WFs decreased during processing (Fig. 1), which was also conducive to improving the mechanical strengths. The tensile modulus first increased and then stabilized upon further increasing the MAPE content (Fig. 6a), while the flexural modulus first increased and then decreased upon increasing the MAPE content (Fig. 6b). Compared with that of W80, the tensile and flexural moduli of the compatibilized UH-WPCs increased by 22.8% at 4 wt.% MAPE and 23.3% at 2 wt.% MAPE, respectively. These results indicate that there was a critical concentration of MAPE for WPCs, beyond which the wetting saturation of WF and interface quality were reached [40]. Moreover, compared with the WF-matrix interface, this result further confirmed that the WF content was no longer the dominant factor determining the tensile and flexural moduli for highly-filled WPCs [30,40]. The un-notched impact strength showed the same trend as the tensile strength, where it increased upon increasing the MAPE content, with a maximum increase of 286.1% for WM80-4 compared with W80 (Fig. 6c). A higher MAPE content formed a flexible interphase around the WFs that enhanced the toughness of the UH-WPCs via the plastic deformation of the flexible

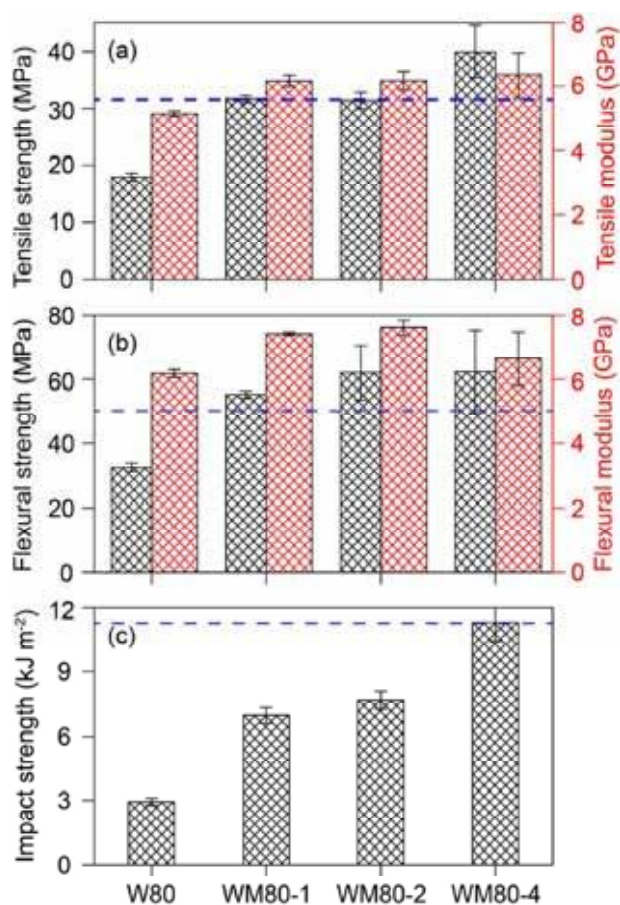


Fig. 6 – Tensile (a), flexural (b), and impact (c) properties of the UH-WPCs with different MAPE contents. (The blue dotted line indicates the mechanical properties of the waste WPCs.)

interphase under the impact force, resulting in more energy absorption during impact [40]. These results further confirm that incorporating MAPE simultaneously reinforced and

toughened the UH-WPCs. The tensile strength, tensile modulus, flexural strength, and flexural modulus of WM80-4 with 4 wt.% MAPE were 26.6%, 50.0%, 26.4%, and 87.9% higher than those of the waste WPCs, respectively. The aforementioned results indicate that the incorporation of waste WFs and using MAPE as compatibilizer may be a facile and low-cost method for recycling end-of-life WPC products into high-performance composites.

3.3. Creep behavior of UH-WPCs

Creep behavior is the intrinsic property of WPCs and exhibits time- and temperature-dependence due to the presence of a thermal-plastic polymer matrix [41–43]. Adding rigid fillers such as WFs or other inorganic particles/fiber can improve the creep resistance of polymer composites by preventing polymer chains mobility [42,44–47]. The creep resistance of both un-compatible and compatible UH-WPCs was greater than that of the waste WPCs and increased upon increasing the WF content. Specifically, the creep strain of the waste WPCs after loading 30 min was 0.035%, which maximally reduced by 48.2% upon increasing the WF content to 85 wt.% for the un-compatible UH-WPCs (W85) (Fig. 7a) due to the high stiffness of WF. Moreover, the residual deformation of the un-compatible UH-WPCs after unloading also varied inversely with the WF content. In addition, the creep strain of the compatible UH-WPCs also greatly decreased upon increasing the WF from 60 to 85 wt.% (Fig. 7b). At 60–80 wt.% WF contents, the creep strains of the composites with/without MAPE were comparable. However, the UH-WPCs with MAPE exhibited greater creep resistance than the UH-WPCs without MAPE at 85 wt.% WF content, due to the decreased internal defects when better interface was achieved. The creep strain decreased by 60.1% for compatible UH-WPCs with 85 wt.% WF (WM85-1) compared with that of the waste WPCs. These results indicate that the creep behavior of the WPCs was dominated by the polymer matrix at low WF contents, while the effect of WF-matrix interfacial interactions became greater for highly-filled WPCs.

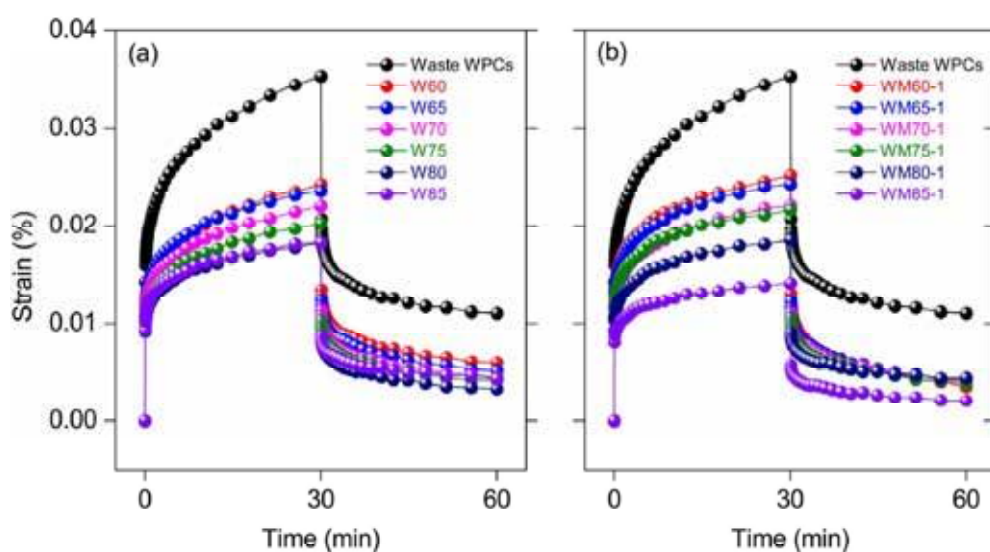


Fig. 7 – Creep strain of UH-WPCs without (a) and with (b) MAPE.

3.4. Dimensional stability of UH-WPCs

The presence of a polymer matrix is the dominant factor leading to the thermal expansion of WPCs [28]. Adding rigid fillers such as inorganic particles or WFs can reduce the linear coefficient of thermal expansion (LCTE) of the resulting polymer composites [48,49]. Compared with the pure HDPE matrix, the LCTE of both waste WPCs and UH-WPCs obviously decreased after incorporating WFs in the matrix. It progressively decreased upon increasing the WF content, indicating that a high WF content improved the thermal expansion resistance of UH-WPCs (Fig. 8). The UH-WPCs with 1 wt.% MAPE showed lower LCTE values compared with their un-compatible counterparts due to the greater restriction of WFs on polymer chains by the improving WF-matrix interfacial adhesion. All UH-WPCs exhibited much lower LCTEs in their length direction than along their width and thickness directions, exhibiting obvious anisotropic thermal expansion. The high pressure during extrusion oriented the WFs along their length direction, while the WFs were randomly distributed in the cross-section transverse to the extrusion direction (width and thickness). The orientation distribution of WFs in different directions was the determinant reason for the anisotropic thermal expansion of the WPCs [29].

Moisture absorption usually leads to dimensional swelling, while desorption leads to dimensional shrinkage. All samples exhibited considerable weight loss on the first day, which gradually balanced over time, indicating that moisture desorption of the UH-WPCs occurred at 80 °C (Fig. 9). Compared with waste WPCs, the weight loss greatly increased upon increasing the WF content for the un-compatible UH-WPCs (Fig. 9a), while only a slight increase was observed for the compatible UH-WPCs (Fig. 9b). This result indicates that moisture absorption was inhibited due to the strengthening of the WF-matrix interface, which decreased the accessibility of hydroxyl groups on WF. Moreover, the UH-WPCs with 1–4 wt.% MAPE possessed a comparable reduction in weight loss (Fig. 9c), indicating that adding 1 wt.% MAPE was sufficient for producing an acceptable WF-matrix interface; therefore, greater weight loss led to greater dimensional shrinkage of UH-WPCs.

The combined effects of thermal expansion and desorption shrinkage on dimensional changes of the UH-WPCs are shown in Fig. 10. Compared with the un-compatible UH-WPCs, waste WPCs with a lower WF content exhibited greater dimensional swelling in the length direction (Fig. 10a), indicating that thermal expansion was higher than desorption shrinkage due to the higher HDPE content. The un-compatible UH-WPCs exhibited dimensional shrinkage upon increasing the WF content from 60 to 85 wt.%, which indicated that the effect of desorption shrinkage was greater than that of thermal expansion at high WF contents. Similar to the length direction, the un-compatible UH-WPCs also exhibited slight dimensional swelling at low WF contents and severe dimensional shrinkage at high WF contents along their width (Fig. 10d); however, all of the un-compatible UH-

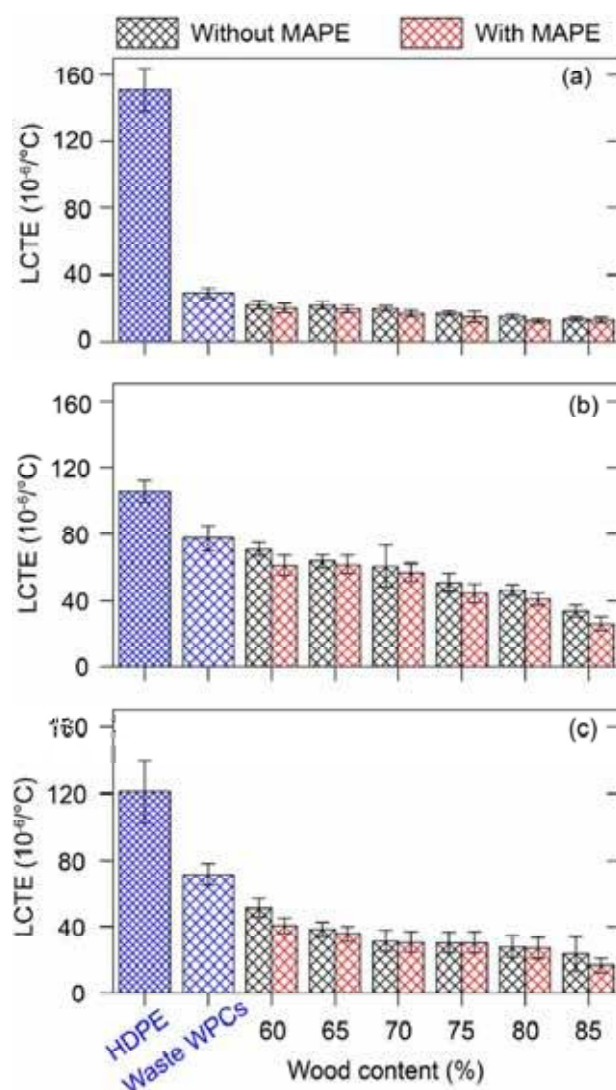


Fig. 8 – The LCTE of UH-WPCs in length (a), width (b), and thickness (c) directions, respectively.

WPCs exhibited severe dimensional shrinkage in their thickness direction, and the thickness dimensional change was about 3 and 10 times higher than that in the width and length directions (Fig. 10g), respectively, which revealed the distinct anisotropic dimensional shrinkage in the UH-WPCs. The noticeable WFs orientation caused by extrusion was the determinant reason for the distinct anisotropic dimensional stability of UH-WPCs. These results illustrated that the effect of moisture absorption or desorption on the dimensional stability was greater than that of thermal expansion, especially for highly-filled WPCs, where shrinkage may generate internal stresses at the WF-matrix interface that can damage and degrade the initial properties of the UH-WPCs [50]. Compared with the un-compatible UH-WPCs, the MAPE-compatible UH-WPCs exhibited considerably smaller

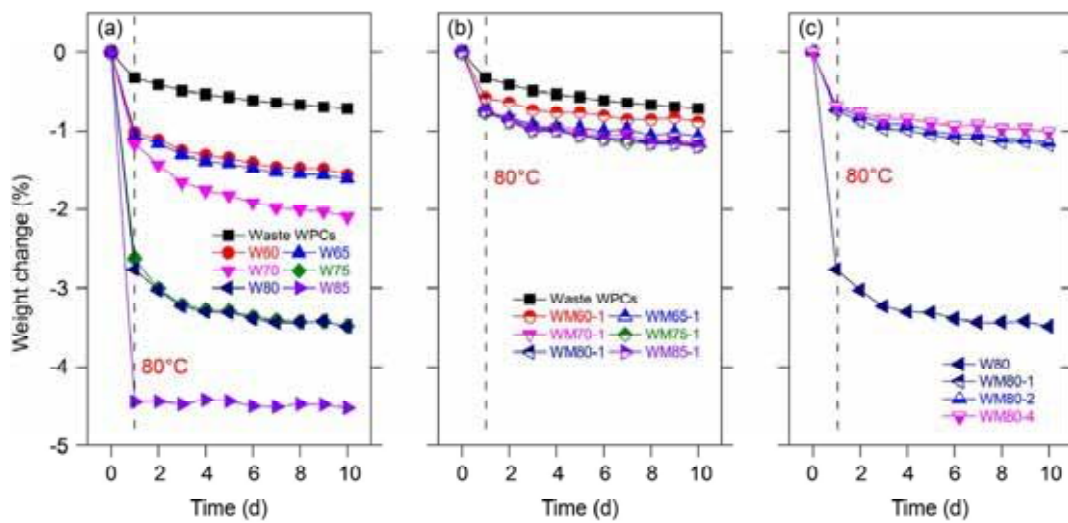


Fig. 9 – The weight loss of UH-WPCs: (a) without MAPE, (b) with MAPE, and (c) with different MAPE contents.

dimensional changes in all directions (Fig. 10b, e, and f). The compatibilized UH-WPCs showed small dimensional changes in both the length and width directions upon increasing the WF content (Fig. 10b and e) due to the improved WF-matrix interface, which decreased moisture absorption. In addition,

the compatibilized UH-WPCs also exhibited the greatest dimensional shrinkage in the thickness direction, which further confirmed the anisotropic dimensional stability of the UH-WPCs. Compared with W80, the dimensional stability was considerably improved by adding 1 wt.% MAPE, and the

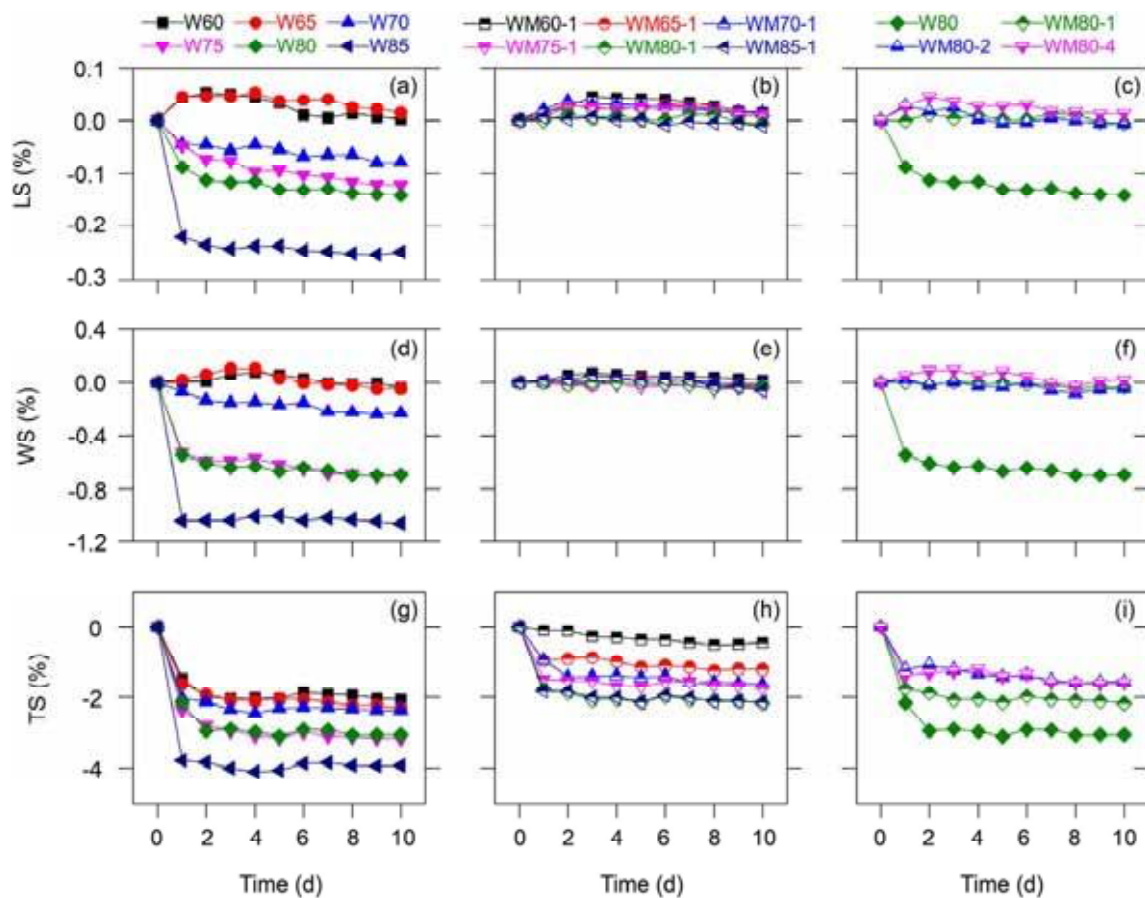


Fig. 10 – The dimensional change of UH-WPCs in length (a, b, and c), width (d, e, and f), and thickness (g, h, and i) directions, respectively.

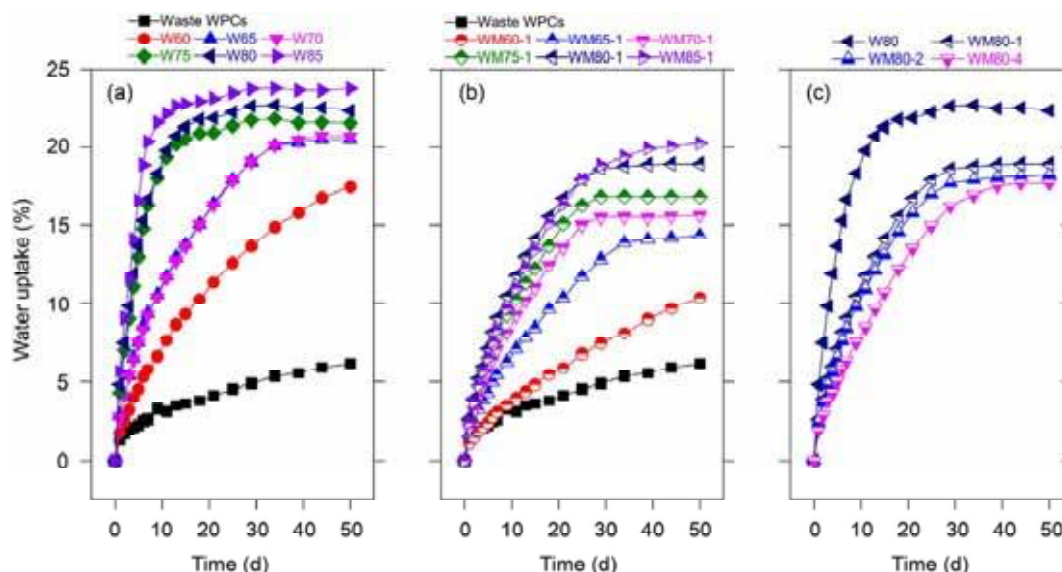


Fig. 11 – Water uptake of UH-WPCs: (a) without MAPE, (b) with MAPE, and (c) with different MAPE contents.

improvement was more pronounced at a higher MAPE content (Fig. 10c, f, and i). These results indicate that the dimension shrinkage due to moisture desorption can offset the thermal expansion to some degree. Improving the WF-matrix interface by using a compatibilizer can increase the dimensional stability of highly-filled WPCs.

3.5. Water absorption of UH-WPCs

The water absorption behavior of WPCs exhibited an important effect on durability especially for the outdoor applications, and it usually acts as a plasticizer resulting in an irreversible degradation [21]. Compared with waste WPCs sample, the equilibrium water absorption (EWA) and water absorption rate (WAR) of all the UH-WPCs noticeably increased upon increasing the WF content (Fig. 11a and b), due to the association of hydrophilic groups of WFs with water [21]. The composites with 1 wt.% MAPE exhibited considerably lower EWA and WAR values than their un-compatible counterparts. The reduce in water absorption of the compatibilized UH-WPCs was because MAPE improved the WF-matrix interfacial adhesion [37], which was confirmed by the SEM results (Fig. 3). Adding MAPE could help polymer matrix encapsulate more WFs and prevent the water penetrate between the WF-matrix interface [51]. In addition, both the EWA and WAR greatly decreased upon further increasing the MAPE content at 80 wt.% WFs (Fig. 11c). The EWA of W80 was 22.31% after 50 days immersion, while it was 17.71% for WM80-4. The only difference between W80 and WM80-4 was their MAPE content, in which W80 possessed only 1.82 wt.% provided by waste WPCs, while WM80-4 had 5.45 wt.% MAPE. A higher MAPE content with better flowability could consume many more hydroxyl groups

on the WFs surface, which allowed it to wet WFs more efficiently [52].

Similar to the combine effect of heat and humidity on the dimensional stability, the anisotropic dimensional swelling of UH-WPCs was also investigated and measured in the length, width, and thickness directions (Fig. 12). It has been proved that the wood cell walls swelling is the key determinant for WPCs dimensional swelling during water immersion [37]. Compared with waste WPCs, the maximum dimensional swelling of the UH-WPCs increased upon increasing the WF content, and the equilibrium swelling compatibilized with 1 wt.% MAPE was noticeably lower than that of the un-compatible UH-WPCs counterparts, which is corresponding with the EWA results. The presence of 1 wt.% MAPE acted as a compatibilizer which improved the interfacial adhesion and, thus, prevented the dimensional swelling by reducing water penetration between WFs and the polymer matrix. However, many more hydroxyl groups were exposed in the un-compatible UH-WPCs, which promoted the entrance of water with hydrogen bonding sites in the wood cell wall. Moreover, the incorporation of 1–4 wt.% MAPE in UH-WPCs resulted in a comparable decrease in dimensional swelling (Fig. 12c, f, and i), indicating that WFs can be completely enveloped and wetted by the polymer matrix by adding a moderate amount of MAPE. Besides, the thickness swelling of all UH-WPCs was about 3 and 10 times higher than that in the width and length directions, respectively. These results further confirmed the anisotropic water absorption of UH-WPCs. It has been reported that WFs orientation caused by extrusion is the determinant reason that resulted in anisotropic properties of WPCs, and the WFs with higher aspect ratio usually led to more obvious anisotropy [29].

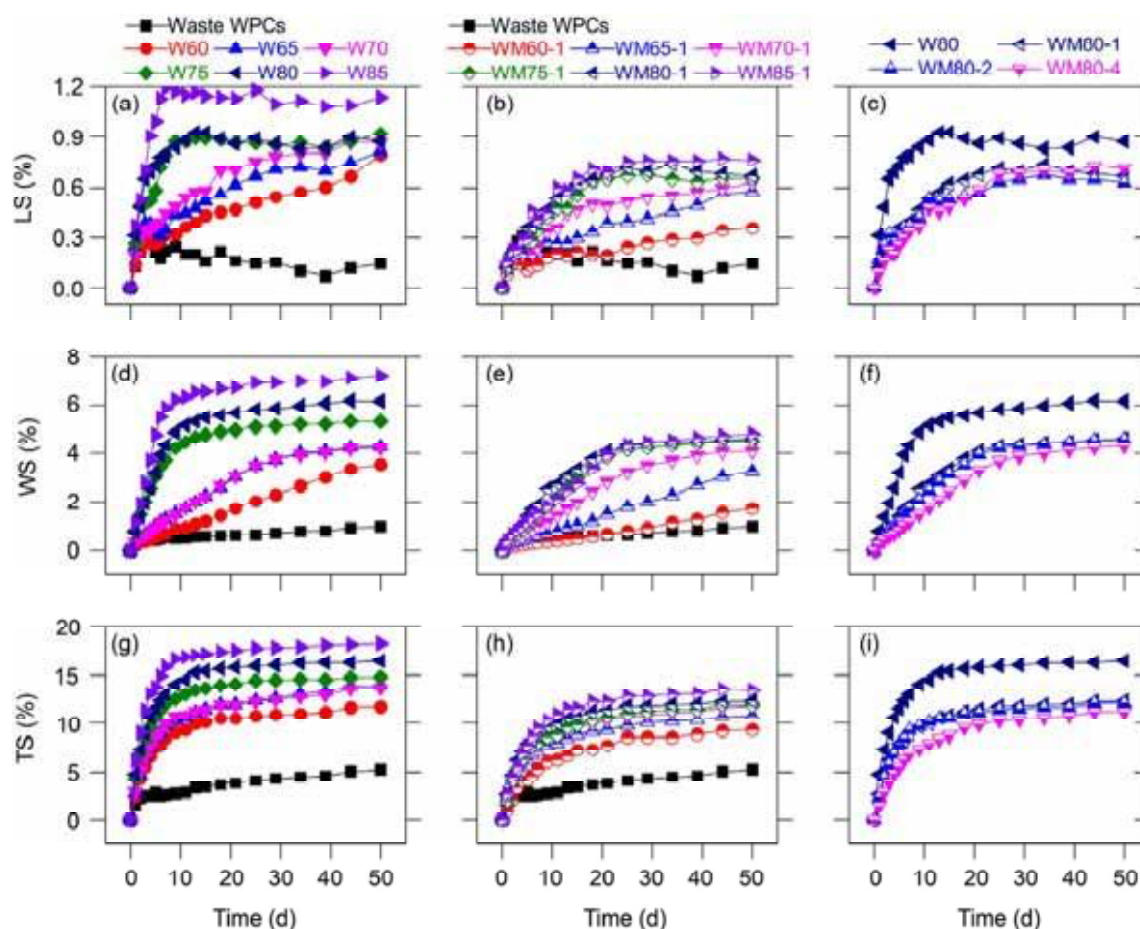


Fig. 12 – Dimensional swelling of UH-WPCs in length direction (a, b, and c), width direction (d, e, and f), and thickness direction (g, h, and i), respectively.

4. Conclusions

Low-cost, high-strength, and high-dimensional-stability UH-WPCs were successfully fabricated by reprocessing end-of-life WPC products with waste WFs using MAPE as a compatibilizer, to achieve a sustainable strategy for clean and cyclic processing in the WPC industry. The following conclusions were obtained:

- (1) The addition of 1 wt.% MAPE improved the WF-matrix interfacial interactions and protected WFs from damage during reprocessing due to the improved plasticization and wettability on WF. The number of large WFs increased upon increasing the MAPE content from 1 to 4 wt.%.
- (2) The compatibilized UH-WPCs exhibited much higher mechanical properties (tensile, flexural, and impact) than their un-compatibilized counterparts owing to the greater size of WFs and better interface with the presence of MAPE. Specifically, the UH-WPCs with 80 wt.% WF and 1 wt.% MAPE (WM80-1) showed the maximum increase in tensile, flexural, and impact strengths were

76.8%, 69.6%, and 136.9% compared with those of the un-compatibilized UH-WPCs with 80 wt.% WF (W80), respectively. Moreover, the tensile strength and modulus, flexural strength and modulus of the WM80-4 loaded with 4 wt.% MAPE were increased by 26.6%, 50.0%, 26.4%, and 87.9% compared with those of the waste WPCs, respectively. The WM80-4 with 80% wt.% WF had a similar impact strength to the waste WPCs with 47.6 wt.% WF.

- (3) The creep resistance of both un-compatibilized and compatibilized UH-WPCs was greater than that of the waste WPCs and increased upon increasing the WF content. The creep strain of W85 and WM85-1 decreased by 48.2% and 60.1% after loading 30 min compared with that of waste WPCs respectively.
- (4) The un-compatibilized UH-WPCs exhibited considerable anisotropic dimensional stability, and the effect of moisture desorption on the dimensional stability was higher than that of thermal expansion at high WF contents (>70 wt.%). The compatibilized UH-WPCs exhibited better dimensional stability than their un-compatibilized counterparts due to the enhanced WF-matrix interface. The water absorption and

dimensional swelling of the compatibilized UH-WPCs were considerably lower than those of their uncompatibilized counterparts.

- (5) The incorporation of waste WFs and MAPE in moderation to waste WPC formulations may provide a low-cost and facile method to recycle end-of-life WPC products into high-performance UH-WPCs. This can increase production efficiency, minimize waste, and align with the circular economy. Finally, recycling end-of-life WPCs into new products will be a complex process and involves many factors, which need to be further investigated.

CRediT authorship contribution statement

Haiyang Zhou: Methodology, Investigation, Formal analysis, Writing - original draft, Writing - review & editing. Wenjuan Li: Investigation, Data curation, Formal analysis. Xiaolong Hao: Writing - review & editing, Investigation. Guanggong Zong: Validation, Software. Xin Yi: Software, Methodology. Junjie Xu: Software, Validation. Rongxian Ou: Conceptualization, Supervision, Project administration, Methodology, Funding acquisition, Writing - review & editing. Qingwen Wang: Conceptualization, Supervision, Funding acquisition, Writing - review & editing.

Declaration of Competing Interest

The authors declare that they have no known competing financial interests or personal relationships that could have appeared to influence the work reported in this paper.

Acknowledgments

This work was supported by the National Natural Science Foundation of China (Grant Nos. 31901251 and 32071698), the Guangdong Forestry Science and Technology Innovation Project (No. 2020KJCX008), and the Research and Development Program in Key Areas of Guangdong Province (2020B0202010008).

Appendix A. Supplementary data

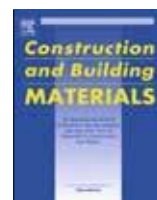
Supplementary data to this article can be found online at <https://doi.org/10.1016/j.jmrt.2022.02.091>.

REFERENCES

- [1] Vaisanen T, Das O, Tomppo L. A review on new bio-based constituents for natural fiber-polymer composites. *J Clean Prod* 2017;149(15):582–96. <https://doi.org/10.1016/j.jclepro.2017.02.132>.
- [2] Faruk O, Bledzki AK, Fink H-P, Sain M. Biocomposites reinforced with natural fibers: 2000–2010. *Prog Polym Sci* 2012;37(11):1552–96. <https://doi.org/10.1016/j.progpolymsci.2012.04.003>.
- [3] Koivuranta E, Hietala M, Ämmälä A, Oksman K, Ilikainen M. Improved durability of lignocellulose-polypropylene composites manufactured using twin-screw extrusion. *Composites Part A-Appl S* 2017;101:265–72. <https://doi.org/10.1016/j.compositesa.2017.06.024>.
- [4] Zhang Q, Khan MU, Lin X, Cai H, Lei H. Temperature varied biochar as a reinforcing filler for high-density polyethylene composites. *Compos B Eng* 2019;175:107151. <https://doi.org/10.1016/j.compositesb.2019.107151>.
- [5] Pickering KL, Efendy MGA, Le TM. A review of recent developments in natural fibre composites and their mechanical performance. *Composites Part A-Appl S* 2016;83:98–112. <https://doi.org/10.1016/j.compositesa.2015.08.038>.
- [6] Suffo M, Mata M, Molina SI. A sugar-beet waste based thermoplastic agro-composite as substitute for raw materials. *J Clean Prod* 2020;257:120382.
- [7] Dun M, Hao J, Wang W, Wang G, Cheng H. Sisal fiber reinforced high density polyethylene pre-preg for potential application in filament winding. *Compos B Eng* 2019;159:369–77. <https://doi.org/10.1016/j.compositesb.2018.09.090>.
- [8] Lu W, Yu W, Zhang B, Dou X, Han X, Cai H. Kevlar fibers reinforced straw wastes-polyethylene composites: combining toughness, strength and self-extinguishing capabilities. *Compos B Eng* 2021;223:109117. <https://doi.org/10.1016/j.compositesb.2021.109117>.
- [9] Xu B-R, Deng C, Li Y-M, Lu P, Zhao P-P, Wang Y-Z. Novel amino glycerin decorated ammonium polyphosphate for the highly-efficient intumescent flame retardance of wood flour/polypropylene composite via simultaneous interfacial and bulk charring. *Compos B Eng* 2019;172:636–48. <https://doi.org/10.1016/j.compositesb.2019.05.099>.
- [10] Arribasplata-Seguin A, Quispe-Dominguez R, Tupia-Anticona W, Acosta-Sullcahuaman J. Rotational molding parameters of wood-plastic composite materials made of recycled high density polyethylene and wood particles. *Compos B Eng* 2021;217:108876. <https://doi.org/10.1016/j.compositesb.2021.108876>.
- [11] Petchwattana N, Covavisaruch S, Sanetuntikul J. Recycling of wood-plastic composites prepared from poly(vinyl chloride) and wood flour. *Construct Build Mater* 2012;28:557–60. <https://doi.org/10.1016/j.conbuildmat.2011.08.024>.
- [12] Zong G, Hao X, Hao J, Tang W, Fang Y, Ou R, et al. High-strength, lightweight, co-extruded wood flour-polyvinyl chloride/lumber composites: effects of wood content in shell layer on mechanical properties, creep resistance, and dimensional stability. *J Clean Prod* 2020;244:118860. <https://doi.org/10.1016/j.jclepro.2019.118860>.
- [13] Taheri H, Hietala M, Suopajarvi T, Liimatainen H, Oksman K. One-step twin-screw extrusion process to fibrillate deep eutectic solvent-treated wood to be used in wood fiber-polypropylene composites. *ACS Sustainable Chem Eng* 2021;9(2):883–93. <https://doi.org/10.1021/acssuschemeng.0c07750>.
- [14] Tao Y, Li P, Cai L, Shi SQ. Flammability and mechanical properties of composites fabricated with CaCO₃-filled pine flakes and Phenol Formaldehyde resin. *Compos B Eng* 2019;167:1–6. <https://doi.org/10.1016/j.compositesb.2018.12.005>.
- [15] Yonny Martinez L, Juarez Benigno P, Donatian G, Fabricio Gomes G, Fermín Correa M, Anna Clara Theodoro N. Production of wood-plastic composites using cedrela odorata sawdust waste and recycled thermoplastics mixture from post-consumer products - a sustainable approach for cleaner

- production in Cuba. *J Clean Prod* 2020;244:118723. <https://doi.org/10.1016/j.jclepro.2019.118723>.
- [16] Duigou AL, Pillin I, Bourmaud A, Davies P, Baley C. Effect of recycling on mechanical behaviour of biocompostable flax/poly(l-lactide) composites. *Composites Part A-Appl S* 2008;39:1471–8. <https://doi.org/10.1016/j.compositesa.2008.05.008>.
- [17] Li M, Pu Y, Thomas VM, Yoo CG, Ozcan S, Deng Y, et al. Recent advancements of plant-based natural fiber-reinforced composites and their applications. *Compos B Eng* 2020;200:108254. <https://doi.org/10.1016/j.compositesb.2020.108254>.
- [18] Teuber L, Osburg V-S, Toporowski W, Militz H, Krause A. Wood polymer composites and their contribution to cascading utilisation. *J Clean Prod* 2016;110:9–15. <https://doi.org/10.1016/j.jclepro.2015.04.009>.
- [19] Rosenstock Voltz L, Di Guiseppe I, Geng S, Oksman K. The effect of recycling on wood-fiber thermoplastic composites. *Polymers* 2020;12(8):1750. <https://doi.org/10.1002/app.37775>.
- [20] Beg MDH, Pickering KL. Reprocessing of wood fibre reinforced polypropylene composites. Part I: effects on physical and mechanical properties. *Composites Part A-Appl S* 2008;39:1091–100. <https://doi.org/10.1016/j.compositesa.2008.04.013>.
- [21] Jubinville D, Esmizadeh E, Tzoganakis C, Mekonnen T. Thermo-mechanical recycling of polypropylene for the facile and scalable fabrication of highly loaded wood plastic composites. *Compos B Eng* 2021;219:108873. <https://doi.org/10.1016/j.compositesb.2021.108873>.
- [22] Dickson AR, Even D, Warnes JM, Fernyhough A. The effect of reprocessing on the mechanical properties of polypropylene reinforced with wood pulp, flax or glass fibre. *Composites Part A-Appl S* 2014;61:258–67. <https://doi.org/10.1016/j.compositesa.2014.03.010>.
- [23] Fonseca-Valero C, Ochoa-Mendoza A, Arranz-Andrés J, González-Sánchez C. Mechanical recycling and composition effects on the properties and structure of hardwood cellulose-reinforced high density polyethylene eco-composites. *Composites Part A-Appl S* 2015;69:94–104. <https://doi.org/10.1016/j.compositesa.2014.11.009>.
- [24] Soccalingame L, Bourmaud A, Perrin D, Bénézet J-C, Bergeret A. Reprocessing of wood flour reinforced polypropylene composites: impact of particle size and coupling agent on composite and particle properties. *Polym Degrad Stabil* 2015;113:72–85. <https://doi.org/10.1016/j.polymdegradstab.2015.01.020>.
- [25] Barteau G, Azoti W, Gautreau M, Francart C, Alès G, Jmal H, et al. Recycling of wood-reinforced poly-(propylene) composites: a numerical and experimental approach. *Ind Crop Prod* 2021;167:113518. <https://doi.org/10.1016/j.indcrop.2021.113518>.
- [26] Beg MDH, Pickering KL. Reprocessing of wood fibre reinforced polypropylene composites. Part II: hygrothermal ageing and its effects. *Composites Part A-Appl S* 2008;39:1565–71. <https://doi.org/10.1016/j.compositesa.2008.06.002>.
- [27] Lila MK, Singhal A, Banwait SS, Singh I. A recyclability study of bagasse fiber reinforced polypropylene composites. *Polym Degrad Stabil* 2018;152:272–9. <https://doi.org/10.1016/j.polymdegradstab.2018.05.001>.
- [28] Hao X, Zhou H, Xie Y, Mu H, Wang Q. Sandwich-structured wood flour/HDPE composite panels: reinforcement using a linear low-density polyethylene core layer. *Construct Build Mater* 2018;164:489–96. <https://doi.org/10.1016/j.conbuildmat.2017.12.246>.
- [29] Hao X, Zhou H, Mu B, Chen L, Guo Q, Yi X, et al. Effects of fiber geometry and orientation distribution on the anisotropy of mechanical properties, creep behavior, and thermal expansion of natural fiber/HDPE composites. *Compos B Eng* 2020;185:107778. <https://doi.org/10.1016/j.compositesb.2020.107778>.
- [30] Balasuriya PW, Ye L, Mai YW. Mechanical properties of wood flake–polyethylene composites. Part I: effects of processing methods and matrix melt flow behaviour. *Composites Part A-Appl S* 2001;32(5):619–29. [https://doi.org/10.1016/S1359-835X\(00\)00160-3](https://doi.org/10.1016/S1359-835X(00)00160-3).
- [31] Sykacek E, Hrabalova M, Frech H, Mundigler N. Extrusion of five biopolymers reinforced with increasing wood flour concentration on a production machine, injection moulding and mechanical performance. *Composites Part A-Appl S* 2009;40(8):1272–82. <https://doi.org/10.1016/j.compositesa.2009.05.023>.
- [32] Huang L, Wu Q, Wang Q, Wolcott M. Interfacial crystals morphology modification in cellulose fiber/polypropylene composite by mechanochemical method. *Composites Part A-Appl S* 2020;130:105765. <https://doi.org/10.1016/j.compositesa.2020.105765>.
- [33] Balasuriya PW, Ye L, Mai YW, Wu J. Mechanical properties of wood flake-polyethylene composites. II. Interface modification. *J Appl Polym Sci* 2002;83(12):2505–21. <https://doi.org/10.1002/app.10189>.
- [34] Lu JZ, Wu Q, Negulescu II. Wood-fiber/high-density-polyethylene composites: coupling agent performance. *J Appl Polym Sci* 2005;96(1):93–102. <https://doi.org/10.1002/app.21410>.
- [35] Shu-Kai Yeh, Kwang-Jea Kim, Rakesh K. Synergistic effect of coupling agents on polypropylene-based wood–plastic composites. *J Appl Polym Sci* 2012;127(2):1047–53. <https://doi.org/10.1002/app.37775>.
- [36] Huang CW, Yang TC, Wu TL, Ke-Chang H, Wu JH. Effects of maleated polypropylene content on the extended creep behavior of wood-polypropylene composites using the stepped isothermal method and the stepped isostress method. *Wood Sci Technol* 2018;52:1313–30. <https://doi.org/10.1007/s00226-018-1037-7>.
- [37] Ou R, Xie Y, Wolcott MP, Sui S, Wang Q. Morphology, mechanical properties, and dimensional stability of wood particle/high density polyethylene composites: effect of removal of wood cell wall composition. *Mater Des* 2014;58:339–45. <https://doi.org/10.1016/j.matdes.2014.02.018>.
- [38] Yang S, Wei B, Wang Q. Superior dispersion led excellent performance of wood-plastic composites via solid-state shear milling process. *Compos B Eng* 2020;200:108347. <https://doi.org/10.1016/j.compositesb.2020.108347>.
- [39] Ranganathan N, Oksman K, Nayak SK, Sain M. Structure property relation of hybrid biocomposites based on jute, viscose and polypropylene: the effect of the fibre content and the length on the fracture toughness and the fatigue properties. *Composites Part A-Appl S* 2016;83:169–75. <https://doi.org/10.1016/j.compositesa.2015.10.037>.
- [40] Liu H, Wu Q, Han G, Yao F, Kojima Y, Suzuki S. Compatibilizing and toughening bamboo flour-filled HDPE composites: mechanical properties and morphologies. *Composites Part A-Appl S* 2008;39(12):1891–900. <https://doi.org/10.1016/j.compositesa.2008.09.011>.
- [41] Hung KC, Wu TL, Chen YL, Wu JH. Assessing the effect of wood acetylation on mechanical properties and extended creep behavior of wood/recycled-polypropylene composites. *Construct Build Mater* 2016;108:139–45. <https://doi.org/10.1016/j.conbuildmat.2016.01.039>.
- [42] Yang T-C, Wu T-L, Hung K-C, Chen Y-L, Wu J-H. Mechanical properties and extended creep behavior of bamboo fiber reinforced recycled poly(lactic acid) composites using the time–temperature superposition principle. *Construct Build Mater* 2015;93:558–63. <https://doi.org/10.1016/j.conbuildmat.2015.06.038>.

- [43] Yahyaei-Moayyed M, Taheri F. Experimental and computational investigations into creep response of AFRP reinforced timber beams. *Compos Struct* 2011;93(2):616–28. <https://doi.org/10.1016/j.compstruct.2010.08.017>.
- [44] Georgiopoulos P, Kontou E, Christopoulos A. Short-term creep behavior of a biodegradable polymer reinforced with wood-fibers. *Compos B Eng* 2015;80:134–44. <https://doi.org/10.1016/j.compositesb.2015.05.046>.
- [45] Hao X, Zhou H, Xie Y, Xiao Z, Wang H, Wang Q. Mechanical reinforcement and creep resistance of coextruded wood flour/polyethylene composites by shell-layer treatment with nano- and micro-SiO₂ particles. *Polym Compos* 2018;40(4):1576–84. <https://doi.org/10.1002/pc.24901>.
- [46] Yang JL, Zhang Z, Schlarb AK, Friedrich K. On the characterization of tensile creep resistance of polyamide 66 nanocomposites. Part I. Experimental results and general discussions. *Polymer* 2006;47(8):2791–801. <https://doi.org/10.1016/j.polymer.2006.02.065>.
- [47] Hao X, Yi X, Sun L, Tu D, Wang Q, Ou R. Mechanical properties, creep resistance, and dimensional stability of core/shell structured wood flour/polyethylene composites with highly filled core layer. *Construct Build Mater* 2019;226:879–87. <https://doi.org/10.1016/j.conbuildmat.2019.07.329>.
- [48] Sun L, Zhou H, Zong G, Ou R, Fan Q, Xu J, et al. Effects of SiO₂ filler in the shell and wood fiber in the core on the thermal expansion of core–shell wood/polyethylene composites. *Polymers* 2020;12(11):2570. <https://doi.org/10.3390/polym12112570>.
- [49] Nakagaito AN, Yano H. The effect of fiber content on the mechanical and thermal expansion properties of biocomposites based on microfibrillated cellulose. *Cellulose* 2008;15(4):555–9. <https://doi.org/10.1007/s10570-008-9212-x>.
- [50] Gholampour AA, Ozbakkaloglu T. A review of natural fiber composites: properties, modification and processing techniques, characterization, applications. *J Mater Sci* 2019;55:829–92. <https://doi.org/10.1007/s10853-019-03990-y>.
- [51] Hosseinaei O, Wang S, Enayati AA, Rials TG. Effects of hemicellulose extraction on properties of wood flour and wood-plastic composites. *Composites Part A-Appl S* 2012;43(4):686–94. <https://doi.org/10.1016/j.compositesa.2012.01.007>.
- [52] Hao X, Xu J, Zhou H, Tang W, Li W, Wang Q, et al. Interfacial adhesion mechanisms of ultra-highly filled wood fiber/polyethylene composites using maleic anhydride grafted polyethylene as a compatibilizer. *Mater Des* 2021;212:110182. <https://doi.org/10.1016/j.matdes.2021.110182>.



Conductive and fire-retardant wood/polyethylene composites based on a continuous honeycomb-like nanoscale carbon black network

Haiyang Zhou^a, Zefang Xiao^a, Yonggui Wang^a, Xiaolong Hao^b, Yanjun Xie^{a,*}, Yongming Song^a, Fengqiang Wang^a, Qingwen Wang^{b,*}

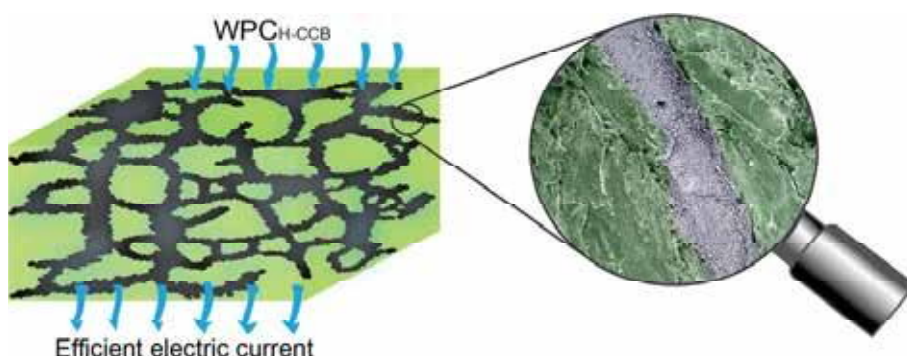
^aKey Laboratory of Bio-based Material Science and Technology (Ministry of Education), College of Material Science and Engineering, Northeast Forestry University, 26 Hexing Road, Harbin 150040, China

^bCollege of Materials and Energy, South China Agricultural University, 483 Wushan Road, Guangzhou 510642, China

HIGHLIGHTS

- A continuous honeycomb-like conductive carbon-black network in WPC was constructed.
- The WPC_{H-CCB} had excellent conductivity compared with the WPC_{U-CCB}.
- The conductivity of the WPC_{H-CCB} was higher than the HDPE_{H-CCB} at low carbon-black content.
- The WPC_{H-CCB} had excellent electromagnetic shielding property compared with the WPC_{U-CCB}.
- The WPC_{H-CCB} had excellent flame retardancy compared with the WPC_{U-CCB}.

GRAPHICAL ABSTRACT



ARTICLE INFO

Article history:

Received 2 February 2019

Received in revised form 16 September 2019

Accepted 23 October 2019

Keywords:

Wood plastic composite
Carbon black
Honeycomb-like network
Conductivity
Flame retardancy

ABSTRACT

This study prepares multi-functional wood/polyethylene composites (WPCs) by addition of a small amount of nanoscale conductive carbon black (CCB), leading to honeycomb-distributed WPC (WPC_{H-CCB}). The conductivity, electromagnetic interference shielding (EMI SE), and flame-retardancy of WPC_{H-CCB} were comparatively studied with the uniformly-distributed WPC (WPC_{U-CCB}) prepared through a conventional melt-blending process. The conductivity and EMI SE of the WPC_{H-CCB} reached up to $1.5 \times 10^{-2} \text{ S} \cdot \text{cm}^{-1}$ and 20.2 dB at 3 wt% CCB content, respectively. In comparison, the conductivity and EMI SE of the WPC_{U-CCB} only had $8.3 \times 10^{-14} \text{ S} \cdot \text{cm}^{-1}$ and 5.0 dB. Moreover, the cone calorimetric analysis revealed that the WPC_{H-CCB} had lower smoke production and heat release than the WPC_{U-CCB}.

© 2019 Elsevier Ltd. All rights reserved.

1. Introduction

Wood plastic composites (WPCs) are a class of recyclable and sustainable materials that have been extensively used for

construction, decking, wallboard, and garden furniture [1–3]. However, the presence of plastic in WPCs can result in static electricity when people walk on it [4]. Furthermore, both the main components in WPCs, wood flour and plastic, are flammable and thus are a fire risk [5,6]. These issues limit their application range.

To eliminate the static electricity, 3% carbon black and 20% graphite have been added together into WPC by one-step melt

* Corresponding authors.

E-mail addresses: yxie@nefu.edu.cn (Y. Xie), qwwang@scau.edu.cn (Q. Wang).

compounding, resulting in a conductivity of $10^{-6} \text{ S}\cdot\text{cm}^{-1}$, which meets the antistatic requirements ($>10^{-7} \text{ S}\cdot\text{cm}^{-1}$) [7,8]. In addition, the incorporation of carbon nanotubes into WPC by one-step melt blending can also achieve a good conductivity ($10^{-8} \text{ S}\cdot\text{cm}^{-1}$) at a 12% loading level [9]. Moreover, various flame retardants such as ammonium polyphosphate [10,11] and magnesium hydroxide [12] have been used to improve the flame retardancy of WPCs. Generally, the high additives content (10–50 wt%) is required to achieve a continuous network of additives, resultantly obtaining sufficient conductivity and flame retardancy [6,13]. In addition, the high load of additives can result in loss of mechanical-strength and cost increase [14,15]. The preparation of sufficient conductive and flame-retardant WPCs with a load of additives lower than 10% is still rare.

In 1971, a “segregated structure” was proposed to create conductive polymer in order to reduce the amount of additives [16]. Afterwards, various methods have been developed for the preparation of conductive polymer composites [8,17–19]. With the “segregated structure”, the conductive particles were dispersed only at the interface between the polymeric pellets rather than being uniformly distributed throughout the whole matrix. However, the “segregated structures” were basically constructed in high-melt-viscosity polymer matrices (mainly ultrahigh molecular polyethylene) to prevent the migration of the conductive particles into the polymer interior [20].

In order to address the issue of high load of CCB in WPCs, we develop a honeycomb-like CCB network in this study based on the view of “segregated structure” using a two-step blending technique. The formation of honeycomb-like network should be crucial because it may form a thin-layer CCB with a high distribution density encapsulating the WPC domains, which could dramatically reduce the load of CCB in WPCs and achieve an efficient conductivity and fire retardancy. The efficacy of the honeycomb-like WPC in conductivity and fire retardancy was compared to that of a WPC in which the carbon black was uniformly distributed by the traditional melt-blending method. In addition, the conductive efficacy of the network was also studied in the high-density polyethylene (HDPE) and the WPC.

2. Materials and methods

2.1. Materials

Wood flour retained on a 100-mesh sieve (ca. $150 \mu\text{m}$) was prepared from poplar wood (*Populus adenopoda* Maxim) in our laboratory. High density polyethylene (HDPE) pellets were purchased from the Daqing Petrochemical Company (Daqing, China). The HDPE has a density of $0.95 \text{ g}\cdot\text{cm}^{-3}$ and a melt flow index of $0.9 \text{ g}\cdot(10 \text{ min})^{-1}$ measured at 190°C . Maleic anhydride-grafted polyethylene (MAPE) pellets with a melt flow index of $2 \text{ g}\cdot(10 \text{ min})^{-1}$ measured at 190°C and a grafting ratio of 0.9 wt% were obtained from Shanghai Sunny New Technology Development Co., Ltd., Shanghai, China. A lubricant composed of stearic acid (#1801) and polyethylene wax (1:1 in weight) was supplied by Nanjing Adisi Import & Export Co., Ltd., Nanjing, China. The nanoscale conductive carbon black (CCB) with a conductivity of $0.58 (\pm 0.14) \text{ S}\cdot\text{cm}^{-1}$ was obtained from Cabot Corp., Boston, MA, USA.

2.2. Preparation of WPC

2.2.1. Preparation of uniformly distributed WPC

The HDPE powder, dry wood flour (moisture content $< 3\%$), MAPE, lubricant, and CCB were compounded at a specific ratio (Table 1) for 8 min at ambient temperature using a high-speed mixer. The compounded mixtures were melt-blended through a

twin-screw extruder (L/D ratio 30, SH30, Nanjing Rubber Machinery Corp., Nanjing, China) with a pressure of 4 MPa, a speed of 40 rpm and a temperature range of $145\text{--}165^\circ\text{C}$ (Fig. 1a). The resulting extrudates were smashed to obtain the pellets without CCB or the pellets with uniformly-distributed CCB. The resulting pellets were further fractionated into three fractions with a diameter of approximately 2, 4 and 6 mm, respectively, for subsequent use. The pellets without CCB and the pellets with uniformly-distributed CCB were paved in a square stainless-steel mold measuring $160 \times 160 \times 3 \text{ mm}$ (length \times width \times thickness, for the conductivity test) or $160 \times 160 \times 3.5 \text{ mm}$ (for the fire retardancy test), respectively, followed by molding into plates at 180°C for 3 min with a pressure of 12 MPa using a flat vulcanizing machine (XH-406B; Zhuosheng Machinery Equipment Co., Ltd., Dongguan, China). Subsequently, the machine was cooled slowly to room temperature in a cold compression mode. The compressed WPC panels obtained from the pellets without CCB and the pellets with uniformly-distributed CCB are referred to as WPC_{CTRL} and WPC_{U-CCB}, respectively.

2.2.2. Preparation of honeycomb-like distributed WPC (HDPE)

The pellets without CCB prepared in Section 2.2.1 were mixed with the desired amount of CCB (Table 1) using a high-speed mixer for 6 min at room temperature. The surface of the pellets was coated with the nano-CCB by physical adsorption (Fig. 1b). As a contrast, the same size of HDPE pellets was also coated the same amount of CCB. The CCB-coated pellets were molded by compression into panels as described above. The resulting WPC and HDPE panels with a honeycomb-like CCB network are referred to as WPC_{H-CCB} and HDPE_{H-CCB}, respectively.

2.3. Measurements and characterizations

2.3.1. Morphological analysis

The dried CCB, the pellets without CCB, the pellets coated with CCB, and the tensile fractured surface of the WPC_{U-CCB} were examined by scanning electron microscopy (SEM) using a FEI Quanta 200 field-emission scanning electron microscope (FEI Co., Hillsboro, OR, USA) at an accelerating voltage of 12.5 kV.

The small plates of $35 \times 10 \times 3 \text{ mm}^3$ were sawed from the WPC panels and cut into 0.1-mm-thick films using a microtome. The morphology of the films was observed under an optical microscope (Aigo GE-5; Huaqi Information Digital Technology Co., Ltd., Beijing, China).

2.3.2. Bulk conductivity measurements

The WPC panels with the size of $100 \times 100 \times 3 \text{ mm}^3$ were used to test the bulk conductivity. When the bulk conductivity of the sample was $> 10^{-8} \text{ S}\cdot\text{cm}^{-1}$, the sample was measured using a four-probe tester (Pro4-4000; Lucas-Signatone Corp., Gilroy, CA, USA). For each sample, eight points were measured. In the case when the bulk conductivity was below $10^{-8} \text{ S}\cdot\text{cm}^{-1}$, the sample was measured using a Zc-36 high-resistance meter (Yang Gao Electrical Appliance Co., Ltd., Shanghai, China). All measurements were performed in triplicate and the average values were used as results.

2.3.3. Electromagnetic interference (EMI) shielding measurements

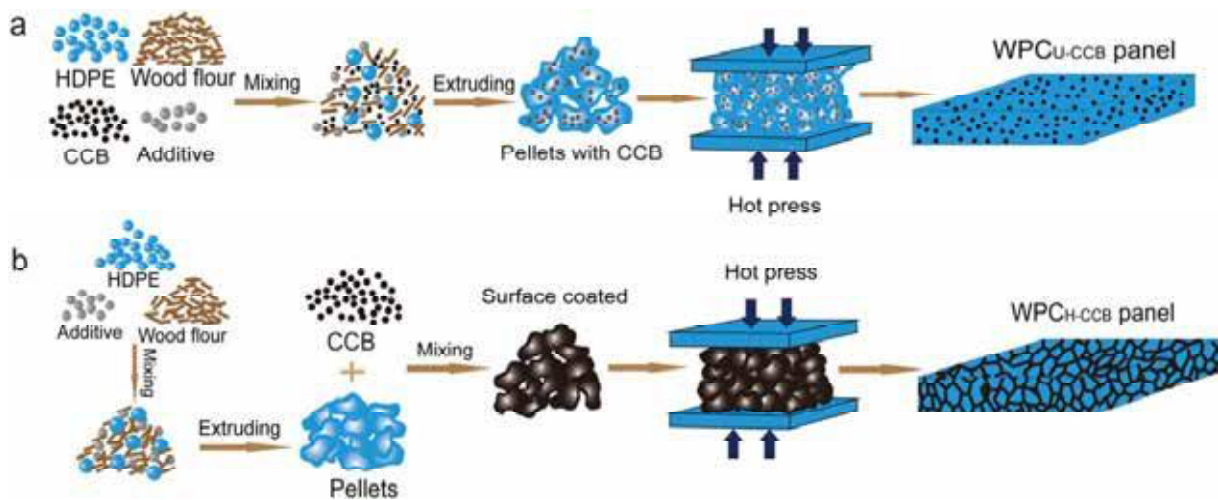
The EMI shielding efficacy (SE) was measured at the frequency of 8–12.5 GHz using a Vector Network Analyzer (N5227A; Agilent Technologies, Santa Clara, CA, USA) at 25°C and 50% relative humidity. The samples were carefully cut into $22.86 \times 10.6 \times 3.5 \text{ mm}^3$ cuboids to precisely fit into the waveguide opening.

Table 1

Formulations of the WPC panels prepared from pellets without CCB and pellets with the uniformly-distributed CCB, respectively (wt%).

Sample*	CCB	WF	HDPE	MAPE	Lubricant
WPC _{CTRL}	0	50	45	3	2
WPC _{U-CCB0.5}	0.5	49.5	45	3	2
WPC _{U-CCB1}	1	49	45	3	2
WPC _{U-CCB2}	2	48	45	3	2
WPC _{U-CCB3}	3	47	45	3	2
WPC _{H-CCB0.5}	0.5	49.5	45	3	2
WPC _{H-CCB1}	1	49	45	3	2
WPC _{H-CCB2}	2	48	45	3	2
WPC _{H-CCB3}	3	47	45	3	2

*The subscript CTRL, U-CCB, H-CCB, and the number behind identify WPC panel compressed from the pellets without CCB, the WPC panel compressed from pellets with uniformly-distributed CCB, the WPC panel compressed from pellets with honeycomb-distributed CCB and the CCB content, respectively.

**Fig. 1.** Scheme of the fabrication process of the WPC_{U-CCB} (a) and WPC_{H-CCB} (b).

2.3.4. Cone calorimeter (CONE) tests

The combustion test was conducted using a cone calorimeter (Fire Testing Technology Ltd., East Grinstead, UK) according to ISO 5660-1 at a heat flux of $50 \text{ kW} \cdot \text{m}^{-2}$. The heat release rate (HRR), total heat release (THR), smoke production rate (SPR), total smoke production (TSP), and residual mass were recorded and analyzed. After the ash on the residue was blown off, the bottom char was fractured by hand and the fractured cross-sections were observed by SEM, as described above.

3. Results and discussion

3.1. Morphology of WPC

The CCB particles were spherical with a diameter ranging from 10 to 40 nm (Fig. 2a). They aggregated into larger clusters due to the interaction between particles under the influence of van der Waals force and electrostatic force [21,22]. The CCB particles had a rough surface and thereby a higher surface area, which may facilitate the development of stronger adhesion with the pellets [23]. The pellets had a rough surface on which the wood particles were imbedded in the HDPE matrix (Fig. 2b). The CCB particles were visible on the pellets coated with 0.5% CCB (Fig. 2c) and the number of CCB particles on the pellets increased with increasing CCB content (Fig. 2d). The pellets were sufficiently covered with CCB particles at 1% content (Fig. 2d). After the CCB-coated pellets were compressed into WPC panels, the CCB lamella structures with different thickness were formed depending on the content of CCB as observed on the tensile-fractured surface of WPC_{H-CCB} (Fig. 2e and g). Also,

the CCB network clearly exhibited a mixture of CCB and HDPE as observed at a higher magnification (Fig. 2f). This can be due to the diffusion of melt HDPE polymer into the CCB layer during the hot compression of the WPC panels. Moreover, bulk CCB domains accompanied by numerous micro-cracks were also observed from in the WPC_{H-CCB3}, as a result of the severe agglomeration of carbon black (Fig. 2h). The diffusion of the ductile HDPE polymer enhances the interfacial interaction between the CCB network and WPC. Such aggregated CCB structure could not be diffused completely by melted HDPE, which would result in a decrease of the mechanical properties. Compared to the WPC_{H-CCB}, the WPC_{U-CCB3} had no continuous lamellar CCB structure and the CCB particles were randomly distributed within the polymer networks (not shown).

3.2. Bulk conductivity

The WPC_{CTRL} exhibited insulating characteristics with quite low conductivity at around $1.89 \times 10^{-14} \text{ S} \cdot \text{cm}^{-1}$ due to lack of free electrons in WPC_{CTRL} (the black dashed line in Fig. 3a). Compared with the WPC_{CTRL}, the incorporation of the CCB led to a considerable increase in conductivity through the two-step blending process. With the increase of the CCB content from 0 to 1%, the conductivity of WPC_{H-CCB} dramatically increased to $7.1 \times 10^{-4} \text{ S} \cdot \text{cm}^{-1}$, resulting in a conductive material (Fig. 3a). When the CCB content was further increased from 1% to 3%, only a slight increase in the conductivity of WPC_{H-CCB} is observed, indicating that a sufficiently continuous honeycomb-like CCB network had been constructed at a CCB content of 1% (Fig. 3a) [24–26]. In contrast, there was no significant increase in the conductivity of WPC_{U-CCB} at the CCB content of $\leq 3\%$ (Fig. 3a). Moreover, our previous study revealed that

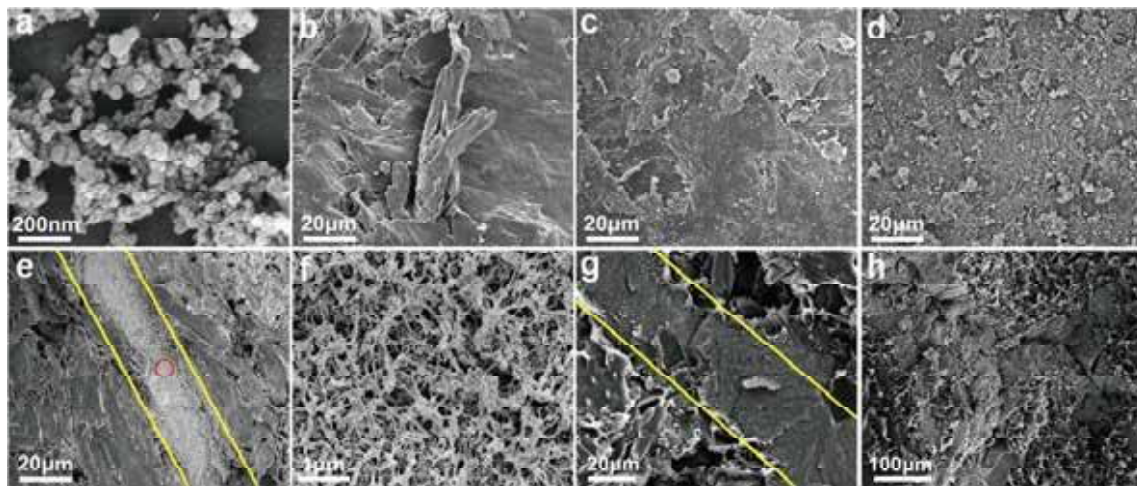


Fig. 2. SEM images of CCB nanoparticles (a), the wood flour/polyethylene composite pellets (b), the pellets coated with 0.5% CCB (c), the pellets coated with 1% CCB (d), the tensile fractured surface of the WPC_{U-CCB2} with different magnifications (e and f), and the tensile fractured surface of the WPC_{H-CCB3} with different magnifications (g and h). Red circle in (e) demonstrates the region shown in (f). (For interpretation of the references to colour in this figure legend, the reader is referred to the web version of this article.)

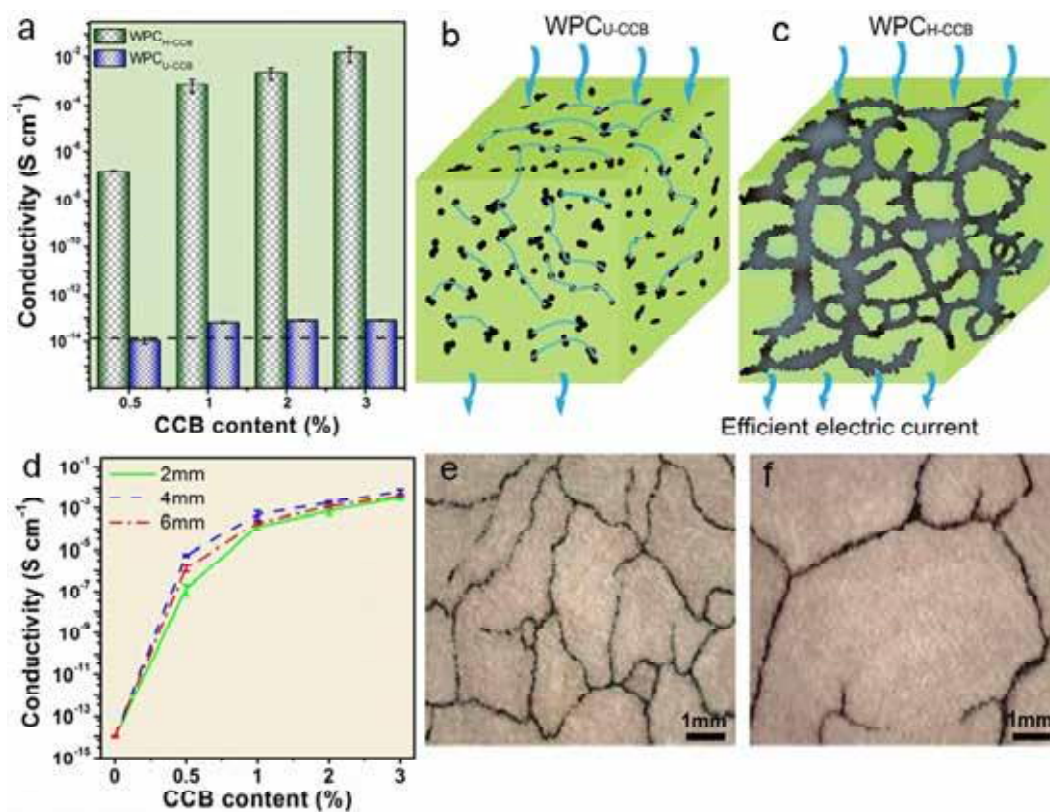


Fig. 3. Conductivity of the WPC_{H-CCB} at various CCB contents (a); schematic electric current passing through the WPC_{U-CCB} (b) and the WPC_{H-CCB} (c), respectively; effect of pellet sizes on the conductivity of the WPC_{H-CCB} (d); optical microscopic images of the internal structure of the WPC_{H-CCB0.5} prepared from CCB-coated pellets with a diameter of 2 mm (e) and 6 mm (f), respectively.

the conductivity of the WPC_{U-CCB} with 12% CCB is even lower than that of the WPC_{H-CCB0.5} obtained in this study. This could be due to the insufficient construction of a continuous CCB conductive network using the conventional one-step blending process. The continuity of the conductive CCB has a decisive effect on the conductivity of the CCB-filled WPCs. When the low-content CCB was uniformly-distributed in the WPC, the continuity may hardly be established (Fig. 3b). In comparison, the continuity can be easily

established by the honeycomb-like structural design, where the limited amount of CCB particles formed an interconnected network for delivering the electric current (Fig. 3c) [27]. Thus, the formation of a honeycomb-like continuous CCB network using this two-step blending procedure has an incredible advantage for the construction of CCB-based conductive WPC, resulting in higher conductivity by 10 orders of magnitude for the WPC_{H-CCB1} compared to WPC_{U-CCB1}.

The main challenge for the formation of a continuous honeycomb-like CCB network with sufficient conductivity is to perform the process in such a way that the CCB can form and maintain a continuous layer covering the pellets with adequate thickness and network density during the hot-press process. Thus, the size of the pellets also exerted a certain effect on the conductivity of the resulting WPC_{H-CCB} (Fig. 3d). The WPC_{H-CCB} prepared using pellets of moderate size (Ø4 mm) were more effective in improving the conductivity than those prepared using the pellets with the other two sizes (Ø2 mm and Ø6 mm). As shown in Fig. 3e and f, the network density decreased with the increase of the size of the pellets from 2 to 6 mm. The WPC_{H-CCB} with 2-mm size pellets resulted in a thinner CCB layer, which led to relatively poor delivery of electric current compared with the WPC_{H-CCB} formed by 4-mm size pellets (Fig. 3e). In addition, compared with 4-mm size pellets, the lower conductivity of WPC_{H-CCB} formed with 6-mm size pellets is assumed to be related to the low density of the CCB network. The ease of breakage of the larger pellets during the hot compression process is probably the other reason that leads to discontinuity of the CCB network (Fig. 3f) [22].

The conductivity between the WPC_{H-CCB} and the HDPE_{H-CCB} was also compared. The conductivity of the honeycomb-distributed WPC was higher than the honeycomb-distributed HDPE when the CCB content was lower than 1% (Fig. 4a). This may be due to the lower melt viscosity of the original HDPE compared with the WPC (Fig. 4b), giving rise to some CCB penetrating into the HDPE pellets during hot-pressing, thus resulting in the CCB conductive network was less densely packed than the honeycomb-distributed WPC (Fig. 4c vs d). For sufficient carbon black loading ($\geq 1\%$), even if the CCB would diffuse into HDPE region, the relatively continuous conductive networks could be established.

3.3. Electromagnetic interference (EMI) shielding efficacy

The EMI shielding efficacy (SE) of a material is defined as $SE_{Total} = -10 \log(P_t/P_i)$, where P_t and P_i are the transmitted and incident electromagnetic power, respectively [28,29]. The SE_{Total} consists of the absorption SE (SE_A), reflectance SE (SE_R), and multiple reflections SE (SE_M). The SE_M can be negligible when SE_{Total} is > 10 dB [20–30]. In this study, the SE_{Total} of the WPC_{CTRL} was close to zero (Fig. 5a), suggesting an absence of EMI shielding ability. The addition of CCB to form WPC_{H-CCB} gave rise to the EMI shielding ability. Specifically, with an increase in the CCB content from 0.5 to 3%, the SE_{Total} of WPC_{H-CCB} increased from around 5 dB to about 20 dB. Both the WPC_{H-CCB2} and WPC_{H-CCB3} had a SE_{Total} of > 10 dB. The high SE_{Total} can mainly be attributed to SE_A as the measured SE_R and the SE_M were almost zero (not shown). The EMI shielding ability of the WPC_{U-CCB3} was considerably greater than the WPC_{U-CCB3} at the highest CCB content (Fig. 5b).

The SE_{Total} of WPC_{U-CCB3} was around 5 dB, which is only a level of the WPC_{H-CCB0.5} (Fig. 5b). The high efficacy of the honeycomb-like CCB network at low CCB content contributes to reduce the cost and promotes its large-scale application.

3.4. Combustion behavior

Two HRR peaks can be observed for the WPC_{CTRL}, WPC_{H-CCB} and WPC_{U-CCB}. The initial peak originated from the burning of the WPC surface and the second resulted from the combustion of the bottom layer (Fig. 6a) [31]. In comparison to the WPC_{CTRL}, the WPC_{H-CCB3} exhibited a decrease and delay in the second HRR peak, which was accompanied by a reduction in THR (Fig. 6a and b). These results can be explained by the efficient coating of the pellets with the incombustible CCB particles in the WPC_{H-CCB}, thereby preventing the heat and O_2 from penetrating into the pellets [32,33]. In contrast, the WPC_{U-CCB3} with the uniformly-distributed CCB only showed a minor decrease in the HRR and THR (Fig. 6a and b). This suggests that the uniform distribution of 3% CCB is not sufficient to physically shield the inflammable WPC [34].

The WPC_{CTRL} released considerable smoke during combustion, which consisted mainly of combusted polymeric fragments and gases produced from the decomposed HDPE and wood flour [31,35]. After introduction of the honeycomb-like CCB network, the SPR and TSP of the WPC_{H-CCB3} were considerably reduced (Fig. 6c and d). The second peak of the SPR was reduced by 71.3% and the TSP was reduced by 32.6%. The WPC_{U-CCB3} showed only a slight decrease in the SPR and TSP compared with the WPC_{CTRL} (Fig. 6c and d). The higher efficacy in smoke suppression of the WPC_{H-CCB}, compared with the WPC_{U-CCB}, is mainly due to the sufficient coverage of CCB to shield the material from the heat and O_2 .

Due to the presence of incombustible CCB, both the WPC_{U-CCB3} and WPC_{H-CCB3} exhibited higher mass retention than the WPC_{CTRL} (Fig. 7a). Moreover, the WPC_{H-CCB3} had the highest mass retention due to the excellent fire-retardant characteristic, which is consistent with the heat and smoke release results. We assumed that the CCB does not inflame under the Cone test conditions. The residues of the WPC_{U-CCB3} were approximately equivalent to the sum of the residues of the WPC_{CTRL} and the added CCB (Fig. 7b). In contrast, the residual increment of the WPC_{H-CCB3} is much higher than the sum of the residues of the WPC_{CTRL} and the added CCB. This further demonstrates that the fire resistance of the WPC_{H-CCB3} with honeycomb-like CCB network is much superior to that of the WPC_{U-CCB3} with a uniformly-distributed CCB network.

Both the WPC_{U-CCB3} and WPC_{H-CCB3} plates with a thickness of 3.5 mm were burned into ash with a thickness of approximately 2 mm and 6 mm, respectively. The obtained ashes exhibited an upper ash layer and bottom char layer (Fig. 8a and b). This increased thickness of the residuals from the combusted

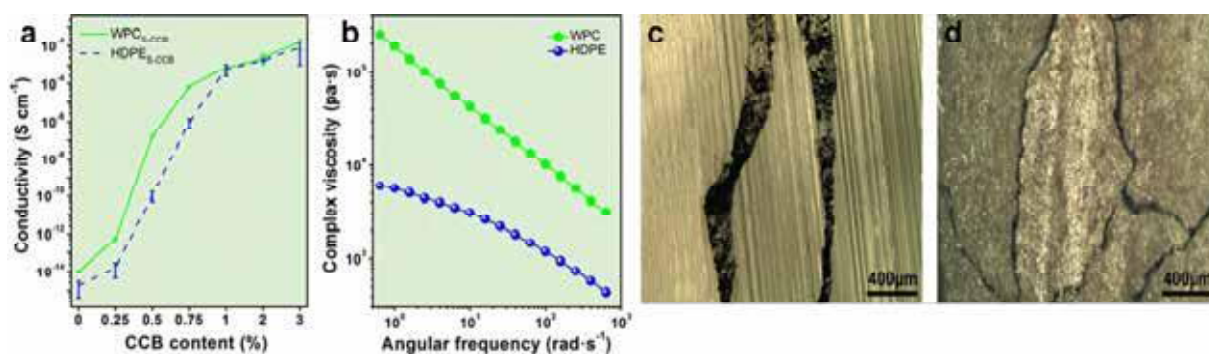


Fig. 4. Conductivity of the honeycomb-distributed WPC and HDPE (a), complex viscosity (η^*) of WPC and HDPE (b); polarizing microscope photograph of HDPE_{1-CCB0.5} (c) and WPC_{H-CCB0.5} (d).

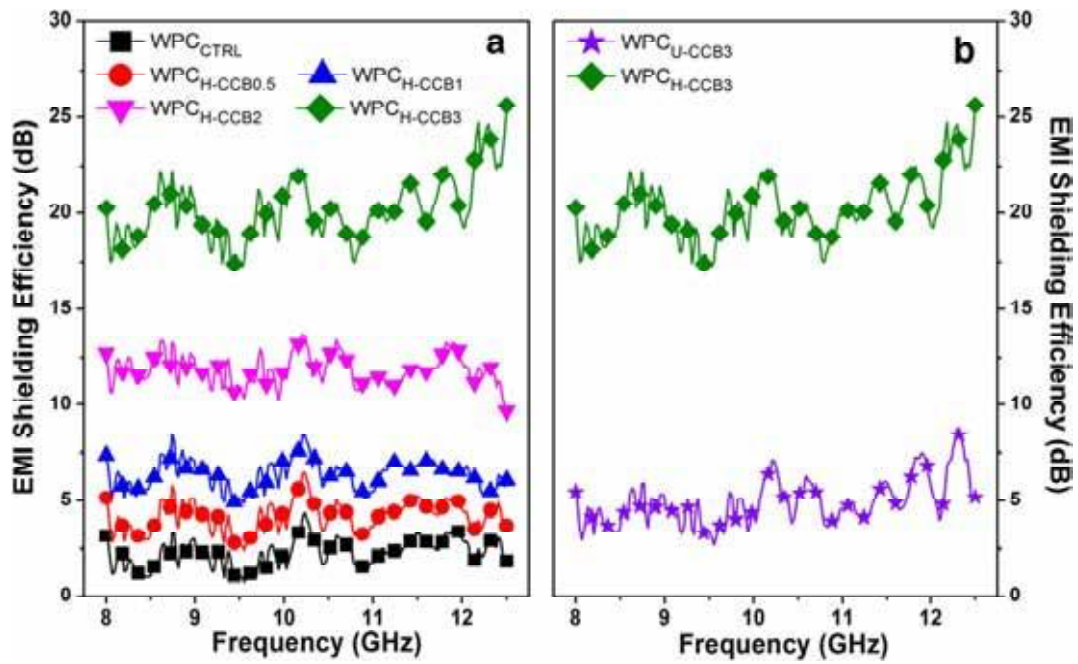


Fig. 5. EMI shielding efficacy of the WPC_{CTRL} and the WPC_{H-CCB} (a); Comparison of EMI shielding efficacy between the WPC_{U-CCB3} and the WPC_{H-CCB3} (b).

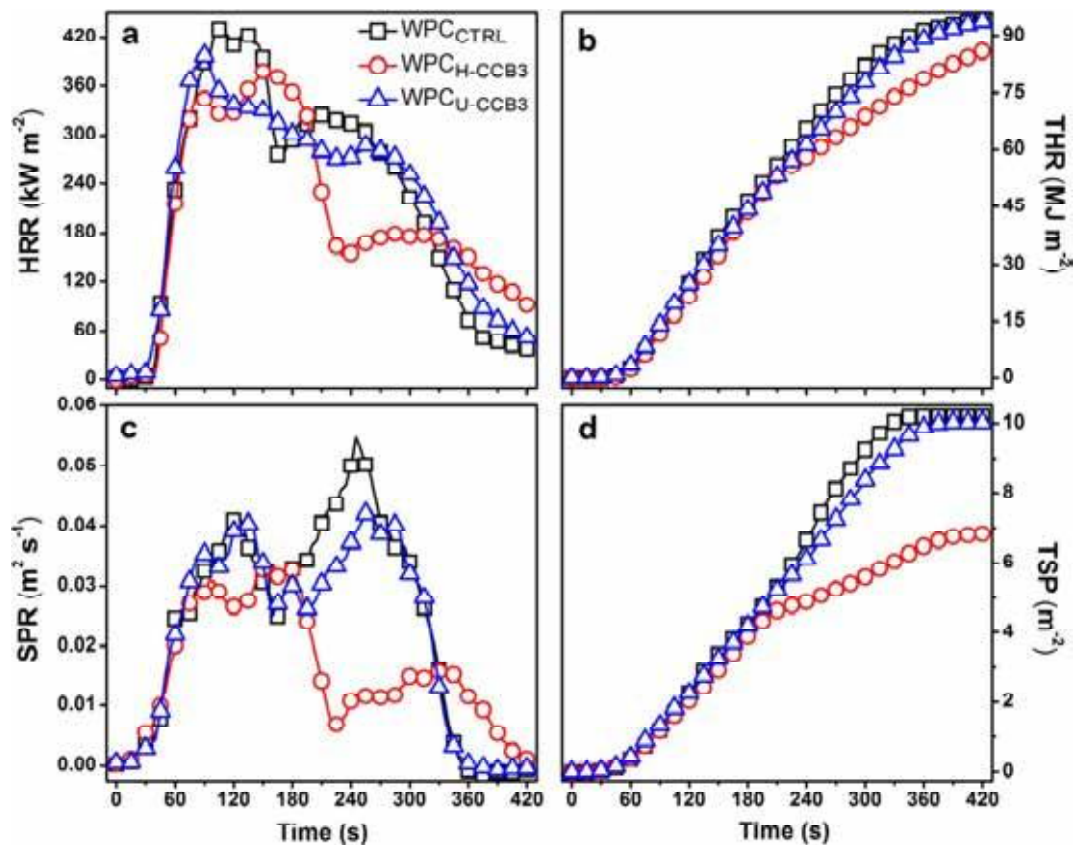


Fig. 6. (a) Heat release rate (HRR), (b) total heat release (THR), (c) smoke production ratio (SPR), and (d) total smoke production (TSP) of WPC_{CTRL}, WPC_{U-CCB3}, and WPC_{H-CCB3} during the CONE combustion process.

WPC_{H-CCB3} is due to the inflation resulted from the trapped gas within the CCB network. The insufficient combustion of the WPC_{H-CCB3} is probably another reason. In addition, numerous incompletely burned wood fragments can be observed in the ash

of the WPC_{H-CCB3}, indicating excellent fire resistance (Fig. 8c). In contrast, the ash of the WPC_{U-CCB3} mainly contained carbon aggregates, which indicated a relatively complete combustion (Fig. 8d).

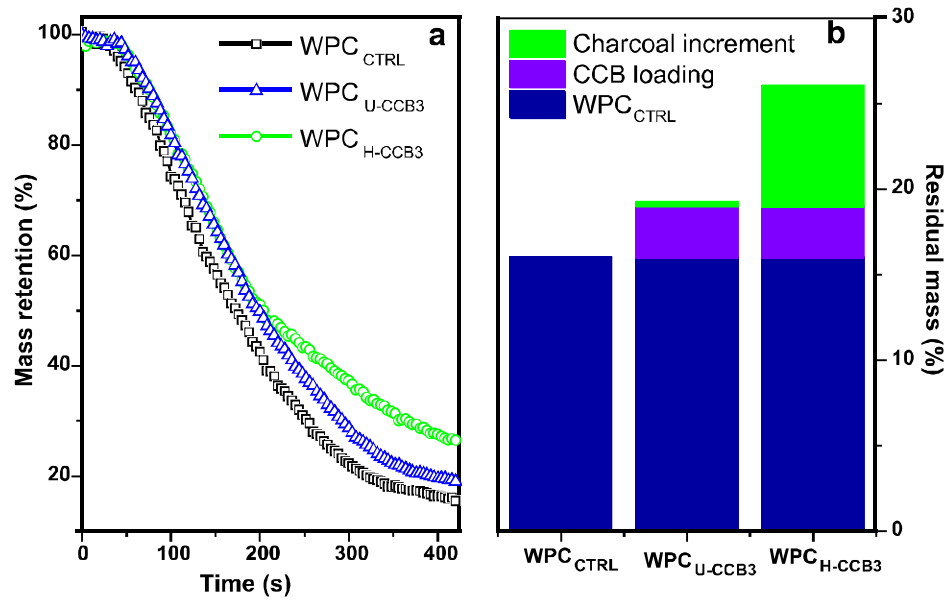


Fig. 7. The mass retention during the combustion (a) and the residual mass after combustion (b) of the WPC_CTRL, WPC_U-CCB3, and WPC_H-CCB3, respectively.

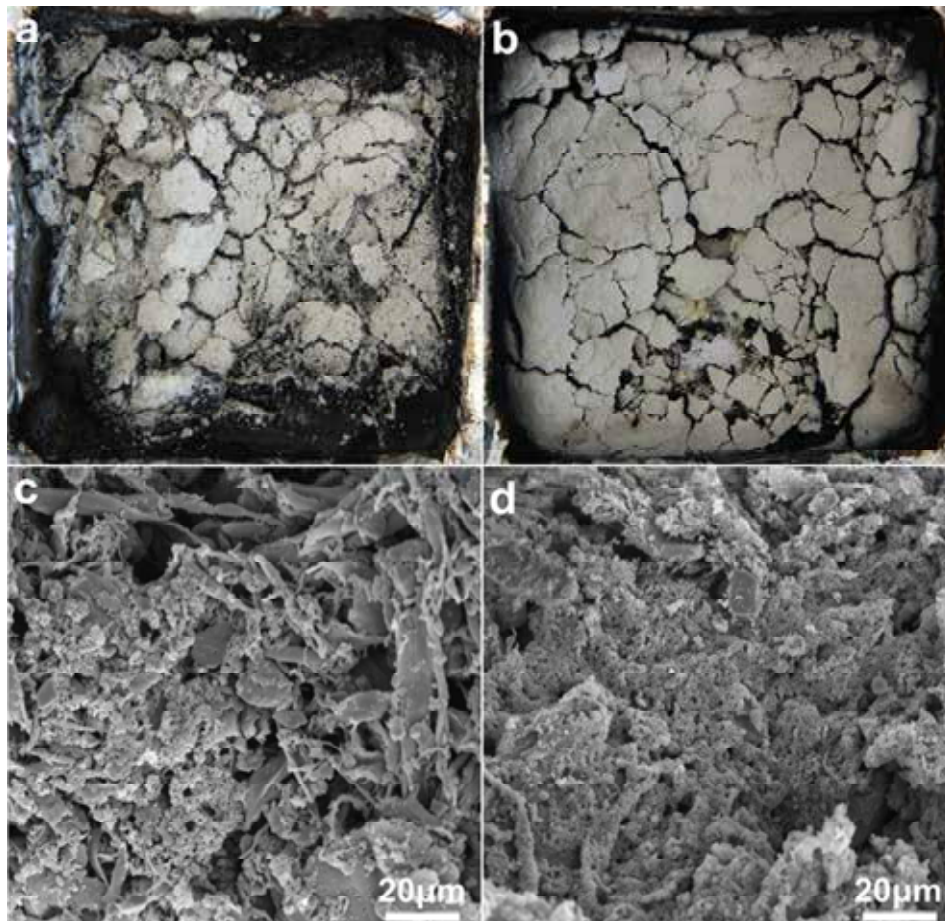


Fig. 8. The digital photographs (a, b) and SEM (c, d) of the residues of the WPC_H-CCB3 (a, c), and WPC_U-CCB3 (b, d) after combustion tests.

4. Conclusions

In this study, the WPC with a continuous and honeycomb-like CCB network (WPC_H-CCB) was prepared. Compared with the uniformly-distributed WPC (WPC_U-CCB) prepared through a

conventional one-step melt-blending process, the WPC_H-CCB exhibited superior characteristics in regard to conductivity, EMI shielding, and flame retardancy at considerably low CCB content (namely, low cost). The resulting WPC_H-CCB confers such WPC great application potential as building materials, such as antistatic floor,

electromagnetic shielding and flame-retardant wall. The results presented herein also demonstrated an efficient and facile procedure to pursue further advances of WPCs with desired functions through the formation of honeycomb-like functional additives network.

Declaration of Competing Interest

The authors declare that they have no known competing financial interests or personal relationships that could have appeared to influence the work reported in this paper

Acknowledgements

The authors are grateful to the support from the National Key Research and Development Program of China (2017YFD0600204) and the National Natural Science Foundation of China (31470585 & 31500469).

References

- [1] V. Mazzanti, F. Mollica, Bending properties of wood flour filled polyethylene in wet environment, *Procedia Eng.* 200 (2017) 68–72.
- [2] X. Hao, H. Zhou, Y. Xie, H. Mu, Q. Wang, Sandwich-structured wood flour/HDPE composite panels: Reinforcement using a linear low-density polyethylene core layer, *Constr. Build. Mater.* 164 (2018) 489–496.
- [3] L. Teuber, V.S. Osburg, W. Toporowski, H. Militz, A. Krause, Wood polymer composites and their contribution to cascading utilisation, *J. Clean. Prod.* 110 (2016) 9–15.
- [4] Y. Zhou, L. Ning, X. Li, J. Zhang, Y. Lu, J. He, Effect of natural flake graphite on triboelectrification electrostatic potential of bamboo flour/high-density polyethylene composites, *Wood. Sci. Technol.* 49 (2015) 1269–1280.
- [5] Y.H. Guan, J.Q. Huang, J.C. Yang, Z.B. Shao, Y.Z. Wang, An effective way to flame-retard biocomposite with ethanolamine modified ammonium polyphosphate and its flame retardant mechanisms, *Ind. Eng. Chem. Res.* 54 (2015) 3524–3531.
- [6] Y. Ren, Y. Wang, L. Wang, T. Liu, Evaluation of intumescent fire retardants and synergistic agents for use in wood flour/recycled polypropylene composites, *Constr. Build. Mater.* 76 (2015) 273–278.
- [7] F. Yu, F. Xu, Y. Song, Y. Fang, Z. Zhang, Q. Wang, F. Wang, Expandable graphite's versatility and synergy with carbon black and ammonium polyphosphate in improving antistatic and fire-retardant properties of wood flour/polypropylene composites, *Polym. Composite.* 38 (2017) 767–773.
- [8] H. Pang, L. Xu, D.X. Yan, Z.M. Li, Conductive polymer composites with segregated structures, *Prog. Polym. Sci.* 39 (2014) 1908–1933.
- [9] X. Zhang, X. Hao, J. Hao, Q. Wang, Effect of the addition of carbon nanomaterials on electrical and mechanical properties of wood plastic composites, *Polymers.* 9 (2017) 128–134.
- [10] M. Pan, C. Mei, J. Du, G. Li, Synergistic effect of nano silicon dioxide and ammonium polyphosphate on flame retardancy of wood fiber–polyethylene composites, *Compos. Part. A-Appl. S.* 66 (2014) 128–134.
- [11] Z.X. Zhang, J. Zhang, B.X. Lu, Z.X. Xin, C.K. Kang, J.K. Kim, Effect of flame retardants on mechanical properties, flammability and foamability of PP/wood–fiber composites, *Compos. Part. B-Eng.* 43 (2012) 150–158.
- [12] L. Sun, Q. Wu, Y. Xie, F. Wang, Q. Wang, Thermal degradation and flammability properties of multilayer structured wood fiber and polypropylene composites with fire retardants, *RSC. Adv.* 6 (2016) 13890–13897.
- [13] N. Suppakarn, K. Jarukumjorn, Mechanical properties and flammability of sisal/PP composites: effect of flame retardant type and content, *Compos. Part. B-Eng.* 40 (2009) 613–618.
- [14] S. Li, X. Li, C. Chen, H. Wang, Q. Deng, M. Gong, D. Li, Development of electrically conductive nano bamboo charcoal/ultra-high molecular weight polyethylene composites with a segregated network, *Compos. Sci. Technol.* 132 (2016) 31–37.
- [15] Q. Liu, J. Tu, X. Wang, W. Yu, W. Zheng, Z. Zhao, Electrical conductivity of carbon nanotube/poly(vinylidene fluoride) composites prepared by high-speed mechanical mixing, *Carbon* 50 (2012) 339–341.
- [16] A. Malliaris, D.T. Turner, Influence of particle size on the electrical resistivity of compacted mixtures of polymeric and metallic powders, *J. Appl. Phys.* 42 (1971) 614–618.
- [17] J. Du, L. Zhao, Y. Zeng, L. Zhang, F. Li, P. Liu, C. Liu, Comparison of electrical properties between multi-walled carbon nanotube and graphene nanosheet/high density polyethylene composites with a segregated network structure, *Carbon* 49 (2011) 1094–1100.
- [18] M. Ghislandi, E. Tkalya, B. Marinho, C.E. Koning, G.D. With, Electrical conductivities of carbon powder nanofillers and their latex-based polymer composites, *Compos. Part. A-Appl. S.* 53 (2013) 145–151.
- [19] B. Wang, H. Li, L. Li, P. Chen, Z. Wang, Q. Gu, Electrostatic adsorption method for preparing electrically conducting ultrahigh molecular weight polyethylene/graphene nanosheets composites with a segregated network, *Compos. Sci. Technol.* 89 (2013) 180–185.
- [20] L.C. Jia, D.X. Yan, C.H. Cui, X. Jiang, X. Ji, Z.M. Li, Electrically conductive and electromagnetic interference shielding of polyethylene composites with devisable carbon nanotube networks, *J. Mater. Chem. C* 3 (2015) 9369–9378.
- [21] A. Schröder, M. Klüppel, R.H. Schuster, Characterisation of surface activity of carbon black and its relation to polymer–filler interaction, *Macromol. Mater. En.* 292 (2007) 885–916.
- [22] F.E. Alam, W. Dai, M. Yang, S. Du, X. Li, J. Yu, N. Jiang, C.T. Lin, In-situ formation of cellular graphene framework in thermoplastic composites leading to superior thermal conductivity, *J. Mater. Chem. A* 5 (2017) 1–7.
- [23] S. Ban, K. Malek, C. Huang, Z. Liu, A molecular model for carbon black primary particles with internal nanoporosity, *Carbon* 49 (2011) 3362–3370.
- [24] G. Long, C. Tang, K. Wong, C. Man, M. Fan, W. Lau, T. Xu, B. Wang, Resolving the dilemma of gaining conductivity but losing environmental friendliness in producing polystyrene/graphene composites via optimizing the matrix–filler structure, *Green. Chem.* 15 (2013) 821–828.
- [25] I. Jurewicz, P. Worajittiphon, A.A. King, P.J. Sellin, J.L. Keddie, A.B. Dalton, Locking carbon nanotubes in confined lattice geometries—a route to low percolation in conducting composites, *J. Phys. Chem. B* 115 (2011) 6395–6400.
- [26] J.R. Potts, O. Shankar, L. Du, R.S. Ruoff, Processing–morphology–property relationships and composite theory analysis of reduced graphene oxide/natural rubber nanocomposites, *Macromolecules* 45 (2012) 6045–6055.
- [27] C.H. Cui, D.X. Yan, H. Pang, X. Xu, L.C. Jia, Z.M. Li, Formation of a segregated electrically conductive network structure in a low-melt-viscosity polymer for highly efficient electromagnetic interference shielding, *ACS. Sustain. Chem. Eng.* 4 (2016) 4137–4145.
- [28] J. Wang, C. Xiang, Q. Liu, Y. Pan, J. Guo, Ordered mesoporous carbon/fused silica composites, *Adv. Funct. Mater.* 18 (2008) 2995–3002.
- [29] F. Sharif, M. Arjmand, A.A. Moud, U. Sundararaj, E.P.L. Roberts, Segregated hybrid poly(methyl methacrylate)/graphene/magnetite nanocomposites for electromagnetic interference shielding, *ACS. Appl. Mater. Inter.* 9 (2017) 14171–14179.
- [30] Z. Chen, C. Xu, C. Ma, W. Ren, H.M. Cheng, Lightweight and flexible graphene foam composites for high-performance electromagnetic interference shielding, *Adv. Mater.* 25 (2013) 1296–1300.
- [31] Z. Xiao, J. Xu, C. Mai, H. Militz, Q. Wang, Y. Xie, Combustion behavior of Scots pine (*Pinus sylvestris* L.) sapwood treated with a dispersion of aluminum oxychloride-modified silica, *Holzforschung* 70 (2016) 1–9.
- [32] Q. Fu, L. Medina, Y. Li, F. Carosio, A. Hajian, L.A. Berglund, Nanostructured wood hybrids for fire-retardancy prepared by clay impregnation into the cell wall, *ACS. Appl. Mater. Inter.* 9 (2017) 36154–36163.
- [33] Q. Zhao, B. Zhang, H. Quan, R.C.M. Yam, R.K.K. Yuen, R.K.Y. Li, Flame retardancy of rice husk-filled high-density polyethylene eco-composites, *Compos. Sci. Technol.* 69 (2009) 2675–2681.
- [34] S. Bourbigot, S. Duquesne, Fire retardant polymers: recent developments and opportunities, *J. Mater. Chem.* 17 (2007) 2283–2300.
- [35] B. Guo, Y. Liu, Q. Zhang, F. Wang, Q. Wang, Y. Liu, J. Li, H. Yu, Efficient flame-retardant and smoke-suppression properties of Mg–Al-layered double-hydroxide nanostructures on wood substrate, *ACS. Appl. Mater. Inter.* 9 (2017) 23039–23047.



Effects of fiber geometry and orientation distribution on the anisotropy of mechanical properties, creep behavior, and thermal expansion of natural fiber/HDPE composites

Xiaolong Hao¹, Haiyang Zhou¹, Binshan Mu, Lei Chen, Qiong Guo, Xin Yi, Lichao Sun, Qingwen Wang^{*}, Rongxian Ou^{**}

College of Materials and Energy, South China Agricultural University, Guangzhou, 510642, PR China

ARTICLE INFO

Keywords:

Polymer-matrix composites (PMCs)
Anisotropy
Mechanical properties
Creep

ABSTRACT

Natural fiber/high-density polyethylene (HDPE) composites (NFPCs) were fabricated via extrusion using three types of natural fibers from poplar wood (PW), radiata pine (RP), and rice husk (RH), respectively. The specimens were cut from the extruded samples at various off-axis angles (from 0° to 90°). The effect of fiber geometry and orientation distribution on the mechanical properties, creep behavior, and thermal expansion of the NFPCs was investigated. The natural fibers in the composites showed a preferential orientation along the extrusion direction, as evidenced by the optics micrographs. The flexural properties and impact strength of the NFPCs were the highest at zero angle and decreased considerably with increasing orientation angle, which was further validated by the finite element analysis. At zero angle, the PW/HDPE composites had the highest flexural and impact strength and the smallest creep strain and thermal expansion, but a small difference in mechanical properties was observed at 90° among the NFPCs. The significant anisotropy of properties at various angles of the PW/HDPE composites was due to the high aspect ratio (L/D) of poplar wood fiber. These results indicate that high fiber L/D and orientation distribution had a beneficial effect on the properties of NFPCs.

1. Introduction

Natural fiber/plastic composites (NFPCs) mainly composed of natural fibers (NFs) and thermoplastics have been widely applied in various industries such as building, construction, furniture, and automotive [1–5]. The predominant process technologies of NFPCs include extrusion, injection molding, and hot pressing [2,6–9]. Extrusion and injection molding can obtain highly oriented NF and compact structure due to contraction flow and high pressure [10,11]. However, the NFs exhibited random orientation in hot-pressed NFPCs because there is no unidirectional flow during hot pressing [7]. In addition, fibers in outer layers are oriented in the main flow direction but oriented perpendicular to flow in core layer by injection molding [12,13], while fiber orientation and boundary layers are less distinct with extrusion because of lower pressure and shearing compared to injection molding [6]. Therefore, NFs with higher orientation in extruded NFPCs usually exhibit higher reinforcing efficacy than those in hot-pressed or

injection-molded NFPCs at high fiber contents (over 60 wt%). NF orientation also results in shear-thinning behavior which decreases melt viscosity of NFPCs at high processing speed [14]. Consequently, fiber orientation distribution has an important influence on properties of NFPCs fabricated by different processing methods [6,15,16].

NFs made from different wood species exhibited different geometries (e.g. size and aspect ratio (L/D)) even though they were subjected to the same grinding method, resulting from their differences in anatomical structure and chemical composition [17]. NFs with different chemical compositions and L/D affect the processability, thermal, physical, and mechanical properties of NFPCs [18–22]. The effect of NF size on properties of NFPCs showed opposite results in different reports [7,23]. Usually, NFs with higher L/D may contribute to higher reinforcing efficacy for NFPCs [1,4,10,24,25]. The level of stress transfer depends on fiber-matrix interfacial adhesion and fiber orientation [3,6,15], and the efficacy of stress transfer from matrix to fiber increased with increasing fiber length until reaching a critical value [6,15,25]. Low L/D generally

* Corresponding author.

** Corresponding author.

E-mail addresses: qwwang@scau.edu.cn (Q. Wang), rongxian_ou@scau.edu.cn (R. Ou).

¹ Xiaolong Hao and Haiyang Zhou are co-first authors of the article.

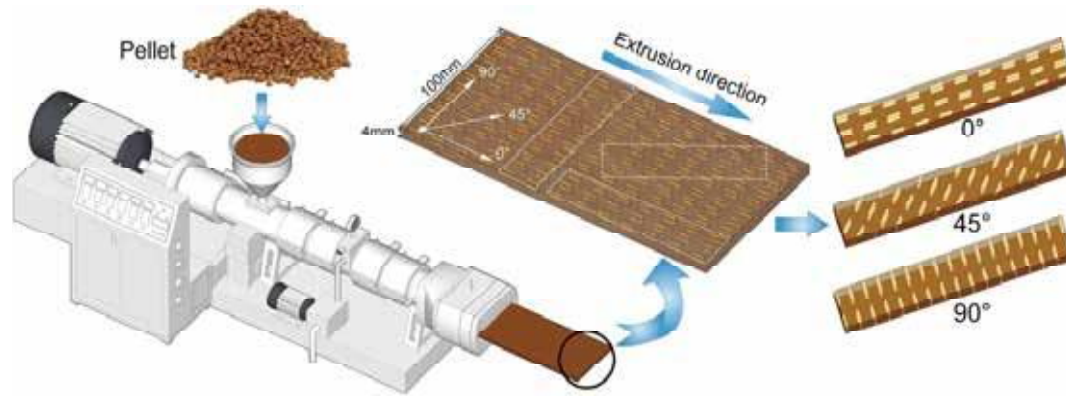


Fig. 1. Schematic of the NFPCs fabrication and sampling direction.

Table 1

Temperature of heating zone, melt pressure, feeding speed, and screw speed during the extrusion process of NFPCs.

Extruder	Temperature in different heating zone (°C)								Melt pressure (MPa)	Feed speed (kg h ⁻¹)	Rotary speed (rpm)
	1	2	3	4	5	6	7	Die			
Twin screw	145	150	155	160	160	165	165	165	—	10	40
Single screw	145	155	160	165	—	—	—	165	8–9	3	12

gives rise to stress concentration and accordingly decreases the mechanical properties of NFPCs [6]. Therefore, fiber geometry is another dominant factor that affects the properties of NFPCs. Many studies have focused on the effects of particle size or L/D on composite properties [26], but few studies have focused on the property anisotropy of NFPCs influenced by fiber orientation with different geometries.

This study aimed to investigate the effect of fiber geometry and orientation distribution on the property anisotropy of extruded NFPCs. Three types of NFs were prepared in-house by milling and screening in the same way. The anisotropy of mechanical properties, creep behavior, and thermal expansion of the resulting NFPCs was systematically investigated at different fiber orientation angles (from 0° to 90°) to the extrusion direction.

2. Experimental

2.1. Materials

HDPE (5000s) pellet with a density of 0.95 g cm⁻³ and a melt flow rate of 0.90 g (10 min)⁻¹ (190 °C, 2.16 kg according to ASTM D1238) was purchased from Daqing Petrification Company (Daqing, China). NFs with a size of -40 + 80 mesh from poplar wood (*Populus adenopoda* Maxim.) (PW), radiata pine (RP), and rice husk (RH) were prepared in-house by a cutter mill (FY600, Fuyang machinery Co., Ltd., China) and a vibrating screen (HFC-600, Dongguan Huanxin machinery Co., Ltd., China). Maleic anhydride grafted polyethylene (MAPE) had a maleic anhydride grafting ratio of ca. 1 wt% and a melt flow rate of 1.7 g (10 min)⁻¹. Stearic acid lubricant (#1801) had a density of 0.85 g cm⁻³ and a melt point of 65 °C. Both of them were purchased from Rizhisheng Company (Nantong, China).

2.2. Preparation of the composites

Three types of NFs were oven-dried at 103 °C for 24 h to reach a moisture content of 1–2%. The dry NFs, HDPE, MAPE, and lubricant were mixed in a specific ratio (60 : 35 : 3 : 2) in a high-speed mixer (1500 r min⁻¹, HRS-10, Dongguan Huanxin Machinery Co., Ltd, China) for 10 min at 80 °C. They were melted blending using a co-rotating twin-screw extruder (L/D = 30, SJSH-30, Nanjing Rubber Machinery Factory, China), and afterward extruded through a single-screw extruder (L/D =

45, SJ-45, Nanjing Rubber Machinery Factory, China) to fabricate a profile measuring 100 mm × 4 mm (width × thickness). The specimens cut from the extruded profiles at different inclination angles (0°, 30°, 45°, 60°, 90°) to the extrusion direction (Fig. 1) were used for flexural, impact, creep, and thermal expansion tests. The processing parameters for the twin- and single-screw extruders are presented in Table 1.

2.3. Fiber size and morphology

After sputter coating with a thin gold layer, fiber morphology of the dried NFs before and after extrusion processing was observed by a scanning electron microscope (Quanta 200; FEI Co., USA). Fiber geometry was observed using a stereomicroscope (Leica S8AP0, Wetzlar, Germany) equipped with a Leica camera (Model DFC295). An image analysis software (Image-ProPlus 6.0) was used to analyzed the length and diameter of individual fiber, and the L/D was accordingly calculated.

2.4. Characterization of the composites

2.4.1. Morphological analysis

Thin slices (0.10–0.13 mm) were cut from the extruded profiles in thickness along the extrusion direction and cross-planar transverse to extrusion direction, respectively, and fiber orientation distribution was observed using an optics microscope (SMART-POL, Chongqing Optec Instrument Co., Ltd, China).

2.4.2. Mechanical testing

Unnotched impact tests (ASTM D6110) with the sample size of 80 mm × 10 mm × 4 mm (length × width × thickness) were conducted using an impact tester (XJUD-5.5, Jinjian, Chengde, China). Three-point bending tests (ASTM D790) with sample size of 80 × 13 × 4 mm (length × width × thickness) were conducted using a universal testing machine (CMT5504, MTS Systems Co., Ltd., Shenzhen, China). The impact and flexural tests were performed under the condition of 25 °C and 50% RH. At least 10 replicates were tested for each testing.

2.4.3. Creep analysis

A dynamic mechanical analyzer (Q800, TA Instruments Inc., USA) was used to test the short-term creep behavior of the specimens with size

Table 2

The parameters of NFs and HDPE measured at 25 °C were used for the finite element analysis.

Type	Young's modulus (GPa)	Poisson ratio	Density (g cm ⁻³)
NFs	11.0	0.36	0.56
HDPE	0.87	0.38	0.95

of 35 mm × 12 mm × 4 mm (length × width × thickness) in single cantilever configuration. Isothermal creep tests were performed at 30 °C, and a 2 MPa load was applied on the specimens for 30 min followed by releasing the load for 30 min [27].

2.4.4. Thermomechanical analysis

Thermal expansion of the specimens measuring 10 mm × 10 mm × 4 mm (length × width × thickness) was analyzed using a thermo mechanical analyzer (Q400, TA Instruments Inc., USA) at different inclination angles to the extrusion direction. A quartz probe was in close contact with the specimens under a force of 0.05 N. The testing was run at a heating rate of 3 °C min⁻¹ from -40 to 90 °C under a high purity nitrogen atmosphere with a 50 ml min⁻¹ flow rate.

2.4.5. Finite element analysis (FEA)

The finite element analysis of flexural property of the extruded NFPCs was conducted using Abaqus 6.13 software at different off-axis angles. For simplicity, NFs and HDPE matrix were supposed to be isotropic materials, respectively. The specimens for FEA were the same dimensions as the flexural specimens. The parameters of NFs and HDPE matrix used for FEA were presented in Table 2 [16,27,28].

3. Results and discussion

3.1. Morphological analysis

The cutter-milled NFs exhibited different morphologies and sizes

even though they were prepared in the same way (Fig. 2a–c). This was attributed to the differences in chemical composition and microstructure of cell walls [17]. PW and RP were relatively more regular in geometry than RH. PW exhibited cylindrical shape (Fig. 2a) with the highest L/D (Table 3), while RP exhibited spheroidal shape with the larger diameter (Fig. 2b). RH showed plate-like structure with inorganic silicon compounds on the surface (Fig. 2c). The PW, RP, and RH exhibited a gradually decreasing average L/D of 3.64, 2.52, and 2.18, respectively. Both fiber length and L/D were obviously decreased after extrusion processing (Fig. 2d–f), and the decreased degree of L/D was 31.0%, 20.2%, and 25.7% for PW, RP, and RH, respectively (Table 3). Moreover, the width of L/D distributions was also obviously decreased after extrusion processing (Fig. 3). This was attributed to the fact that the fibers undergo considerable damage like splitting, peeling, and squeezing as a result of the high shear force from extruder screws [29]. The L/D still decreased in the following order: PW > RP > RH. The spheroidally shaped RP was splitted into plate-like particles (Fig. 2e) and the RH was damaged to fine particles (Fig. 2f) after extrusion.

On the sectioned surface of the extrudates, NFs were clearly oriented in the extrusion direction (Fig. 4a–c). The fiber orientation may explained by the contraction flow resulting from high extrusion pressure [10]. However, NFs showed randomly distribution at cross section transverse to the extrusion direction (Fig. 4d–f). The size of NFs was markedly different. The PW exhibited the highest L/D (Fig. 4a), and most of the RH was damaged, resulting in fine particles (Fig. 4c), which accords with the results from SEM micrographs (Fig. 2f).

3.2. Mechanical properties

The effect of NF type and fiber off-axis angle on the flexural strength (σ) and modulus (E) of the NFPCs was shown in Fig. 5. Flexural strength of the NFPCs increased with increasing fiber L/D (Fig. 5a), especially at the lower off-axis angles (0° and 30°). PW/HDPE had the highest σ at all angles, followed by RP/HDPE and RH/HDPE. According to the classical theory of mechanics, load applied to a fiber-reinforced composite is

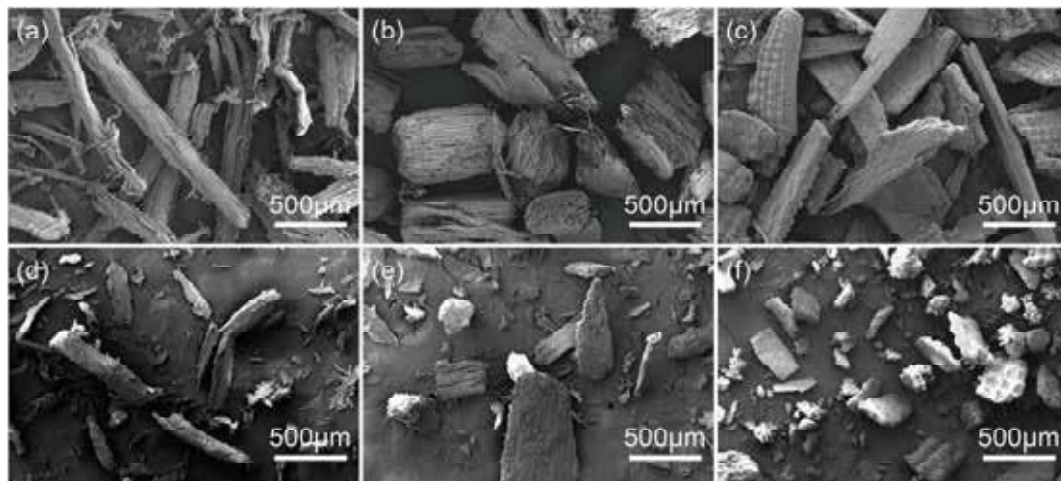


Fig. 2. Micrographs of NFs before extrusion processing (a) PW, (b) RP, (c) RH, and after extrusion processing (d) PW, (e) RP, (f) RH.

Table 3

Fiber characteristics of the natural fibers.

Fiber types	Fiber number		Average length (μm)		Average diameter (μm)		Average L/D	
	Before ^a	After ^b	Before ^a	After ^b	Before ^a	After ^b	Before ^a	After ^b
PW	442	440	616.2 ± 540.3	380.9 ± 291.6	172.3 ± 154.5	157.9 ± 127.9	3.64 ± 1.72	2.51 ± 1.03
RP	479	431	493.0 ± 401.7	292.9 ± 258.7	235.2 ± 204.1	157.0 ± 150.0	2.52 ± 1.31	2.01 ± 0.74
RH	455	501	466.7 ± 341.2	214.3 ± 146.0	252.0 ± 185.5	141.2 ± 101.3	2.18 ± 1.33	1.62 ± 0.55

Note: ^a and ^b represent fiber characteristics before and after extrusion processing, respectively.

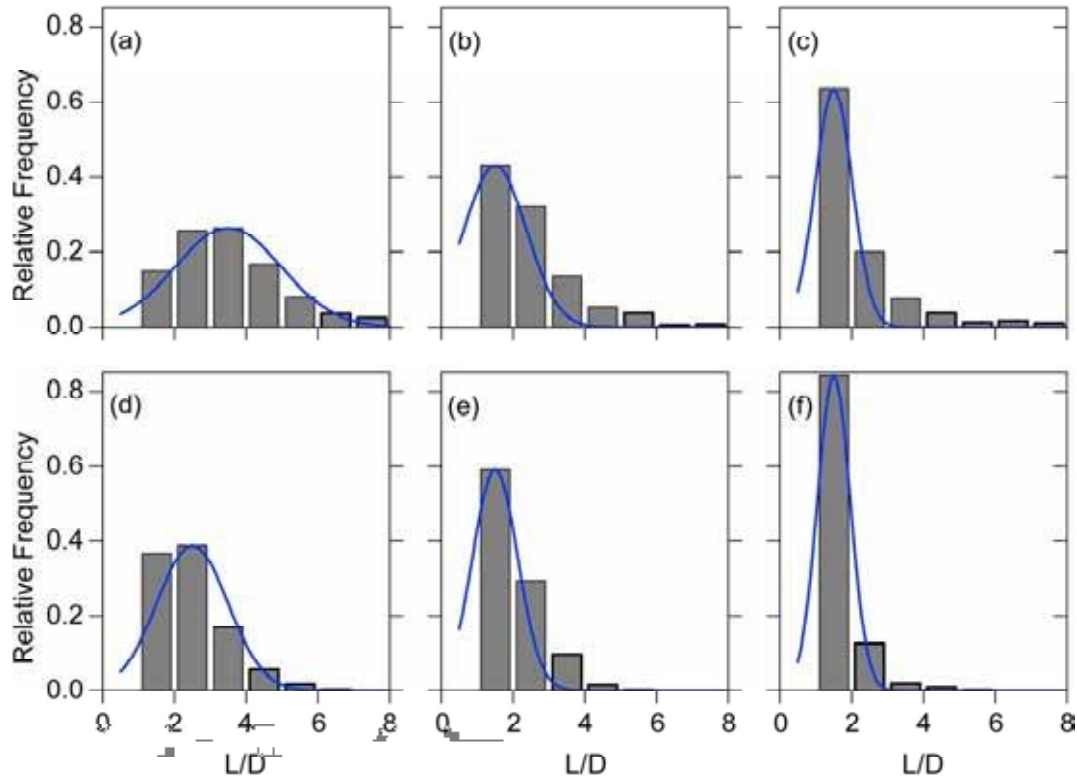


Fig. 3. Distributions of NFs L/D before extrusion processing (a) PW, (b) RP, (c) RH, and after extrusion processing (d) PW, (e) RP, (f) RH.

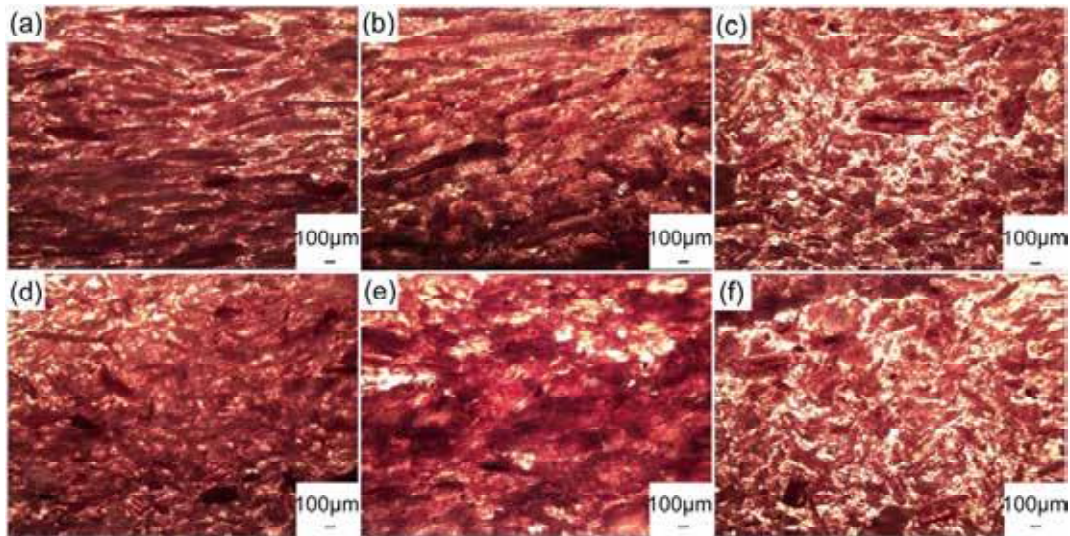


Fig. 4. Optics micrographs of NFPCs along the extrusion direction (a) PW/HDPE, (b) RP/HDPE, (c) RH/HDPE, and at cross section transverse to extrusion direction (d) PW/HDPE, (e) RP/HDPE, (f) RH/HDPE.

transferred to the fibers from the matrix by shear stress along the fiber-matrix interface [30]. The highest σ of PW/HDPE could be due to PW's high L/D. Stress transfer from HDPE matrix to NFs could be improved by increasing fiber L/D, which facilitates the absorption and spreading of energy for the composites [6,15,25]. Flexural strength and modulus of PW/HDPE decreased significantly with increasing fiber off-axis angle. Anisotropy ratios were calculated to be $\sigma_0/\sigma_{90} = 1.86$ for strength and $E_0/E_{90} = 2.16$ for modulus. RP/HDPE and RH/HDPE as well exhibited obvious reduction in σ and E with increasing fiber off-axis angle. The strength and modulus anisotropy ratios were 1.48 and 1.54 for RP/HDPE and 1.37 and 1.13 for RH/HDPE, respectively. This reveals

property anisotropy and deterioration in flexural properties of the NFPCs with increasing fiber off-axis angle, especially for PW/HDPE containing NFs with higher L/D. The reason for the reduction of flexural properties may be the fact that the NFPCs with transverse fiber orientation (90°) failed at the particular point, and cannot contribute further in the NFPCs failure [16,31]. Therefore, the on-axis (0°) flexural properties of NFPCs were strongly dependent on NF properties, while the off-axis properties were determined by polymer matrix properties [31]. Considering that the anisotropy of HDPE matrix after extrusion process may also affect the property anisotropy of NFPCs, the flexural property of the neat HDPE was also tested in the same way (Fig. 5). The results

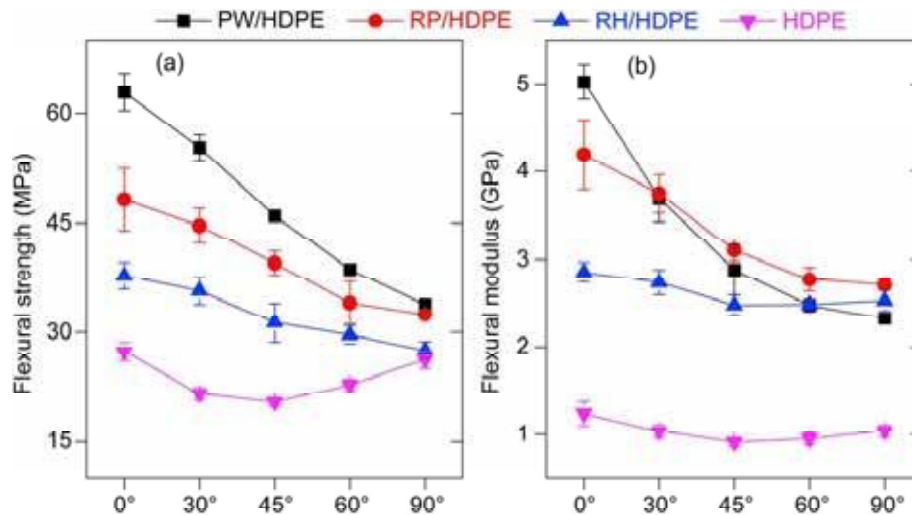


Fig. 5. (a) Flexural strength (σ) and (b) flexural modulus (E) of NFPCs at different orientation angles.

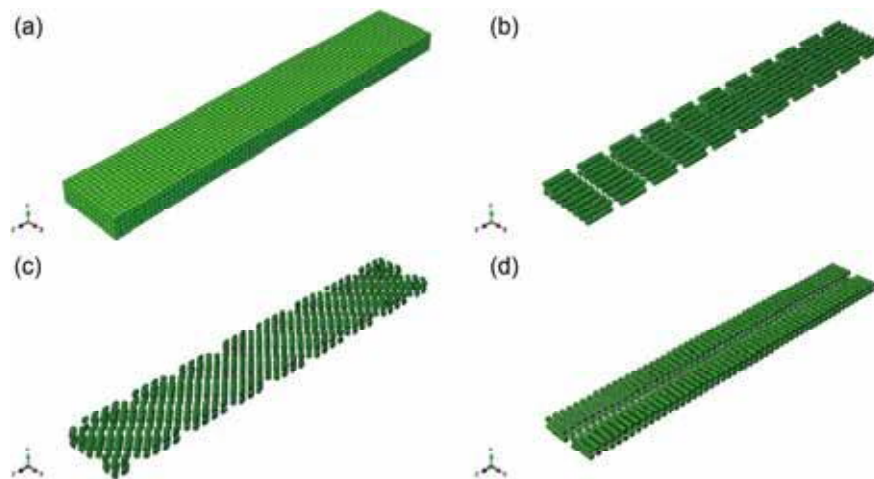


Fig. 6. Schema graph of the flexural samples for finite element modelling: (a) sample for flexural modelling, (b) fiber orientation at 0°, (c) fiber orientation at 45°, and (d) fiber orientation at 90°.

showed that σ of neat HDPE did not decrease linearly with increasing fiber off-axis angle like the NFPCs. The σ decreased first and then increased, and the lowest σ appeared at 45°. The E of neat HDPE only exhibited slight decrease from 0° to 90° and was significantly lower than that of the NFPCs. Therefore, these results further verified the effect of NFs orientation distribution with different geometries on the property anisotropy of NFPCs.

To clarify why the variation in fiber off-axis angle results in anisotropy of flexural properties, the stress and strain distributions of the NFPCs were simulated by FEA under constant load. The NFs were assumed as homogeneous cylindrical fibers with a specific L/D of 3, which is close to the L/D values of PW before and after extrusion. Three different off-axis angles (0°, 45°, and 90°) were chosen (Fig. 6). The HDPE matrix was assumed to be homogeneous in the NFPCs. For simplicity, the simulation results only exhibited the flexural stress field along z-axis direction and deflection field along y-axis direction, respectively (Fig. 7). Higher stress values mean higher stress concentration, and higher deflection values mean poorer deformation resistance. The simulated results showed that the stress concentration was more obvious for the composites with higher off-axis angles. This indicates that the stress can be efficiently transferred to the NFs from the HDPE matrix at on-axis direction (0°), and the transfer efficacy decreased with increasing off-axis angle to 90° (Fig. 7a, c, & e). The

smallest and highest flexural strain was observed for the NFPCs with fiber off-axis angle of 0° and 90°, respectively (Fig. 7b and f). This implies that NFs along the on-axis direction exhibits higher load-carrying ability and accordingly endows the NFPCs with higher mechanical property. The simulation results further demonstrate that the NFPCs have obvious anisotropic flexural properties that depend on fiber orientation angle.

The unnotched impact strength (UNIS) of a composite includes of the crack initiation and propagation energy, in which the former dominates [32]. The crack propagation energy dissipates through various mechanisms, including the work-of-fracture between the reinforcing fiber and the matrix, and the energy dissipated from multiple different fiber-matrix interactions, such as sliding, debonding, fiber pullout, etc. [33]. PW/HDPE had the highest UNIS (Fig. 8), which may be due to the higher L/D of PW. Pullout of long fibers dissipates high energy [20]. The lowest UNIS of RH/HDPE may be resulted from the inorganic silicon compounds on RH surface, which resulted in weak RH-HDPE interactions. The weak RH-HDPE interface acted as stress concentration sites decreasing the crack initiation energy from particle pullout significantly. Furthermore, it is found that the UNIS decreased with increasing fiber off-axis angle for all three composites. This was probably, in part, because the longitudinal fracture strength of NFs is higher than the transverse one, resulting in a decrease of work-of-fracture of

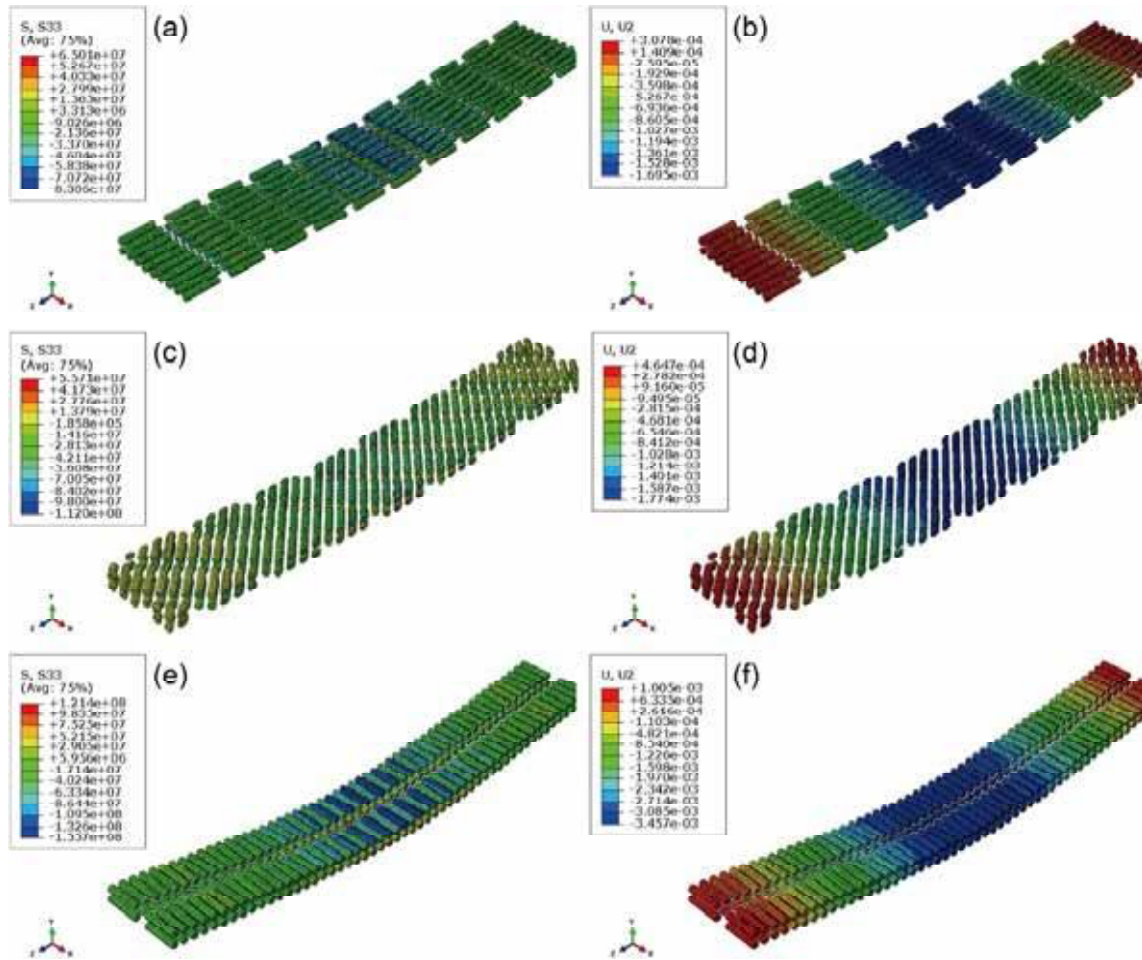


Fig. 7. Simulated flexural stress and strain field at different orientation angles: (a) stress at 0°, (b) deflection at 0°, (c) stress at 45°, (d) deflection at 45°, (e) stress at 90°, and (f) deflection at 90°.

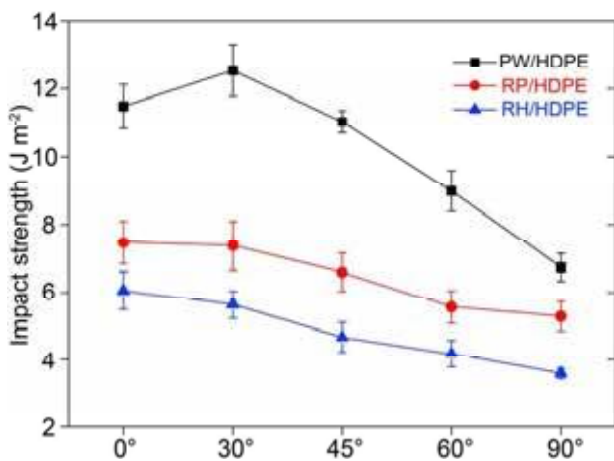


Fig. 8. Unnotched impact strength of NFPCs with different orientation angles.

NFs and the energy dissipated from NF-HDPE interactions when fiber off-axis angle increased [31].

3.3. Creep behavior of the composites

Creep behavior is the intrinsic property of NFPCs and exhibits time or temperature-dependent due to the presence of thermoplastic matrix

[34–37]. Generally, creep resistance of NFPCs can be effectively improved by increasing content of stiff NFs or adding other rigid fillers [35,38–40]. The presence of rigid fillers increases creep resistance by hindering the mobility of polymer chains [41,42]. The creep strain of PW/HDPE, RP/HDPE, and RH/HDPE at 0° was 0.022%, 0.025%, and 0.036%, respectively (Fig. 9). This indicates that creep resistance of NFPCs increased with fiber L/D. The creep strain of PW/HDPE was 0.022% and 0.041% at 0° and 90°, respectively, increasing by about 86% from 0° to 90° (Fig. 9a). The residual strain after unloading also increased with increasing fiber off-axis angle. The creep strain for RP/HDPE and RH/HDPE increased by about 36% and 17%, respectively, when changing fiber off-axis angle from 0° to 90° (Fig. 9b and c). The results illustrate that NFs had higher load-carrying capacity along on-axis orientation than off-axis direction. PW/HDPE exhibited the best longitudinal creep resistance but the highest anisotropic creep resistance upon fiber off-axis angle, which was attributed to PW's highest L/D. These findings accord with the results for flexural strength as mentioned above.

3.4. Thermal expansion of the composites

The thermal expansion of PW/HDPE, RP/HDPE, and RH/HDPE along the extrusion direction at 90 °C was 4.36%, 5.34%, and 9.52%, respectively (Fig. 10). This indicates that resistance to thermal deformation of NFPCs increased with fiber L/D. The thermal expansion of all three NFPCs increased with increasing fiber off-axis angle. The NFPCs exhibited the highest thermal expansion perpendicular to the extrusion

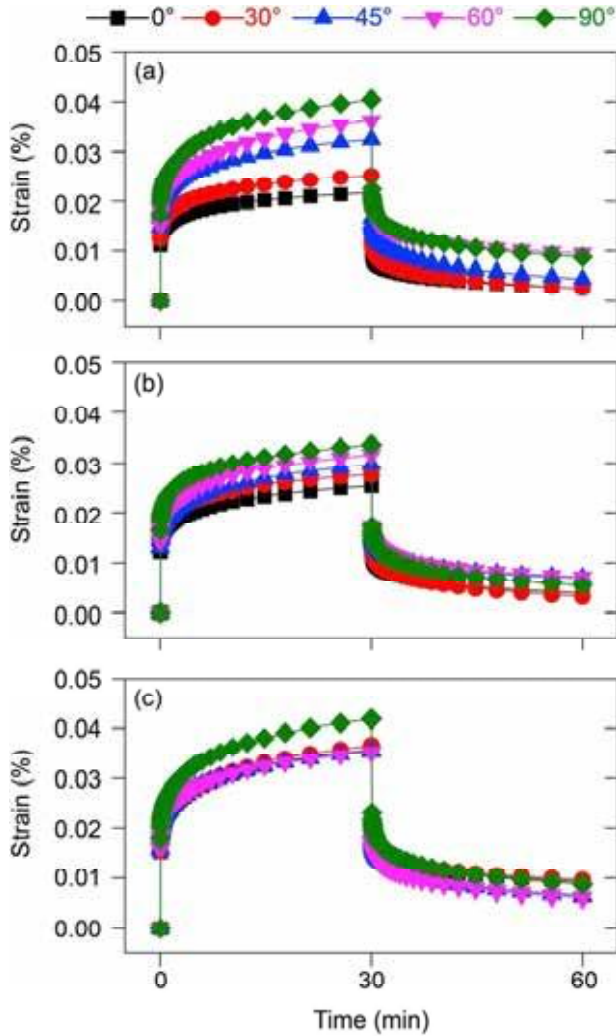


Fig. 9. Creep strain of NFPCs at different orientation angles: (a) PW/HDPE, (b) RP/HDPE, and (c) RH/HDPE.

direction (90°) over the entire temperature range. PW/HDPE had the highest anisotropy of thermal expansion upon varying fiber off-axis angle. It had been proved that thermal expansion behavior of NFPCs was dominated by thermoplastic matrix [43], and filling negative thermal expansion fillers can reduce the thermal expansion of polymers [44–47]. In order to further analyze the effect of varying aspect ratio on the thermal expansion of NFPCs, dimensional change of NFPCs varying with average L/D at different temperature was shown in Fig. 11. It was observed that thermal expansion decreased obviously by increasing L/D at extrusion direction (0°), however, thermal expansion increased with increasing L/D at 90° (Fig. 11a and b). In addition, the difference of thermal expansion at different angles was more obvious with higher L/D, especially at high temperature (Fig. 11b). Therefore, fiber orientation and L/D were the main reasons for reducing the thermal expansion of NFPCs.

The linear coefficient of thermal expansion (LCTE) of HDPE ($179 \times 10^{-6} \text{ } ^\circ\text{C}^{-1}$) is about 18 times that of solid wood ($10 \times 10^{-6} \text{ } ^\circ\text{C}^{-1}$) [43]. The LCTE of all NFPCs samples was positively correlated with temperature: the higher the temperature, the higher the LCTE values (Fig. 12). PW/HDPE exhibited the lowest longitudinal LCTE (0°) and the highest transversal LCTE (90°), respectively, compared to RP/HDPE and RH/HDPE. It has been proved that fillers with high L/D can provide remarkable mechanical constraint to the deformation of polymer matrix by interfering with the inside thermal stress distribution, which can

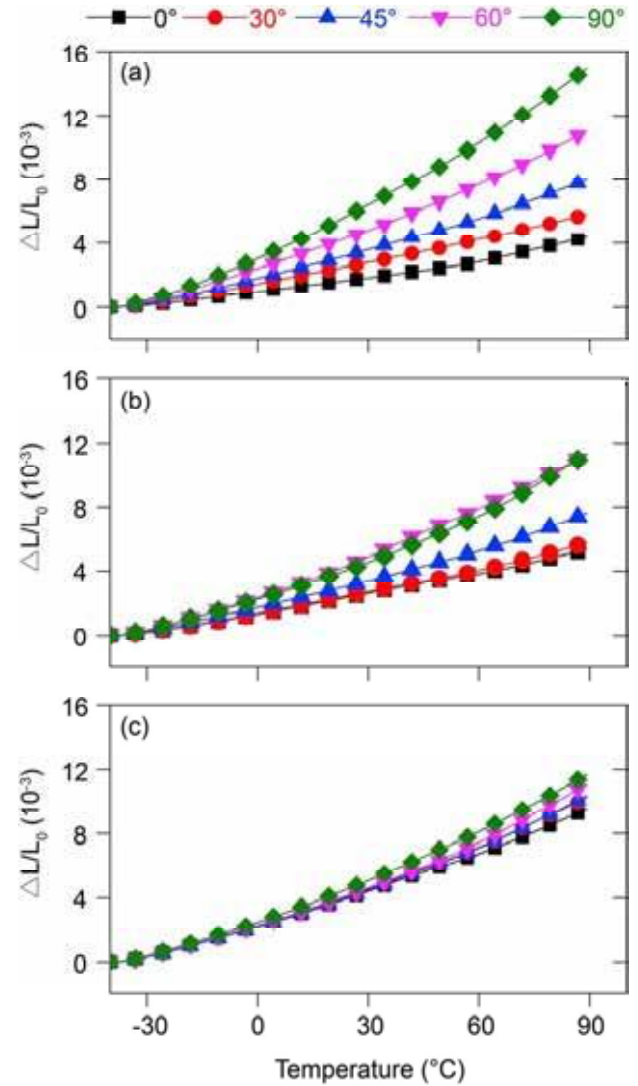


Fig. 10. Dimensional change of NFPCs at different orientation angles: (a) PW/HDPE, (b) RP/HDPE, and (c) RH/HDPE.

considerably decrease the composite LCTE [47]. These results further demonstrate that fiber orientation with specific L/D can lead to thermal expansion anisotropy for NFPCs.

4. Conclusions

NFPCs were prepared by extrusion using three types of NFs with different fiber geometries. The effect of fiber geometry and orientation distribution on the anisotropy of mechanical properties, creep behavior, and thermal expansion was investigated. The properties of NFPCs were highly depended on fiber L/D and orientation distribution. The NFPCs with NFs of higher L/D had higher flexural and impact strength regardless of NF orientation angle, but showed higher anisotropy of mechanical properties upon NF orientation angle. The NFPCs with on-axis oriented NFs exhibited the highest mechanical properties, creep resistance, and dimensional stability. These properties decreased with increasing NF off-axis angle. These results demonstrate that on-axis orientation of NFs with specific L/D could provide an effective strategy for reinforcing NFPCs.

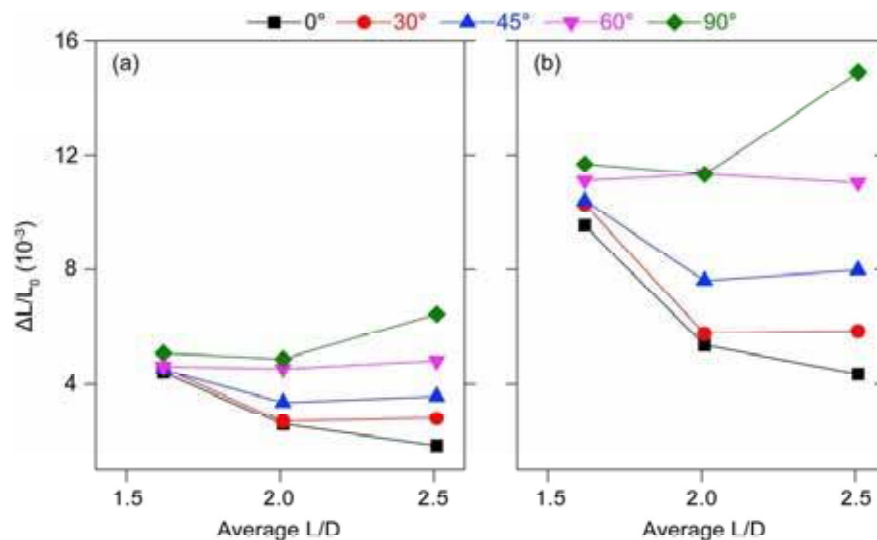


Fig. 11. Dimensional change of NFPCs varying with average L/D at different temperature: (a) 30 °C and (b) 90 °C.

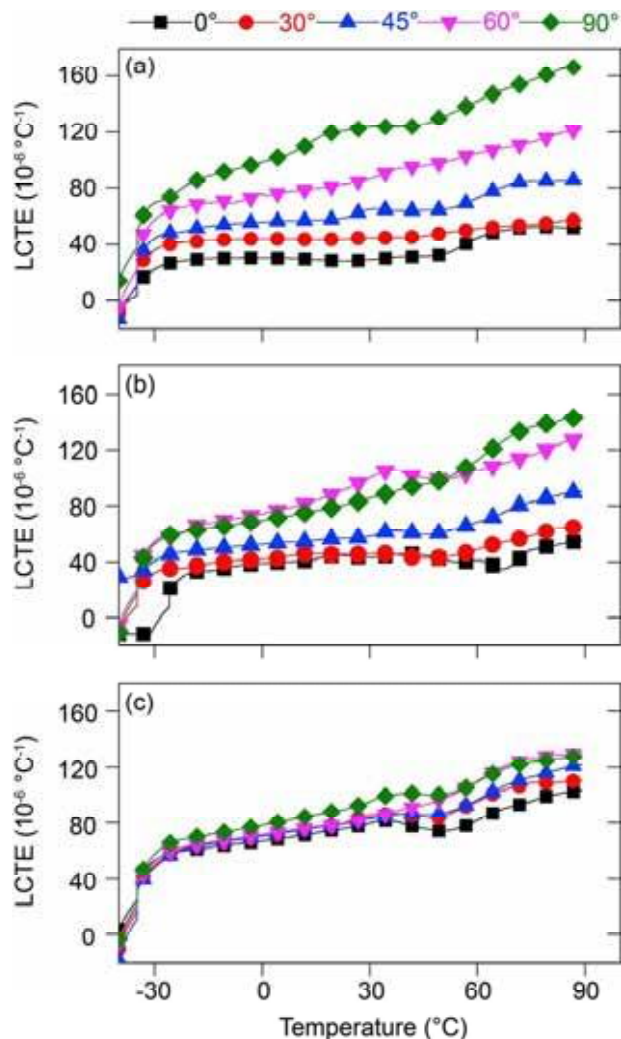


Fig. 12. Linear coefficient of thermal expansion (LCTE) of NFPCs at different orientation angles: (a) PW/HDPE, (b) RP/HDPE, and (c) RH/HDPE.

Declarations of competing interest

None.

Acknowledgments

This work was supported by the National Natural Science Foundation of China (Nos. 31870547, 31901251 and 31700494), the Project funded by China Postdoctoral Science Foundation (No. 2019M652919), the National Key Research and Development Program of China (Nos. 2019YFD1101203 and 2019YFD1101204), the Project of Guangzhou Municipal Key Laboratory of Woody Biomass Functional New Materials, China (No. 201905010005), and the Project of Key Disciplines of Forestry Engineering of Bureau of Education of Guangzhou Municipality, China.

References

- [1] Jeamtrakul S, Kositchaiyong A, Markpin T, Rosarpitak V, Sombatsompop N. Effects of wood constituents and content, and glass fiber reinforcement on wear behavior of wood/PVC composites. *Compos B Eng* 2012;43(7):2721–9.
- [2] Ayilimis N, Benthien JT, Thoemen H. Effects of formulation variables on surface properties of wood plastic composites. *Compos B Eng* 2012;43(2):325–31.
- [3] Li Y. Effect of coupling agent concentration, fiber content, and size on mechanical properties of wood/HDPE composites. *Int J Polym Mater* 2012;61(11):882–90.
- [4] Hietala M, Samuelsson E, Niinimäki J, Oksman K. The effect of pre-softened wood chips on wood fibre aspect ratio and mechanical properties of wood-polymer composites. Part A-Appl. S. 2011;42(12):2110–6.
- [5] Lau K-t, Hung P-y, Zhu M-H, Hui D. Properties of natural fibre composites for structural engineering applications. *Compos B Eng* 2018;136:222–33.
- [6] Migneault S, Koubaa A, Erchiqui F, Chaala A, Englund K, Wolcott MP. Effects of processing method and fiber size on the structure and properties of wood-plastic composites. *Compos. Part A-Appl S* 2009;40(1):80–5.
- [7] Siddikur Rahman K, Islam MN, Ratul SB, Dana NH, Musa SM, Hannan MO. Properties of flat-pressed wood plastic composites as a function of particle size and mixing ratio. *J Wood Sci* 2018;64(3):279–86.
- [8] Balla VK, Kare KH, Satyavolu J, Singh P, Tadimetri JGD. Additive manufacturing of natural fiber reinforced polymer composites: processing and prospects. *Compos B Eng* 2019;174:106956.
- [9] Elsabbagh A, Ramzy A, Steuernagel L, Ziegmann G. Models of flow behaviour and fibre distribution of injected moulded polypropylene reinforced with natural fibre composites. *Compos B Eng* 2019;162:198–205.
- [10] Migneault S, Koubaa A, Erchiqui F, Chaala A, Englund K, Wolcott MP. Application of micromechanical models to tensile properties of wood-plastic composites. *Wood Sci Technol* 2010;45(3):521–32.
- [11] Tanguy M, Bourmaud A, Beaugrand J, Gaudry T, Baley C. Polypropylene reinforcement with flax or jute fibre; Influence of microstructure and constituents properties on the performance of composite. *Compos B Eng* 2018;139:64–74.
- [12] Michaeli W, Menges G. Prediction of product properties in extrusion and injection molding. *Adv Polym Technol* 1989;9(1):69–85.

- [13] Hidalgo-Salazar MA, Salinas E. Mechanical, thermal, viscoelastic performance and product application of PP- rice husk Colombian biocomposites. *Compos B Eng* 2019;176:107135.
- [14] Guo G, Lee YH, Rizvi GM, Park CB. Influence of wood fiber size on extrusion foaming of wood fiber/HDPE composites. *J Appl Polym Sci* 2008;107(6):3505–11.
- [15] Chaudemanche S, Perrot A, Pimbert S, Lecompte T, Faure F. Properties of an industrial extruded HDPE-WPC: the effect of the size distribution of wood flour particles. *Constr Build Mater* 2018;162:543–52.
- [16] Ibrahim SB, Cheikh RB. Influence of fibre orientation and volume fraction on the tensile properties of unidirectional Alfa-polyester composite. *Compos Sci Technol* 2007;67(1):140–7.
- [17] Mu B, Wang H, Hao X, Wang Q. Morphology, mechanical properties and dimensional stability of Biomass particles/high density polyethylene composites: effect of species and composition. *Polymers* 2018;10(308):1–15.
- [18] Liu R, Peng Y, Cao J, Chen Y. Comparison on properties of lignocellulosic flour/polymer composites by using wood, cellulose, and lignin flours as fillers. *Compos Sci Technol* 2014;103:1–7.
- [19] Ou R, Xie Y, Wolcott MP, Yuan F, Wang Q. Effect of wood cell wall composition on the rheological properties of wood particle/high density polyethylene composites. *Compos Sci Technol* 2014;93:68–75.
- [20] Ou R, Xie Y, Wolcott MP, Sui S, Wang Q. Morphology, mechanical properties, and dimensional stability of Biomass particles/high density polyethylene composites: effect of removal of wood cell wall composition. *Mater Des* 2014;58:339–45.
- [21] Langhorst A, Paxton W, Bollin S, Frantz D, Burkholder J, Kiziltsa A, et al. Heat-treated blue agave fiber composites. *Compos B Eng* 2019;165:712–24.
- [22] Wechsler A, Molina J, Cayumil R, Núñez Decap M, Ballerini-Arroyo A. Some properties of composite panels manufactured from peach (*Prunus persica*) pits and polypropylene. *Compos B Eng* 2019;175:107152.
- [23] Leu S-Y, Yang T-H, Lo S-F, Yang T-H. Optimized material composition to improve the physical and mechanical properties of extruded wood-plastic composites (WPCs). *Constr Build Mater* 2012;29:120–7.
- [24] Siwek S, Oktavee J, Grasselt-Gille S, Wagenführ A. Influence of different wood flour fractions on the mechanical properties of injection molded WPC with cellulose propionate. *Eur. J. Wood Wood Prod.* 2017;76(2):499–507.
- [25] Ashori A, Nourbakhsh A. Reinforced polypropylene composites: effects of chemical compositions and particle size. *Bioresour Technol* 2010;101(7):2515–9.
- [26] Codou A, Misra M, Mohanty AK. Sustainable biocarbon reinforced nylon 6/ polypropylene compatibilized blends: effect of particle size and morphology on performance of the biocomposites. *Compos. Part A-Appl S* 2018;112:1–10.
- [27] Hao X, Zhou H, Xie Y, Mu H, Wang Q. Sandwich-structured wood flour/HDPE composite panels: reinforcement using a linear low-density polyethylene core layer. *Constr Build Mater* 2018;164:489–96.
- [28] Cen-Puc M, Oliva-Avilés AI, Avilés F. Thermoresistive mechanisms of carbon nanotube/polymer composites. *Physica E* 2018;95:41–50.
- [29] Balasuriya PW, Ye L, Mai YW. Mechanical properties of wood flake-polyethylene composites. Part I: effects of processing methods and matrix melt flow behaviour. *Compos. Part A-Appl S* 2001;32(5):619–29.
- [30] Gibson RF. Principles of composite material mechanics. Crc Press; 2011.
- [31] Baghaei B, Skrifvars M, Salehi M, Bashir T, Rissanen M, Nousiainen P. Novel aligned hemp fibre reinforcement for structural biocomposites: porosity, water absorption, mechanical performances and viscoelastic behaviour. *Compos. Part A-Appl S* 2014;61:1–12.
- [32] Ou R, Hui Z, Sui S, Song Y, Wang Q. Reinforcing effects of Kevlar fiber on the mechanical properties of wood-flour/high-density-polyethylene composites. *Compos. Part A-Appl S* 2010;41(9):1272–8.
- [33] López JP, Gironès J, Mendez JA, Pèlach MA, Vilaseca F, Mutjé P. Impact and flexural properties of stone-ground wood pulp-reinforced polypropylene composites. *Polym Compos* 2013;34(6):842–8.
- [34] Hung KC, Wu TL, Chen YL, Wu JH. Assessing the effect of wood acetylation on mechanical properties and extended creep behavior of wood/recycled-polypropylene composites. *Constr Build Mater* 2016;108:139–45.
- [35] Yang T-C, Wu T-L, Hung K-C, Chen Y-L, Wu J-H. Mechanical properties and extended creep behavior of bamboo fiber reinforced recycled poly(lactic acid) composites using the time-temperature superposition principle. *Constr Build Mater* 2015;93:558–63.
- [36] Yahyaiei-Moayyed M, Taheri F. Experimental and computational investigations into creep response of AFRP reinforced timber beams. *Compos Struct* 2011;93(2): 616–28.
- [37] Emara M, Torres I, Baena M, Barris C, Moawad M. Effect of sustained loading and environmental conditions on the creep behavior of an epoxy adhesive for concrete structures strengthened with CFRP laminates. *Compos B Eng* 2017;129:88–96.
- [38] Georgiopoulos P, Kontou E, Christopoulos A. Short-term creep behavior of a biodegradable polymer reinforced with wood-fibers. *Compos B Eng* 2015;80: 134–44.
- [39] Hao X, Zhou H, Xie Y, Xiao Z, Wang H, Wang Q. Mechanical reinforcement and creep resistance of coextruded wood flour/polyethylene composites by shell-layer treatment with nano- and micro-SiO₂ particles. *Polym Compos* 2018;157:6–84.
- [40] Durante M, Formisano A, Boccarusso L, Langella A, Carrino L. Creep behaviour of polylactic acid reinforced by woven hemp fabric. *Compos B Eng* 2017;124:16–22.
- [41] Yang JL, Zhang Z, Schlarb AK, Friedrich K. On the characterization of tensile creep resistance of polyamide 66 nanocomposites. Part I. Experimental results and general discussions. *Polymer* 2006;47(8):2791–801.
- [42] Hao X, Yi X, Sun L, Tu D, Wang Q, Ou R. Mechanical properties, creep resistance, and dimensional stability of core/shell structured wood flour/polyethylene composites with highly filled core layer. *Constr Build Mater* 2019;226:879–87.
- [43] Nakagaito AN, Yano H. The effect of fiber content on the mechanical and thermal expansion properties of biocomposites based on microfibrillated cellulose. *Cellulose* 2008;15(4):555–9.
- [44] Takenaka K, Ichigo M, Takenaka K, Ichigo M. Thermal expansion adjustable polymer matrix composites with giant negative thermal expansion filler. *Compos Sci Technol* 2014;104:47–51.
- [45] Wu Q, Chi K, Wu Y, Lee S. Mechanical, thermal expansion, and flammability properties of co-extruded wood polymer composites with basalt fiber reinforced shells. *Mater Des* 2014;60:334–42.
- [46] Takezawa A, Kobashi M, Takezawa A, Kobashi M. Design methodology for porous composites with tunable thermal expansion produced by multi-material topology optimization and additive manufacturing. *Compos B Eng* 2018;131:21–9.
- [47] Ren L, Pashayi K, Fard HR, Kotha SP, Borca-Tasciuc T, Ozisik R. Engineering the coefficient of thermal expansion and thermal conductivity of polymers filled with high aspect ratio silica nanofibers. *Compos B Eng* 2014;58(1):228–34.



RESEARCH ARTICLE



Polymer
COMPOSITES

WILEY

Comparative study on the effects of silica size and dispersion mode on the fire retardancy of extruded wood fiber/HDPE composites

Haiyang Zhou^{1,2} | Xiaolong Hao^{1,2} | Xiaoyu Wang³ | Tao Liu^{1,2} |
Lichao Sun^{1,2} | Xin Yi^{1,2} | Qingwen Wang^{1,2} | Rongxian Ou^{1,2}

¹Guangdong Laboratory for Lingnan Modern Agricultural Science and Technology, South China Agricultural University, Guangzhou, China

²Key Laboratory for Biobased Materials and Energy of Ministry of Education, College of Materials and Energy, South China Agricultural University, Guangzhou, China

³College of Arts, South China Agricultural University, Guangzhou, China

Correspondence

Qingwen Wang and Rongxian Ou, Key Laboratory for Biobased Materials and Energy of Ministry of Education, College of Materials and Energy, South China Agricultural University, 483 Wushan Road, Guangzhou 510642, China.
Email: qwwang@scau.edu.cn (Q. W.) and rongxian_ou@scau.edu.cn (R. O.)

Funding information

Project of Key Disciplines of Forestry Engineering of Bureau of Education of Guangzhou Municipality; Guangdong Forestry Science and Technology Innovation Project, Grant/Award Number: 2020KJCX008; National Key Research and Development Program of China, Grant/Award Number: 2019YFD1101204; National Natural Science Foundation of China, Grant/Award Number: 31901251; Project of Guangzhou Municipal Key Laboratory of Woody Biomass Functional New Materials, Grant/Award Number: 201905010005

Abstract

The inflammability of wood fiber/high-density polyethylene composites (WPCs/HDPE) remains a limitation for its application. Here the authors sought to improve the flame retardancy of WPCs by incorporating uniformly dispersed SiO₂. Specifically, micron- and nano-SiO₂ were incorporated into HDPE via dry blending (dry dispersion) or solution blending (wet dispersion), to prepare the compounded matrices for the WPCs. The effects of SiO₂ size and dispersion mode on the thermal stability and fire retardancy of WPCs were investigated. The results indicated that the nano-SiO₂ was more beneficial to improve the thermal stability of WPCs than the micron-SiO₂, especially incorporating via wet dispersion. The cone calorimetry tests revealed that incorporating 9 wt% micron-SiO₂ slightly decreased the heat release and smoke production of the WPCs. The incorporation of nano-SiO₂ in WPCs showed a moderate reduction in the heat release, while slightly increased the smoke production. The wet dispersion presented minor advantage over dry dispersion in improving the flame retardancy of WPCs. In addition, the dynamic thermal-mechanical analysis revealed that the WPCs containing wet-dispersed micron- or nano-SiO₂ exhibited a higher storage modulus compared to that dry-dispersed SiO₂.

KEYWORDS

dispersion, fire retardancy, SiO₂, storage modulus, thermal stability, wood plastic composites

1 | INTRODUCTION

Wood fiber (WF) is often employed as a reinforcer in composites due to its high rigidity, biodegradability, renewability, and low cost.^[1–3] The incorporation of WF in polymer results in wood-polymer composites (WPCs), which are environmentally friendly materials that have been widely used in building materials, logistics packaging, and decorative materials.^[4,5] However, both the WF and polymer in WPCs are flammable, thus posing a fire risk that extremely limits its application.^[6,7]

Many efforts have been implemented to reduce the flammability of WPCs.^[8] The incorporation of 30 wt% ammonium polyphosphate (APP) was found to result in the reduction of the peak heat release rate (PHRR) of WF/HDPE composites by 27.1%, and the flexural strength was found to decrease by 20.0% due to the agglomeration of APP.^[6] The total smoke production (TSP) of WF/polyvinyl chloride composites containing 6 wt% micron-scale zinc borate was 55.2% lower than the unfilled control, and the tensile and flexural strength was 19.9% and 8.5% lower, respectively.^[9] The incorporation of 25 wt% expandable graphite into WF/HDPE reduced the PHRR and total heat release (THR) by 74.3% and 56.8%, respectively, and the tensile and impact strength decreased by 18.0% and 15.3%, respectively.^[10] In these studies, higher loading of flame retardants was required for efficiently fire retardancy due to their insufficient dispersity, while the high load of flame retardant can result in the cost increase and the loss of mechanical properties of WPCs.

SiO₂ is a potential fire retardant that can improve the mechanical properties, fire retardancy, and thermal stability of polymers and WFs.^[11–13] For instance, the addition of 36 wt% amino-functionalized nano-SiO₂ (20 nm) was found to increase the flexural modulus of epoxy by 50.0% and double its toughness, as well as delay the ignition time due to the physical shielding of nano-SiO₂.^[14] Compared with the nonfilled HDPE, the elastic modulus of the HDPE filled with 8 wt% organic modified nano-SiO₂ (12 nm) increased by 46%, and the PHRR decreased by 35.9%. The maximum degradation temperature of HDPE increased by 92.0°C after incorporating 8 wt% organic-SiO₂.^[15] Coating nano-SiO₂ on the surface of wood-derived fiber was found to increase Young's modulus and prolong the fiber fracture time during combustion.^[16] In the authors' previous studies, the incorporation of 9 wt% well-dispersed nano-SiO₂ increased the tensile and flexural strength of the WPCs by 12.5% and 16.7%, respectively. In addition, the incorporating of well-dispersed micron-SiO₂ decreased the tensile and flexural strength by 21.8% and 9.9%, respectively.^[17] There remains a lack of research on the

effect of nano- and micron-SiO₂ and their dispersion on the thermal stability and fire retardancy of WPCs.

The key challenge in preparing SiO₂ fire retardant WPCs is to address the dispersion of SiO₂ in the matrix. In this study, micron- and nano-size SiO₂ were dispersed in ethanol solution, respectively. Vinyl trimethoxy silane (VTS) and dicumyl peroxide (DCP) were used to enhance the dispersity of SiO₂ and to improve the interfacial bonding between SiO₂ and HDPE. Maleic anhydride-grafted polyethylene (MAPE) was used to improve the compatibility between HDPE and WF. The thermal stability, fire retardancy, and storage modulus of the resulting WPCs were compared with those of WPCs directly filled with SiO₂ in the dry state.

2 | EXPERIMENTAL

2.1 | Materials

High-density polyethylene (HDPE) granules (density 0.954 g/cm³, melt flow index 0.9 g/10 minutes) were obtained from Petrochemical Co., Ltd. (Daqing, China). The granules were ground into powder (200 µm) using a grinder (SMP-200; Song Ben Plastic Machinery Co., Ltd., Zhangjiagang, China). Dry poplar WF (*Populus adenopoda* Maxim) (moisture content <3%) with lengths of 200 to 400 µm (the length to diameter ratio was 4.5) was prepared in-house. MAPE pellets with the grafting ratio 0.9 wt% and the melt flow index 1.9 g/10 minutes were obtained from Hecheng Chemical Co., Ltd. (Guangzhou, China). Stearic acid and polyethylene wax at a mass ratio of 1:1 were used as a compounded lubricant that obtained from Adisi Co., Ltd. (Nanjing, China). SiO₂ with average diameters of approximately 5 µm and 12 nm was obtained from Mengtaihu Industrial Co., Ltd. (Shanghai, China); the nano-SiO₂ was white and the micron-SiO₂ was gray in color. Dicumyl peroxide (DCP) was supplied by the Guangfu Fine Chemical Research Institute (Tianjin, China). VTS was supplied by Chi Ye Silicone Co., Ltd. (Shanghai, China). The ethanol solution (ethanol/water = 95/5 in volume) was created with commercial products of analytical grade.

2.2 | Dispersion of SiO₂ in the HDPE

2.2.1 | Dispersion by the direct compounding method (dry dispersion)

The HDPE powder and micron- or nano-SiO₂ particles were compounded using a low-speed blender at room

temperature for 8 minutes (SHR-50A, Huaming Machinery Company, Zhangjiagang, China). Subsequently, the premixture underwent melt blending in a corotating twin-screw extruder (SH30, Nanjing Rubber Machinery Corp., China) at a temperature from 145°C to 165°C. The extrudate was cut into pellets as the matrix for the preparation of WPCs filled with untreated SiO₂ in the subsequent step.

2.2.2 | Dispersion by the solution compounding method (wet dispersion)

A calculated amount of VTS (Table 1) was added to a blended solvent (ethanol/water = 95/5 in volume) and vigorously stirred for 1 hour through a specially-designed conical mixing head.^[17] After that, the micron- or nano-SiO₂ was slowly added into the solution and continuously stirred for 7 hours. Subsequently, the HDPE powder and DCP were poured into the suspension under continuous stirring. Finally, the ethanol in the suspension was volatilization in a fume hood for 12 hours and then dehydrated in a vacuum oven at 50°C. The dried product was melt-compounded in the twin-screw extruder at a temperature range of 145°C to 165°C (Figure 1). The extrudate was pelletized as the matrix for the WPCs filled with VTS-treated SiO₂.

2.3 | Preparation of WPC specimens

Appropriate amounts (Table 1) of HDPE filled with untreated SiO₂ (dry dispersion) or VTS-treated SiO₂ (wet dispersion) were, respectively, compounded with WF, MAPE pellets, and lubricant using a high-speed mixer for 8 minutes. The mixture was fed into a corotating twin-screw extruder for melt blending at temperatures from

155°C to 175°C. The extrudate was pelletized and subsequently added into a single-screw extruder (SJ-45, Nanjing Rubber Machinery Factory, China) to produce a continuous WPC band measuring 4 × 40 mm² (thickness × width). The WPCs filled with nano- and micron-SiO₂ via dry dispersion were denoted as C_{nS} and C_{mS}, respectively. The WPCs filled with nano- and micron-SiO₂ via wet dispersion were denoted as C_{TnS} and C_{TmS}, respectively.

2.4 | Characterizations

A scanning electron microscope (SEM) (FEI QuanTa200, FEI Co, Hillsboro, Oregon) coupled with an energy-dispersive X-ray spectrometer (EDX) was employed to

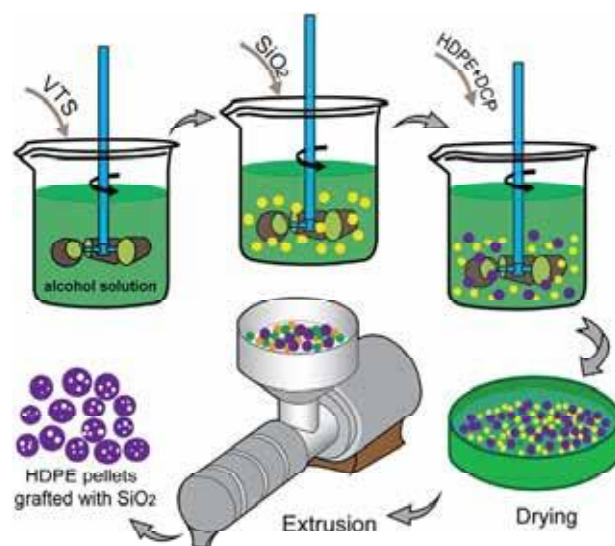


FIGURE 1 Schematic of the fabrication process of SiO₂ modified high-density polyethylene (HDPE) via wet dispersion [Color figure can be viewed at wileyonlinelibrary.com]

TABLE 1 Formulation of WPC filled with various contents of nano-SiO₂ (wt%)

Sample ^a	WF	HDPE	MAPE	Lubricant	Nano-SiO ₂	DCP ^b	VTS ^c
C _{CTRL}	55	40	3	2	0	—	—
C _{nS1}	55	40	3	2	1	—	—
C _{nS5}	55	40	3	2	5	—	—
C _{nS9}	55	40	3	2	9	—	—
C _{TnS1}	55	40	3	2	1	0.04	0.01
C _{TnS5}	55	40	3	2	5	0.04	0.05
C _{TnS9}	55	40	3	2	9	0.04	0.09

Abbreviations: DCP, dicumyl peroxide; HDPE, high-density polyethylene; MAPE, maleic anhydride-grafted polyethylene; WF, wool fiber; WPC, wood-polymer composite; VTS, vinyl trimethoxy silane.

^aThe number behind the subscript nS or TnS identify the SiO₂ content.

^bThe weight ratio of DCP to HDPE is 1:1000.

^cThe weight ratio of VTS to SiO₂ is 1:100.

observe the morphologies of the original micron-SiO₂ and the fractured surfaces of the WPC samples at an accelerating voltage of 12.5 kV. Transmission electron microscopy (TEM) was performed on a JEM-2100 microscope (JEOL, Tokyo, Japan) at a 200-kV accelerating voltage to observe the nano-SiO₂.

Torque rheological analysis was carried out with a torque rheometer (HAAKE PolyLab OS, Thermo Fisher Scientific). Tests were run at 165°C and 100 rpm, and the feeding volume was 75%. Three repetitions were completed for each group.

Thermogravimetric (TG) analysis was conducted on a PerkinElmer Pyris 6 TGA. The test samples (10 mg) were placed in vitreous SiO₂ pans, and then heated from 40°C to 600°C at a heating rate of 10°C·min⁻¹ under a high-purity nitrogen atmosphere with a 20 mL min⁻¹ flow rate. All measurements were performed in triplicate, and the average values were used as the results.

Cone calorimeter (CONE) (Fire Testing Technology, Ltd., East Grinstead, UK) testing was conducted to investigate the combustion of WPC samples (100 × 100 × 3.5 mm³) according to the ISO 5660-1 standard under a heat flux of 50 kW m⁻². The parameters of the heat release rate (HRR), THR, smoke production rate (SPR), TSP, and residual mass were analyzed. All measurements were conducted in triplicate. The appearances of the residuals after combustion were obtained by digital camera. The morphologies of the char layers were observed via SEM.

The dynamic thermomechanical analysis (DMA) tests were conducted using a dynamic mechanical analyzer (Q800; TA Instruments Inc., New Castle, Delaware). The sample dimension was 35 × 12 × 3.5 mm³. Tests were performed using single-cantilever strain-controlled mode with an oscillating amplitude of 15 μm and a frequency

of 1 Hz. The temperature was swept from -10°C to 130°C at a heating rate of 3°C·min⁻¹. The average data from triplicate measurements were used as results.

3 | RESULTS AND DISCUSSION

3.1 | Morphological analysis

The micron-SiO₂ particles exhibited spherical morphologies with diameters ranging from 1 to 10 μm (Figure 2A). Some microspheres were agglomerated and formed larger clusters as a result of the electrostatic force.^[18] The SEM image of the fractured WPCs showed that the micron-SiO₂ incorporated via dry dispersion were agglomerated in the WPCs and divorced from the HDPE matrix (Figure 2B). The high-magnification image showed that the de-bonded micron-SiO₂ exhibited a smooth surface, indicating a weak interfacial bonding between micron-SiO₂ and the HDPE (Figure 2C). Conversely, the VTS-treated micron-SiO₂ via wet dispersion exhibited relatively homogeneous dispersion in the WPCs (Figure 2D). Moreover, the failure mainly appeared at the HDPE matrix rather than at the borderline between the micron-SiO₂ and HDPE (Figure 2E), suggesting a strong interfacial interaction between wet-dispersed micron-SiO₂ and HDPE.

The diameter of the nano-SiO₂ was 10 to 15 nm, and it also aggregated into clusters, as observed by TEM (Figure 2F). The nano-SiO₂ was too small to be distinguished clearly from the other components in the WPCs, even at a high magnification (Figure 2G,H). The WPCs filled with nano-SiO₂ via wet dispersion presented brittle fracture relative to that via dry dispersion due to the formation of covalent cross-linking between the nano-SiO₂ and

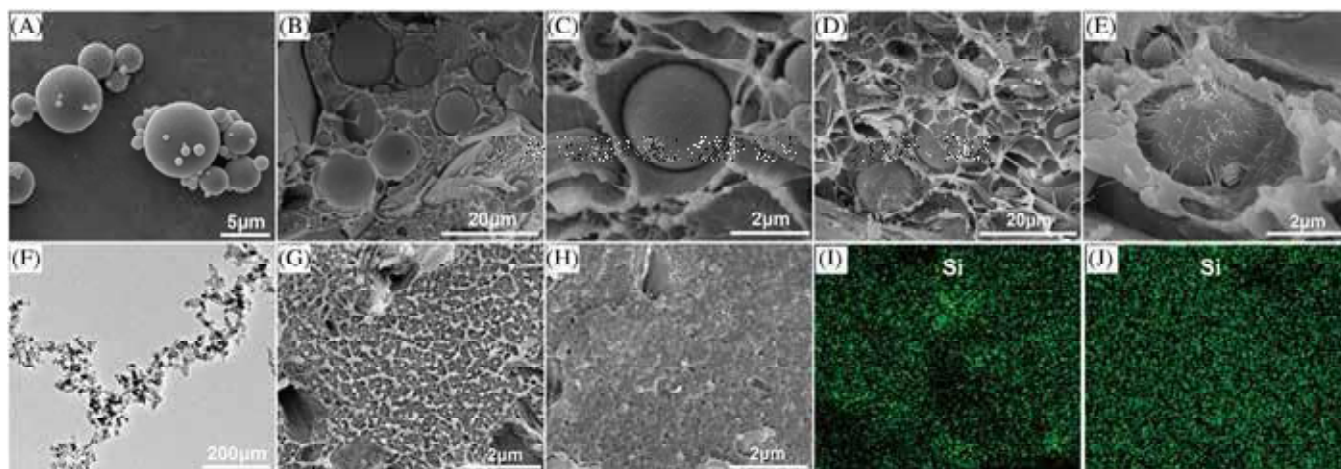


FIGURE 2 Micrographs of micron-SiO₂ (A, ×5000); 9% micron-SiO₂ filled WPCs via dry dispersion (B, ×2000; C, ×10 000); 9% micron-SiO₂ filled WPCs via wet dispersion (D, ×2000; E, ×10 000); micrographs of nano-SiO₂ (F, ×100 000); 9% nano-SiO₂ filled WPCs via dry dispersion (G, ×10 000), 9% nano-SiO₂ filled WPCs via wet dispersion (H, ×10 000); EDX elemental mapping analysis of 9% nano-SiO₂ filled WPCs via dry dispersion, I and wet dispersion, J, respectively [Color figure can be viewed at wileyonlinelibrary.com]

HDPE (Figure 2G,H). EDX was employed to analyze the distribution of nano-SiO₂. It was found that wet-dispersed nano-SiO₂ was more uniform in the WPCs than that via dry dispersion (Figure 2I,J).

The coupling mechanism between the treated micron-SiO₂ and HDPE was the occurrence of radical reactions. Specifically, VTS hydrolysis generated three highly active silanol groups that condensed with —Si—OH on the nano-SiO₂ surface (Figure 3), resulting in strong —Si—O—Si— bonds; thus, the —C=C— bonds from the VTS were present on the micron-SiO₂ surface.^[19] The —C=C— on the micron-SiO₂ surface and the C—H from HDPE were broken by DCP to form C—C and C· radicals under the high temperature and shear force in the twin-screw extruder; the radicals combined together

to form C—C covalent bonds. As a result, VTS-treated SiO₂ and HDPE were connected by covalent bonds. This reaction has been proven in the authors' previous study.^[17]

3.2 | Torque rheological analysis

Compared with the unfilled WPCs, the incorporation of 1% and 5% micron-SiO₂ via dry dispersion had no significant effect on the equilibrium torque and temperature of WPCs, while they slightly decreased at the micron-SiO₂ content of 9% (Figure 4A). This was because the spherical micron-SiO₂ as a lubricant reduced the interfacial friction between HDPE chains. By contrast, an increased

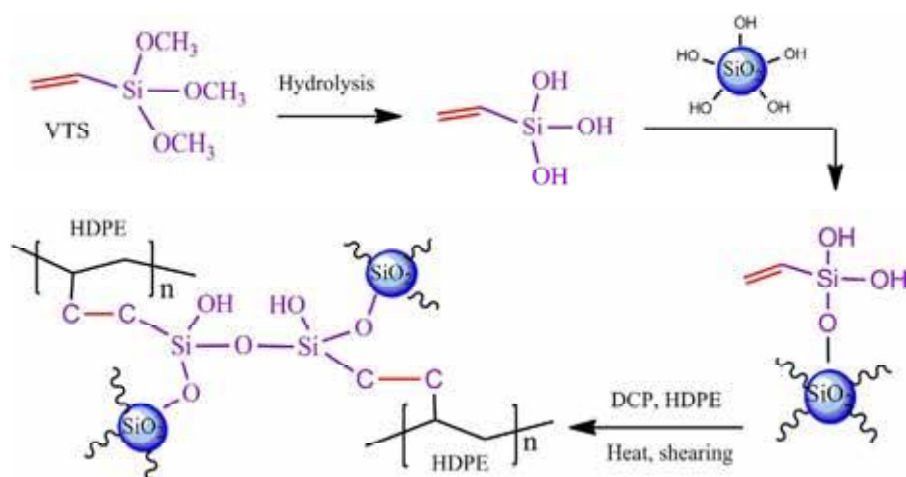


FIGURE 3 The reaction process between VTS-treated SiO₂ and high-density polyethylene (HDPE) [Color figure can be viewed at wileyonlinelibrary.com]

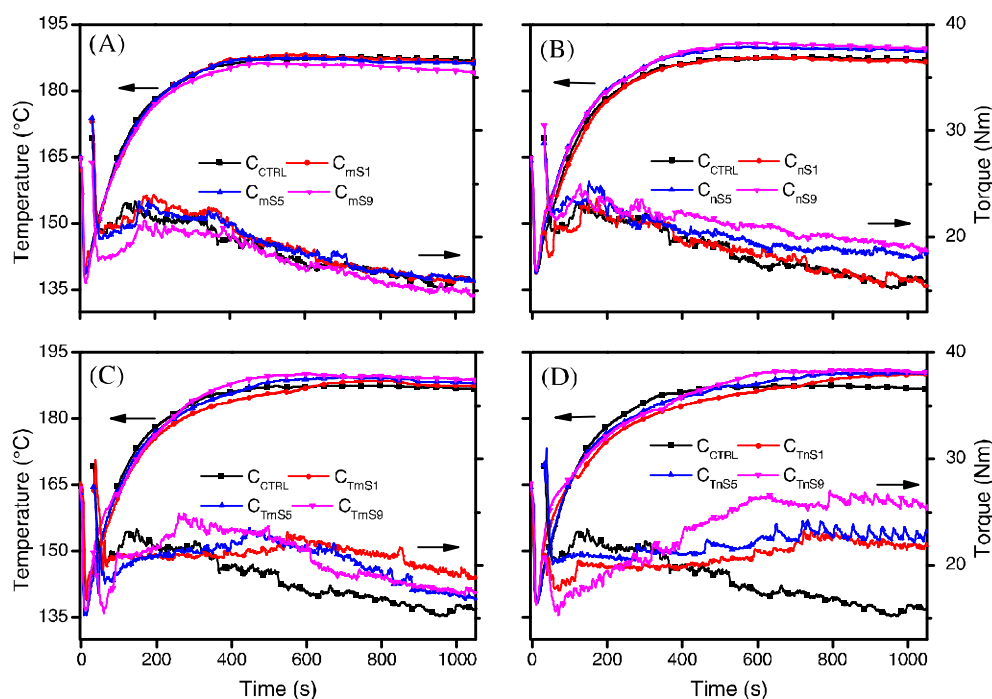
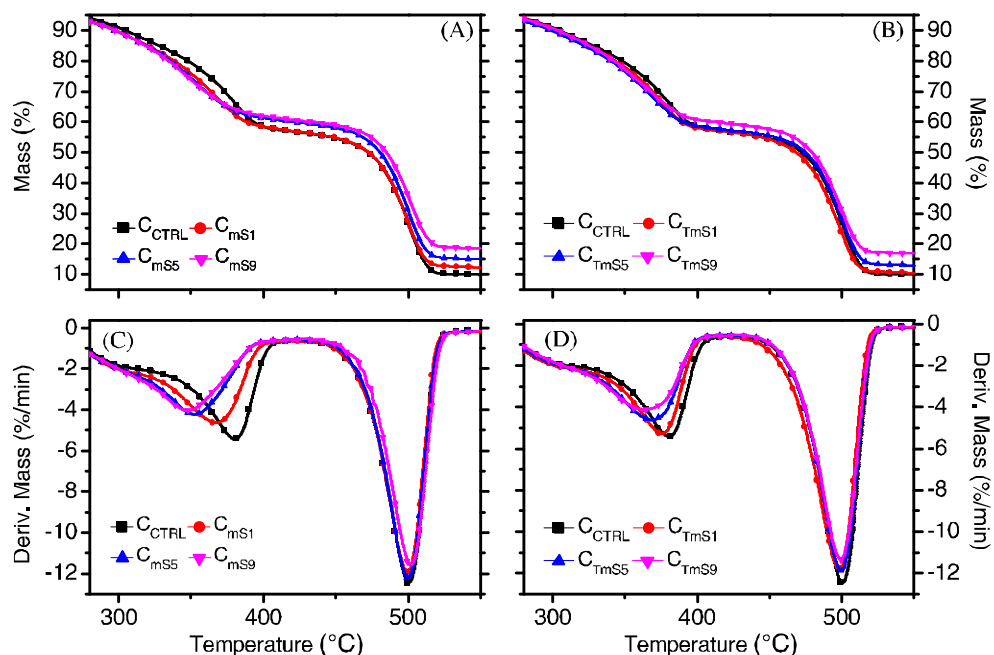


FIGURE 4 Torque rheological of wood-polymer composite (WPCs) filled with SiO₂: micron-SiO₂ filled WPCs via dry dispersion, A; nano-SiO₂ filled WPCs via dry dispersion, B; micron-SiO₂ filled WPCs via wet dispersion, C; nano-SiO₂ filled WPCs via wet dispersion, D [Color figure can be viewed at wileyonlinelibrary.com]

FIGURE 5 TG, A and DTG, C curves of micron-SiO₂ filled WPCs via dry dispersion; TG, B and DTG, D curves of micron-SiO₂ filled WPCs via wet dispersion [Color figure can be viewed at wileyonlinelibrary.com]



equilibrium temperature and torque were achieved after adding nano-SiO₂ into the WPCs via dry dispersion, which was ascribed to the nano-SiO₂ restraining the mobility of the HDPE chains (Figure 4B).^[20]

Compared with the dry-dispersed micron-SiO₂, wet-dispersed and VTS-treated micron-SiO₂ improved the equilibrium torque and temperature of the resulting WPCs (Figure 4C). This was because the covalent bonding between the micron-SiO₂ and HDPE increased the melting viscosities of the final WPCs. Compared with the unfilled WPCs, the fusion torques of the WPCs filled with nano-SiO₂ via wet dispersion increased with the prolonged time (Figure 4D), demonstrating the additional occurrence of cross-linking reactions between the nano-SiO₂ and HDPE under the high temperature and shear stress. Compared to the micron-SiO₂, the incorporation of nano-SiO₂ into the WPCs via wet dispersion caused a higher equilibrium temperature and torque (Figure 4C, D). This was because there were more cross-linking sites between nano-SiO₂ and HDPE as compared with the micron-SiO₂ due to the nanometer effect.

3.3 | Thermal stability

The thermal degradation of the WPCs was divided into two stages. The first stage mainly corresponded to the decomposition of WF (ca. 350°C), and the second stage mainly corresponded to the degradation of HDPE (ca. 500°C).^[21] The unfilled WPC exhibited a residual yield of 8.90%. The residual of WPCs filled with micron-SiO₂ increased with the incremental micron-SiO₂ content, and

TABLE 2 TG data of WPC filled with micron- or nano-SiO₂

Sample code	First mass loss stage		Second mass loss stage	
	T _{peak1} (°C)	Peak mass loss rate (mg/°C)	T _{peak2} (°C)	Peak mass loss rate (mg/°C)
C _{CTRL}	380.12	5.43	500.43	12.48
C _{mS1}	367.81	4.63	499.05	12.00
C _{mS5}	352.17	4.24	499.72	12.20
C _{mS9}	347.73	4.04	501.57	11.60
C _{TmS1}	375.33	5.27	497.70	11.82
C _{TmS5}	368.24	4.63	499.89	11.88
C _{TmS9}	363.68	4.12	499.09	11.35
C _{nS1}	381.83	5.34	501.27	11.99
C _{nS5}	379.23	5.23	502.54	10.99
C _{nS9}	379.57	5.13	505.66	10.05
C _{TnS1}	378.94	5.30	502.32	11.97
C _{TnS5}	377.79	5.20	506.24	10.43
C _{TnS9}	380.93	4.86	507.04	9.92

Note: T_{peak1} and T_{peak2} represent the temperature corresponding to the maximum decomposition rate of wood flour and HDPE, respectively.

Abbreviations: HDPE, high-density polyethylene; TG, thermogravimetric; WPC, wood-polymer composite.

the increments mainly came from the amount of micron-SiO₂ loading (Figure 5A,B). The incorporation of micron-SiO₂ via dry dispersion resulted in the accelerated

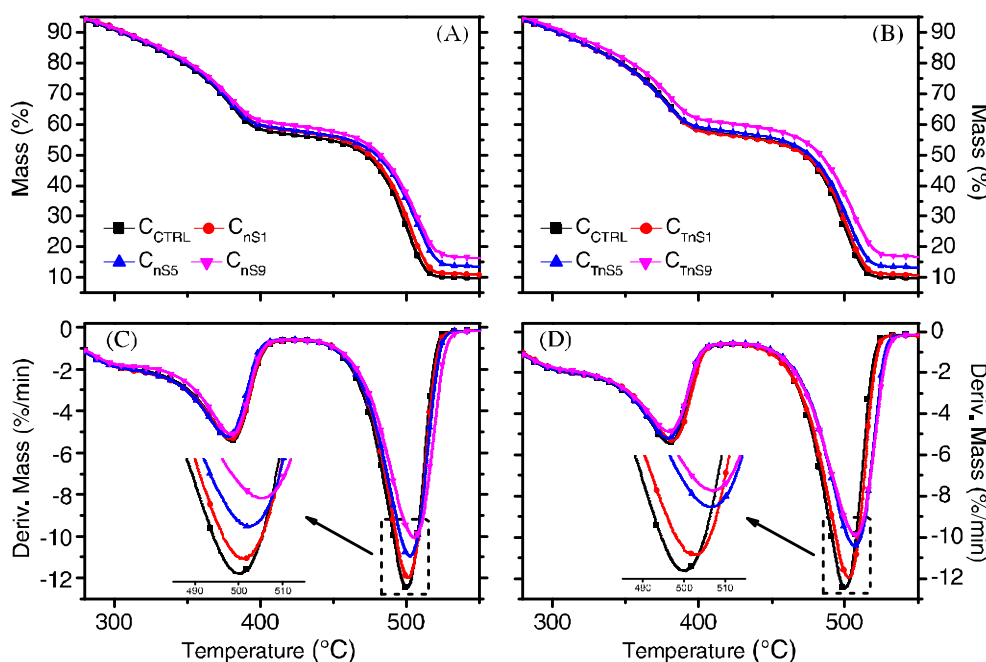


FIGURE 6 TG, A and DTG, C curves of nano-SiO₂ filled WPCs via dry dispersion; TG, B and DTG, D curves of nano-SiO₂ filled WPCs via wet dispersion [Color figure can be viewed at wileyonlinelibrary.com]

degraded of WF, as evidenced by the decrease in the peak temperature of WF degradation (Figure 5C and Table 2). This may have been due to the higher thermal conductivity of micron-SiO₂ (1.31 W/m·K) facilitated the heat transfer in WPCs.^[22] Additionally, adding micron-SiO₂ into WPCs via dry dispersion disturbed the continuity of the HDPE matrix, thus reducing the protection of HDPE on the WF.^[23] Analogously, the degradation temperature of WF in the WPCs decreased when micron-SiO₂ was incorporated via wet dispersion (Figure 5D and Table 2), but the decrement was lower than that via dry dispersion. This may be because the uniform dispersion and well interfacial bonding of micron-SiO₂ in HDPE slightly improved the viscosity of the WPCs (Figure 4C), and therefore delayed the degradation of WF compared to dry dispersion. The maximum mass loss rates of WPCs decreased with the increase of micron-SiO₂ (Figure 5C,D) because the highly thermally-stable micron-SiO₂ reduced the degradation kinetics of the WPCs.^[24]

The residual masses of WPCs filled with nano-SiO₂ via dry and wet dispersion were higher than that of the unfilled WPCs, and the increments mainly resulted from the amount of nano-SiO₂ loading (Figure 6A,B). Compared with the micron-SiO₂, the nano-SiO₂ had unnoticeable effect on the degradation process of WF in WPCs (Figure 6C,D), while it increased the peak temperatures of HDPE degradation. By incorporating 9 wt% nano-SiO₂ via dry and wet dispersion, the degradation temperatures of HDPE increased by 5.23°C and 6.61°C, respectively (Table 2), indicating the improvements in thermal stability of the WPCs. This was because the nano-SiO₂ was more dominant than micron-SiO₂ in

restricting the thermal mobility of HDPE chains as a result of its nano-size.^[25] The maximum mass loss rates of HDPE degradation decreased with the increase of nano-SiO₂ due to the fact that the highly thermally-stable nano-SiO₂ exerted shielding effect (Figure 6C,D).

3.4 | Combustion characteristics

During the early stage of combustion, a protective char from the charred WF was formed on the unfilled WPCs surface, which reduced the HRR, as demonstrated by a shoulder at approximately 90 seconds in the HRR curve (Figure 7A). Then this protection broke down, and resulted in an increase of the HRR, which reached a PHRR of 451 kW/m². The incorporation of 1 and 5 wt% SiO₂ showed no significant effect on the heat and smoke release of WPCs and thus are not presented here. Compared with that of the unfilled WPCs, the PHRR of the WPCs filled with 9% micron-SiO₂ via dry and wet dispersion decreased by 14.7% and 17.1%, respectively, and the THR decreased by 14.2% and 16.3%, respectively (Figure 7A,C and Table 3). This was due to the shielding effect of noncombustible micron-SiO₂ on the substance. The advantages of wet dispersion over dry dispersion in reducing HRR and THR were attributed to the increased viscosity of the WPCs by wet dispersion (Figure 4C).^[26]

Compared with micron-SiO₂-filled WPCs, the HRR curves of the WPCs filled with nano-SiO₂ tended to flatten (Figure 7B,D), indicating that the heat release was evenly distributed with time and no instantaneous heat release during the combustion process, which was

FIGURE 7 Heat release rate (HRR) of the micron-, A and nano-SiO₂, B filled WPCs via dry and wet dispersion; total heat release (THR) of the micron-, C and nano-SiO₂, D filled WPCs via dry and wet dispersion [Color figure can be viewed at wileyonlinelibrary.com]

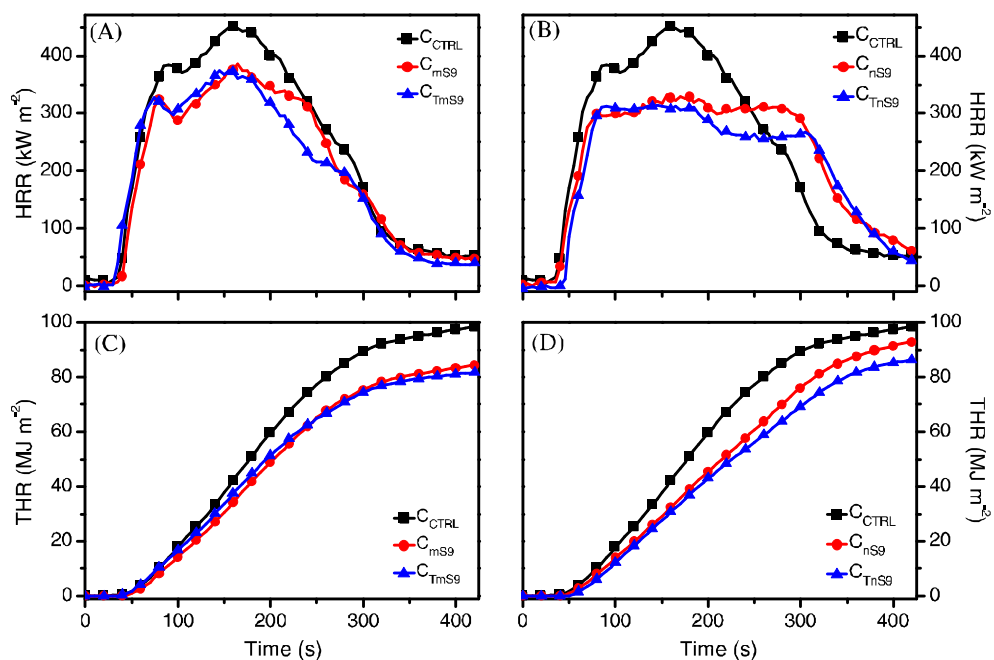
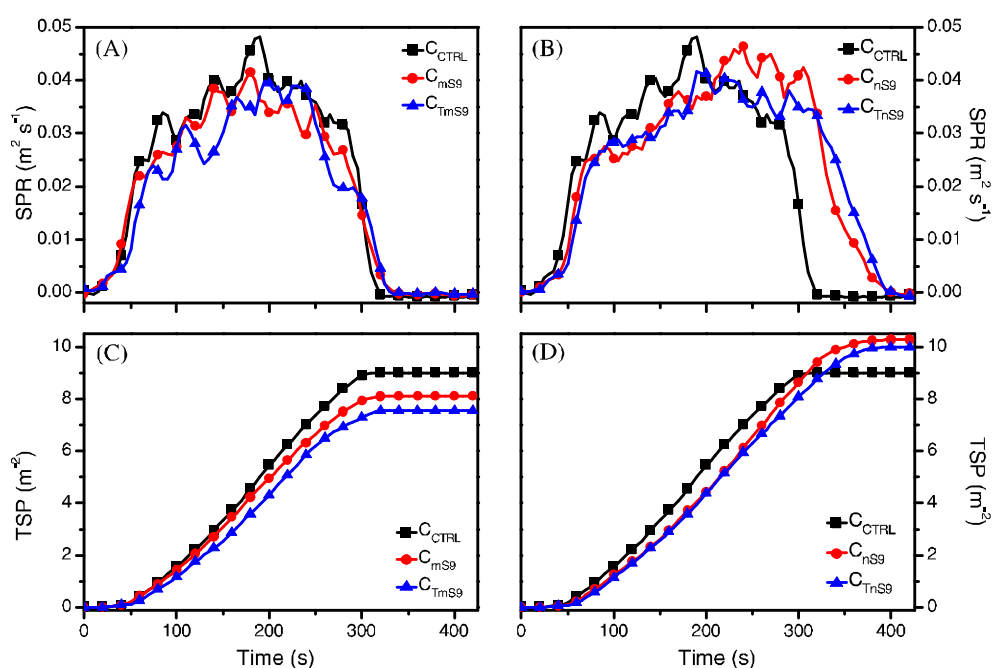


TABLE 3 Cone calorimeter data of WPC filled with 9 wt% micron- or nano-SiO₂

Sample	PHRR (kW m ⁻²)	THR (MJ m ⁻²)	Average HRR (kW m ⁻²)	Average SPR (10 ⁻² m ² s ⁻¹)	TSP (m ² /kg)
C_CTRL	451.07 ± 15.1	98.33 ± 4.2	231.74 ± 11.3	2.10 ± 0.3	9.01 ± 1.2
C_mS9	384.91 ± 13.2	84.34 ± 2.5	198.72 ± 8.4	2.10 ± 0.2	8.13 ± 0.8
C_TmS9	373.91 ± 11.5	81.81 ± 3.2	192.69 ± 7.1	1.90 ± 0.1	7.57 ± 0.5
C_nS9	331.75 ± 13.5	92.87 ± 4.0	218.89 ± 10.3	2.42 ± 0.15	10.29 ± 1.3
C_TnS9	312.62 ± 10.7	86.23 ± 2.9	202.89 ± 8.6	2.35 ± 0.21	10.00 ± 1.0

Abbreviations: PHRR, peak heat release rate; SPR, smoke production rate; THR, total heat release; WPC, wood-polymer composite.

FIGURE 8 Smoke production rate (SPR) of the micron-, A and nano-SiO₂, B filled WPCs via dry and wet dispersion; total smoke production (TSP) of the micron-, C and nano-SiO₂, D filled WPCs via dry and wet dispersion [Color figure can be viewed at wileyonlinelibrary.com]



beneficial to reduce the risk of fire.^[27] The PHRR of WPCs filled with nano-SiO₂ via dry and wet dispersion decreased by 26.4% and 30.7%, respectively, as compared with that of the unfilled WPCs (Table 3). The slight predominance of wet dispersion over dry dispersion in reducing HRR was due to the higher viscosity of WPCs filled with wet-dispersed nano-SiO₂, which was more favorable to resist the impulse of fire when burning. The most important mechanisms of nano-SiO₂ to reduce the HRR of WPCs were the shielding and carbonization,^[28,29] which would be analyzed in detail later.

The smoke yielded during unfilled WPCs combustion consists mainly of organic debris, carbonaceous suspended particles, and gases decomposed by WF and

HDPE.^[2] After the incorporation of micron-SiO₂ via dry and wet dispersion, the SPR and TSP of WPCs were slightly decreased due to the shielding of micron-SiO₂ (Figure 8A,C and Table 3). In the case of WPCs filled with nano-SiO₂ via dry and wet dispersion, the SPR and TSP increased after 250 seconds compared with that of unfilled WPCs (Figure 8A,C). This was because the nano-SiO₂, unlike the micron-SiO₂, was able to promote WF carbonization (Figure 10D,E), and the black carbon particles were released from the residual cracks, increasing the smoke release (Figure 8B).^[30] Similar to SPR, the TSP increased as well at the later stage of combustion (Figure 8D).

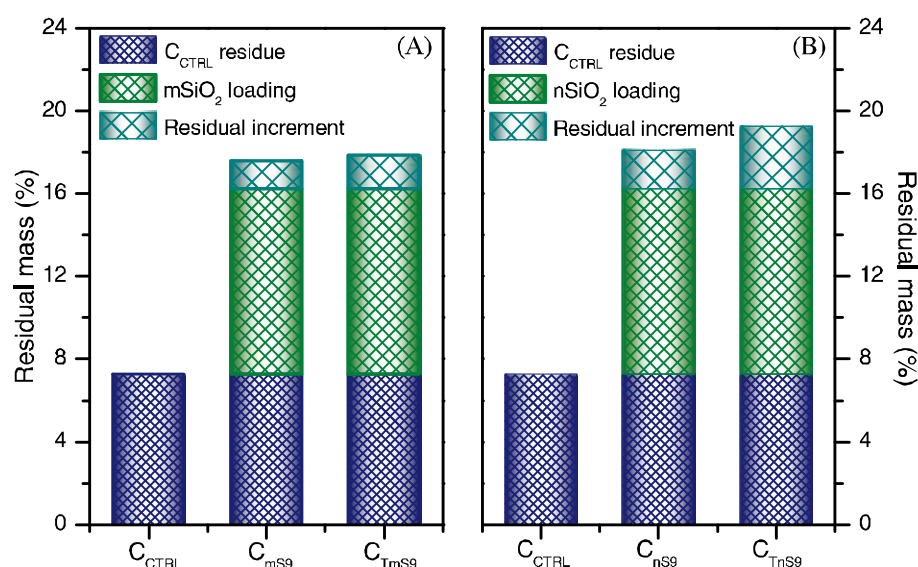


FIGURE 9 The residual mass of WPCs filled with 9% SiO₂ based on the unfilled wood-polymer composites (WPCs) after combustion: 9% micron-SiO₂ filled WPCs via dry and wet dispersion, A; and 9% nano-SiO₂ filled WPCs via dry and wet dispersion, B [Color figure can be viewed at wileyonlinelibrary.com]



FIGURE 10 Digital photographs of the wood-polymer composites (WPCs) residuals: unfilled WPCs, A; micron-SiO₂ filled WPCs via dry dispersion, B; micron-SiO₂ filled WPCs via wet dispersion, C; nano-SiO₂ filled WPCs via dry dispersion, D; nano-SiO₂ filled WPCs via wet dispersion, E [Color figure can be viewed at wileyonlinelibrary.com]

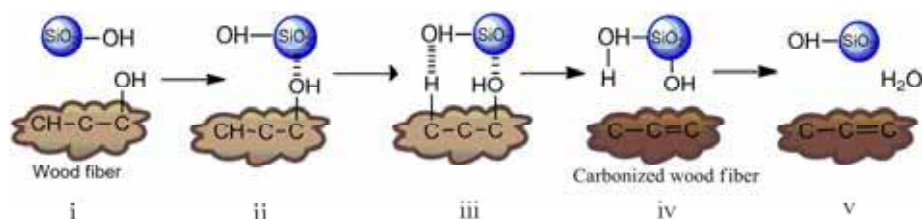
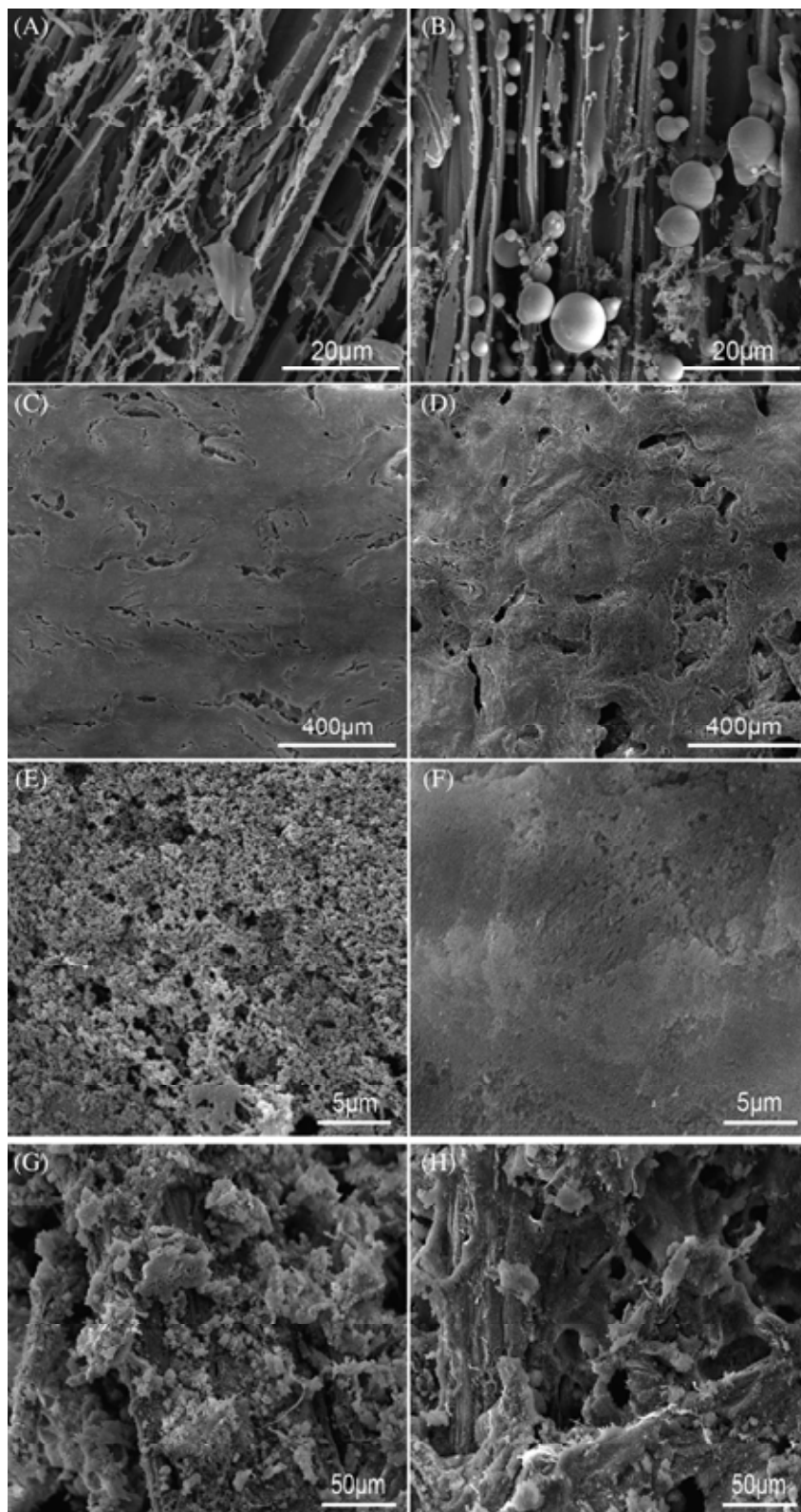


FIGURE 11 Schematic representation of the reaction mechanisms between nano-SiO₂ and wood fiber during combustion [Color figure can be viewed at wileyonlinelibrary.com]

FIGURE 12 SEM of the residuals of unfilled and 9% SiO₂ filled wood-polymer composites (WPCs): unfilled WPCs, A; WPCs filled with micron-SiO₂ via dry dispersion, B; the crust-like nano-SiO₂ from WPCs filled with nano-SiO₂ via dry dispersion (C, $\times 100$, E, $\times 5000$); the crust-like nano-SiO₂ from WPCs filled with nano-SiO₂ via wet dispersion (D, $\times 100$, F, $\times 5000$); the bottom residuals of WPCs filled with nano-SiO₂ via dry, G and wet, H dispersion, respectively



The residuals yielded from WPCs filled with 9% micron-SiO₂ via both dry and wet dispersion were higher than those yielded from the unfilled WPCs, and there still remained a residual increment after deducting the amount of micron-SiO₂ (Figure 9A). Compared with

micron-SiO₂, the incorporation of nano-SiO₂ into WPCs further increased the residual increment, especially incorporating by wet dispersion mode (Figure 9B). This further demonstrates the physical shielding and catalytic char-forming effect of nano-SiO₂.

The macro-morphology of the residual after combustion is crucial to the analysis of the flame retardant mechanism. The unfilled WPCs were basically burnt into broken and discontinuous fragments (Figure 10A). Compared with the unfilled WPCs, the residual from the WPCs filled with 9% micron-SiO₂ via dry dispersion presented a gray-white upper layer consisting mainly of micron-SiO₂ (Figure 10B); the bottom was a layer of char consisting of incompletely burned WF (not shown), indicating that the micron-SiO₂ exerted slight protective effect on the substrate. Compared with dry dispersion, the incorporation of micron-SiO₂ in WPCs via wet dispersion resulted in a relatively compact and continuous residual structure (Figure 10C) due to the increased viscosity of the WPCs, which slightly increased the fire retardancy.^[31]

The residuals of the WPCs filled with nano-SiO₂ via both dry and wet dispersion exhibited obvious two-layer structures with different colors (Figure 10D,E). The white crust-like layer was formed due to nano-SiO₂ deposition. The nano-SiO₂ gradually accumulated on the residual surface under the influence of heat flux after the organic components of the WPCs decomposed and gasified during combustion.^[32] The bottom layer was mainly composed of the carbonized WF. The thermally-stable nano-SiO₂-char structure inhibited the transfer of heat, combustible volatiles, and O₂ between the gas phase and the condensed phase and reduced the burning rate of WPCs.^[33] However, the residual of the WPCs filled with nano-SiO₂ via dry dispersion was severely broken during the later stage of combustion (Figure 10D), and the fragile residual resulted in the undesirable fire retardancy

(Figures 7B,D and 8B,D). Compared with dry dispersion, the residual of the WPCs filled with nano-SiO₂ via wet dispersion was less fragile (Figure 10E), while the occurrence of cracks on the residual surface still led to the release of the carbon particles, which increased the SPR and TSP (Figure 8B,D).

The mechanism of nano-SiO₂ catalyzed the charring of WF is shown in Figure 11. The silanol groups on the nano-SiO₂ surface served as active catalytic sites for Brønsted acids that catalyzed the charring of WF by removing H and O. Specifically, WF adsorbed on the Brønsted acids site of nano-SiO₂ (i → ii), and H element from WF transferred to the silanol group on the nano-SiO₂ surface (iii), then alkene was formed and desorbed (iv). After that, water was formed and desorbed, and catalyst was regenerated (v).^[34] The carbonized layer helped hinder the diffusion of heat and O₂ in the substrate.^[35]

SEM was employed to further observe the residual structures of the WPCs. The residual of unfilled WPCs partially retained the char-skeleton structure of WF (Figure 12A). In the case of WPCs filled with micron-SiO₂ via dry dispersion, the residual surfaces presented a lot of clear micron-SiO₂, which exerted a slight protection on the bottom substance (Figure 12B). The residual structure of WPCs filled with micron-SiO₂ via wet dispersion was similar to that via dry dispersion (not shown). For the residual of WPCs filled with nano-SiO₂ via dry dispersion, there were many pores on the crust-like nano-SiO₂ layer, which were smaller than that via wet dispersion (Figure 12C,D). The high-magnification images of the crust-like nano-SiO₂ showed that the arrangement of nano-SiO₂ was looser by dry dispersion than by wet

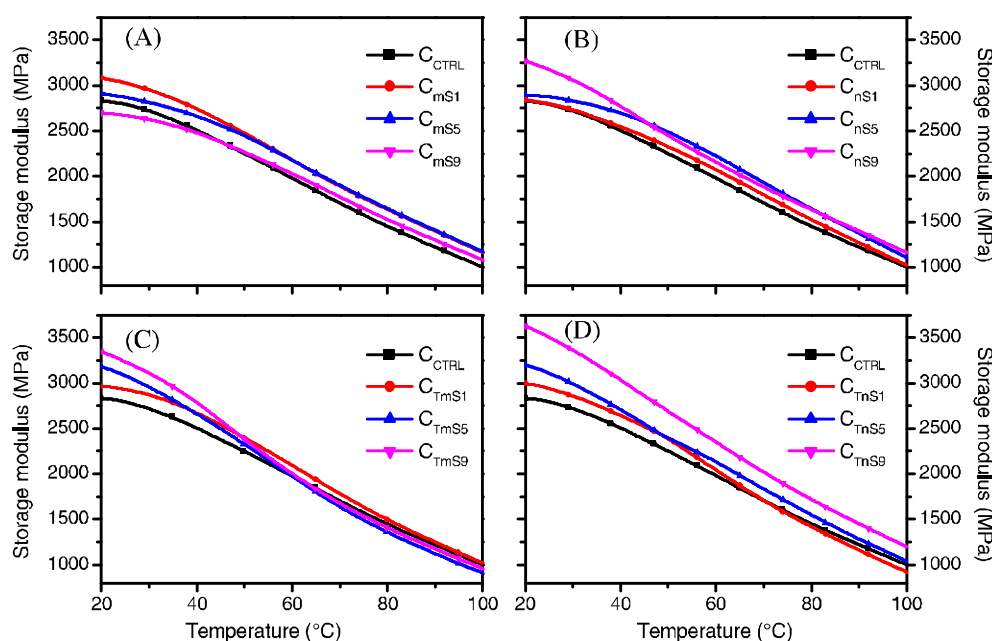


FIGURE 13 Normalized storage modulus of wood-polymer composites (WPCs): micron-SiO₂ filled WPCs via dry dispersion, A; nano-SiO₂ filled WPCs via dry dispersion, B; micron-SiO₂ filled WPCs via wet dispersion, C; nano-SiO₂ filled WPCs via wet dispersion, D [Color figure can be viewed at wileyonlinelibrary.com]

dispersion (Figure 12E,F). The larger holes on the crust-like nano-SiO₂ layer after wet dispersion resulted from the lack of channels to release gases generated from the bottom substance; thus, the gas impingement created holes on the crust-like nano-SiO₂. The presence of holes provided channels for the transfer of combustibles and oxygen, and therefore it was disadvantageous to reduce the combustion performance. For the bottom residual structure, complete char frameworks covered by nano-SiO₂ aggregates were observed (Figure 12G,H) and these nano-SiO₂ aggregates served as barriers, which was beneficial to reduce the heat release and smoke production.

3.5 | Dynamic mechanical analysis

The storage modulus of WPCs filled with micron-SiO₂ via dry dispersion decreased with the increasing micron-SiO₂ content, which was lower than the unfilled WPCs at 9 wt% loading level (Figure 13A). This was due to a lack of interfacial bonding between micron-SiO₂ and HDPE.^[36] Compared with the unfilled WPCs, the incorporation of micron-SiO₂ via wet dispersion improved the storage modulus of WPCs (Figure 13C). This was due to the uniform dispersion and good interfacial bonding so that the rigidity of micron-SiO₂ in WPCs was well exploited.^[37,38]

The WPCs filled with nano-SiO₂ via dry and wet dispersion exhibited a higher storage modulus than the unfilled WPCs due to the nano-size effect, namely the large surface area of nano-SiO₂ that hindered the chain relaxation of HDPE (Figure 13B,D).^[39] The storage modulus of SiO₂-filled WPCs via wet dispersion was higher than that via dry dispersion (Figure 13D,B). This was because the homogeneous dispersion and strong interface bonding of nano-SiO₂ in HDPE facilitated the efficient transfer of stress from WPCs to nano-SiO₂, which fully exerted the rigidity of nano-SiO₂.

4 | CONCLUSIONS

This study mainly compared the effects of SiO₂ size (micron- and nano-scale) and dispersion mode (dry and wet dispersion) on the thermal stability and fire retardancy of WPCs. The results showed that the micron-SiO₂ advanced the degradation of WF, but had no effect on the thermal stability of the final WPCs. While, the incorporation of nano-SiO₂ improved the thermal stability of WPCs. Compared with the unfilled WPCs, the fire retardancy of the WPCs exhibited slight increase (<20%) after incorporating 9% micron-SiO₂ via either dry or wet dispersion, and the increment via wet dispersion was

higher than that via dry dispersion due to the uniform dispersion and the well bonding of micron-SiO₂ in HDPE. The heat release rates of the nano-SiO₂-filled WPCs via dry and wet dispersion, respectively, decreased by 26.4% and 30.7% due to the shielding and the catalytic carbonization of nano-SiO₂. However, the SPR slightly increased at the later stage of combustion after incorporating nano-SiO₂. The synergistic fire retardancy of nano-SiO₂ and smoke suppressant on WPCs will be explored in future research. The dynamic thermomechanical tests revealed that the incorporation of nano-SiO₂ improved the storage modulus of WPCs in the case of uniform dispersion and strong bonding in HDPE.

ACKNOWLEDGMENTS

This work was supported by the National Key Research and Development Program of China (No. 2019YFD1101204), the National Natural Science Foundation of China (No. 31901251), the Guangdong Forestry Science and Technology Innovation Project (No. 2020KJCX008), the Project of Guangzhou Municipal Key Laboratory of Woody Biomass Functional New Materials (No. 201905010005), and the Project of Key Disciplines of Forestry Engineering of Bureau of Education of Guangzhou Municipality.

ORCID

Haiyang Zhou  <https://orcid.org/0000-0002-6629-9952>
Xiaolong Hao  <https://orcid.org/0000-0003-0172-1136>

REFERENCES

- [1] R. Liu, Y. Chen, J. Cao, *ACS Appl. Mater. Inter.* **2016**, 8, 161.
- [2] H. Zhou, Z. Xiao, Y. Wang, X. Hao, Y. Xie, Y. Song, F. Wang, Q. Wang, *Constr. Build. Mater.* **2020**, 233, 117369.
- [3] L. Liu, Z. Wang, Y. Yu, S. Fu, Y. Nie, H. Wang, P. Song, *ACS Sustainable Chem. Eng.* **2019**, 7, 18453.
- [4] J. Jiang, C. Mei, M. Pan, J. Cao, *Polym. Compos.* **2020**, 41, 1090.
- [5] X. Hao, H. Zhou, B. Mu, L. Chen, Q. Guo, X. Yi, L. Sun, Q. Wang, R. Ou, *Compos. Part B.* **2020**, 185, 107778.
- [6] Y. H. Guan, J. Q. Huang, J. C. Yang, Z. B. Shao, Y. Z. Wang, *Ind. Eng. Chem. Res.* **2015**, 54, 3524.
- [7] L. Liu, M. Qian, P. a. Song, G. Huang, Y. Yu, S. Fu, *ACS Sustainable Chem. Eng.* **2016**, 4, 2422.
- [8] C. Ding, M. Pan, H. Chen, S. Zhang, C. Mei, *Constr. Build. Mater.* **2020**, 248, 118661.
- [9] Y. Fang, Q. Wang, C. Guo, Y. Song, P. A. Cooper, *J. Anal. Appl. Pyrol.* **2013**, 100, 230.
- [10] G. Bai, C. Guo, L. Li, *Constr. Build. Mater.* **2014**, 50, 148.
- [11] S. Bourbigot, S. Duquesne, *J. Mater. Chem.* **2007**, 17, 2283.
- [12] P. Fei, Z. Guo, C. Ye, Z. Teng, Q. Chen, G. Zhang, Y. Zhuang, W. Lai, H. Xiong, J. Cai, *Constr. Build. Mater.* **2019**, 201, 728.
- [13] W. He, P. Song, B. Yu, Z. Fang, H. Wang, *Prog. Mater. Sci.* **2020**, 114, 100687.
- [14] N. Roenner, K. Hutheising, A. Fergusson, G. Rein, *Fire. Safety. J.* **2017**, 91, 200.

- [15] A. Dorigato, A. Pegoretti, A. Frache, *J. Therm. Anal. Calorim.* **2012**, *109*, 863.
- [16] O. Nechyporchuk, R. Bordes, T. Kohnke, *ACS Appl. Mater. Inter.* **2017**, *9*, 39069.
- [17] H. Zhou, X. Hao, H. Wang, X. Wang, T. Liu, Y. Xie, Q. Wang, *J. Mater. Sci.* **2018**, *53*, 1899.
- [18] R. Wang, D. Zhuo, Z. Weng, L. Wu, X. Cheng, Y. Zhou, J. Wang, B. Xuan, *J. Mater. Chem. A* **2015**, *3*, 9826.
- [19] X. Hao, H. Zhou, Y. Xie, Z. Xiao, H. Wang, Q. Wang, *Polym. Compos.* **2018**, *40*, 1576.
- [20] Q. Jiasheng, H. Pingsheng, *J. Mater. Sci.* **2003**, *38*, 2299.
- [21] J. Zhang, Q. Wu, G. Li, M. Li, X. Sun, D. Ring, *RSC Adv.* **2017**, *7*, 24895.
- [22] A. M. Díez-Pascual, C. Xu, R. Luque, *J. Mater. Chem. B.* **2014**, *2*, 3065.
- [23] Z. X. Zhang, J. Zhang, B. X. Lu, Z. X. Xin, C. K. Kang, J. K. Kim, *Compos. Part B.* **2012**, *43*, 150.
- [24] K. Chrissafis, K. M. Paraskevopoulos, E. Pavlidou, D. Bikiaris, *Thermochim. Acta* **2009**, *485*, 65.
- [25] A. K. Mishra, A. S. Luyt, *Polym. Degrad. Stabil.* **2008**, *93*, 1.
- [26] T. Kashiwagi, J. W. Gilman, K. M. Butler, T. Kashiwagi, *Fire Mater.* **2000**, *24*, 277.
- [27] L. Sun, Q. Wu, Y. Xie, F. Wang, Q. Wang, *RSC Adv.* **2016**, *6*, 13890.
- [28] H. Gu, J. Guo, Q. He, S. Tadakamalla, X. Zhang, X. Yan, Y. Huang, H. A. Colorado, S. Wei, Z. Guo, *Ind. Eng. Chem. Res.* **2013**, *52*, 7718.
- [29] I. Turku, T. Karki, A. Puurtinen, *Fire Mater.* **2008**, *42*, 198.
- [30] Q. Zhao, B. Zhang, H. Quan, R. C. M. Yam, R. K. K. Yuen, R. K. Y. Li, *Compos. Sci. Technol.* **2009**, *69*, 2675.
- [31] T. Kashiwagi, M. Mu, K. Winey, B. Cipriano, S. R. Raghavan, S. Pack, M. Rafailovich, Y. Yang, E. Grulke, J. Shields, R. Harris, J. Douglas, *Polymer.* **2008**, *49*, 4358.
- [32] T. Kashiwagi, R. H. Harris, X. Zhang, R. M. Briber, B. H. Cipriano, S. R. Raghavan, W. H. Awad, J. R. Shields, *Polymer* **2004**, *45*, 881.
- [33] H. Yang, B. Yu, X. Xu, S. Bourbigot, H. Wang, P. Song, *Green Chem.* **2020**, *22*, 2129.
- [34] P. Kostestkyy, J. Yu, R. J. Gorte, G. Mpourmpakis, *Catal. Sci. Technol.* **2014**, *4*, 3861.
- [35] S. D. Jiang, Z. M. Bai, G. Tang, L. Song, A. A. Stec, T. R. Hull, Y. Hu, W. Z. Hu, *ACS Appl. Mater. Inter.* **2014**, *6*, 14076.
- [36] S. Fu, P. Song, H. Yang, Y. Jin, F. Lu, J. Yc, Q. Wu, *J. Mater. Sci.* **2010**, *45*, 3520.
- [37] P. A. Song, H. T. Yang, S. Y. Fu, Q. Wu, J. W. Yc, F. Z. Lu, Y. M. Jin, *J. Macromol. Sci. B.* **2011**, *50*, 907.
- [38] X. Zhou, J. Su, C. Wang, C. Fang, X. He, W. Lei, C. Zhang, Z. Huang, *J. Mater. Sci. Technol.* **2020**, *46*, 74.
- [39] Z. H. Qian, Z. L. Peng, *Polym. Compos.* **2019**, *40*, 1740.

How to cite this article: Zhou H, Hao X, Wang X, et al. Comparative study on the effects of silica size and dispersion mode on the fire retardancy of extruded wood fiber/HDPE composites. *Polymer Composites*. 2020;41: 4920–4932. <https://doi.org/10.1002/pc.25763>

Mechanical Properties and Fire Retardancy of Wood Flour/High-Density Polyethylene Composites Reinforced with Continuous Honeycomb-Like Nano-SiO₂ Network and Fire Retardant

Haiyang Zhou^{1,2}, Xiaoyu Wang³, Xiaolong Hao^{1,2}, Qingwen Wang^{1,2,*} and Rongxian Ou^{1,2,*}

¹Key Laboratory for Biobased Materials and Energy of Ministry of Education, College of Materials and Energy, South China Agricultural University, Guangzhou, 510642, China

²Guangdong Laboratory for Lingnan Modern Agricultural Science and Technology, Guangzhou, 510642, China

³College of Arts, South China Agricultural University, Guangzhou, 510642, China

*Corresponding Authors: Qingwen Wang. Email: qwwang@scau.edu.cn; Rongxian Ou. Email: rongxian_ou@scau.edu.cn

Received: 22 February 2020; Accepted: 02 April 2020

Abstract: The mechanical properties of wood flour/high-density polyethylene composites (WPC) were improved by adding a small amount of nano-SiO₂ to obtain a network-structured WPC with a continuous honeycomb-like nano-SiO₂ network. The wood flour was modified with a fire retardant (a mixture of sodium octabonate and amidine urea phosphate) to improve its fire retardancy. The flexural properties, creep resistance, thermal expansion, and fire retardancy of the WPC were compared to a control (WPC_{CTRL}) without nano-SiO₂ or fire retardant. The flexural strength and modulus of the WPC containing only 0.55 wt.% nano-SiO₂ were 6.6% and 9.1% higher than the control, respectively, while the creep strain and thermal expansion rate at 90°C were 33.8% and 13.6% lower, respectively. The cone calorimetry tests revealed that the nano-SiO₂ network physically shielded the WPC, giving it lower heat release and smoke production rates. The thermal expansion was further decreased by incorporating fire retardants into the WPC, which showed the lowest total heat release and total smoke production and the highest mass retention. This study demonstrates a facile procedure for producing WPC with desired performances by forming a continuous honeycomb-like network by adding a small amount of nanoparticles.

Keywords: Wood plastic composites; nano-SiO₂; mechanical properties; creep; fire retardancy

1 Introduction

Wood flour/thermoplastic composites (WPC) are environmentally-friendly materials that have been extensively used in building, decorative, and logistics packing materials [1–3]. Nonpolar polyolefins (polyethylene and polypropylene) are used as thermoplastics in WPCs due to their facile processing and forming, low cost, and similar processing temperatures to wood flour. The wood flour originates from wood processing residues, waste wood products, and agricultural and forestry residues. Weak interfaces are formed between the polar wood flour and nonpolar polyolefins due to their surface energy differences,



This work is licensed under a Creative Commons Attribution 4.0 International License, which permits unrestricted use, distribution, and reproduction in any medium, provided the original work is properly cited.

which results in low mechanical strength and creep resistance of the resulting WPC, which limit their applications and shorten their service life [4–6].

Many studies have investigated methods to improve the strength and creep resistance of WPC [7], including increasing interfacial compatibility and adding inorganic nanoparticles. For example, grafting a mixture of polyethylene and polypropylene with maleic anhydride monomers improved the compatibility between grafted polymers and wood flour. The flexural strength and modulus of the resulting WPC increased by 117% and 29%, respectively, while the creep strain was lowered [8]. The incorporation of maleic anhydride-grafted polypropylene into wood fiber/polypropylene composites increased the creep modulus by nearly 28.0% at 60°C [9]. The creep resistance of wood flour/polypropylene composites increased by about 15% and 22.5% after the addition of 1 wt.% nanoclay and transition metal-modified nanoclay, respectively [10]. The flexural strength and modulus of polylactic acid composites after the wood fiber was modified with 3 wt.% organo-montmorillonite increased by 30.7% and 46.8%, respectively [11].

Nano-SiO₂ is a commercially-available inorganic filler that is easy to produce on large scales, low-cost, and easily undergoes surface modification. It has the potential to improve the creep resistance and fire retardancy of WPC [11,12]. The incorporation of 8 wt.% SiO₂ in polyethylene/polypropylene/flax ternary composites significantly reduced the creep strain and improved the relaxation modulus [12]. Adding 14 wt.% nano-SiO₂ to wood flour/polyethylene composites reduced the average heat release rate and total heat release by 30.3% and 12.8%, respectively, while it increased the smoke release [13]. To obtain satisfactory creep resistance and fire retardation, high nano-SiO₂ loadings are required when using traditional processes to directly disperse nano-SiO₂ in WPC [14,15]. This increases the cost and decreases the mechanical properties of WPC due to the agglomeration of nano-SiO₂ [15].

In order to enhance the mechanical properties and creep resistance of WPC, a continuous honeycomb-like nano-SiO₂ network was formed in a WPC using solution mixing, rotary evaporation, and mold pressing. In the network-structured WPC, SiO₂ nanoparticles were distributed only at the boundaries between the WPC pellets instead of uniformly throughout the WPC. Thus, the amount of nano-SiO₂ was significantly reduced. In order to further improve the fire retardancy of the network-structured WPC, wood flour modified with fire retardants (amidine urea phosphate and sodium octaborate tetrahydrate) was used to fabricate WPC. The flexural properties, creep resistance, thermal expansion, and fire retardancy of the resulting WPC were evaluated.

2 Experimental

2.1 Materials

HDPE pellets with a density of 0.954 g/cm³ and a melt flow index of 0.9 g/10 min were obtained from Daqing Petrochemical Co., Ltd. (Daqing, China). Wood flour (WF) with a particle size of 40–60 mesh was prepared from poplar wood (*Populus adenopoda* Maxim) in our laboratory. Maleic anhydride-grafted polyethylene (MAPE) pellets with a grafting ratio of 0.9 wt.% and a melt flow index of 1.9 g/10 min were purchased from Sunny New Technology Development Co., Ltd. (Shanghai, China). The lubricant was a mixture of stearic acid and polyethylene wax (1:1 in mass, Adisi Co., Ltd., Nanjing, China). SiO₂ nanoparticles with an average diameter of 10–15 nm (marked as nSiO₂) were obtained from Meng Tai Hu Industrial Co., Ltd. (Shanghai, China). The fire retardant (FR) was a mixture of guanylurea phosphate (abbr: GUP; molecular formula: C₂H₉N₄O₅P; purity: 99.04%; free phosphoric acid content: 0.41%) and sodium octaborate tetrahydrate (abbr: DOT; molecular formula: Na₂B₈O₁₃·4H₂O; melting point: 741°C). The mass ratio of GUP-to-DOT was 7:3 and was made in-house. Vinyltrimethoxysilane (abbr: VTS) was purchased from Chi Ye Silicone Co., Ltd. (Shanghai, China). Ethanol solution was obtained from Tianjin Guangfu Co., Ltd. (Tianjin, China).

2.2 Experimental

2.2.1 Fire Retardant Impregnated Poplar Powder

WF was dried in a vacuum oven at 103°C for 12 h to reach 1–2% moisture content. The dried WF was impregnated in a 9 wt.% aqueous solution of fire retardant through vacuum treatment at -0.01 MPa for 6 h. Then, the impregnated WF was drained on a 100-mesh sieve, followed by vacuum drying at 80°C for 12 h to obtain the modified WF (Fig. 1). The weight gain rate of the modified WF was $11.25 \pm 1.06\%$. WF was also treated with distilled water using the same process as the unmodified WF.

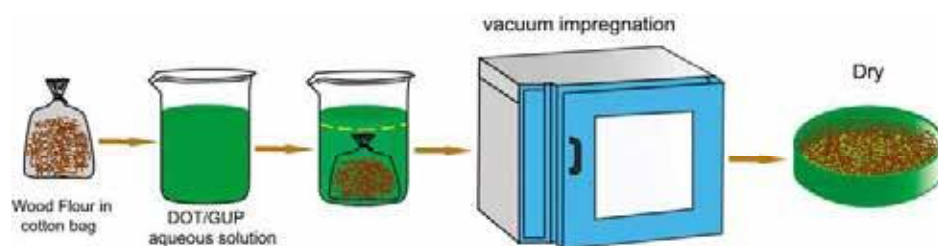


Figure 1: Schematic diagram of wood flour impregnated with fire retardant

2.2.2 Preparation of WPC

The unmodified WF or modified WF and HDPE, MAPE, and lubricant were compounded for 8 min at ambient temperature using a high-speed mixer (SHR-10A; Tongsha Plastic Machinery Company, Zhangjiagang, China). The mixture was melt-blended through a co-rotating twin-screw extruder (diameter = 40 mm, L/D = 30, SJSH-30, Nanjing Rubber Machinery Corp., Nanjing, China) at a temperature range of 145–165°C. The resulting extrudates were pelletized.

Preparation of control WPC and fire retardant (FR)-modified WPC: The obtained pellets were molded into panels (160 mm × 160 mm × 3 mm) using a flat vulcanizing machine (XH-406B; Zhuosheng Machinery Equipment Co., Ltd., Dongguan, China) at 180°C with a pressure of 12 MPa for 3 min after pre-pressing for 15 min. The obtained WPC panels with unmodified WF or modified WF were referred to as WPC_{CTRL} and WPC_F, respectively. The weight ratio of each component in the panels is shown in Tab. 1.

Table 1: Weight ratio of each component in WPC panels (wt.%) (WPC_{CTRL} = control; WPC_S = WPC panel with nSiO₂ network; WPC_F = WPC panel with fire retardant modified wood flour; WPC_{SF} = WPC panel with nSiO₂ network and fire retardant modified wood flour)

Sample	nSiO ₂	Fire retardant	Wood flour	HDPE	MAPE	lubricant
WPC _{CTRL}	0	0	50	45	3	2
WPC _S	0.55	0	49.45	45	3	2
WPC _F	0	5.63	44.37	45	3	2
WPC _{SF}	0.75	5.63	43.62	45	3	2

Preparation of network-structured WPC based on nSiO₂: The pellets obtained in Section 2.2.2 were uniformly mixed with nSiO₂ (3 wt.% based on the WPC pellets) using an electric mixer in an ethanol solution. Subsequently, nSiO₂-coated WPC pellets were obtained after evaporating ethanol. The nSiO₂-coated pellets were screened through a 30-mesh sieve to remove self-agglomerated nSiO₂. The WPC panels prepared using the nSiO₂-coated pellets with unmodified WF and modified WF were marked as

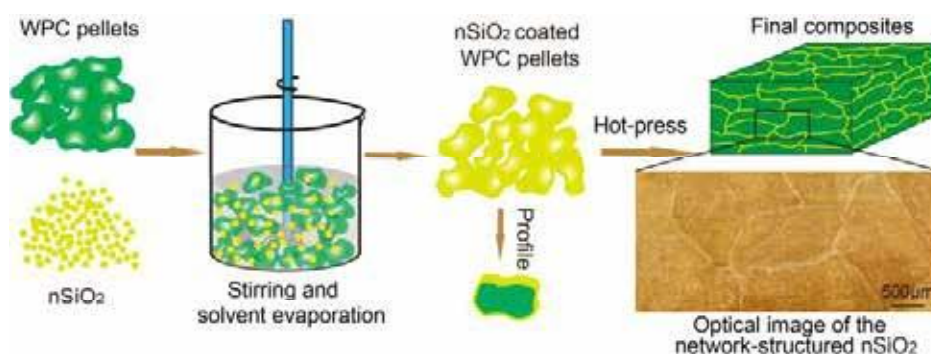


Figure 2: Schematic diagram of processing process of the network-structured WPC

WPC_S and WPC_{SF}, respectively. The amounts of nSiO₂ coated on the pellets were calculated and are shown in Tab. 1. In the network-structured WPC panels, nSiO₂ was distributed at the boundary between the WPC pellets (Fig. 2). The optical microscopic image in Fig. 2 shows that nSiO₂ formed a continuous honeycomb-like network in the WPC.

2.3 Characterization

The micro-morphologies of the WPC pellets and the cross-sections of the WPC panels were observed using a scanning electron microscope (SEM, FEI QuanTa200, FEI Co., Hillsboro, OR, USA) at an accelerating voltage of 12.5 kV. The WPC pellets and panels were sputter-coated with gold. In addition, the elemental distribution of the surfaces of the WPC pellets was analyzed using energy-dispersive spectrometry (EDS).

The flexural properties of the WPC panel samples (80 mm × 13 mm × 4 mm) were analyzed by a universal mechanical testing machine (CMT5504, MTS Systems Co., Ltd, China) according to ASTM D790-10. Eight replicates were tested for each group.

Creep and relaxation tests of samples (35 mm × 12 mm × 3.5 mm) were performed on a dynamic mechanical analyzer (Q800, TA Instruments Inc., SA). Isothermal (50°C) creep was tested for 50 min under a load of 2 MPa within the elastic deformation regime. Relaxation was tested under a constant strain of 0.1%, and the change in the relaxation modulus was recorded.

Thermal expansion of the specimens measuring 10 mm × 10 mm × 3.5 mm (length × width × thickness) was analyzed along the thickness direction using a thermomechanical analyzer (Q400, TA Instruments Inc., USA). Specimens were heated from room temperature to 100°C at a heating rate of 20 °C/min and then held at 100°C for 3 min to eliminate the thermal history and moisture. A quartz probe was in contact with the specimens under a loaded of 0.05 N. The tests were conducted from −40°C to 90°C at a heating rate of 3°C/min under a nitrogen atmosphere.

The fire retardancy tests of WPC specimens measuring 100 mm × 100 mm × 3.5 mm were conducted using a cone calorimeter (Fire Testing Technology Ltd., East Grinstead, UK) according to ISO 5660-1 at a heat flux of 50 kW/m². The heat release rate (HRR), total heat release (THR), smoke production rate (SPR), total smoke production (TSP), and residual mass were recorded. Two replicates were tested for each group. The residuals after combustion were analyzed by a digital camera and SEM.

3 Results and Discussion

3.1 Morphological Analysis

The WPC_{CTRL} pellets had a rough and uneven surface on which the WF was imbedded in an HDPE matrix (Fig. 3a). The surface morphology of the WPC_F pellets was similar to that of the WPC_{CTRL} pellets

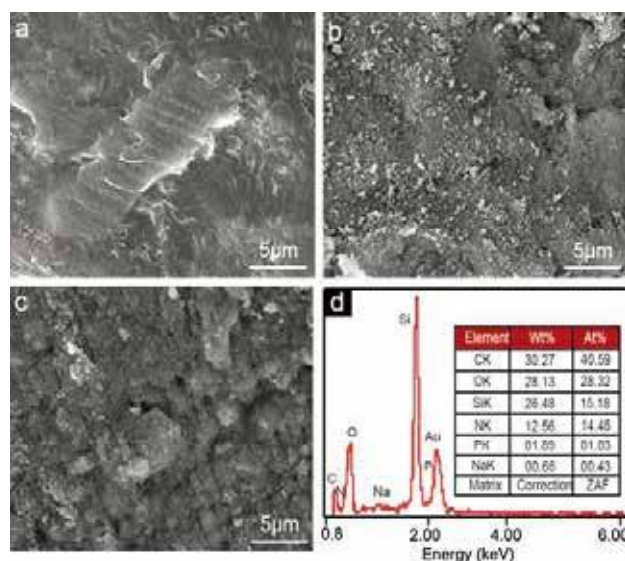


Figure 3: SEM micrographs of the surface of the WPC control pellets (a), the WPC pellets coated with nano-SiO₂ (b), and the fire retardant modified WPC pellets coated with nano-SiO₂ (c); EDS corresponding to Fig. 3c (d)

(not shown). The nSiO₂ particle aggregates were visible on the WPC_S pellets (Fig. 3b). For the WPC_{SF} pellets, the nSiO₂ particles and WF were enveloped by a viscous substance (Fig. 3c). The EDS result showed that the viscous substance contained a small amount of N and P (Fig. 3d), indicating that it may be the product of dissolving GUP in ethanol. The viscous substance could facilitate the adhesion of more nSiO₂ particles, as demonstrated by the higher nSiO₂ content on the WPC_{SF} pellet surface than on the WPC_S pellet surface (Tab. 1).

The SEM micrographs of the cross-sections of the flexural-fractured WPC panels are shown in Fig. 4. The HDPE matrix underwent plastic deformation, as shown in the fracture cross-sections of the WPC_{CTRL} and WPC_F (Figs. 4a and 4b). This was a result of the flexural failure loading mode [16]. A continuous nSiO₂-rich region was observed on the fractured cross-section of WPC_S (Fig. 4c). This region exhibited brittle fracture compared with the WPC region due to the high nSiO₂ content, and there was no obvious boundary between the WPC pellets after hot-pressing. Furthermore, the high-magnification images of the nSiO₂-rich region showed a mixture of nSiO₂ and HDPE (Fig. 4d) due to the diffusion of molten HDPE into the nSiO₂ lamella during hot-pressing. Compared with the WPC_S, the WPC_{SF} showed a wider nSiO₂-rich region on the fractured cross-section (Fig. 4e) due to the higher nSiO₂ content. The nSiO₂-rich region of WPC_{SF} (Fig. 4f) exhibited more ductile fracture behavior compared with WPC_S (Fig. 4d), possibly because the viscous substance enveloping the nSiO₂ surface reduced the interfacial compatibility between nSiO₂ and HDPE in the nSiO₂-rich region of WPC_{SF}.

3.2 Flexural Properties

The flexural strength of WPC_S (37.3 MPa) was higher than that of WPC_{CTRL} (35.0 MPa) due to the formation of a rigid nSiO₂ network (Fig. 5a) which could transfer stress due to its compatibility with the HDPE matrix [17]. Compared with the WPC_{CTRL}, the flexural strength of WPC_F (33.5 MPa) was slightly lower due to the weak interfacial bonding between the fire retardant-impregnated WF and HDPE matrix [18,19]. The flexural strength of WPC_{SF} (33.0 MPa) was further decreased compared with that of WPC_F because the viscous substance weakened the nSiO₂ network.

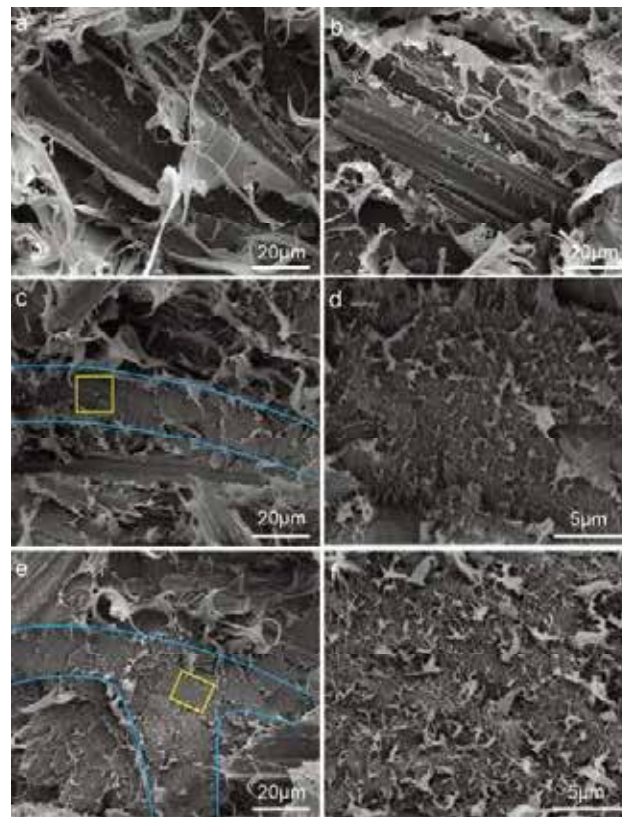


Figure 4: SEM micrographs of the flexural-fractured section of the WPC control panel (a, $\times 1000$), WPC panel with fire retardant modified wood flour (b, $\times 1000$), WPC panel with nSiO₂ network (c, $\times 1000$; d $\times 5000$), and WPC panel with nSiO₂ network and fire retardant modified wood flour (e, $\times 1000$; f, $\times 5000$). Yellow rectangles in (c) and (e) demonstrate the region shown in (d) and (f), respectively

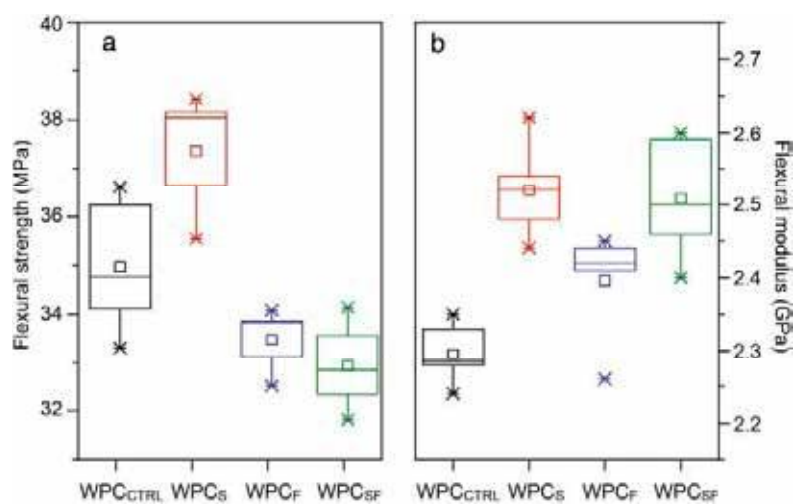


Figure 5: Flexural strength (a) and flexural modulus (b) of the WPC. (The abbreviations in the figure are the same with Tab. 1)

The flexural modulus of WPC_S was 9.1% higher than that of the WPC_{CTRL} due to the formation of a rigid nSiO₂ network (Fig. 5b). Unlike flexural strength, the flexural modulus of WPC_F was higher than that of WPC_{CTRL}. This was attributed to the positive effect of the rigid fire-retardant particles (DOT and GUP) on the modulus, which compensated for the negative effect of the weak interfacial effect between the modified-WF and HDPE [20]. The flexural modulus of WPC_{SF} was higher than that of WPC_F, which may have resulted from the combined action of rigid fire retardant particles and nSiO₂ network.

3.3 Creep and Relaxation Analysis

The creep resistances of the four WPC panels followed the order: WPC_{CTRL} < WPC_F < WPC_{SF} < WPC_S (Fig. 6a). The creep strain of WPC_S (0.047%) was significantly lower than that of WPC_{CTRL} (0.071%) after applying an external force for 45 min. This was attributed to the formation of a rigid nSiO₂ network in WPC_S, which served as a rigid support that transmitted stress and provided deformation resistance. Compared with WPC_{CTRL}, the lower creep strain of WPC_F arose due to the introduction of the rigid fire retardant [1]. The creep strain of WPC_{SF} was slightly higher than that of WPC_S, possibly because the viscous substance wrapping the nSiO₂ reduced the rigidity of the nSiO₂ network in WPC_{SF}. Similar to the improved creep resistance, the relaxation moduli of WPC_S, WPC_F, and WPC_{SF} were higher than that of WPC_{CTRL} (Fig. 6b). The relaxation modulus of WPC_S was 21.3% higher than that of WPC_{CTRL}, indicating that the introduction of a rigid nSiO₂ network effectively resisted the deformation of WPC caused by the constant external force.

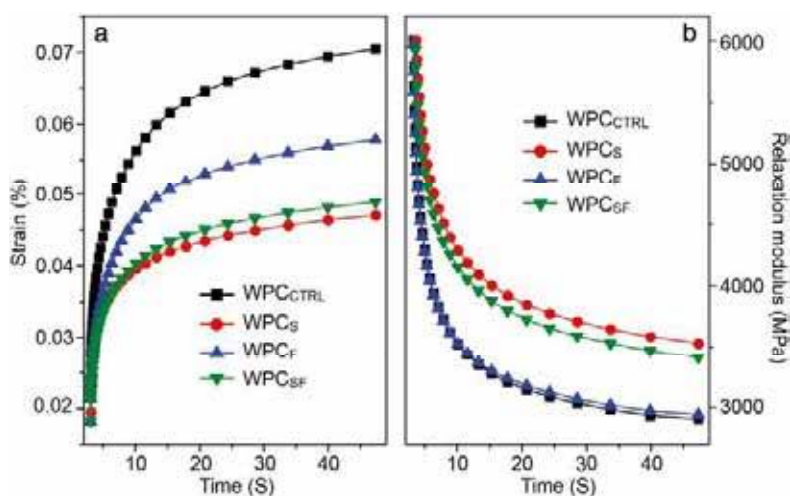


Figure 6: Creep strain (a) and relaxation modulus (b) of the WPC. (The abbreviations in the figure are the same with Tab. 1)

3.4 Thermal Expansion Behavior

The thermal expansion rates of WPC_S, WPC_F, and WPC_{SF} were lower than that of WPC_{CTRL} and ranged from -40 to 90°C (Fig. 7a). This was due to the presence of a rigid nSiO₂ network and fire retardant which were inherently not prone to thermal expansion [21]. The WPC_{SF} showed the lowest thermal expansion rate over the test temperature range compared with the other WPC panels due to its higher nSiO₂ content. The thermal expansion rates of WPC_{SF}, WPC_F, WPC_S, and WPC_{CTRL} at 90°C were 19.9%, 24.3%, 24.2%, and 28.0%, respectively. The linear coefficient of thermal expansion (LCTE) increased with temperature, and a higher increment was observed after 50°C (Fig. 7b). This was because the thermal motion of HDPE increased with the temperature, causing an increase in the macroscopic volume of WPC [22]. It

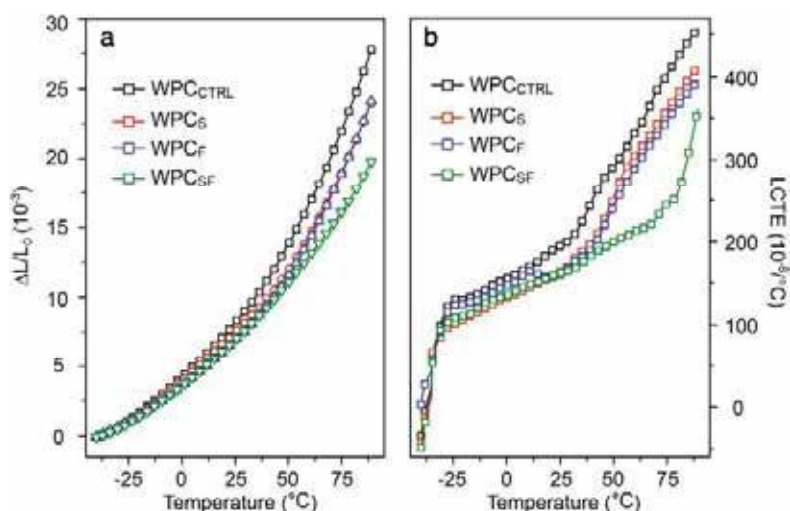


Figure 7: Thermal expansion rate (a) and linear coefficient of thermal expansion (b) of the WPC. (The abbreviations in the figure are the same with Tab. 1)

was found that the LCTE of WPC_{SF} was significantly lower than that of WPC_{CTRL}, suggesting that the wider rigid nSiO₂ network region effectively reduced the thermal expansion.

3.5 Combustion Characteristics

The WPC_{CTRL} was burned to ashes (Fig. 8a). The white residual material on the surface of WPC_S was nSiO₂, and the bottom was mainly carbonized wood flour (Fig. 8b). The cracks produced on the WPC_S

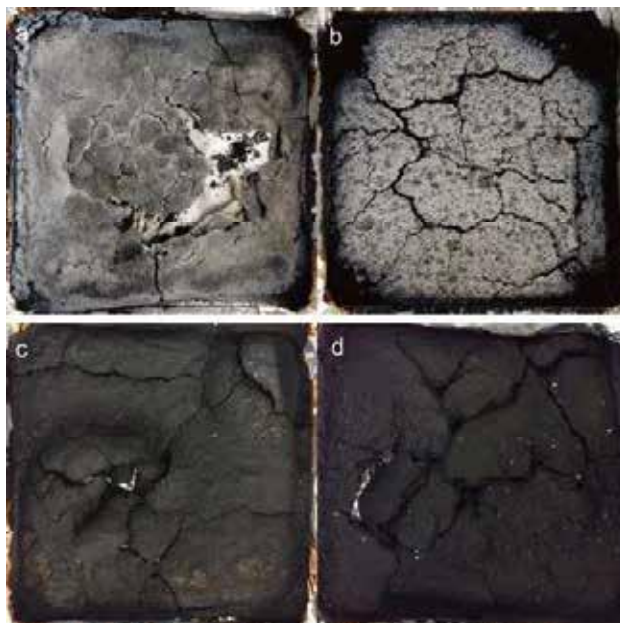


Figure 8: Digital photographs of the residues of four kinds of WPC after cone test: WPC control panel (a), WPC panel with nSiO₂ network (b), WPC panel with fire retardant modified wood flour (c), and WPC panel with nSiO₂ network and fire retardant modified wood flour (d)

residuals were caused by the gas impact, which was responsible for the higher smoke release of WPC_S after 300 s. The residuals of WPC_F also exhibited cracks (Fig. 8c). The combustion residuals of WPC_{SF} were thicker than those of WPC_F because the wider nSiO₂ network region hindered the gas release and the gas impulse caused the expansion of the residuals [4] (Fig. 8d). The physical integrity of the WPC_F and WPC_{SF} residues were poor, indicating a weak strength, which did not help reduce the heat and smoke release of WPC_F and WPC_{SF}. In contrast to WPC_S, no nSiO₂ was deposited on the surface of the WPC_{SF} residues, possibly because the APP and PPA produced by the decomposition of GUP reacted with nSiO₂ to form pyrophosphate silicon [13].

The WPC_{CTRL} was burnt into short carbon fragments (Fig. 9a). Compared with WPC_{CTRL}, the EDS results indicated the formation of an nSiO₂ crust on the residuals surface of WPC_S (Fig. 9b) and a complete carbon skeleton of WF on the bottom of the residuals (not shown). The residuals of WPC_F were dense (Fig. 9c), and their surfaces were coated by lamellar sodium octabonate (Fig. 9d). P and N were detected on the WPC_F residuals by EDS (Fig. 9d), indicating that the degradation products of GUP, such as PPA, also remained on the surface of the residuals. Similar to WPC_F, compact residuals were observed for WPC_{SF} (Fig. 9e). Its surface was coated by a layer of a glassy substance containing Na, P, N, and Si (Fig. 9f), which indicated that this film may be composed of sodium octabonate, polyphosphoric acid, pyrophosphate silicon, and unreacted nSiO₂.

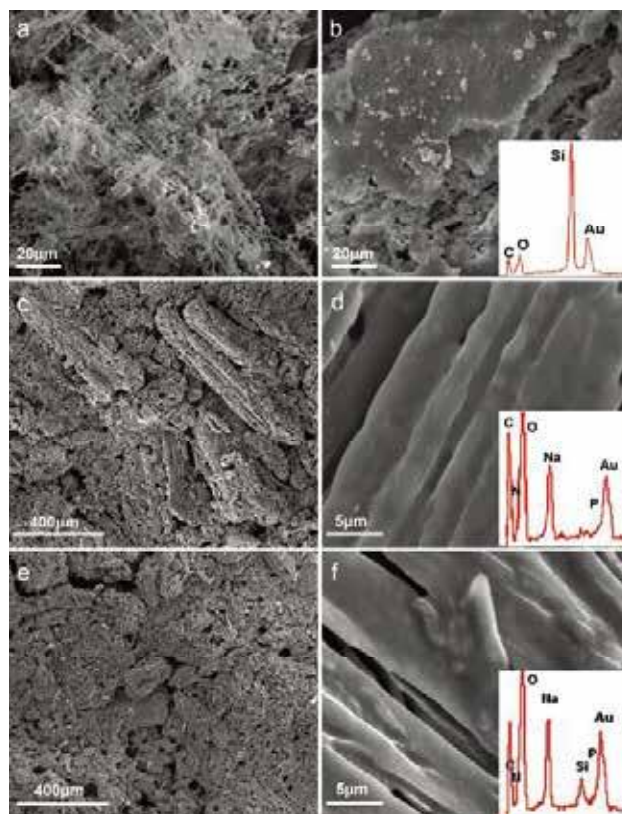


Figure 9: SEM of the WPC residual: the WPC_{CTRL} (a, $\times 1000$), the surface of WPC_S (b, $\times 1000$), the surface of WPC_F (c, $\times 100$; d, $\times 5000$), the surface of WPC_{SF} (e, $\times 100$; f, $\times 5000$), the line drawings in the lower right corner of figure (b), (d), and (f) are from EDS. (The abbreviations are the same with Tab. 1)

Compared with WPC_{CTRL} , the HRR of WPC_S decreased slightly before 300 s during combustion (Fig. 10a) because the $nSiO_2$ network exerted physical shielding and catalytic charring effects [23]. However, the $nSiO_2$ loading (0.55%) was insufficient to significantly decrease the HRR of WPC_S . After 300 s of combustion, the HRR of WPC_S was higher than that of WPC_{CTRL} (Fig. 10a) due to the formation of a large number of cracks on the surface of the residuals (Fig. 8b). These cracks provided channels for heat and combustible gases to penetrate, increasing the HRR [24]. The HRR and THR of WPC_F were lower than those of WPC_{CTRL} (Figs. 10a and 10b). The reasons for the reduction may be as follows: (1) the thermal decomposition reactions of the fire retardant (GUP and DOT) could absorb heat from the fire source. The small molecular gases (H_2O , NH_3 , and CO_2) produced by the decomposition of GUP and DOT could reduce the O_2 concentration, which decreased oxidative pyrolysis [25]; (2) the glassy sodium borate that was produced from the degradation of DOT coated the residuals and provided physical protection [26]; (3) the decomposition products of GUP may have catalyzed the charring of WF [20]. Compared with WPC_F , WPC_{SF} showed a slightly lower HRR and THR, which may have been due to the synergistic effect of the $nSiO_2$ network and fire retardants (DOT and GUP).

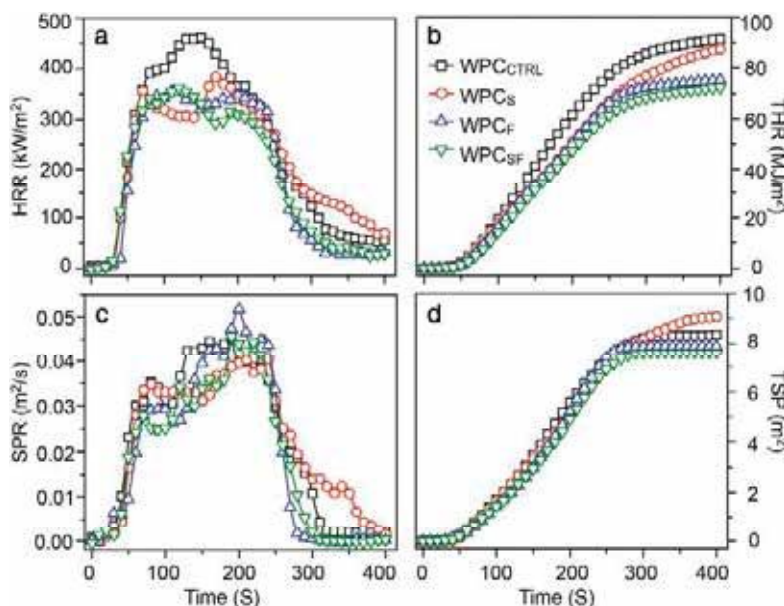


Figure 10: Heat release rate (HRR) (a), total heat release (THR) (b), smoke production rate (SPR) (c), and total smoke production (TSP) (d) of the WPC. (The abbreviations in the figure are the same with Tab. 1)

The SPR and TSP of WPC_S were higher after 300 s compared with those of WPC_{CTRL} (Figs. 10c and 10d). These increased values were due to the production of cracks in the residues during the later stage of combustion, which resulted in the combustion of the bottom substances and an increased smoke release [24]. As for WPC_F , an instantaneous increase in SPR was observed at 200 s. This may be due to the release of the bottom substances due to the local collapse of the residuals (Fig. 8c). The SPR and TSP of WPC_{SF} were lower than those of WPC_{CTRL} , although cracking occurred in the WPC_{SF} residuals (Fig. 8d). The shielding effect of the glassy sodium borate on the bottom substances and the release of H_2O , NH_3 , and CO_2 during combustion reduced the combustion power, which decreased the smoke release of WPC_{SF} .

The combustion reactions are shown in Fig. 11. The silanol groups on the $nSiO_2$ surface acted as active catalytic sites for Brønsted acids that catalyzed the carbonization of WF in WPC_S and WPC_{SF} by removing H

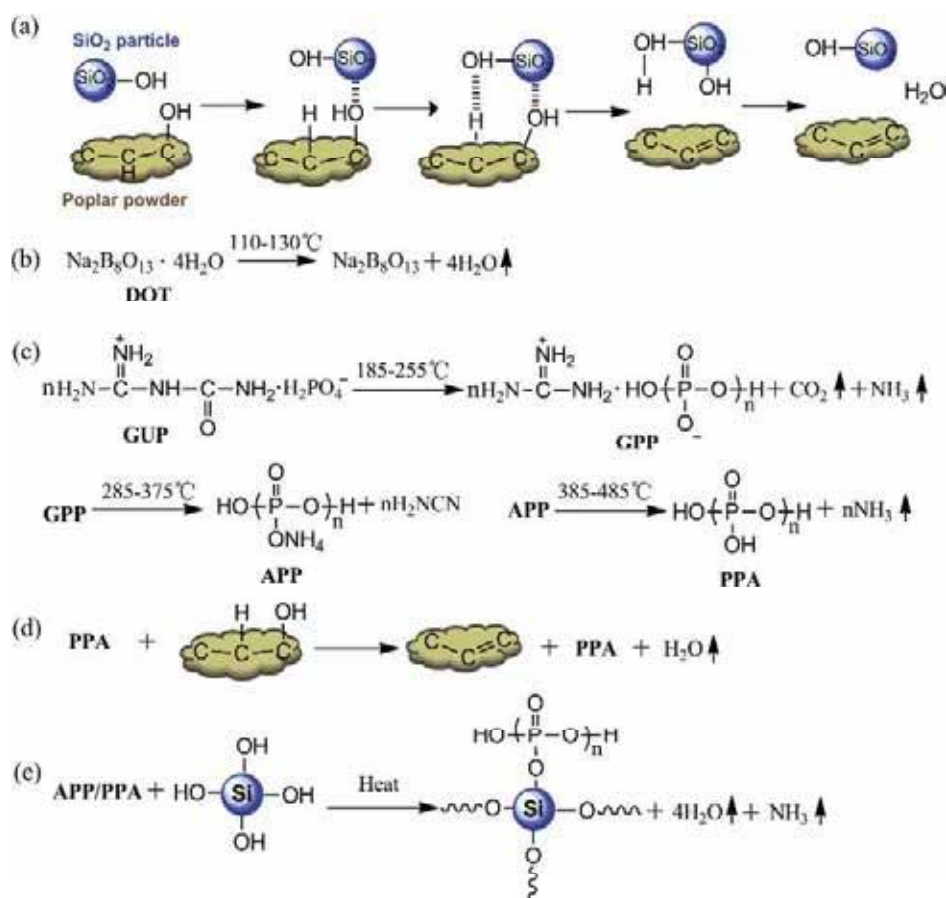


Figure 11: Possible reactions during combustion

and O (Fig. 11a). The formation of a carbonized layer protected the substrate from fire and heat, which decreased the heat release [27]. The DOT in WPC_F and WPC_{SF} decomposed into non-combustible sodium borate and water at 130°C. The sodium borate acted as a barrier, and the water could absorb heat as it evaporated, which both helped reduce the burning rate [28] (Fig. 11b). The GUP decomposed into CO₂, NH₃, and condensed guanidine phosphate (GPP) at temperatures higher than 185°C. The produced GPP further decomposed into ammonium polyphosphate (APP) above 285°C, and the APP decomposed into polyphosphate acid (PPA) and NH₃ above 380°C [29]. The APP and PPA then catalyzed the carbonization of WF by removing H and O [30] (Figs. 11c and 11d), and the formation of a stable carbon layer played a shielding effect to isolate the heat and O₂. The APP or PPA generated during combustion reacted with the nSiO₂ in WPC_{SF} to produce pyrophosphate silicon, H₂O, and NH₃, which could absorb heat and dilute O₂ (Fig. 11e) [13].

The mass retention of WPC_S was similar to that of WPC_{CTRL} (7.2%) after burning for 400 s due to the extremely low nSiO₂ loading in WPC_S (Fig. 12). The mass retention of WPC_F and WPC_{SF} was obviously higher than that of WPC_{CTRL} due to the formation of stable carbon layers. The mass-loss rates (the slope of the curve) of WPC_S, WPC_F, and WPC_{SF} were lower than WPC_{CTRL}, which indicated that the introduction of an nSiO₂ network and fire retardant reduced the burning rate of WPC.

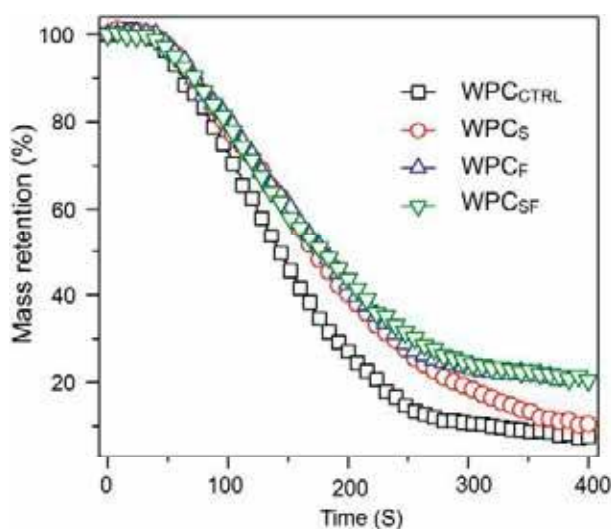


Figure 12: The mass retention of the WPC during combustion. (The abbreviations in the figure are the same with Tab. 1)

4 Conclusions

In this study, a facile approach was used to fabricate WPC with a continuous honeycomb-like nano-SiO₂ network (WPC_S). The rigid nano-SiO₂ network improved the strength and dimensional stability of WPCs at a considerably low nano-SiO₂ content (0.55 wt.%) compared with WPC_{CTRL}. When the WF was modified with fire retardants (DOT and GUP), the flexural modulus and creep resistance of the network-structured WPC (WPC_{SF}) also increased compared with WPC_{CTRL}. WPC_{SF} showed the lowest thermal expansion rate and LCTE, and its flexural strength only decreased by 5.5% compared with that of WPC_{CTRL}. Additionally, WPC_{SF} showed an improved fire retardancy compared with WPC_{CTRL}. The results presented here demonstrated that an efficient and facile procedure could be used to produce WPC with desired functions through the formation of continuous honeycomb-like nanoparticle networks.

Funding Statement: This work was supported by the National Key Research and Development Program of China (Nos. 2019YFD1101204 and 2019YFD1101203), the National Natural Science Foundation of China (Nos. 31870547 and 31901251), the Project funded by China Postdoctoral Science Foundation (No. 2019M652919), the Research and Development Program in Key Areas of Guangdong Province (No. 2020B020216002), the Project of Guangzhou Municipal Key Laboratory of Woody Biomass Functional New Materials (No. 201905010005), and the Project of Key Disciplines of Forestry Engineering of Bureau of Education of Guangzhou Municipality.

Conflicts of Interest: The authors declare that they have no conflicts of interest to report regarding the present study.

References

- Hao, X., Yi, X., Sun, L., Tu, D., Wang, Q. et al. (2019). Mechanical properties, creep resistance, and dimensional stability of core/shell structured wood flour/polycarbonate composites with highly filled core layer. *Construction and Building Materials*, 226, 879–887. DOI 10.1016/j.conbuildmat.2019.07.329.
- Meenakshi, C. M., Krishnamoorthy, A. (2019). Study on the effect of surface modification on the mechanical and thermal behaviour of flax, sisal and glass fiber-reinforced epoxy hybrid composites. *Journal of Renewable Materials*, 7(2), 153–169. DOI 10.32604/jrm.2019.00046.

3. Tazi, M., Erchiqui, F., Godard, F., Kaddami, H. (2014). Evaluation of mechanical properties and durability performance of HDPE-wood composites. *Journal of Renewable Materials*, 2(4), 258–263. DOI 10.7569/JRM.2014.634120.
4. Zhou, H., Xiao, Z., Wang, Y., Hao, X., Xie, Y. et al. (2020). Conductive and fire-retardant wood/polyethylene composites based on a continuous honeycomb-like nanoscale carbon black network. *Construction and Building Materials*, 233, 117369–117377. DOI 10.1016/j.conbuildmat.2019.117369.
5. Guan, Y. H., Huang, J. Q., Yang, J. C., Shao, Z. B., Wang, Y. Z. (2015). An effective way to fire-retard biocomposite with ethanolamine modified ammonium polyphosphate and its fire retardant mechanisms. *Industrial & Engineering Chemistry Research*, 54(13), 3524–3531. DOI 10.1021/acs.iecr.5b00123.
6. Hao, X., Zhou, H., Wang, Q., Wang, H., Song, Y. et al. (2018). Reinforcement of wood flour/HDPE composite with a copolyester of p-hydroxy benzoic acid and 2-hydroxy-6-naphthoic acid. *Journal of Applied Polymer Science*, 47338(15), 1–8. DOI 10.1002/app.47338.
7. Subrahmanian, V., Albert, N. E. M. (2019). Studies on physical chemistry of rubber-rice husk ash composites. *Journal of Renewable Materials*, 7(2), 171–192. DOI 10.32604/jrm.2019.00090.
8. Gao, H., Xie, Y., Ou, R., Wang, Q. (2012). Grafting effects of polypropylene/polyethylene blends with maleic anhydride on the properties of the resulting wood-plastic composites. *Composites Part A: Applied Science and Manufacturing*, 43(1), 150–157. DOI 10.1016/j.compositesa.2011.10.001.
9. Lee, S. Y., Yang, H. S., Kim, H. J., Jeong, C. S., Lim, B. S. et al. (2004). Creep behavior and manufacturing parameters of wood flour filled polypropylene composites. *Composite Structures*, 65(3–4), 459–469. DOI 10.1016/j.compstruct.2003.12.007.
10. Yadav, S. M., Yusoh, K. B. (2018). Subsurface mechanical properties and subsurface creep behaviour of modified nanoclay-based wood-plastic composites studied by nanoindentation. *Polymer Bulletin*, 76(5), 2179–2196. DOI 10.1007/s00289-018-2497-5.
11. Liu, R., Luo, S., Cao, J., Peng, Y. (2013). Characterization of organo-montmorillonite (OMMT) modified wood flour and properties of its composites with poly(lactic acid). *Composites Part A: Applied Science and Manufacturing*, 51, 33–42. DOI 10.1016/j.compositesa.2013.03.019.
12. Siengchin, S., Dangtungee, R. (2014). Polyethylene and polypropylene hybrid composites based on nano silicon dioxide and different flax structures. *Journal of Thermoplastic Composite Materials*, 27(10), 1428–1447. DOI 10.1177/0892705714526916.
13. Pan, M., Mei, C., Du, J., Li, G. (2014). Synergistic effect of nano silicon dioxide and ammonium polyphosphate on flame retardancy of wood fiber-polyethylene composites. *Composites Part A: Applied Science and Manufacturing*, 66, 128–134. DOI 10.1016/j.compositesa.2014.07.016.
14. Zhou, H., Hao, X., Wang, H., Wang, X. Y., Liu, T. et al. (2018). The reinforcement efficacy of nano- and microscale silica for extruded wood flour/HDPE composites: the effects of dispersion patterns and interfacial modification. *Journal of Materials Science*, 53(3), 1899–1910. DOI 10.1007/s10853-017-1650-0.
15. Pan, M. Z., Lian, H. L., Mei, C. T. (2012). Flammability of nano silicon dioxide-wood fiber-polyethylene composites. *Journal of Composite Materials*, 47(12), 1471–1478. DOI 10.1177/0021998312448499.
16. Jiang, L., Wolcott, M. P., Zhang, J., Englund, K. (2007). Flexural Properties of surface reinforced wood/plastic deck board. *Polymer Engineering & Science*, 47(3), 281–288. DOI 10.1002/pen.20705.
17. Potts, J. R., Shankar, O., Du, L., Ruoff, R. S. (2012). Processing-morphology-property relationships and composite theory analysis of reduced graphene oxide/natural rubber nanocomposites. *Macromolecules*, 45(15), 6045–6055. DOI 10.1021/ma300706k.
18. Donmez, C. A., Mengeloğlu, F., Karakus, K. (2015). Effect of boric acid and borax on mechanical, fire and thermal properties of wood flour filled high density polyethylene composites. *Measurement*, 60, 6–12. DOI 10.1016/j.measurement.2014.09.078.
19. Baysal, E., Yalinkilic, M. K., Altinok, M., Sonmez, A., Peker, H. et al. (2007). Some physical, biological, mechanical, and fire properties of wood polymer composite (WPC) pretreated with boric acid and borax mixture. *Construction and Building Materials*, 21(9), 1879–1885. DOI 10.1016/j.conbuildmat.2006.05.026.

20. Ayırlmis, N., Akbulut, T., Dundar, T., Mengeloglu, F., Buyuksari, U. et al. (2012). Effect of boron and phosphate compounds on physical, mechanical, and fire properties of wood-polypropylene composites. *Construction and Building Materials*, 33, 63–69. DOI 10.1016/j.conbuildmat.2012.01.013.
21. Suzuki, N., Kiba, S., Yamauchi, Y. (2011). Bimodal filler system consisting of mesoporous silica particles and silica nanoparticles toward efficient suppression of thermal expansion in silica/epoxy composites. *Journal of Materials Chemistry*, 21(38), 14941–14947. DOI 10.1039/c1jm12405f.
22. Rao, Y. Q., Blanton, T. N. (2008). Polymer nanocomposites with a low thermal expansion coefficient. *Macromolecules*, 41(3), 935–941. DOI 10.1021/ma7020216.
23. Kashiwagi, T., Gilman, J. W., Butler, K. M., Harris, R. H., Asano, A. (2000). Fire retardant mechanism of silica gel/silica. *Fire & Materials*, 24, 277–289. DOI 10.1002/1099-1018(200011/12)24:63.0.CO;2-A.
24. Zhao, Q., Zhang, B., Quan, H., Yam, R. C. M., Yuen, R. K. K. et al. (2009). Fire retardancy of rice husk-filled high-density polyethylene ecocomposites. *Composites Science and Technology*, 69(15–16), 2675–2681. DOI 10.1016/j.compscitech.2009.08.009.
25. Winandy, J. E., Wang, Q., White, R. H. (2008). Fire-retardant-treated strandboard: properties and fire performance. *Wood and Fiber Science*, 40(1), 62–71. DOI 10.1177/0040517507082635.
26. Wu, G. F., Xu, M. (2014). Effects of boron compounds on the mechanical and fire properties of wood-chitosan and high-density polyethylene composites. *BioResources*, 9, 4173–4193.
27. Tsutsumi, K., Kurata, N., Takata, E., Furuichi, K., Nagano, M. et al. (2014). Silicon semiconductor-assisted Brønsted acid-catalyzed dehydration: highly selective synthesis of 5-hydroxymethylfurfural from fructose under visible light irradiation. *Applied Catalysis B: Environmental*, 147, 1009–1014. DOI 10.1016/j.apcatb.2013.10.032.
28. Wang, Q., Li, J., Winandy, J. (2004). Chemical mechanism of fire retardance of boric acid on wood. *Wood Science and Technology*, 38(5), 375–389. DOI 10.1007/s00226-004-0246-4.
29. Li, B., Zhang, X., Su, R. (2002). An investigation of thermal degradation and charring of larch lignin in the condensed phase: the effects of boric acid, guanlyl urea phosphate, ammonium dihydrogen phosphate and ammonium polyphosphate. *Polymer Degradation and Stability*, 75(1), 35–44. DOI 10.1016/S0141-3910(01)00202-6.
30. Samyn, F., Bourbigot, S., Duquesne, S., Delobel, R. (2007). Effect of zinc borate on the thermal degradation of ammonium polyphosphate. *Thermochimica Acta*, 456(2), 134–144. DOI 10.1016/j.tca.2007.02.006.



Simultaneously strengthening and toughening reprocessable basswood through reactive waterborne acrylic resin impregnation

Jiahua Zhou^{a,b}, Xiaolong Hao^{a,b}, Haiyang Zhou^{b,*}, Rongxian Ou^{a,b,*}, Qingwen Wang^{a,b}

^a Institute of Biomass Engineering, Key Laboratory of Energy Plants Resource and Utilization (Ministry of Agriculture and Rural Affairs), South China Agricultural University, 483 Wushan Road, Guangzhou 510642, China

^b Key Laboratory for Biobased Materials and Energy of Ministry of Education, College of Materials and Energy, South China Agricultural University, 483 Wushan Road, Guangzhou, 510642, China

ARTICLE INFO

Keywords:

Wood modification
Strengthening and toughening
Resin impregnation
Waterborne acrylic resin
Reprocessability

ABSTRACT

It is indeed challenging to simultaneously strengthen and toughen woody material while maintaining its recyclability using existing modification technology. In this study, we have successfully fabricated high-performance and re-processable basswood with outstanding dimensional stability through reactive waterborne acrylic resin impregnation. The pathways of resin movement within the basswood's multi-scale structure were discussed in detail. In comparison with unmodified wood, the compressive strength parallel/perpendicular to the grain, hardness, and modulus of rupture (MOR) were increased by 73.8 %, 179.4 %, 406.1 %, and 113.6 %, respectively. The compressive strength reached the standard of C70 degree for concrete, and MOR complied with the highest standard (TB20) of hardwood used as a building material. Moreover, the impact bending strength was enhanced by 113.1 % compared with the unmodified wood. Additionally, the water uptake of modified wood was 85.4 % lower than the unmodified wood, and the anti-swelling effect reached up to 42.8 %. Furthermore, the modified wood demonstrated recyclability and retained satisfactory strength after reprocessing, with the tensile strength of the first recovery reaching 22.5 MPa and the flexural strength reaching 31.5 MPa. This study thus provided a novel strategy for creating high-performance and recyclable wood, which holds significant promise for expanding the application area of woody materials, especially as a replacement for non-renewable materials such as concrete in the construction field.

1. Introduction

The emergence of the “double carbon” strategy has brought increased attention to wood as a lightweight, high-strength, environmentally friendly material, offering the additional benefit of carbon sequestration [1–3]. However, the contradiction between timber supply and demand has become more pronounced [4] due to the scarcity of high-quality hardwood resources, domestic bans on natural forest exploitation, and foreign restrictions on timber exports. The limited properties of available wood constrain its potential for high-value-added applications, such as structural materials and smart buildings.

Wood modification, encompassing physical modification [5–7] and chemical modification [8–13], has been widely employed to enhance the properties of wood. Despite these efforts, achieving simultaneous improvements in the strength and toughness of wood remains a

considerable challenge in existing literature. Generally, the enhancement of mechanical strength is often accompanied by a decrease in toughness, as observed in processes like heat treatment, furfurylated modification, or 1,3-dimethylol-4,5-dihydroxy-ethyleneurea (DMDHEU) impregnation [14–21]. This outcome arises from the decomposition of hemicellulose and lignin in the wood due to the excessively high temperatures or improper pH values [21]. Furthermore, the intrusion of small molecules into the cell wall, followed by cross-linking to form a three-dimensional structure, hinders the movement of macromolecules, leading to a reduction in wood toughness. Examples include phenolic resin and urea-formaldehyde resin [18–20]. However, wood is often required to exhibit both high strength and desirable toughness in certain applications.

Polymer monomer modification offers a fresh approach [22–26], where organic monomers polymerized through free radical initiation to

* Corresponding authors at: Institute of Biomass Engineering, Key Laboratory of Energy Plants Resource and Utilization (Ministry of Agriculture and Rural Affairs), South China Agricultural University, 483 Wushan Road, Guangzhou 510642, China (R. Ou).

E-mail addresses: hyzhou@scau.edu.cn (H. Zhou), rongxian_ou@scau.edu.cn (R. Ou).

<https://doi.org/10.1016/j.cej.2024.151313>

Received 16 February 2024; Received in revised form 3 April 2024; Accepted 14 April 2024

Available online 15 April 2024

1385-8947/© 2024 Elsevier B.V. All rights reserved.

improve physical and mechanical properties of wood. This method helps prevent degradation of wood components, especially hemicellulose, as free radical initiators are generally not acidic or alkaline. Acrylates are commonly used as polymer monomers [21,27–29]. For instance, Montanari *et al.* reported on a new fully bio-based transparent wood biocomposite, achieved with a novel limonene acrylate monomer. This monomer is impregnated and readily polymerized in a delignified, succinylated wood substrate to form transparent biocomposites with excellent mechanical properties [27]. X. Zhang *et al.* developed modified poplar wood with high fire resistance, dimensional stability, and mechanical strength by combining the impregnation of N/P-doped acrylic resin and unilateral surface densification [28].

While there has been extensive research on wood modification, the recycling and utilization of modified wood have been rarely addressed. Some modifiers form a three-dimensional network structure [30], making the recycling of modified wood very difficult, as they are generally infusible or insoluble. Realizing the recovery or recycling of modified wood would be more environmentally friendly than degradation or incineration. Drawing an analogy to plastics, although biodegradable plastics can return carbon and nutrients to the soil, the energy and resources associated with their production are effectively lost [31].

Currently, discarded or modified wood is extracted with useful substances such as lignin [32] or crushed and added with adhesive to prepare artificial boards or as auxiliary materials for other composite materials [33,34], or dissolved with an acidic solution to prepare wood pulp [35] or incinerated. However, these methods often require the additional chemicals. If the modified wood could be recovered and recycled without adding extra chemicals, it would not only broaden its application but also significantly extend its life cycle, making it most environmentally friendly. Arkema's thermoplastic recyclable liquid resin which polymerizes through free radical initiation into a polyacrylate, offers inspiration in solving the challenge of recycling modified wood, given its use for laminating with continuous long fibers (carbon fiber, glass fiber) [36,37].

In this study, we introduce an approach to simultaneously strengthen and toughen wood through impregnation using the Elium®1880 resin and describe the enhancement mechanism in detail. Additionally, we discuss the reprocessability of the modified wood. This study provided a novel strategy for wood modification, holding significant promise for expanding the application area of woody materials, particularly as a replacement for non-renewable materials such as concrete in the construction field.

2. Material and methods

2.1. Materials

Plain-sawn basswood (*Tilia cordata* Mill.) lumbers without defects were used with an air-dry density of 0.52–0.56 g cm⁻³ and a dimension of 200 × 100 × 10 mm (L × T × R). The low viscosity thermoplastic reactive liquid acrylic resin (Elium®1880) and an initiator were supplied by ARKEMA (China) Investment Co., Ltd. (Shanghai, China).

Table 1
Information on the resin.

	Information
Appearance	Light yellow transparent liquid
Liquid density	1.01 g cm ⁻³
Viscosity	100 mPa s at 25 °C
Main component	Methyl methacrylate-ethyl acrylate monomer and prepolymer
Molecular weight ^a	80–480 Da
Process time	45–70 min
Flexural strength	110 MPa
Initiator	Dibenzoyl peroxide

^a : The liquid chromatography-mass spectrometry spectra of the resins are displayed in Fig. S1.

Additional details regarding the resin are presented in Table 1.

2.2. Preparation of polyacrylate-reinforced basswood composites

The process of preparing polyacrylate-reinforced basswood composites is depicted in Fig. 1. Basswood lumbers with an oven-dried density of 0.48–0.52 g cm⁻³ were selected to minimize the influence of wood variability. The wood samples were placed in a Teflon (PTFE) container. Solutions of acrylic resin with 1.5 wt% initiators were uniformly mixed under stirring for 3 min. The mixed solutions were then poured into the container to submerge the wood samples. Eight impregnation processes were conducted as detailed in Table 2. After impregnation, any residual resin on the sample surface was blotted away using dustless papers. The impregnated samples were then placed into a vacuum-sealed bag and heated for 2 h at 30 °C, followed by 2 h at 80 °C. Vacuum sealing was employed to prevent the volatilization of small molecules and the oxygen inhibition of free radical polymerization of acrylic resin.

2.3. Characterization

The details pertaining to the characterization of the modified wood samples are provided in the Supplementary Information section.

3. Results and discussion

3.1. Physical properties

The resin impregnated effectively increased the density and reduced the porosity of basswood (Fig. 2). The oven-dried density gradually increased from 0.50 to 1.10 g cm⁻³, while the porosity decreased from an initial 64.6 % to 14.0 %, lower than the porosity (22.0 %) observed in epoxy impregnated and compressed wood [38]. The WPG of A30 was only 14.7 %. In the absence of external forces, the resin entered the wood to a limited extent through capillarity and diffusion. Therefore, impregnation pressure plays a crucial role in the impregnation effect. For V10, the WPG increased substantially, reaching 46.3 %. This is due to the resin further entering under pressure difference and the extraction of gas from within the wood during the vacuuming process, which provides more space for the resin to fill in. Subsequently, WPG showed a linear improvement with the increase of impregnation time and pressure, from V10/A30 to V10/P60-6. Among these, the WPG of V10/P60-6 reached to 123.1 %. This suggests that the synergistic effect of vacuum and pressure effectively improve the WPG of wood.

If vacuuming is omitted, although more resin enters at extra pressure, the compressed air inside the wood prevents further resin filling. Additionally, when the pressure is released, the expanded air causes some resin to be expelled, leading to a reduction in WPG. In addition to WPG, the values of VFP are also noteworthy. As depicted in Fig. 2a, the resin filled only 9.8 % of the pores treated with A30. After vacuum impregnation for 10 min, the resin filled 28.3 % of the pores, and even occupied up to 78.5 % of the pores treated with V10/P60-6.

Surface color: The Lab values for each group are shown in Fig. 2b. A positive value of “a” indicated a red color family, while a positive value of “b” indicated a yellow color family. As the impregnation time and pressure increased, the value of “L” showed a tendency to decrease, while the value of “a” and “b” presents an upward trend (Fig. 2b). Overall, the wood became more yellow and darker after impregnation with resin. The greater the resin filling, the larger the color difference between the modified wood and the unmodified wood (Fig. 2c).

Surface roughness: The smoothness of the modified wood improved compared with the unmodified wood because the flowing resin filled the exposed cell and vessel lumina on the wood surface (Fig. 2d). However, when the impregnation time was extended to 70 min (V10/P60-1 and V10/P60-6), the roughness increased compared to the results obtained with shorter impregnation times.



Fig. 1. Schematic diagram of the preparation of modified basswood.

Table 2

The impregnation process used for the samples.

Sample	Impregnation process
A30	Atmospheric impregnation for 30 min
V10	Vacuum impregnation for 10 min
V10/A10	Vacuum impregnation for 10 min and atmospheric impregnation for 10 min
V10/A30	Vacuum impregnation for 10 min and atmospheric impregnation for 30 min
V10/P30-1	Vacuum impregnation for 10 min and pressure impregnation at 1 bar for 30 min
V10/P60-1	Vacuum impregnation for 10 min and pressure impregnation at 1 bar for 60 min
V10/P30-6	Vacuum impregnation for 10 min and pressure impregnation at 6 bar for 30 min
V10/P60-6	Vacuum impregnation for 10 min and pressure impregnation at 6 bar for 60 min

Note: A represents atmospheric impregnation; V stands for vacuum impregnation; P denotes pressure impregnation; the numbers following the letters represent the impregnation duration; the numbers following the “-” denote the impregnation pressure.

3.2. Reaction mechanism

Based on the FTIR spectrum (Fig. 3), it is evident that the C = C peak at 1676 cm^{-1} observed in uncured resin disappears in the resin after polymerization and in the modified wood. This indicates that the resin polymerizes from unsaturated small molecules to saturated macromolecules in the presence of initiator, and that the resin cures completely under the set curing process. The C = O stretching vibration of the modified wood at 1734 cm^{-1} was enhanced compared to that of the unmodified wood due to the superimposition of the peak of resin at the corresponding position. Additionally, the coupling peak of the saturated and unsaturated C – H stretching vibration (near 2996 cm^{-1}) in acrylate appeared in the modified wood, as well as the peaks of C – H bending vibration at 844 and 755 cm^{-1} [39]. These findings indicate that the resin successfully permeated and polymerized within the wood. The modified wood exhibited characteristic peaks that were the superimposition of the peaks of unmodified wood and impregnated resin. No new absorption peaks appeared, suggesting that the resin did not chemically react with the wood, consistent with the findings of Y. Dong [40].

3.3. Distribution of resin

The distribution of resin under different impregnation processes significantly influences the properties of modified wood. The superficial densities of A30 slightly increased due to a small amount of resin entering the wood via the pits on the tangential section, while its density in the intermediate layer was almost the same as the unmodified wood (Fig. 4a–b), indicating a poor impregnation effect. The density of the intermediate layer from V10 to V10/P60-6 gradually increased, signifying high penetration. The resin amount near the surfaces is significantly higher than that in the intermediate layer from V10 to V10/P60-1. Conversely, the density distribution curves of V10/P30-6 and V10/P60-6 exhibited the opposite trend, with the resin content in the intermediate layer is higher than that on the surfaces. This discrepancy arose because the resin near the surfaces is liable to recoil out during pressure relief. The densities of V10/P30-6 and V10/P60-6 in the intermediate layer were essentially steady and reached a peak among all modified woods, achieving excellent impregnation volumes and a homogeneous distribution of resin within a short impregnation time.

The resin in wood primarily derives from longitudinal transport, especially through the vessels due to the existence of perforation between vessel element and relies on the penetration in the radial and tangential direction, i.e., from the pits. At smaller pressures, there was a large difference in transport efficiency between the two routes, faster in the longitudinal direction and slower in the transverse direction, resulting in a varied distribution of the resin. At higher pressures, the resin penetrated not only into the vessels but also into the fiber cell lumens through pits, achieving better penetrance and superior homogeneity.

Basswood, a diffuse porous wood with slightly larger pores and few to medium wood ray, exhibited vessel diameters above $50\text{ }\mu\text{m}$ (Fig. 4c–d). The vessels serve as the main open axial flow path through the wood due to existing perforations between the vessel elements. After 10 min of vacuum impregnation, the resin filled only the vessel lumens but did not enter the fiber cell lumens due to the tiny communicative channel (i.e. pits) between the cells (Fig. 4e). With higher pressures and longer times, small molecules in resin sequentially entered the fiber cell lumens through the connecting pits in both radial and tangential directions (Fig. 4g). At a higher magnification, it can be observed that the resin was tightly bonded to the wood cell wall (Fig. 4f–h). Although the resin was not chemically cross-linked with the wood, the promising interfacial bond allowed the resin to be stabilized inside the wood.

The 3D structure of the samples was further investigated using

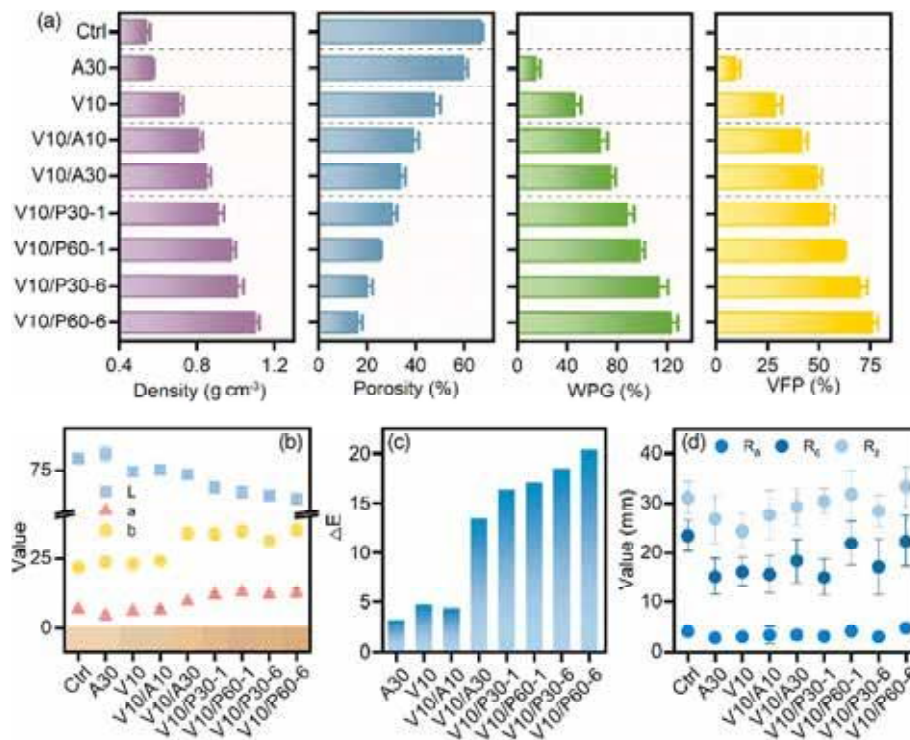


Fig. 2. Physical properties of the unmodified and modified wood: (a) density, porosity, weight percent gain (WPG), volume filling percentage (VFP), (b) surface color, (c) color difference, (d) surface roughness.

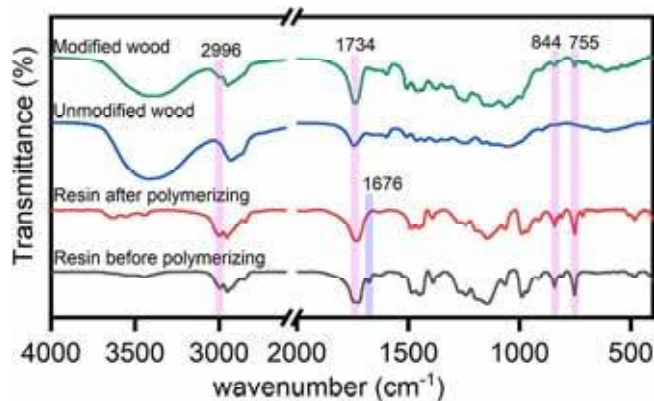


Fig. 3. FT-IR spectrogram.

micro-CT (Fig. 5). It was found that the original basswood contained 35.54 vol% wood phase and 64.46 vol% pore phase, which is quite similar to the calculated values of 35.42 % wood phase and 64.58 % pore phase (Fig. 2a). A new WPG was calculated based on the volume percentage and density of each phase. The porosity and WPG of modified wood obtained from micro-CT were compared with the calculated values (Table 3). For the V10 sample, the porosity obtained by CT was slightly smaller than the calculated value. This difference may be due to the existence of micropores in the wood after the resin polymerized in it, which were difficult to detect by CT with a resolution of 5 μm . Conversely, for V10/P60-6, the CT-derived porosity is slightly higher than the calculated value. This could be attributed to the leaching of wood cell wall substances by the organic solvents in the resin under prolonged high-pressure impregnation, resulting in the development of macropores within the cell wall or the filling of these macropores with resin. This could cause an increase in the CT value and a decrease in the calculated value of the porosity. The decrease in the volume percentage of wood phase from unmodified wood to V10/P60-6 (Fig. 5a-2 and c-2),

also indicated that a small amount of cell wall substances was leached out. The results of pore distribution (Fig. 5a-5, b-5, and c-5) also indicated that the wood vessels were filled with resin after vacuum impregnation for 10 min. The pores (30–50 μm) were occupied after applying pressure, and the pore sizes changed from the macropores to the micropores.

3.4. Water resistance and anti-swelling effect

Following impregnation modification, the water resistance of the basswood was significantly improved. As illustrated in Fig. 6a, after soaking for 288 h, the water uptake of V10 (51.9 %) was reduced by 55.5 % compared to the unmodified wood (116.6 %). The water uptake gradually decreased with the improvement of the impregnation time and pressure. The water uptake of V10/P60-6 was further reduced to 17.0 %, indicating an 85.4 % decrease compared to unmodified wood. The substantial filling of the wood pores by the polymerized resin prevents water from entering and accumulating in the wood, thereby enhancing its dimensional stability. Subsequently, the thickness swelling of the wood was reduced (Fig. 6b), with the maximum reduction from 9.6 % before modification to 4.9 % after modification, representing a 49.2 % decrease. Additionally, the ASE reached up to 42.8 % (Fig. 6c). This is attributed to the physical barrier formed by the *in-situ* polymerization of the resin, primarily in the wood, which reduces the availability of –OH groups in the wood cell wall, leading to a notable reduction in water uptake. Moreover, methacrylates can infiltrate the cell walls [41], further enhancing the dimensional stability of the modified wood.

The enhancement in water resistance is further supported by the WCA test. The mean WCA values at 100 s are shown in Fig. 6d. The WCA of the modified wood showed a significant increase compared to the unmodified wood. Not only did the WCA increase, but the residence time of the droplet on the surface of the modified wood was also prolonged. At 20 s, the droplet on unmodified wood nearly disappeared. However, the WCA was still above 55° at 600 s for V10/PI30-6 and V10/

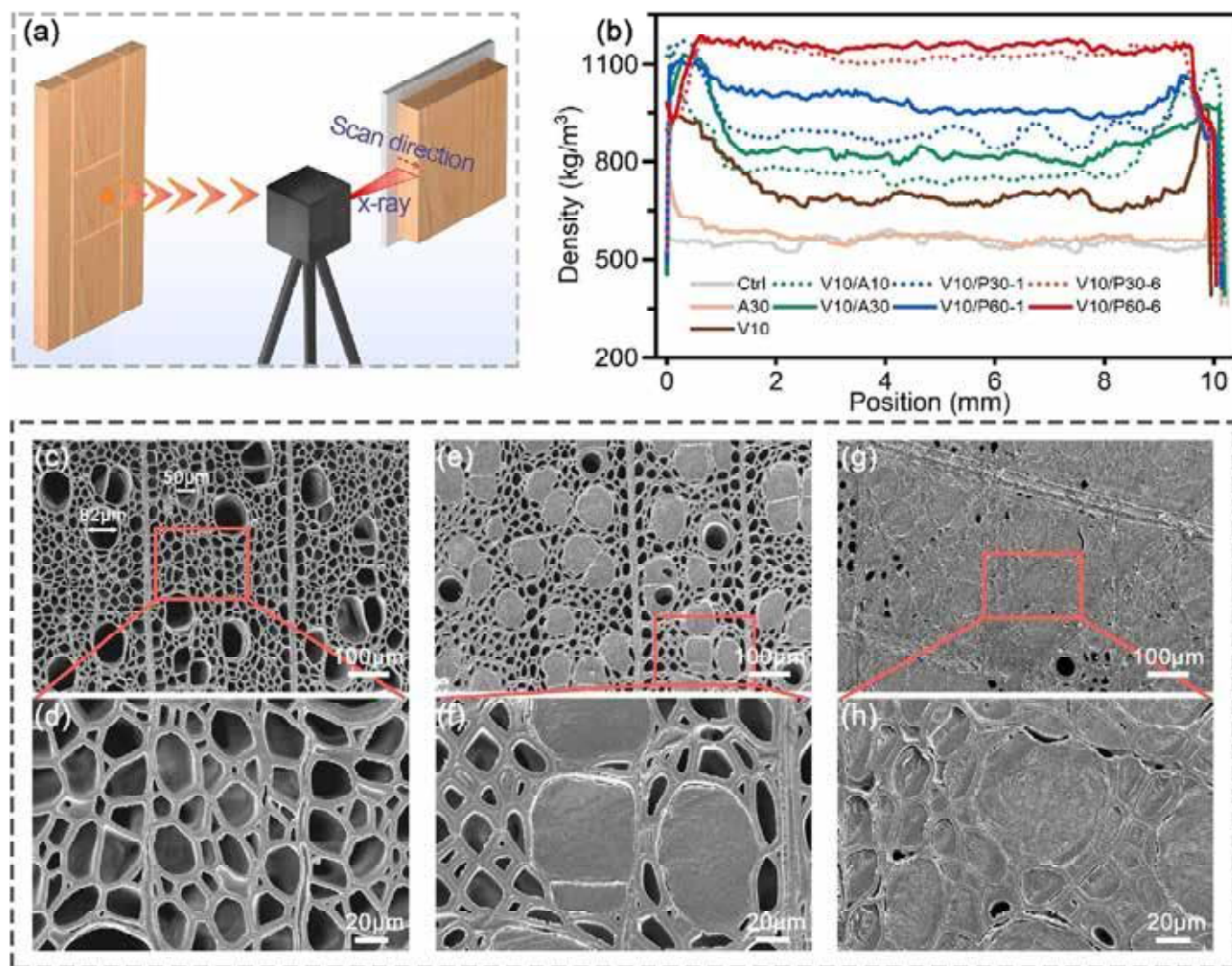


Fig. 4. Distribution of resin: (a) vertical density profile (VDP) measurements schematic, (b) VDP curves, SEM of (c-d) unmodified wood, (e-f) V10, and (g-h) V10/P60-6.

P60-6 (Fig. S2), indicating that the modified wood was less susceptible to water infiltration and intrusion, consequently reducing the dimensional changes of the wood due to moisture. In addition to water, moisture is another common factor causing dimensional changes in wood. The incorporation of resin reduces the absorption of moisture, as confirmed by the reduction of EMC.

3.5. Mechanical properties

Compressive strength is a vital parameter for measuring the mechanical properties of wood, especially as a building material. The compressive strength parallel to the grain of wood (CS_{\parallel}) represents the material's strength when damaged. Compression damage perpendicular to the grain of wood is primarily caused by squeezing and flattening of the cells, resulting in a significant deformation [42]. Therefore, the proportional limit strength was taken as compressive strength perpendicular to grain (CS_{\perp}) (Fig. S3a). The modified wood exhibited a notable enhancement in CS_{\perp} (Fig. 7a). CS_{\perp} of V10 was nearly double that of the unmodified wood (3.6 MPa). The reinforcement of V10/P60-6 reached up to 2.8 times that of the unmodified wood.

The connection among microfilaments is non-covalent in the transverse direction, making wood susceptible to compressive force in the cross-grain direction. The filling of resin limits further compressive

strain failure of the wood and provides strong mechanical support, ensuring stress transfer within the wood [26]. With the increase of WPG, CS_{\parallel} gradually increased. The CS_{\parallel} (69.8 MPa) of V10 was significantly increased when the resin was filled wood vessels, by 58.5 % compared to unmodified wood (44.1 MPa). The enhancement effect gradually leveled off from V10 to V10/P60-6. This may be attributed to the filling of the resin in the large channels, forming a uniaxially continuous reinforced polymer, while the polymer within smaller cell lumens contributes less due to its dispersed and non-continuous distribution. Despite the substantial increase in WPG, the further improvement of CS_{\parallel} is limited (Table S1). Nevertheless, CS_{\parallel} reached the standard of C70 degree for concrete, signifying that the prepared modified wood is comparable to high-performance concrete and suitable for use in high-rise buildings exceeding 30 to 60 stories.

With the increase in WPG, the hardness of the modified wood substantially increased (Fig. 7b). The hardness of V10/A10 (4.2 kN) was more than doubled that of unmodified wood (1.6 kN), and the hardness of V10/P60-6 reached a peak (8.4 kN) with an increase of 406.1 %.

Flexural strength, another essential load-bearing parameter of building materials signifies the material's ability to withstand bending loads without fracture. From the stress-strain curves (Fig. S3b), it was observed that beyond the maximum stress, both modified and unmodified wood exhibited ductile damage, i.e., multiple step-by-step damage.

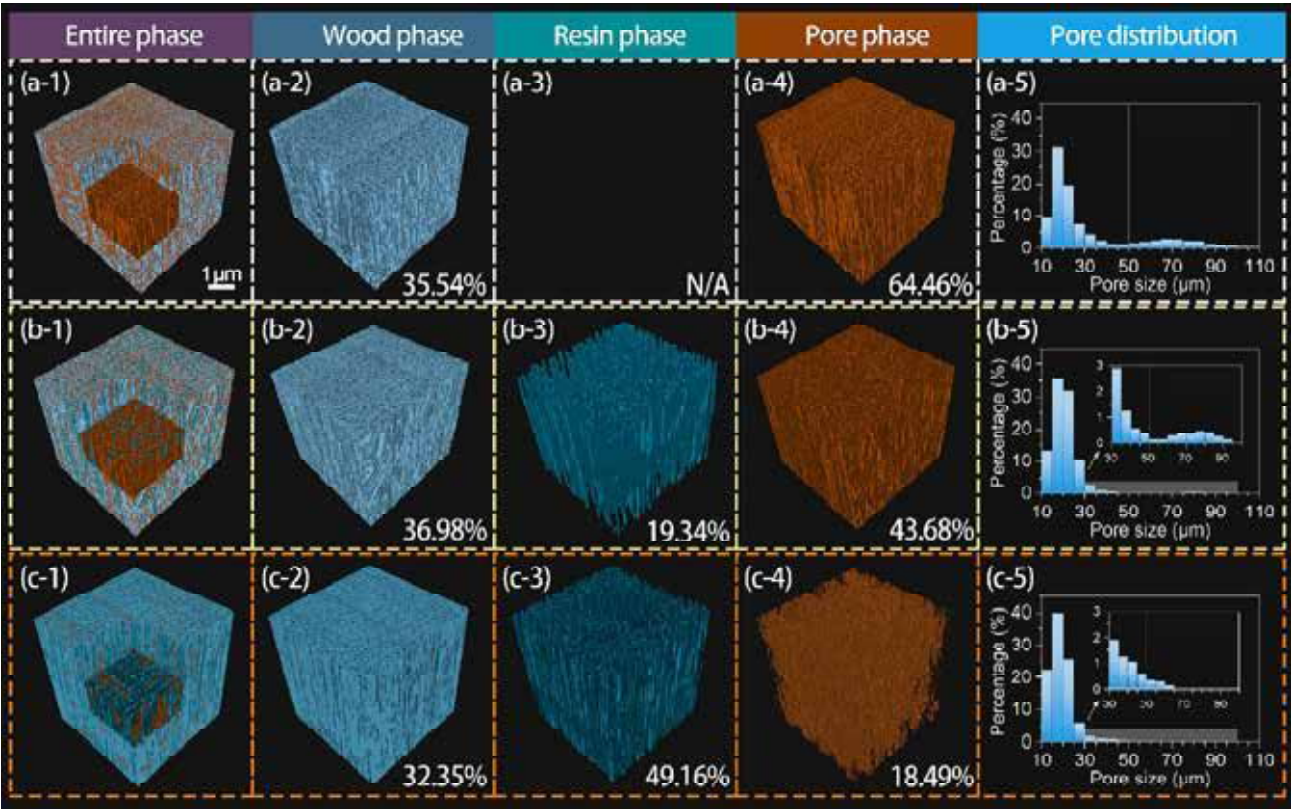


Fig. 5. Micro-CT of samples:(a-1) – (a-5): unmodified basswood, (b-1) – (b-5): V10, (c-1) – (c-5): V10/P60-6, including the entire phase, separated wood, resin, and pore phases; as well as the pore distributions in terms of the analysis of pore phases.

Table 3
The comparative porosity and WPG between formula calculation and micro-CT test.

	Porosity (%)		WPG (%)	
	calculated values	micro-CT values	calculated values	micro-CT values
Control	64.58	64.46	–	–
V10	46.55	43.68	46.27	44.14
V10/P60-6	14.00	18.49	123.14	128.25

The flexural strength dramatically increased after modification by Elium®1880 resin. It is observed that MOR is mostly linearly and positively correlated with WPG (Fig. S3c). Different from MOR, MOE is linear with WPG after WPG exceeds 50 %. As illustrated in Fig. 7c, MOR increased progressively from 81.6 to 174.4 MPa, an increase of 113.6 %; MOE elevated from 10.3 to 14.4 GPa. Modified woods, except for A30, comply with the highest standards (TB20) of hardwood used as a building material according to GB 50206–2012. Additionally, this study achieved more excellent reinforcement compared to the epoxy-modified wood at similar WPG [38].

In conclusion, this study has demonstrated exceptional enhancement closely associated with the excellent performance and sufficient filling level of the resin inside the wood. The monomers enter the pores at impregnation pressure [48,49] and polymerize *in situ* inside the wood, providing additional mechanical support and stabilization of stress within the wood [26]. The polymers inside the wood offer resistance to bending and prevent material damage when subjected to external forces [14].

The strains at break of the modified wood are significantly increased compared to natural wood (Fig. S3d), suggesting that the modified wood can withstand a higher degree of deformation without drastic damage,

indicating an increase in toughness. As shown in Fig. S3f, the brittleness (B_T) of the modified wood is slightly lower than that of the unmodified wood, suggesting that the modification of wood with Elium® resin does not negatively impact the toughness of the wood and may even improve it to a certain degree. To further confirm the toughening effect of the resin despite some uncertainty in the curve fitting, this work tested the IBS. The results, as shown in Fig. 7d, indicated a progressive increase in IBS from 28.7 kJ m⁻² for unmodified wood to 61.1 kJ m⁻² for V10/P60-6, signifying an increase in toughness consistent with the B_T findings. In contrast to modification techniques such as heat treatment, furfuryl alcohol treatment, and DMDHEU resin impregnation, which negatively affect wood toughness [15–21], this work achieved an improvement in toughness as well as strength and stiffness.

Fig. S4 contains macroscopic (a) and microscopic images (b–d) of the impact-damaged sections. On a macroscopic level, the sections of all samples appear extremely undulating and exhibit ductile damage. Microscopically, three forms of impact fracture of modified wood are observed from the SEM: fiber fracture, resin fracture, and resin pull-out. The mechanism of resin toughening wood was discussed from three perspectives. Toughness is the material’s ability to resist crack propagation. Under impact loading, impact energy is absorbed by transverse breakage and splitting of longitudinal cells, respectively, allowing the absorption of more impact energy [14]. The original toughness of the wood is preserved. The monomer and initiator are not acidic or alkaline, the degradation of wood, especially hemicellulose is avoided. When impacted extremely hard, microfibrils are allowed to slide on each other, generating plastic deformation to absorb the energy [50]. In untreated wood, a zig-zag path can be formed in the cell wall between the S2 layer and the S1/S2 interface under loading, which absorbs impact energy very well. The excellent toughness structure between the S1 and S2 layers of wood cell walls is retained when the acrylic polymer mainly fill the cell lumen instead of the cell walls [51–53]. Additionally, the molecular chains of the polymerized resin with linear or lightly branched

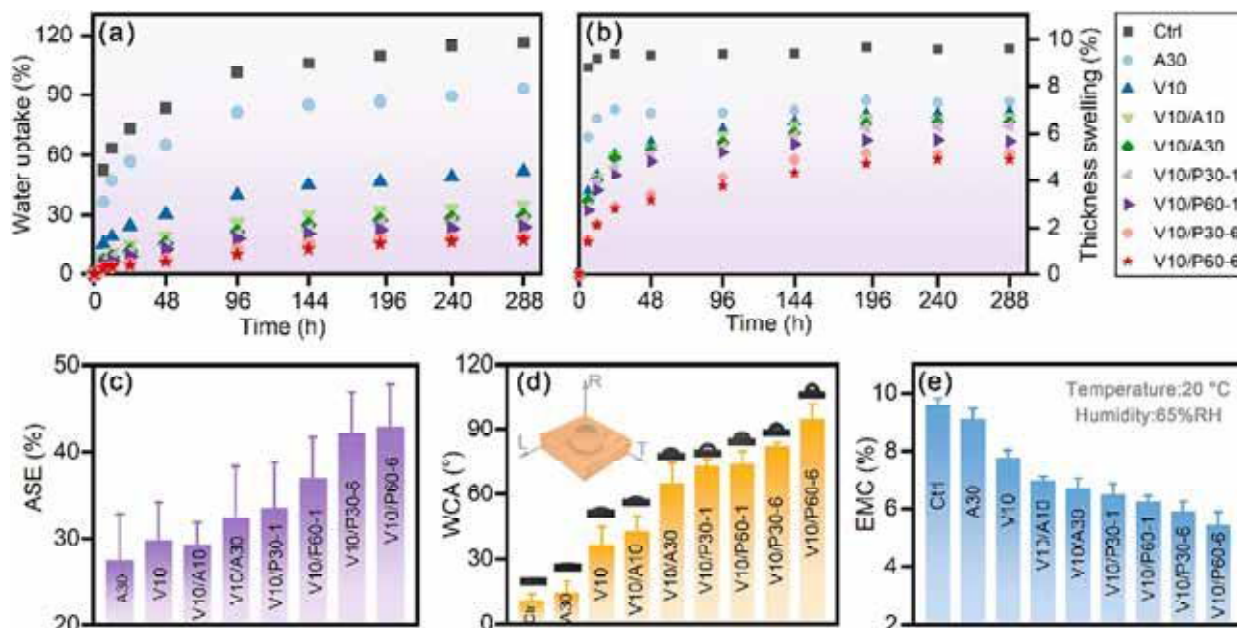


Fig. 6. Water resistance of the samples: (a) water uptake, (b) thickness swelling, (c) anti-swelling effect (ASE), (d) water contact angle (WCA), and (e) equilibrium moisture content (EMC).

structure are prone to movement upon impact, absorbing more energy. This differs from the 3D rigid structures formed by a crosslinking reaction DMDHEU resin modification, which decrease the impact properties of wood. Finally, the interaction between the resin and the wood contributes significantly to toughness, as observed in Fig. S4. Mechanical bond was easily formed between resin and wood cell due to the existence of a large amount of spiral thickening in the inner wall of basswood cell, and more energy is required to overcome this part of the interfacial bond upon impact. The modified wood's inhomogeneity, with several distinct phases, facilitates crack deflection and toughening.

In summary, this work achieves a remarkable enhancement effect compared to other modification methods (Fig. 7e). Notably, a better reinforcement effect than epoxy was achieved using 60 % WPG of the epoxy resin. The flexural strength and modulus, compressed strength, hardness, and toughness are considerably enhanced. The cell wall/polyacrylate becomes the new load-bearing unit after the polymerization of monomers in the cell lumen and ducts, contributing to this comprehensive improvement.

3.6. Thermoplastic processing and properties

The modified wood, after pulverization, underwent reprocessing via hot-pressing at different temperatures to assess its recyclability. It exhibited favorable formability, as shown in Fig. 8a. The colors of the recycled panels were similar when the hot-pressing temperature varied from 160 to 200 °C, but noticeably darkened at 220 °C, possibly due to the thermal decomposition of wood or polymer. The recycled panels exhibited impressive mechanical properties, with the tensile strength of the initial recovery reaching 22.5 MPa and the flexural strength reaching 31.5 MPa. (Fig. 8b-c). The flexural properties improved with increasing temperature. In comparison to reprocessing at 160 °C, the flexural strength and modulus of the panels after reprocessing at 220 °C were increased by 79.9 % and 71.4 %, respectively. The improved interface, resulting from the complete plasticization of the polyacrylates inside the wood at higher temperatures, contributed to the significantly enhanced flexural properties of the panels.

Similarly, akin to the flexural properties, the tensile strength and modulus of the panels gradually increased with temperature up to 200 °C. However, there was a decrease at 220 °C. To explain this

decrease, the TG and DTG of the resin, wood, and modified wood are depicted in Fig. 8d-e. In comparison to the minor mass loss of wood, which was only 0.9 % at 220 °C (Table S2), the mass loss of the resin significantly increased with rising temperature, reaching 6.6 % at 220 °C. This led to a reduction in tensile properties, accompanied by a darkening of the color.

The modified wood underwent repeated pulverization and subsequent hot-pressing at 200 °C for three cycles (Fig. 9a). As depicted in Fig. 9b, after the second cycle, the tensile strength and modulus of the panel decreased by 6.3 % and 22.3 %, respectively. Following the third cycle, the tensile strength of the material showed a recovery, being only 0.9 % lower than the first cycle, while the tensile modulus was comparable to the second cycle. This is due to the multiple thermoplastic processes, which lead to more uniform resin and wood fiber fusion, coupled with better interfacial bonding, implying the strong interfacial forces that need to be overcome.

In contrast to the tensile properties, the flexural properties of the panel gradually decreased with an increase in the number cycles (Fig. 9c). After the third cycle, the flexural strength and modulus exhibited a decrease of 43.3 % and 12.8 %, respectively, compared to the first cycle. This may be attributed to the damage suffered by the wood fibers after pulverization and the degradation of resin after multiple cycles, resulting in shorter chain segments of wood fiber and resin (Fig. S5), thereby leading to weaker resistance to bending. Nonetheless, the tensile properties of the recycled panel are comparable to the wood plastic composites (WPCs) improved by the imine crosslinking network [54], and the flexural properties are stronger than those of the WPCs mold-pressed with 60 wt% HDPE and 40 wt% wood flour, which possessed a flexural strength of 17.9 MPa and flexural modulus of 1.1 GPa [55].

4. Conclusions

This research successfully developed an environmentally friendly, high-strength, and -toughness modified wood through reactive waterborne acrylic resin impregnation process with low energy requirements. The study demonstrated that Elum®1880 resin effectively filled the vessels and cell lumen of the wood. Achieving a high WPG (123.1 %) and uniform resin distribution in a short time was made benefiting from the

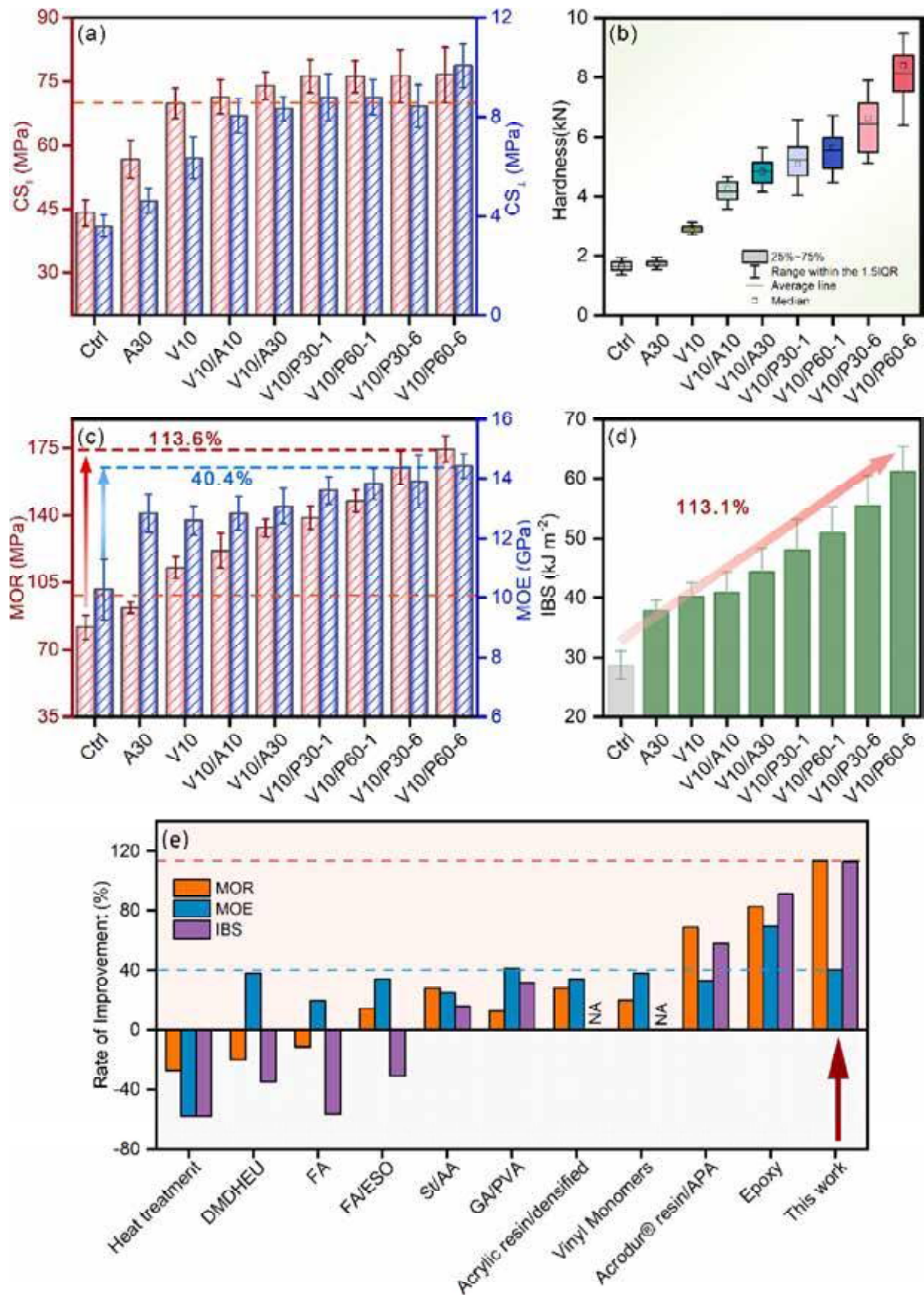


Fig. 7. Mechanical properties of the samples: (a) compressive strength parallel (CS_{||})/perpendicular (CS_⊥) to the grain, the dotted line indicates the strength of concrete C70 grade, (b) hardness, (c) modulus of rupture (MOR) and modulus of elasticity (MOE), the dotted line indicates the highest standards (TB20) of hardwood used as a building material, (d) impact bending strength (IBS), and (e) comparison of the mechanical properties in this study with those in the literature [14,15,21,28,29,43–47].

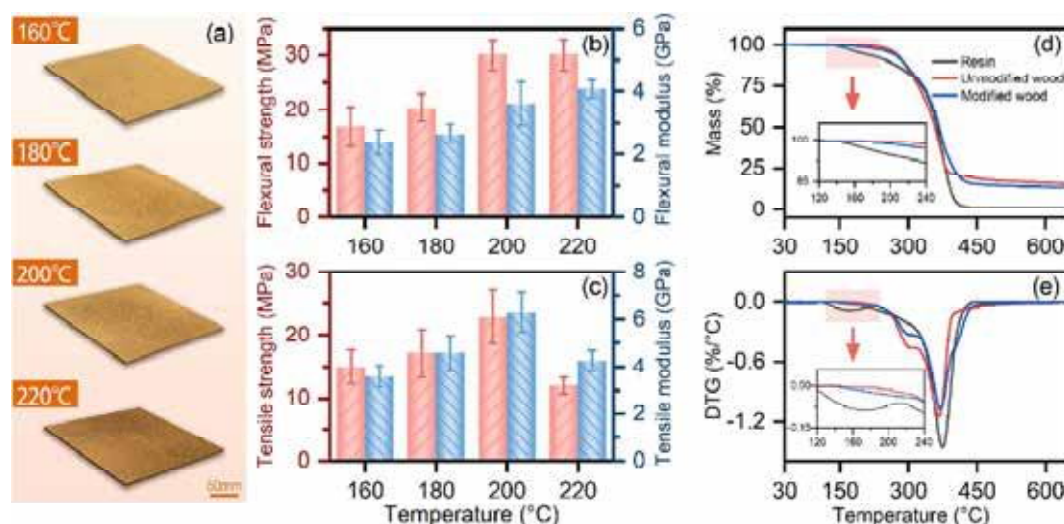


Fig. 8. (a) Photographs of the recycled panels via hot-pressing at different temperatures, (b) flexural and (c) tensile properties of these recycled panels, (d) TGA and (e) DTG curves of resin, unmodified and modified wood.

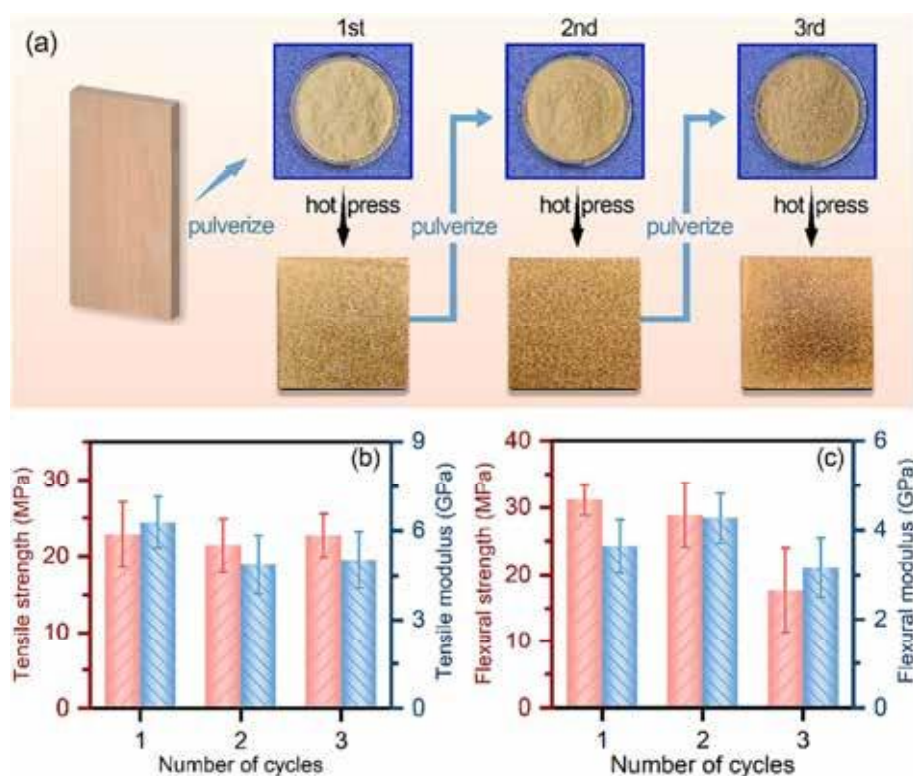


Fig. 9. (a) Pictures illustrating the cyclic processing and the mechanical properties of the recycled panels after various cycles: (b) tensile strength and modulus, (c) flexural strength and modulus.

excellent liquidity of the resin and the high porosity of basswood. Moreover, the bond between the resin and wood interface exhibited high strength. After modification, the dimensional stability of basswood noticeably improved. The overall mechanical properties, encompassing strength, stiffness, toughness, and hardness of the modified basswood, were dramatically enhanced. The cell wall/polyacrylate acted as the new load-bearing unit after the polymerization of monomers in the cell lumen and vessels. The reinforcement effect achieved rivaled that of thermosetting resin on wood, even with a reduced quantity of thermoplastic resin in this study. Maximum increases observed were 113.6 % for MOR, 40.4 % for MOE, 73.8 % for CS_{\parallel} , 179.4 % for CS_{\perp} , and 406.1 %

for hardness. CS_{\parallel} even reached the C70 concrete degree standard, and MOR conformed the highest standards (TB20) for hardwood used in construction material. Additionally, this study significantly improved the toughness of the wood, setting it apart from most reported modification methods. The IBS of modified wood increased by 113.1 % compared to that of the unmodified wood. With its high strength and toughness, the modified wood holds promise for applications in the construction industry and other high-value-added fields. Notably, the modified wood can undergo cyclic processing to generate recycled products with satisfactory strength. Importantly, this modification process aligns entirely with the sustainability of wood modification.

CRediT authorship contribution statement

Jiahua Zhou: Writing – original draft, Software, Formal analysis, Data curation. **Xiaolong Hao:** Software, Funding acquisition, Formal analysis. **Haiyang Zhou:** Writing – review & editing, Supervision, Funding acquisition. **Rongxian Ou:** Writing – review & editing, Supervision, Methodology, Funding acquisition, Conceptualization. **Qingwen Wang:** Supervision, Project administration, Funding acquisition.

Declaration of competing interest

The authors declare that they have no known competing financial interests or personal relationships that could have appeared to influence the work reported in this paper.

Data availability

Data will be made available on request.

Acknowledgments

This work was supported by the National Natural Science Foundation of China (Grant Nos. 32071698 and 32201494), the Research and Development Program of Guangzhou (2024B03J1380), the Guangdong Basic and Applied Basic Research Foundation (2023A1515012640), and the Research and Development Program in Key Areas of Guangdong Province (2020B0202010008).

Appendix A. Supplementary data

Supplementary data to this article can be found online at <https://doi.org/10.1016/j.cej.2024.151313>.

References

- [1] I. Burgert, E. Cabane, C. Zollfrank, L. Berglund, Bio-inspired functional wood-based materials-hybrids and replicates, *Int. Mater. Rev.* 60 (2015) 431–450.
- [2] J. Song, C. Chen, S. Zhu, M. Zhu, J. Dai, U. Ray, Y. Li, Y. Kuang, Y. Li, N. Qispe, Y. Yao, A. Gong, U.H. Leiste, H.A. Bruck, J.Y. Zhu, A. Vellore, H. Li, M.L. Minus, Z. Jia, A. Martini, T. Li, L. Hu, Processing bulk natural wood into a high-performance structural material, *Nature* 554 (2018) 224–228.
- [3] G. Wimmers, Wood: a construction material for tall buildings, *Nat. Rev. Mater.* 2 (2017) 17051.
- [4] F. Jiang, T. Li, Y. Li, Y. Zhang, A. Gong, J. Dai, E. Hitz, W. Luo, L. Hu, Wood-based nanotechnologies toward sustainability, *Adv. Mater.* 30 (2018) 1703453.
- [5] S. Namari, L. Drosky, B. Pudlitz, P. Haller, A. Sotayo, D. Bradley, S. Mehra, C. O'Ceallaigh, A.M. Harte, I. El-Houjeiri, M. Oudjene, Z. Guan, Mechanical properties of compressed wood, *Constr. Build. Mater.* 301 (2021) 124269.
- [6] S. Srivaro, H. Lim, M. Li, S. Jantawee, J. Tomad, Effect of compression ratio and original wood density on pressing characteristics and physical and mechanical properties of thermally compressed coconut wood, *Constr. Build. Mater.* 299 (2021) 124272.
- [7] J. Xu, C. Li, K. Hung, W. Chang, J. Wu, Physicomechanical properties of hydrothermally treated Japanese cedar timber and their relationships with chemical compositions, *J. Mater. Res. Technol.* 21 (2022) 4982–4993.
- [8] H. Chang, S. Chang, Moisture excluding efficiency and dimensional stability of wood improved by acylation, *Bioresour. Technol.* 85 (2002) 201–204.
- [9] Y. Dong, K. Wang, J. Li, S. Zhang, S.Q. Shi, Environmentally benign wood modifications: a review, *ACS Sustainable Chem. Eng.* 8 (2020) 3532–3540.
- [10] L.S. Martin, S. Jelavić, S.M. Cragg, L.G. Thygesen, Furfurylation protects timber from degradation by marine wood boring crustaceans, *Green Chem.* 23 (2021) 8003–8015.
- [11] L.G. Thygesen, G. Beck, N.E. Nagy, G. Alfredsen, Cell wall changes during brown rot degradation of furfurylated and acetylated wood, *Int. Biodeterior. Biodegrad.* 162 (2021) 105257.
- [12] H. Yin, R. Ringman, M.S. Moghaddam, M. Tuominen, A. Dédinaite, M. Wälinder, A. Swerin, S. Bardage, Susceptibility of surface-modified superhydrophobic wood and acetylated wood to mold and blue stain fungi, *Prog. Org. Coat.* 182 (2023) 107628.
- [13] H. Zhou, D. Wen, X. Hao, C. Chen, N. Zhao, R. Ou, Q. Wang, Nanostructured multifunctional wood hybrids fabricated via in situ mineralization of zinc borate in hierarchical wood structures, *Chem. Eng. J.* 451 (2023) 138308.
- [14] D. Guo, N. Guo, F. Fu, S. Yang, G. Li, F. Chu, Preparation and mechanical failure analysis of wood-epoxy polymer composites with excellent mechanical performances, *Compos. Part B-Eng.* 235 (2022) 109748.
- [15] W. Sun, H. Shen, J. Cao, Modification of wood by glutaraldehyde and poly (vinyl alcohol), *Mater. Des.* 96 (2016) 392–400.
- [16] Z. Xiao, Y. Xie, H. Militz, C. Mai, Effects of modification with glutaraldehyde on the mechanical properties of wood, *Holzforchung* 64 (2010) 475–482.
- [17] T. Priadi, S. Hiziroglu, Characterization of heat treated wood species, *Mater. Des.* 49 (2013) 575–582.
- [18] W. Li, M. Liu, H. Wang, Y. Yu, Fabrication of highly stable and durable furfurylated wood materials. Part II: the multi-scale distribution of furfuryl alcohol (FA) resin in wood, *Holzforchung* 74 (2020) 1147–1155.
- [19] L. Emmerich, C. Brischke, S. Bollmus, H. Militz, Dynamic strength properties and structural integrity of wood modified with cyclic *N*-methylol and *N*-methyl compounds, *Holzforchung* 75 (2021) 932–944.
- [20] L. Emmerich, S. Bollmus, H. Militz, Wood modification with DMDHEU (1,3-dimethylol-4,5-dihydroxyethyleneurea) - State of the art, recent research activities and future perspectives, *Wood, Mater. Sci. Eng.* 14 (2019) 3–18.
- [21] W. Che, Z. Xiao, G. Han, Z. Zheng, Y. Xie, Radiata pine wood treatment with a dispersion of aqueous styrene/acrylic acid copolymer, *Holzforchung* 72 (2018) 387–396.
- [22] R.R. Devi, I. Ali, T.K. Maji, Chemical modification of rubber wood with styrene in combination with a crosslinker: effect on dimensional stability and strength property, *Bioresour. Technol.* 88 (2003) 185–188.
- [23] Y. Dong, W. Zhang, M. Hughes, M. Wu, S. Zhang, J. Li, Various polymeric monomers derived from renewable rosin for the modification of fast-growing poplar wood, *Compos. Part B-Eng.* 174 (2019) 106902.
- [24] M.A. Ermeydan, E. Cabane, P. Hass, J. Koetz, I. Burgert, Fully biodegradable modification of wood for improvement of dimensional stability and water absorption properties by poly(ϵ -caprolactone) grafting into the cell walls, *Green Chem.* 16 (2014) 3313.
- [25] D. Guo, X. Shen, F. Fu, S. Yang, G. Li, F. Chu, Improving physical properties of wood-polymer composites by building stable interface structure between swelled cell walls and hydrophobic polymer, *Wood Sci. Technol.* 55 (2021) 1401–1417.
- [26] A.P. Acosta, R. de Avila Delucis, S.C. Amico, D.A. Gatto, Fast-growing pine wood modified by a two-step treatment based on heating and in situ polymerization of polystyrene, *Constr. Build. Mater.* 302 (2021) 124422.
- [27] C. Montanari, Y. Ogawa, P. Olsén, L.A. Berglund, High performance, fully bio-based, and optically transparent wood biocomposites, *Adv. Sci.* 8 (2021) 2100559.
- [28] X. Zhang, Q. Fan, C. Chen, X. Hao, Z. Liu, R. Ou, Q. Wang, Enhanced mechanical performance and fire resistance of poplar wood: Unilateral surface densification assisted with N/P doped acrylic resin impregnation, *Constr. Build. Mater.* 398 (2023) 132470.
- [29] J. Wu, Q. Fan, Q. Wang, Q. Guo, D. Tu, C. Chen, Y. Xiao, R. Ou, Improved performance of poplar wood by an environmentally-friendly process combining surface impregnation of a reactive waterborne acrylic resin and unilateral surface densification, *J. Clean. Prod.* 261 (2020) 121022.
- [30] K. Yue, J. Wu, L. Xu, Z. Tang, Z. Chen, W. Liu, L. Wang, Use impregnation and densification to improve mechanical properties and combustion performance of Chinese fir, *Constr. Build. Mater.* 241 (2020) 118101.
- [31] S. Kakadelis, G. Rosetto, Achieving a circular bioeconomy for plastics, *Science* 373 (2021) 49–50.
- [32] How to turn waste wood into industrial treasure, *Nature* 598 (2021) 10.
- [33] F. Berger, F. Gauvin, H.J.H. Brouwers, The recycling potential of wood waste into wood-wood/cement composite, *Constr. Build. Mater.* 260 (2020) 119786.
- [34] W. Tang, J. Xu, Q. Fan, W. Li, H. Zhou, T. Liu, C. Guo, R. Ou, X. Hao, Q. Wang, Rheological behavior and mechanical properties of ultra-high-filled wood fiber/polypropylene composites using waste wood sawdust and recycled polypropylene as raw materials, *Constr. Build. Mater.* 351 (2022) 128977.
- [35] A. Pazzaglia, M. Gelosia, T. Giannoni, G. Fabbri, A. Nicolini, B. Castellani, Wood waste valorization: Ethanol based organosolv as a promising recycling process, *Waste Manage.* 170 (2023) 75–81.
- [36] S.K. Bhudolia, G. Gohel, K.F. Leong, S.C. Joshi, Damping, impact and flexural performance of novel carbon/Elium® thermoplastic tubular composites, *Compos. Part B-Eng.* 203 (2020) 108480.
- [37] W. Obande, D. Ray, C.M.O. Brádaigh, Viscoelastic and drop-weight impact properties of an acrylic-matrix composite and a conventional thermoset composite - A comparative study, *Mater. Lett.* 238 (2019) 38–41.
- [38] C. Xia, Y. Wu, Y. Qiu, L. Cai, L.M. Smith, M. Tu, W. Zhao, D. Shao, C. Mei, X. Nie, S. Q. Shi, Processing high-performance woody materials by means of vacuum-assisted resin infusion technology, *J. Clean. Prod.* 241 (2019) 118340.
- [39] M. Romanaguire, Elucidating the graft copolymerization of methyl methacrylate onto wood-fiber, *Carbohydr. Polym.* 55 (2004) 201–210.
- [40] Y. Dong, M. Altgen, M. Mäkelä, L. Rautkari, M. Hughes, J. Li, S. Zhang, Improvement of interfacial interaction in impregnated wood via grafting methyl methacrylate onto wood cell walls, *Holzforchung* 74 (2020) 967–977.
- [41] R. Coste, M. Soliman, N.B. Bercu, S. Potiron, K. Lasri, V. Aguié-Béghin, L. Tetard, B. Chabbert, M. Molinari, Unveiling the impact of embedding resins on the physicochemical traits of wood cell walls with subcellular functional probing, *Compos. Sci. Technol.* 201 (2021) 108485.
- [42] A.J.M. Leijten, H.J. Larsen, T.A.C.M. Van der Put, Structural design for compression strength perpendicular to the grain of timber beams, *Constr. Build. Mater.* 24 (2010) 252–257.
- [43] T. Jiang, H. Gao, J. Sun, Y. Xie, X. Li, Impact of DMDHEU resin treatment on the mechanical properties of poplar, *Polym. Polym. Compos.* 22 (2014) 669–674.

- [44] M. Liu, S. Lyu, L. Peng, L. Cai, Z. Huang, J. Lyu, Improvement of toughness and mechanical properties of furfurylated wood by biosourced epoxidized soybean oil, *ACS Sustainable Chem. Eng.* 9 (2021) 8142–8155.
- [45] M. Piernik, M. Woźniak, G. Pinkowski, K. Szentner, I. Ratajczak, A. Krauss, Impact of the heat treatment duration on color and selected mechanical and chemical properties of Scots Pine Wood, *Materials* 15 (2022) 5425.
- [46] H. Qiu, S. Yang, Y. Han, X. Shen, D. Fan, G. Li, F. Chu, Improvement of the performance of plantation wood by grafting water-soluble vinyl monomers onto cell walls, *ACS Sustainable Chem. Eng.* 6 (2018) 14450–14459.
- [47] K. Srinivas, K.K. Pandey, Effect of heat treatment on color changes, dimensional stability, and mechanical properties of wood, *J. Wood Chem. Technol.* 32 (2012) 304–316.
- [48] X. Dong, X. Zhuo, J. Wei, G. Zhang, Y. Li, Wood-based nanocomposite derived by in situ formation of organic-inorganic hybrid polymer within wood via a sol-gel method, *ACS Appl. Mater. Interfaces* 9 (2017) 9070–9078.
- [49] Ü.C. Yildiz, S. Yildiz, E.D. Gezer, Mechanical properties and decay resistance of wood-polymer composites prepared from fast growing species in Turkey, *Bioresour. Technol.* 96 (2005) 1003–1011.
- [50] F. Barthelat, Z. Yin, M.J. Buehler, Structure and mechanics of interfaces in biological materials, *Nat. Rev. Mater.* 1 (2016) 16007.
- [51] M. Henriksson, L.A. Berglund, P. Isaksson, T. Lindström, T. Nishino, Cellulose nanopaper structures of high toughness, *Biomacromolecules* 9 (2008) 1579–1585.
- [52] P.W. Lucas, H.T.W. Tan, P.Y. Cheng, The toughness of secondary cell wall and woody tissue, *Phil. Trans. r. Soc. Lond. B* 352 (1997) 341–352.
- [53] M. Maaß, S. Saleh, H. Militz, C.A. Volkert, The structural origins of wood cell wall toughness, *Adv. Mater.* 32 (2020) 1907693.
- [54] C. Ding, S. Zhang, M. Pan, M.-C. Li, Y. Zhang, C. Mei, Improved processability and high fire safety of wood plastic composites via assembling reversible imine crosslinking network, *Chem. Eng. J.* 423 (2021) 130295.
- [55] K.B. Adhikary, S. Pang, M.P. Staiger, Dimensional stability and mechanical behaviour of wood-plastic composites based on recycled and virgin high-density polyethylene (HDPE), *Compos. Part B-Eng.* 39 (2008) 807–815.



Preparation of waterborne intumescent flame-retardant coatings using adenosine-based phosphonates for wood surfaces

Qingjie Liu, Haolong Luo, Zhenzhong Gao, Yishuai Huang, Jiaming Liang, Haiyang Zhou^{*}, Jin Sun^{*}

Key Laboratory for Biobased Materials and Energy of Ministry of Education, College of Materials and Energy, South China Agricultural University, Guangzhou 510642, China

ARTICLE INFO

Keywords:

Bio-based phosphonate
Adenosine
Thermal stability
Waterborne wood coatings

ABSTRACT

Here, organic solvent-free adenosine-based waterborne flame retardant curing agents were synthesized and introduction into a melamine urea-formaldehyde resin (MUF) to construct flame-retardant coatings for wood surfaces. Adenosine-based phosphonate (APU), composed of adenosine, urea, formaldehyde, and phosphorous acid, was synthesized by the Mannich reaction. The chemical structure of APU was investigated by Fourier-transform infrared (FTIR) spectroscopy, X-ray photoelectron spectroscopy (XPS), and ³¹P nuclear magnetic resonance (NMR) spectroscopy. In contrast to MAW0, the coatings containing APU exhibited similar physical characteristics. MAW4 achieved a vertical combustion (UL-94) V-0 rating and an impressive limiting oxygen index (LOI) of 54.5 %. Cone calorimetry indicated that the time to ignition (TTI) of MAW4 was 89 s, an increase of 790 % compared with MAW0, which may significantly prolong the escape time from a fire. Scanning electron microscopy (SEM), thermal infrared imaging, and Raman spectroscopy all confirmed that continuous and dense char layers reduced the transport of heat, ignitable gases, and smoke. This limited the further pyrolysis and combustion of wood, showing that the waterborne intumescent flame-retardant coatings proposed in this research endowed wood with excellent flame retardancy.

1. Introduction

Wood is used widely in housing, furniture, and automobile manufacturing because of its high strength, lightweight, renewability, and processability [1,2]. However, it is necessary to treat wood to endow it with flame retardancy [3,4], such as by applying flame-retardant coatings on the exterior or impregnating the interior with flame retardants [5,6]. Spraying flame-retardant coatings on the exterior of wood is the most convenient method to impart fire resistance to wood products [7,8]. Flame-retardant coatings must be transparent to show the unique grain of wood [9,10]. Transparent flame-retardant coatings are composed of reactive flame retardants and membrane-forming materials. Intumescent flame retardants containing nitrogen and phosphorus are reactive flame retardants, typically amino resins, which have low toxicity, low smoke formation, and good compatibility with the base resin [11,12]. Intumescent flame retardants produce phosphoric acid derivatives during combustion, which facilitates the dehydration and carbonization of the matrix resin while releasing inert

gases that promote the formation of an intumescent char layer that acts as a gas-phase and condensed-phase flame retardant [13–15]. Therefore, intumescent flame retardants are increasingly popular.

Traditional film-forming substances include acrylic resins [16–18], epoxy resins [19–21], and amino resins [22,23]. UV-curable functional coatings prepared with acrylates as film-forming substances have shown limited fire-resistance enhancements for wood and show significant potential fire risks. In addition, epoxy resins release a significant volume of smoke during combustion, which is often more dangerous than the fire itself. Transparent intumescent flame-retardant coatings composed of modified cyclic phosphonates ester acid and amino resins have shown remarkable fire-retardancy and smoke inhibition properties [24,25]. Regrettably, the organic solvent *n*-butanol is often used to synthesize cyclic phosphate esters, which conflicts with the concept of green chemistry [26,27]. Therefore, the development of environmentally-friendly waterborne intumescent flame-retardant coatings with outstanding fire-retardancy and smoke inhibition properties is crucial.

In the last several years, bio-based raw materials have received

^{*} Corresponding authors.

E-mail addresses: hyzhou@scau.edu.cn (H. Zhou), sunjin@scau.edu.cn (J. Sun).

<https://doi.org/10.1016/j.porgcoat.2023.108061>

Received 21 June 2023; Received in revised form 17 August 2023; Accepted 30 October 2023

Available online 23 November 2023

0300-9440/© 2023 Elsevier B.V. All rights reserved.

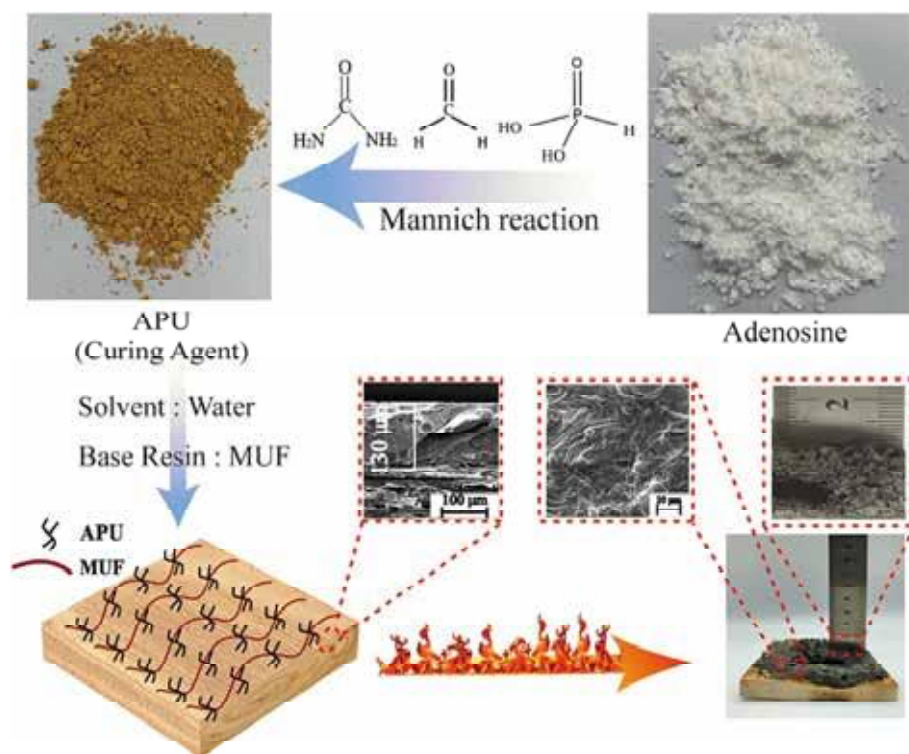
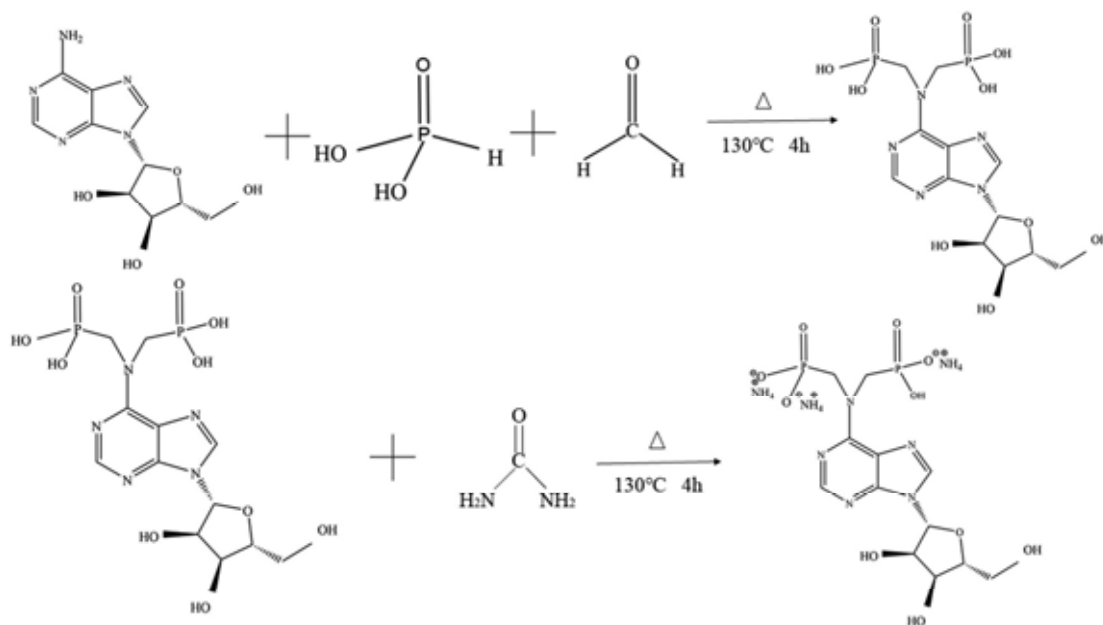


Fig. 1. Describes the manufacture of adenosine-based waterborne transparent intumescent flame-retardant coatings for wood surfaces.



Scheme 1. The synthetic route of APU.

significant attention because of their low costs, eco-friendliness, and regenerative characteristics. Numerous bio-based materials such as alginates [28,29], eugenol [30], tannins [31,32], cardanol [33,34], vanillin [35,36], deoxyribonucleic acid, adenosine triphosphate [37,38] and phytic acid [39,40] have been used as the raw materials to obtain flame retardants. In addition, bio-based materials including tannic acid [41], guanosine 5'-monophosphate disodium salt [42], laccase [43], tea saponin [44], and chitosan [45] have also been widely applied in flame retardant coatings. Among various bio-based materials, adenosine, a compound containing three hydroxyl groups and an amino group, has

been employed extensively in biomedicine because it is an endogenous substance present in all cells of the body. Adenosine has a unique structure and highly reactive functional groups, allowing it to be used to prepare intumescent flame retardants [46,47]. Adenosine occurs widely in the nucleic acids of living organisms, so raw materials are readily available. Second, the active hydroxyl and amino groups of adenosine are easily constructed into renewable multifunctional compounds. The ribose and nitrogen-containing structures of adenosine serve as carbon and gas sources for intumescent flame retardants, which help improve a flame retardant's efficiency [48,49]. Consequently, intumescent flame

Table 1
Recipes for adenosine-based flame retardant coatings.

Coatings	APU(g)	DI(g)	MUF(g)
MAPU0 ^a	0	10	10
MAPU3	3	10	13
MAPU4	4	10	14
MAPU5	5	10	15

^a The curing agent of MAPU0 was 2.0 % mass fraction of NH₄Cl.

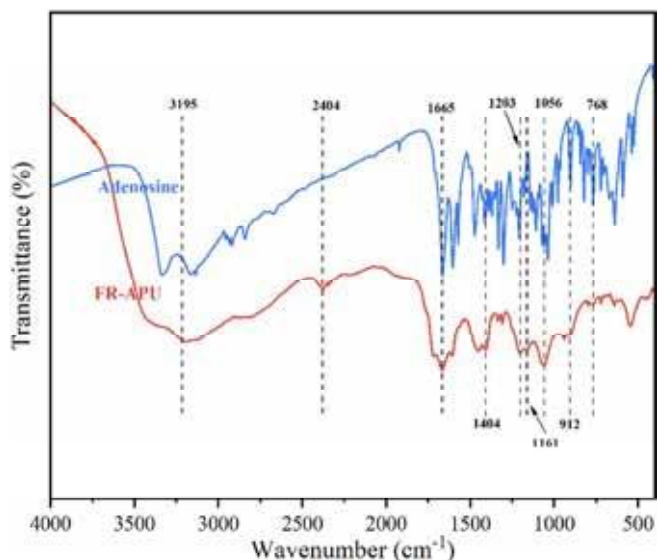


Fig. 2. The FTIR spectra for APU and adenosine.

retardants can be constructed by introducing phosphorus-containing structures through the reactive groups of adenosine. However, there have been few reports about synthetic intumescent flame retardants using adenosine as raw material.

Mannich-type reactions involve the reaction between compounds containing active hydrogen atoms and aldehydes and amines to form β -amino (carbonyl) compounds [50,51]. The mechanism of the Mannich reaction first involves the protonation of a carbonyl group, followed by a nucleophilic reaction of the amine on the protonated carbonyl group to produce an imine ion intermediate. This intermediate then reacts with the compound containing the active hydrogen to produce the final product [52]. The Mannich reaction enables the introduction of N atoms into P-containing compounds and is, therefore, applied extensively to synthesize flame retardants [53–55].

As shown in Fig. 1, we synthesized a novel adenosine-based phosphonate (APU) flame retardant by reacting adenosine, phosphite, formaldehyde, and urea based on Mannich-type reaction. Flame-retardant coatings with different APU contents were constructed on the wood surface. The surface performance of the coatings was analyzed to illustrate the influence of APU on the thermal stability and fire resistance of the flame-retardant coatings. In addition, the flame retardant mechanism of APU was illustrated. This paper proposed a novel strategy for the utilization of adenosine and a new approach for synthesizing waterborne transparent intumescent flame-retardant coatings.

2. Experimental section

2.1. Materials

Adenosine was supplied by Macklin Biotechnology Co., Ltd. (Shanghai, China). Poplar wood was obtained from North Carolina, USA. The formaldehyde aqueous solution (37 %) and ammonium chloride (NH₄Cl) were obtained from Guangzhou Chemical Reagent Factory

Co., Ltd. (Guangdong, China). Phosphorous acid was provided by Fuchen Chemical Reagent Co., Ltd. (Tianjin, China). Urea was supplied by Sanning Chemical Reagent Co., Ltd. (Hubei, China). Melamine urea-formaldehyde resin (MUF) powder was supplied by Ektel New Material Co., Ltd. (Nanjing, China).

2.2. Synthesis of APU

Adenosine (8.01 g, 0.03 mol), formaldehyde (4.87 g, 0.06 mol), and 25 ml distilled water (DI) were added to a three-necked flask (250 ml) fitted with a reflux condenser and a mechanical stirrer and then heated to 50 °C. When adenosine was completely dissolved, H₃PO₃ (4.92 g, 0.06 mol) was added to the mixed solution, and the temperature was raised to 130 °C for 4 h. Subsequently, urea (7.2 g, 0.12 mol) was added to the solution and then reacted at 130 °C for 2 h to obtain the crude product. The crude product was purified by anhydrous ethanol precipitation to obtain the brown-yellow solid product (APU) in 72.4 % yield. Scheme 1 illustrates the synthesis of APU.

2.3. Flame-retardant coatings preparation and application on wood

According to Table 1, different masses of APU were mixed thoroughly with MUF and deionized water and then cured. The samples were denoted as MAPU0, MAPU3, MAPU4, and MAPU5. The flame-retardant coatings were applied uniformly to the wood surface with a fine art scraper at the coating amount of 0.05 g cm⁻². After room-temperature curing, the coated poplar specimens were designated as MAW0, MAW3, MAW4, and MAW5.

2.4. Characterization

Fourier-transform infrared (FTIR) spectroscopy of APU and adenosine was performed using a PerkinElmer Spectrum 100 FTIR spectrometer. X-ray photoelectron spectra (XPS) of APU were recorded using a Thermo Scientific K-Alpha instrument, and all spectra were calibrated to the C 1s peak at 284.8 eV. ³¹P nuclear magnetic resonance (NMR) spectroscopy was conducted on a BRUKER AVANCE NEO 600 MHz spectrometer using deuterium oxide (D₂O) as the solvent.

The thermal stability of the coatings was evaluated with a Netzsch TG209 F1 Libra by heating samples from 35 °C to 800 °C under a nitrogen atmosphere at 10 °C/min⁻¹. The adhesion of the coatings was tested with a QFH-A hundred-grid knife according to ASTM D3359-09. The coatings' pencil hardness was tested by a QHQ-S pencil hardness apparatus following ASTM D3363-2005. The gloss of the coatings was evaluated with a WGG-60 gloss meter following ASTM D523-2014. The water resistance of the coatings was examined according to ASTM D870-02. According to ASTM D5402-06, swabs soaked in ethanol were used to wipe the coatings, and the outcome was documented as the count the substrate was exposed or a maximum of 200 rubs, which was used to illustrate the solvent resistance of the coating. All coatings were coated uniformly on highly-polished silicon chips at 0.05 g cm⁻². Light transmission was recorded using a Thermo Scientific Evolution 220 UV-Vis spectrophotometer at a wavelength range of 400–800 nm.

The limiting oxygen index (LOI) was measured according to ASTM D2863 using a CSI-101G oxygen index tester (coating specimen size = 130 × 6.5 × 4.0 mm³). Vertical combustion (UL-94) tests were performed on a PX-03-001 vertical combustion tester following ASTM D6413 (coating specimen size = 130 × 13 × 4.0 mm³). Cone calorimetry was performed using a CSI-311ZZ cone calorimeter with a heat flux of 50 kW m⁻² following ASTM E1354 (coated specimen size = 100 × 100 × 10 mm³). Thermal infrared images were collected with a Ti200 9 Hz thermal infrared imager. The separation interval between the camera lens and the back of the coating was 30 cm.

The cross-sectional microstructure of the specimens was observed with a Zeiss EVO18 scanning electron microscope (SEM). An Oxford Innca250 energy-dispersive spectrometer was used to scan the surface of

Table 2
Assignment of FT-IR absorption bands of APU.

Peaks position (cm ⁻¹)	Assignment	Reference
3195, 1404	NH ₄ ⁺	[55]
2404	P-OH	[53]
1665	C=N	[56]
1203	P=O	[54]
1161	C-O-C	[56]
1056	C-N	[56]
912	P-O	[54]
768	P-C	[57]

specimens to estimate the relative contents of phosphorus, carbon, nitrogen, and oxygen. To compare the degree of graphitization of the char residues, they were characterized by Raman spectroscopy on a Thermo DXR2xi Raman spectrometer using a 532 nm laser.

3. Results and discussion

3.1. Characterization of APU

The FTIR spectra of APU and adenosine are shown in Fig. 2, and the detailed data are summarized in Table 2. In the FTIR spectrum of APU, characteristic absorption peaks of the C=N, C-O-C, and G-N bonds of adenosine were observed at 1665 cm⁻¹, 1161 cm⁻¹, and 1056 cm⁻¹, respectively [56]. The spectrum also exhibited several new peaks assigned to P-OH, P=O, P-O, and P-C bonds at 2404 cm⁻¹, 1203 cm⁻¹, 912 cm⁻¹, and 768 cm⁻¹, respectively [53,54,57]. Furthermore, the peaks at 3195 cm⁻¹ and 1404 cm⁻¹ were ascribed to the stretching and bending vibrations of ammonium ions [55]. The above analysis evidenced the grafting of flame-retardant molecules onto adenosine. The FTIR spectra tentatively confirm the successful reaction between adenosine and phosphoric acid, formaldehyde, and urea.

The chemical structure of APU was reconfirmed using XPS, and Fig. 3 demonstrates the fitted C 1s, N 1s, O 1s, and P 2p spectra. The C 1s spectrum was subdivided into three fitted peaks at binding energies of 284.80 eV (C-C/C-H), 286.48 eV (C-O/C-N), and 288.70 eV (C=N) [58]. In the N 1s spectrum, the peaks at 399.5 eV, 400.2 eV, and 401.28 eV

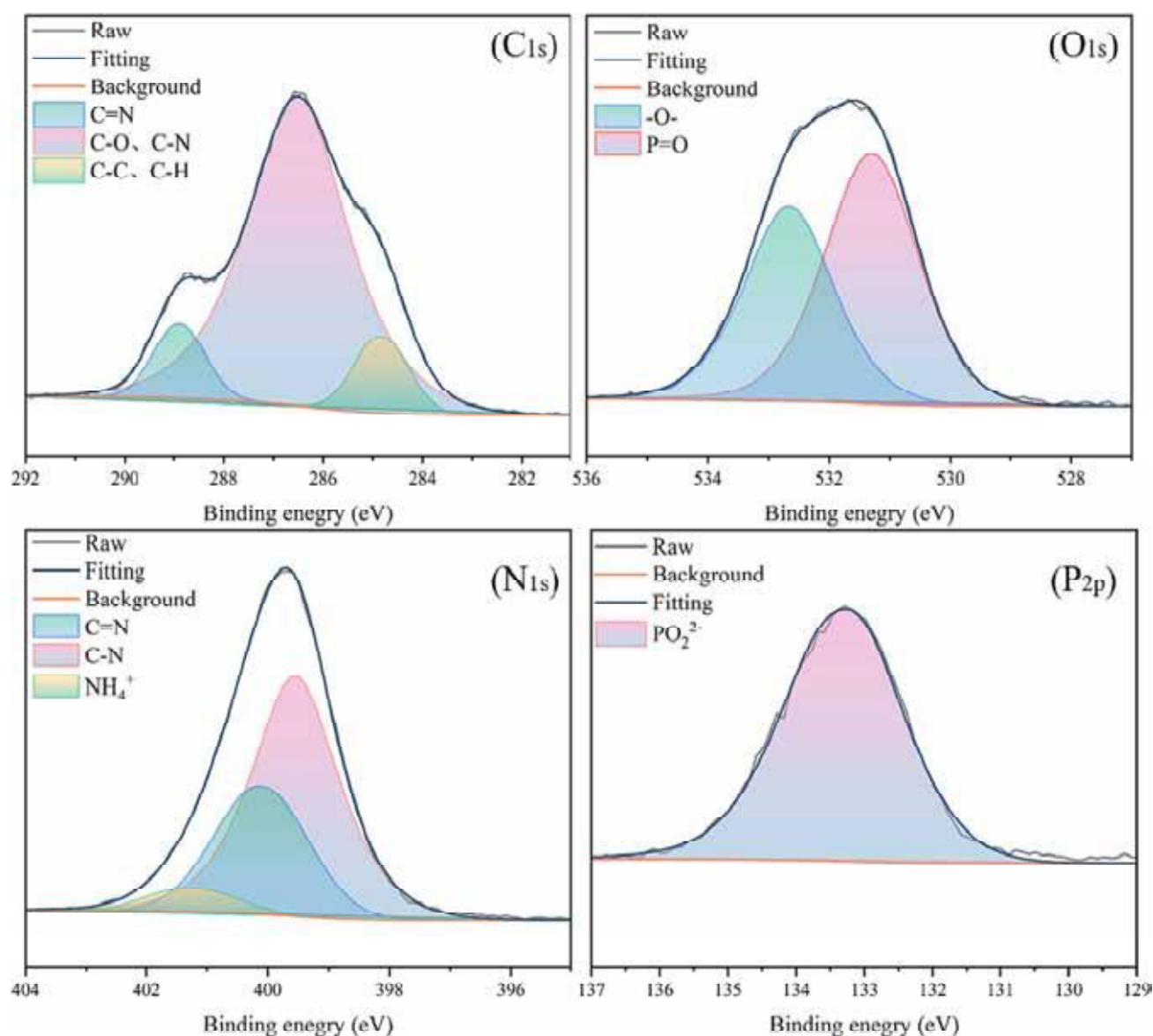


Fig. 3. The XPS spectrum of the APU.

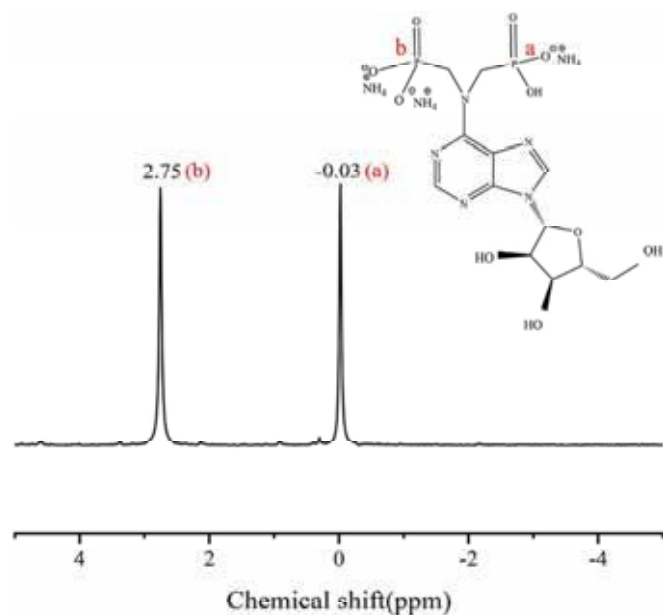


Fig. 4. ^{31}P NMR spectra of APU.

were attributed to the C—N, C=N, and NH_4^+ groups, respectively [58,59]. The P=O peaks appeared at 531.28 eV and 133.2 eV in the fitted O 1s and P 2p spectra, respectively [59,60], which were consistent with the FTIR spectra.

As shown in Fig. 4, signals of -0.03 ppm and 2.75 ppm were significantly observed in the ^{31}P NMR spectrum, which represents phosphorus atoms in the $-(\text{ONH}_4)(\text{OH})\text{P}=\text{O}$ and $-(\text{ONH}_4)_2\text{P}=\text{O}$ groups

[53]. All the above analyses prove the successful synthesis of APU.

3.2. Thermal stability of coatings

The TG and DTG curves of MAPU0, MAPU3, MAPU4, and MAPU5 are shown in Fig. 5, and the relative parameters are enlisted in Table 3. The coatings exhibited three decomposition stages at $35\text{--}220$ °C, $220\text{--}600$ °C, and $600\text{--}800$ °C, respectively. The degradation at

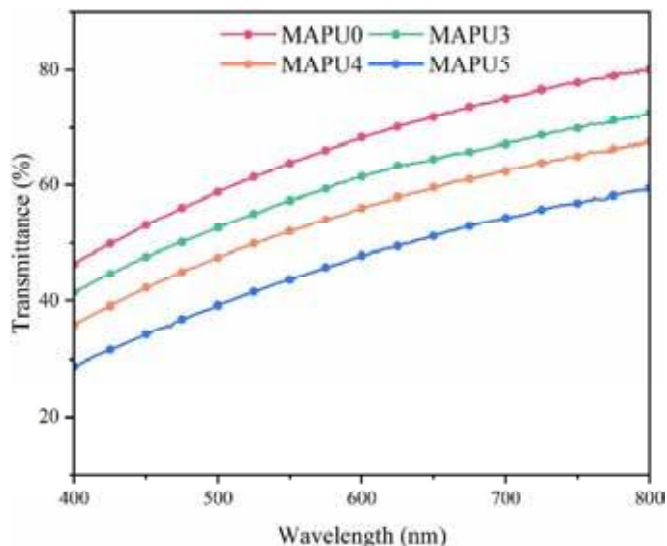


Fig. 6. Transmittance curve of MAPU coatings.

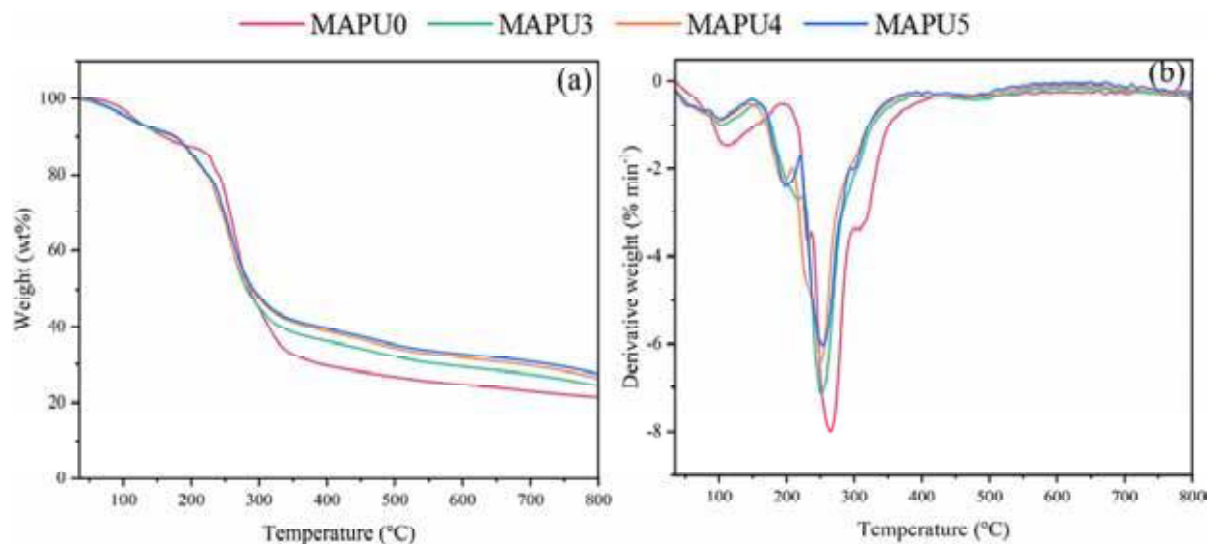


Fig. 5. TG (a) and DTG (b) curves of the adenosine-based flame-retardant coatings.

Table 3

Parameters related to adenosine-based flame-retardant coatings.

Samples	$T_{d5\%}^a$ (°C)	$T_{d10\%}$ (°C)	$T_{d30\%}^b$ (°C)	T_{peak} (°C)	R_{800}^c (wt%)	T_{lim} (°C)
MAPU0	116.0	158.0	256.6	265.0	21.0	100.6
MAPU3	110.5	174.5	244.6	255.5	24.9	96.7
MAPU4	108.5	175.6	245.5	257.0	26.4	96.9
MAPU5	104.0	178.6	248.0	261.6	27.5	97.3

^a The temperature at which the mass of the coating degrades by 5%.

^b The temperature at which the mass of the coating degrades by 30%.

^c R_{800} refers to the residual char yield of the coating after testing at 800 °C.

Table 4
Physical performance parameters of adenosine-based flame retardant coatings.

Samples	Pencil hardness	Adhesion	60° gloss (GU)	Water resistance	Solvent resistance
MAPU0	6H	4B	66.8	No effect on the surface	>200
MAPU3	6H	4B	53.4	No effect on the surface	>200
MAPU4	6H	4B	52.7	No effect on the surface	>200
MAPU5	5H	4B	50.8	No effect on the surface	>200

Table 5
Test results for Poplar wood and flame-retardant specimens UL-94 and LOI.

Samples	LOI (%)	t_1 (s)	t_2 (s)	Dropping	UL-94 rating
PW	22.9	>30	—	No	NR
MAW0	26.3	>30	—	No	NR
MAW3	46.2	0	0	No	V-0
MAW4	54.5	0	0	No	V-0
MAW5	60.4	0	0	No	V-0

35–220 °C was attributed to the release of small molecules and small amounts of inert gases due to the thermal degradation of MUF and APU. $T_{d10\%}$ (the temperature at which the mass of the coating degraded by 10 %) of coatings increased with the APU content, showing that the incorporation of APU enhanced the thermal stability of the coatings at low temperatures [61].

At 220–600 °C, the coatings lost approximately 50 wt%, primarily due to the decomposition of APU and MUF. The thermal decomposition of APU produced phosphorus-containing radicals and phosphate derivatives. The phosphorus-containing radicals eliminated flammable radicals, thus reducing a fire's intensity, while the phosphate derivatives catalyzed the formation of molten char from the carbon-rich components via polymerization and aromatization. They interacted with non-flammable gases such as NH_3 and CO_2 and triazine compounds produced by MUFs to transform the molten char into an intumescent char layer.

The intumescent char served as a thermal insulator and protective layer to prevent heat transfer to the undecomposed layer, thus preventing further thermal decomposition [61,62]. MAPU0 had the highest T_{peak} (the temperature at the maximum degradation rate of the coating) of 265 °C, while T_{peak} for MAPU3 appeared at 255 °C, which was attributed to the accelerated forming of the char layer by pyrophosphoric acid.

The degradation of the coatings at 600–800 °C was ascribed to the decomposition of the unstable carbon-based skeleton. Coatings with APU flame retardant showed a higher residual weight compared with MAPU0.

The heat resistance index temperature (T_{HRI}) was used to describe the thermal stability of coatings and was calculated by the formula [63,64]:

$$T_{\text{HRI}} = 0.49 \times [T_{d5\%} + 0.6 \times (T_{d30\%} - T_{d5\%})]$$

The calculated T_{HRI} values for the four coatings are recorded in Table 3, which indicates that the phosphorus-based flame retardant APU caused the premature degradation and dehydrated charring of the coatings. It also served as an acid source in the condensed phase [12].

3.3. Physical properties and transmittance of coatings

As indicated by Fig. 6, the transparency of coatings gradually declined upon increasing the APU content. The transmittance of MAPU0 and MAPU3 were high and similar, while the transmittance of MAPU5 was significantly lower.

According to specific test criteria, the physical properties of the coatings were measured separately, including pencil hardness, adhesion, water resistance, solvent resistant, and gloss. The physical properties of the coatings are summarized in Table 4. The adhesion of all flame-retardant coatings reached level 4B, which was ascribed to the formation of hydrogen bonds between the flame-retardant coatings containing polar groups and the wood surface during curing. However, the pencil hardness and gloss of MAPU5 decreased slightly upon increasing the APU content because excess APU reduced crosslinking within MUF. Notably, excess APU did not impact the water or solvent resistance of the coatings, and the adenosine-based flame-retardant coatings exhibited excellent water and solvent resistance. The above results indicated that curing MUF with an appropriate amount of APU

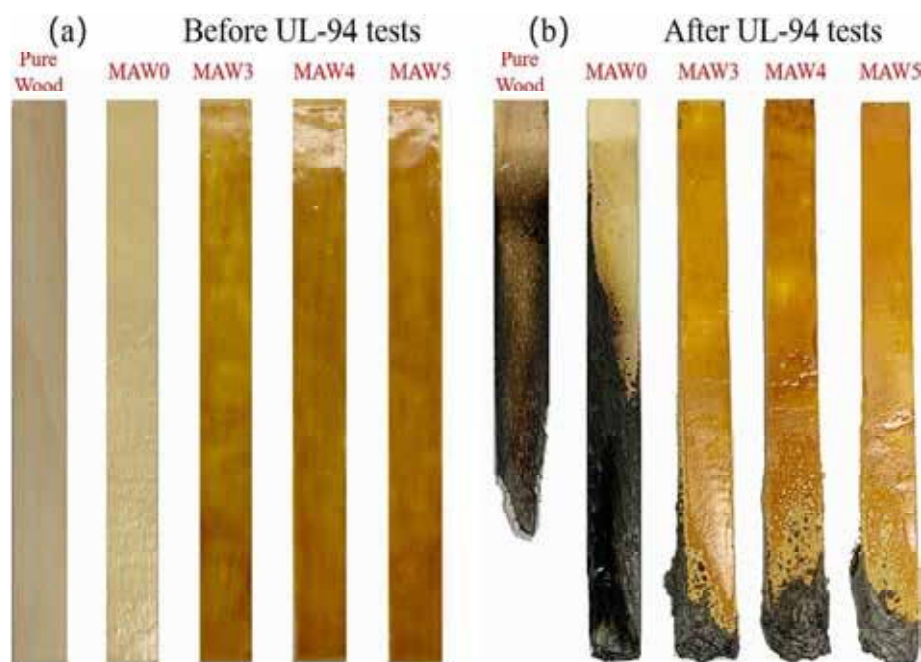


Fig. 7. Photographs of specimens before (a) and after (b) UL-94 testing.

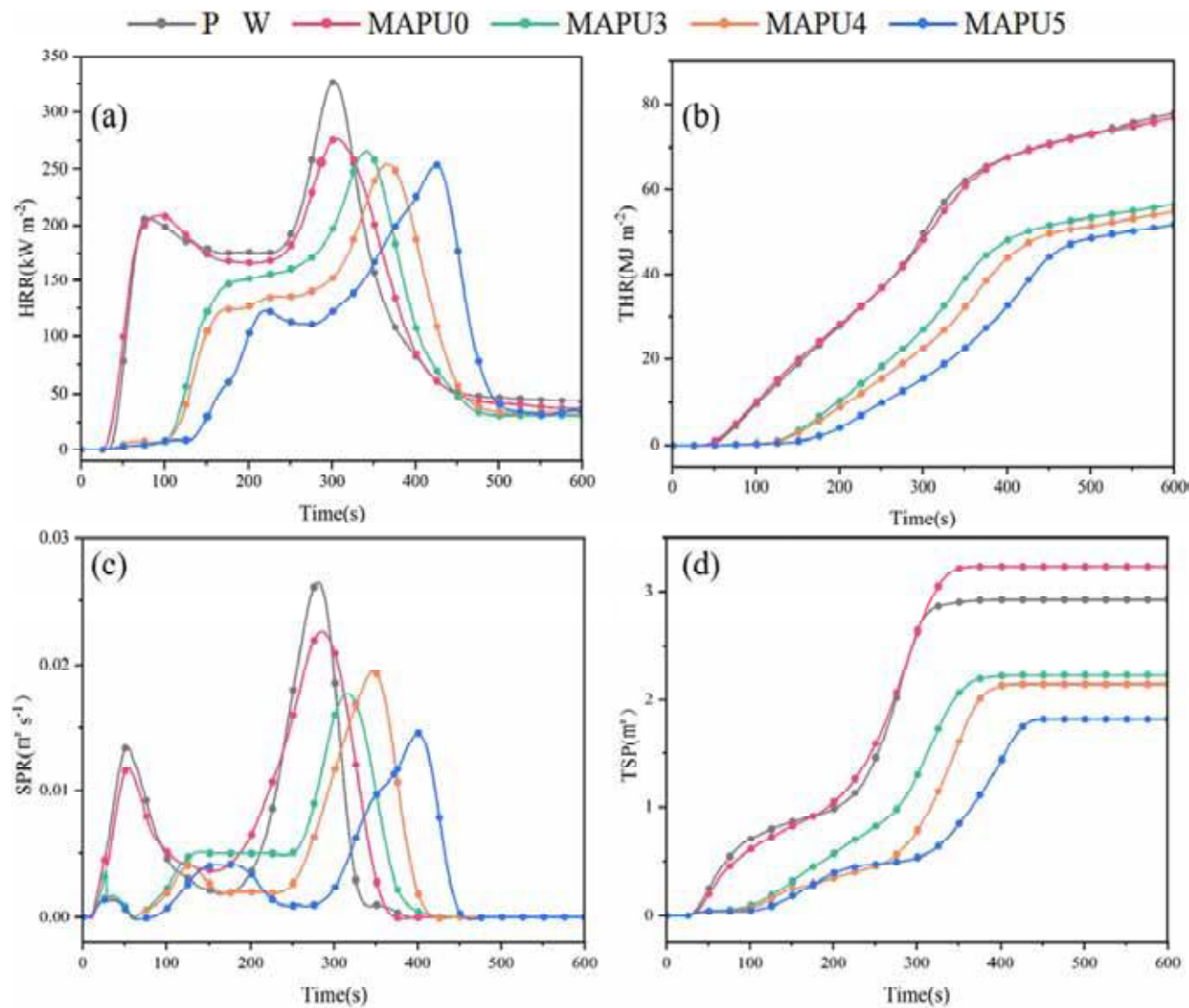


Fig. 8. Specimen CCT results: HRR (a), THR (b), SPR (c), and TSP (d).

Table 6
Combustion parameters in the CCT of the specimen.

Parameter	Pure wood	MAW0	MAW3	MAW4	MAW5
TTI (s)	12	10	75	89	108
PHRR (kW m ⁻²)	206.09/	208.26/	147.72/	135.52/	122.81/
PSPR (m ² s ⁻¹)	0.013/	0.011/	0.005/	0.004/	0.004/
TSP (m ²)	2.91	3.23	2.23	2.15	1.81
Residue (%)	13.74	14.52	17.81	18.58	19.62
Y _{CO} (kg kg ⁻¹)	0.0034	0.0037	0.0046	0.0063	0.0068
Y _{CO2} (kg kg ⁻¹)	1.06	1.05	1.01	0.95	0.85
THR (MJ m ⁻²)	77.76	76.73	56.54	54.85	51.90
ECH (MJ kg ⁻¹)	12.25	12.31	10.95	10.86	10.31
MLR (g s ⁻¹ m ⁻²)	14.17	13.59	12.74	12.07	12.12
TSR (m ² m ⁻²)	333.7	368.8	244.3	237.6	195.7

satisfied the basic requirements of waterborne wood coatings.

3.4. Fire-retardancy of coatings on wood

Table 5 shows the relevant parameters of specimens during UL-94 and LOI tests. In the UL-94 test, MAW3, MAW4m, and MAW5 reached the V-0 rating, but MAW0 failed to pass this rating. MAW0 and poplar wood immediately ignited, followed by the rapid spread of flame to the fixture. However, the coatings cured with APU failed to ignite after two ignitions, and minor amounts of white smoke were produced when the ignition source was removed. As exhibited in Fig. 7, MAW3 (Video S1), MAW4 (Video S2), and MAW5 (Video S3) generated an intumescent char layer over the substrate surface after ignition, effectively isolating the transfer of heat, smoke, and combustible volatiles.

During the LOI tests, the LOI values for pure wood and MAW0 were 22.9 % and 26.3 %, respectively, while upon increasing the APU content, the LOI value of MAW5 increased to 60.4 %. The above test results all proved that waterborne wood coatings showed excellent flame retardancy.

Cone calorimetry was employed to simulate the actual burning process of specimens and assess their flame-retardancy. The heat release rate (HRR), total heat release rate (THR), smoke production rate (SPR), and total smoke production rate (TSP) curves of all specimens are shown

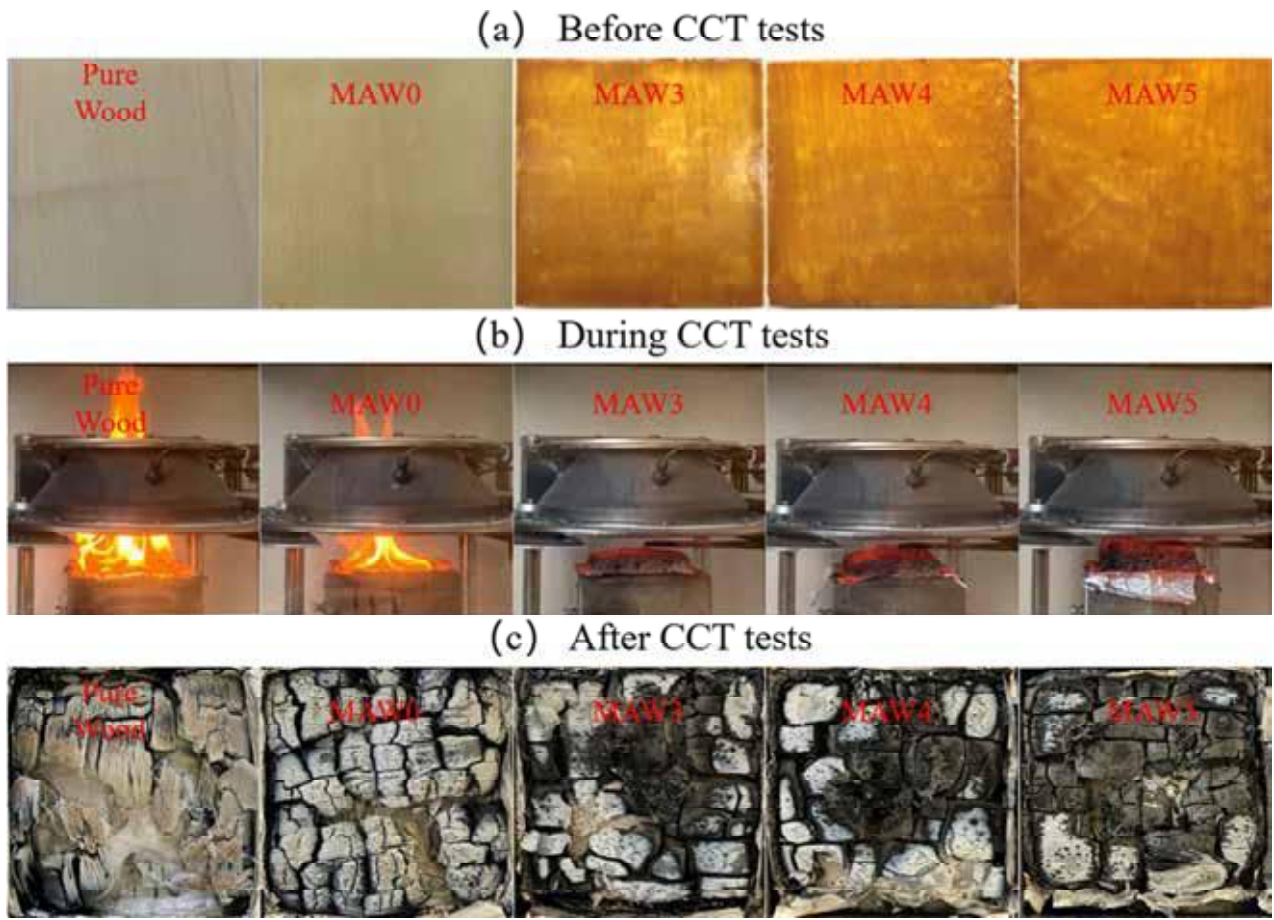


Fig. 9. Digital photographs of the specimen before, after and during the CCT test.

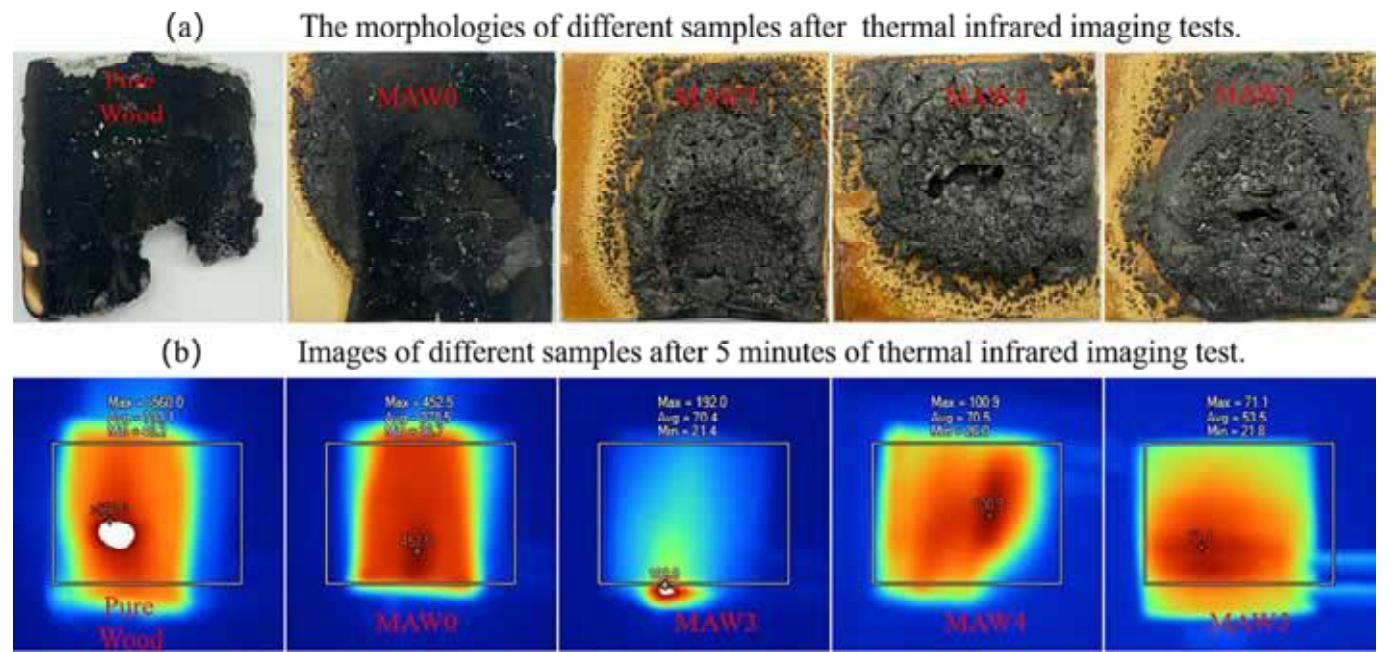


Fig. 10. The morphologies of different samples after 5 min of burning tests.

in Fig. 8, and the detailed data are summarized in Table 6. Digital photographs of the specimens before, after and during the CCT test are shown in Fig. 9. Compared with pure wood, introducing APU

significantly increased the time to ignition (TTI) for specimens, while also remarkably decreasing the TSP and THR. Specifically, TTI increased from 10 s for MAW0 to 89 s for MAW4, and TSP and THR decreased from

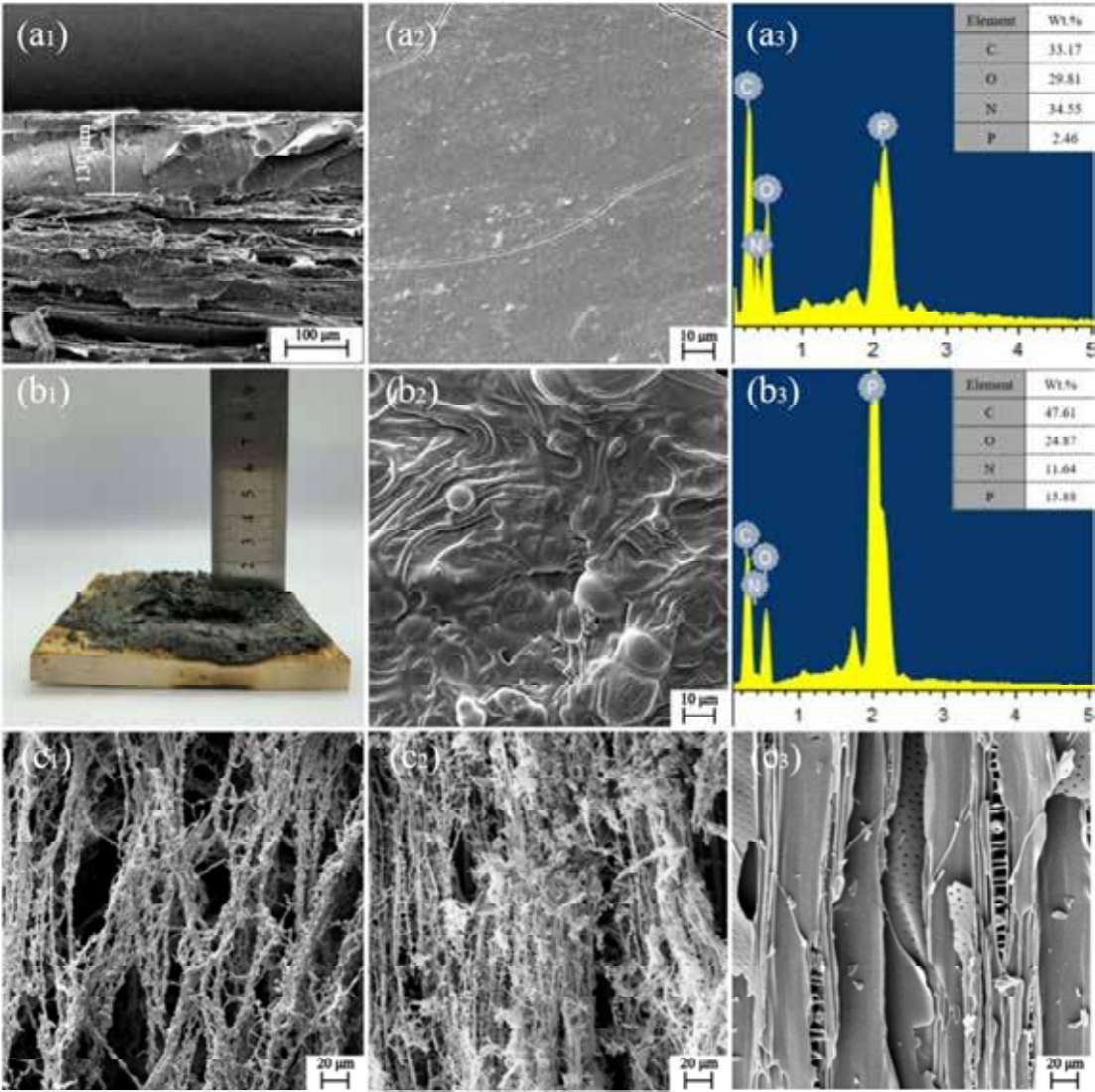


Fig. 11. Cross-sectional image (a₁) surface image of MAW4 (a₂); EDS energy spectrum of coatings surface (a₃) EDS energy spectrum of char residue surface (b₃); the intumescent char layer of MAW4 (b₁ and b₂); Microscopic morphology of the interior structure of pure wood residual char (c₁), MAW0(c₂), and MAW4 (c₃) after the CCT.

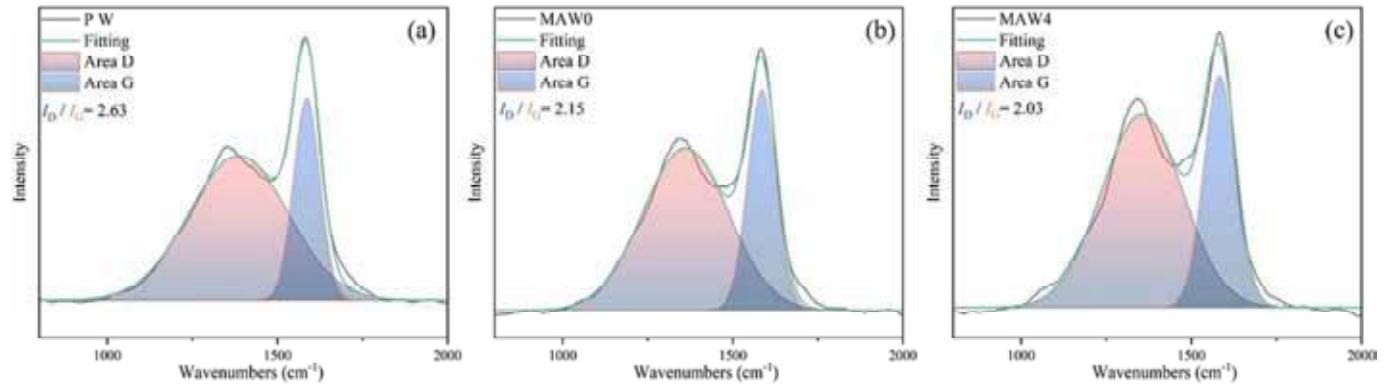


Fig. 12. Raman spectra of the surface char layer.

3.23 m² and 77.76 MJ/m² for MAW0 to 2.15 m² and 54.85 MJ/m² for MAW4, respectively. Compared with MAW0, the THR and TSP of MAW4 decreased by 29.4 % and 33.4 %, respectively. The above results indicated that APU decomposed rapidly during the initial combustion stage,

producing phosphate or pyrophosphate. This promoted the production of a phosphorus-rich char layer over the wood surface, which inhibited further heat transfer and retarded the thermal degradation of wood [65–67].

The two SPR peaks for MAW4 were significantly delayed and reduced compared with those of pure wood. The TSP of MAW0 was higher than that of pure wood due to the higher proportion of C and H elements in MUF, which tended to produce carbon fragments. Consequently, large volumes of smoke were produced due to incomplete combustion during the test. The TSP of pure wood was significantly lower than that of MAW4 and higher than that of MAW0 because APU facilitated smoke generation at the surface of the intumescent char layer of MAW4 and inhibited smoke release. In addition, the average CO yield (Y_{CO}) of MAW4 was higher than that of MAW0, while the CO_2 yield (Y_{CO_2}) was lower than the latter. This was attributed to the flame-retardancy of the coated MAW4, which led to the incomplete combustion of the substrate, and the release of more CO. This further confirmed that APU facilitated the production of a protective char layer and retarded the thermal degradation of wood [18,68,69].

Thermal infrared imaging tests illustrate the heat insulation properties of the flame-retardant coatings. The device was set up, as previously reported [12]. The thermal infrared images and residual carbon after the experiment are shown in Fig. 10. The flames of pure wood and MAW0 spread to the back side after 5 min of burning, showing temperatures of $>560^\circ\text{C}$ and 452.5°C , respectively. Compared with MAW0, the back-side temperatures of MAW3, MAW4, and MAW5 decreased significantly to 192.0°C , 100.9°C , and 71.1°C , respectively. The height of the intumescent char layer increased with the APU content, which protected the wood by insulating it from heat.

3.5. Char residue analysis

Fig. 11a₁ shows a cross-sectional image of MAW4, in which the coatings was about $130\ \mu\text{m}$ thick, while the height of the carbon residue after the test was approximately 1 cm (Fig. 11b₁). The expansion coefficient of MAW4 was 76.9, which indicates that introducing APU significantly enhanced the carbon-forming ability of the coating. Fig. 11a₃ and b₃ show the elemental contents of the coatings and residual char layer of MAW4, respectively. C, N, O, and P elements were observed in both the coatings and carbon residue of MAW4. After testing, the relative content of N significantly decreased, and nC/nO was 1.91, which was 70 % higher than before the test. This indicates that APU promoted the dehydration and carbonization of the coatings and the release of non-combustible gases such as NH_3 and H_2O . According to the apparent morphology of the residual carbon of MAW4 (Fig. 11b₂), it formed a continuous and homogeneous char layer at the wood surface. Fig. 12c₁–c₃ exhibit the internal residual char micromorphologies after cone calorimetry for pure wood, MAW0, and MAW4. In the residual char of pure wood and MAW0, only the basic fiber structure remained, while MAW4 retained the complete structure of wood, indicating that the intumescent char prevented the transmission of heat and combustible gases and maintained the integrity of the internal structure of the wood. The above results indicate that APU protected wood via gas-phase and condensed-phase mechanisms.

To better demonstrate the protective function of flame-retardant coatings for wood substrates, the graphitization of pure wood, MAW0, and MAW4 char residues was evaluated by Raman spectroscopy (Fig. 12a–c). The spectra of each sample showed two intense peaks near $1350\ \text{cm}^{-1}$ and $1585\ \text{cm}^{-1}$, which corresponded to the D and G bands, which represent amorphous carbon and graphitized carbon, respectively. Generally, the degree of graphitization in char is expressed by the ratio of the integrated peak intensities. When the value of I_D/I_G was lower, the degree of graphitization of the residual carbon was higher, and the higher graphitization of the char layer improved the flame-retardancy [70,71]. The values of I_D/I_G for pure wood, MAW0, and MAW4 were 2.63, 2.15, and 2.03, respectively. These values indicate that APU promoted the formation of ordered and dense carbon structures that inhibited gas and mass transfer and provided better protection for wood substrates.

3.6. Fire-retardancy and smoke suppression mechanism

During the initial stages of combustion, the coatings underwent thermal decomposition to release small-molecule gases and inert gases that reduced the oxygen concentration in the environment and retarded the degradation of the coatings. As the temperature increased, APU decomposed into phosphate derivatives that catalyzed the formation of phosphorus-rich crosslinked molten carbon by polymerization and aromatization of the carbon-rich components. The coatings continued to decompose, releasing non-combustible gases that inflated the melted carbon to form intumescent char layers. The transmission of heat and combustible gas was limited by the intumescent char layer at the surface, which prevented further thermal degradation of the substrate.

4. Conclusions

APU was synthesized from adenosine, formaldehyde, phosphite, and urea, and its structure was investigated by FTIR, XPS, and NMR. Then, APU and MUF were mixed to prepare waterborne transparent flame-retardant coatings that were applied to wood surfaces. The results indicated that MAW4 passed the UL-94 V-0 rating, demonstrating LOI values of 54.5 % and a TTI of 89 s. The THR and TSP of MAW4 decreased by 29.4 % and 33.4 %, respectively, which indicated that the adenosine-based flame-retardant coatings showed excellent fire-retardancy and smoke suppression. The SEM images and Raman spectra revealed the formation of a continuous and homogeneous char layer in the flame-retardant coatings during combustion. MAW4 exhibited good physical properties and was suitable for daily applications. This paper proposed a novel strategy for the utilization of adenosine and a new approach for synthesizing waterborne transparent intumescent flame-retardant coatings.

Supplementary data to this article can be found online at <https://doi.org/10.1016/j.porgcoat.2023.108061>.

CRediT authorship contribution statement

Qingjie Liu: Performing experiments, Writing, Designing research, Data analysis. Haolong Luo: Performing experiments, Investigation. Zhenzhong Gao: Data analysis, Supervision. Yishuai Huang: Investigation. Jiaming Liang: Investigation. Haiyang Zhou *: Designing research, Data analysis. Jin Sun *: Writing, Data analysis, Supervision.

Declaration of competing interest

The authors declare that they have no known competing financial interests or personal relationships that could have appeared to influence the work reported in this paper.

Data availability

Data will be made available on request.

Acknowledgements

This work was financially supported by the National Key Research and Development Program of China (2022YFD2200702), the National Natural Science Foundation of China (32201494).

References

- [1] M. Li, X. Hao, M. Hu, Y. Huang, C. Tang, Y. Chen, L. Li, Synthesis of vanillin-based flame retardant epoxy coating on wood surface, *Prog. Org. Coat.* 172 (2022), 107161.
- [2] L. Zhou, Y. Fu, Flame-retardant wood composites based on immobilizing with chitosan/sodium phytate/Nano-TiO₂-ZnO coatings via layer-by-layer self-assembly, *Coatings* 10 (3) (2020) 296.

- [3] X. Zhao, Z. Liang, Y. Huang, Y. Hai, X. Zhong, S. Xiao, S. Jiang, Influence of phytic acid on flame retardancy and adhesion performance enhancement of poly (vinyl alcohol) hydrogel coating to wood substrate, *Prog. Org. Coat.* 161 (2021), 106453.
- [4] K. Wang, S. Wang, D. Meng, D. Chen, C. Mu, H. Li, J. Sun, X. Gu, S. Zhang, A facile preparation of environmentally-benign and flame-retardant coating on wood by comprising polysilicate and boric acid, *Cellulose* 28 (18) (2021) 11551–11566.
- [5] Y. Wang, X. Kou, H. Shi, J. Zhao, J. Deng, X. A, Enhanced flame retardancy of modified β -cyclodextrin doped silica fume-based geopolymeric coating covered on plywood, *Constr. Build. Mater.* 330 (2022) 127231.
- [6] D. Meng, K. Wang, S. Wang, Y. Qiu, X. Gu, J. Sun, H. Li, S. Zhang, Preparation of ultra-flame retardant wood materials with mechanical reinforcement and water resistance through biomimetic mineralization of carbonated apatite, *Cellulose* 30 (1) (2023) 525–537.
- [7] L. Yan, Z. Xu, X. Wang, Synergistic effects of organically modified montmorillonite on the flame-retardant and smoke suppression properties of transparent intumescent fire-retardant coatings, *Prog. Org. Coat.* 122 (2018) 107–118.
- [8] L. Yan, Z. Xu, D. Liu, Synthesis and application of novel magnesium phosphate ester flame retardants for transparent intumescent fire-retardant coatings applied on wood substrates, *Prog. Org. Coat.* 129 (2019) 327–337.
- [9] L. Yan, Z. Xu, X. Wang, Synergistic flame-retardant and smoke suppression effects of zinc borate in transparent intumescent fire-retardant coatings applied on wood substrates, *J. Therm. Anal. Calorim.* 136 (4) (2019) 1563–1574.
- [10] Z. Xu, Z. Chu, L. Yan, Enhancing the flame-retardant and smoke suppression properties of transparent intumescent fire-retardant coatings by introducing boric acid as synergistic agent, *J. Therm. Anal. Calorim.* 133 (3) (2018) 1241–1252.
- [11] P. Kukla, L. Greiner, S. Eibl, M. Döring, F. Schönberger, Novel phosphorus-containing silazanes as flame retardants in epoxy resins, *React. Funct. Polym.* 170 (2022), 105120.
- [12] F. Song, T. Liu, Q. Fan, D. Li, R. Ou, Z. Liu, Q. Wang, Sustainable, high-performance, flame-retardant waterborne wood coatings via phytic acid based green curing agent for melamine-urea-formaldehyde resin, *Prog. Org. Coat.* 162 (2022), 106597.
- [13] F. Xu, H. Zhang, J. Wu, Synergistic catalytic flame retardant effect of zirconium phosphate on the poplar plywood, *Construct. Build. Mater.* 290 (2021), 123208.
- [14] Y. Wang, J. Deng, J. Zhao, H. Shi, Facile preparation of aluminum triphosphate-containing intumescent flame-retarding coatings using aliphatic waterborne polyurethane as the binder, *Prog. Org. Coat.* 147 (2020), 105758.
- [15] Y. Wang, J. Zhao, Benign design of intumescent flame retardant coating incorporated various carbon sources, *Construct. Build. Mater.* 236 (2020), 117433.
- [16] T. Ma, L. Li, Q. Wang, C. Guo, Construction of intumescent flame retardant and hydrophobic coating on wood substrates based on thiol-ene click chemistry without photoinitiators, *Compos. Part B-Eng.* 177 (2019), 107357.
- [17] T. Wang, T. Liu, T. Ma, L. Li, Q. Wang, C. Guo, Study on degradation of phosphorus and nitrogen composite UV-cured flame retardant coating on wood surface, *Prog. Org. Coat.* 124 (2018) 240–248.
- [18] Y. Huang, T. Ma, L. Li, Q. Wang, C. Guo, Facile synthesis and construction of renewable, waterborne and flame-retardant UV-curable coatings in wood surface, *Prog. Org. Coat.* 172 (2022), 107104.
- [19] L. Chen, S. Zeng, Y. Xu, W. Nie, Y. Zhou, P. Chen, Epoxy-modified silicone resin based N/P/Si synergistic flame-retardant coating for wood surface, *Prog. Org. Coat.* 170 (2022), 106953.
- [20] X. Wang, H. Nabipour, Y. Kan, L. Song, Y. Hu, A fully bio-based, anti-flammable and non-toxic epoxy thermosetting network for flame-retardant coating applications, *Prog. Org. Coat.* 172 (2022), 107095.
- [21] M. Li, X. Hao, M. Hu, Y. Huang, Y. Qiu, L. Li, Synthesis of bio-based flame-retardant epoxy co-curing agent and application in wood surface coating, *Prog. Org. Coat.* 167 (2022), 106848.
- [22] Z. Xu, X. Xie, L. Yan, Y. Feng, Fabrication of organophosphate-grafted kaolinite and its effect on the fire-resistant and anti-ageing properties of amino transparent fire-retardant coatings, *Polym. Degrad. Stabil.* 188 (2021), 109589.
- [23] L. Yan, X. Tang, Z. Xu, X. Xie, Fabrication of talc reinforced transparent fire-retardant coating towards excellent fire protection, antibacterial, mechanical and anti-ageing properties, *Polym. Degrad. Stabil.* 203 (2022), 110074.
- [24] L. Yi, Q. Yang, L. Yan, N. Wang, Facile fabrication of multifunctional transparent fire-retardant coatings with excellent fire resistance, antibacterial and anti-ageing properties, *Prog. Org. Coat.* 169 (2022), 106925.
- [25] L. Yan, Z. Xu, N. Deng, Synthesis of organophosphate-functionalized graphene oxide for enhancing the flame retardancy and smoke suppression properties of transparent fire-retardant coatings, *Polym. Degrad. Stabil.* 172 (2020), 109064.
- [26] L.B. Santos, R.S. Assis, J.A. Barreto, M.A. Bezerra, C.G. Novaes, V.A. Lemos, Deep eutectic solvents in liquid-phase microextraction: contribution to green chemistry, *Trac Trend. Anal. Chem.* 146 (2022), 116478.
- [27] Á.I. López-Lorente, F. Peña-Pereira, S. Pedersen-Bjerggaard, V.G. Zuñi, S.A. Ozkan, E. Psillakis, The ten principles of green sample preparation, *Trac Trend. Anal. Chem.* 148 (2022), 116530.
- [28] Y. Zhang, Z. Xiong, H. Ge, L. Ni, T. Zhang, S. Huo, P. Song, Z. Fang, Core-shell biodegraded flame retardants based on chitosan/alginate coated ammonia polyphosphate for enhancing flame retardancy of polylactic acid, *ACS Sustain. Chem. Eng.* 8 (16) (2020) 6402–6412.
- [29] I.P.S. Fernando, W. Lee, E.J. Han, C. Ahn, Alginate-based nanomaterials: fabrication techniques, properties, and applications, *Chem. Eng. J.* 391 (2020), 123823.
- [30] C.H.T.S. Chen, A facile strategy to achieve fully bio-based epoxy thermosets from eugenol, *Green Chem.* 21 (16) (2019) 4475–4488.
- [31] Y. Kim, J. Cho, Y.N. Kim, K.W. Kim, B.W. Lee, J.W. Kim, M. Kim, Y.C. Jung, Recyclable, flame-retardant and smoke-suppressing tannic acid-based carbon-fiber-reinforced plastic, *Compos. Part B-Eng.* 197 (2020), 108173.
- [32] W. Yan, M. Shi, C. Dong, L. Liu, C. Gao, Applications of tannic acid in membrane technologies: a review, *Adv. Colloid Interface* 284 (2020), 102267.
- [33] C. Bo, Z. Shi, L. Hu, Z. Pan, Y. Hu, X. Yang, P. Jia, X. Ren, M. Zhang, Y. Zhou, Cardanol derived P, Si and N based precursors to develop flame retardant phenolic foam, *Sci. Rep.* 10 (1) (2020) 12082.
- [34] M. Ali, Y. Lu, S. Ahmed, S. Khanal, S. Xu, Effect of modified cardanol as secondary plasticizer on thermal and mechanical properties of soft polyvinyl chloride, *ACS Omega* 5 (28) (2020) 17111–17117.
- [35] F. Chu, C. Ma, T. Zhang, Z. Xu, X. Mu, W. Cai, X. Zhou, S. Ma, Y. Zhou, W. Hu, L. Song, Renewable vanillin-based flame retardant toughening agent with ultra-low phosphorus loading for the fabrication of high-performance epoxy thermoset, *Compos. Part B-Eng.* 190 (2020), 107925.
- [36] P. Gnanasekar, M. Feng, N. Yan, Facile synthesis of a phosphorus-containing sustainable biomolecular platform from vanillin for the production of mechanically strong and highly flame-retardant resins, *ACS Sustain. Chem. Eng.* 8 (47) (2020) 17417–17426.
- [37] S. Velasquez, L. Prevedel, S. Valdebenito, A.M. Gorska, M. Golovko, N. Khan, J. Geiger, E.A. Eugenin, Circulating levels of ATP is a biomarker of HIV cognitive impairment, *EBioMedicine* 51 (2020), 102503.
- [38] S.H. Jeong, J.H. Heo, J.W. Lee, M.J. Kim, C.H. Park, J.H. Lee, Bioinspired adenosine triphosphate as an “All-In-One” green flame retardant via extremely intumescent char formation, *ACS Appl. Mater. Interfaces* 13 (19) (2021) 22935–22945.
- [39] Y. Fang, W. Sun, J. Li, H. Liu, X. Liu, Eco-friendly flame retardant and dripping-resistant of polyester/cotton blend fabrics through layer-by-layer assembly fully bio-based chitosan/phytic acid coating, *Int. J. Biol. Macromol.* 175 (2021) 140–146.
- [40] P. Li, B. Wang, Y. Xu, Z. Jiang, C. Dong, Y. Liu, P. Zhu, Ecofriendly flame-retardant cotton fabrics: preparation, flame retardancy, thermal degradation properties, and mechanism, *ACS Sustain. Chem. Eng.* 7 (23) (2019) 19246–19256.
- [41] S. Kulkarni, Z. Xia, S. Yu, W. Kiratitanavut, A.B. Morgan, J. Kumar, R. Mosurkal, R. Nagarajan, Bio-based flame-retardant coatings based on the synergistic combination of tannic acid and phytic acid for nylon-cotton blends, *ACS Appl. Mater. Interfaces* 13 (51) (2021) 61620–61628.
- [42] D. Meng, Y. Li, P. Qi, J. Sun, X. Gu, H. Li, Z. Wang, S. Zhang, Constructing a bio-based flame retardant coating through co-depositing polydopamine and guanosine 5'-monophosphate disodium salt (GMP) for flexible polyurethane foam, *Mater. Today Chem.* 27 (2023), 101320.
- [43] X. Zheng, Y. Dong, X. Liu, Y. Xu, R. Jian, Fully bio-based flame-retardant cotton fabrics via layer-by-layer self assembly of laccase and phytic acid, *J. Clean. Prod.* 350 (2022), 131525.
- [44] W. Qian, X. Li, J. Zhou, Y. Liu, Z. Wu, High synergistic effects of natural-based tea saponin in intumescent flame-retardant coatings for enhancement of flame retardancy and pyrolysis performance, *Prog. Org. Coat.* 127 (2019) 408–418.
- [45] H. Nabipour, X. Wang, L. Song, Y. Hu, A fully bio-based coating made from alginate, chitosan and hydroxyapatite for protecting flexible polyurethane foam from fire, *Carbohydr. Polym.* 246 (2020), 116641.
- [46] Y. Zhao, Z. Xie, Y. Deng, A. Huang, Y. He, B. Wen, X. Liao, R. Chang, G. Zhang, L. Zhu, Y. Wang, T. Li, Y. Zhong, J. Zuo, H. Zhang, M. Chen, J. Liu, X. Chen, H. Liu, Photothermal nanobomb blocking metabolic adenosine-A2AR potentiates infiltration and activity of T cells for robust antitumor immunotherapy, *Chem. Eng. J.* 450 (2022), 138139.
- [47] Z. Zhao, Q. Li, X. Qin, M. Zhang, Q. Du, Y. Luan, An injectable hydrogel reshaping adenosine axis for cancer therapy, *Adv. Funct. Mater.* 32 (24) (2022) 2200801.
- [48] C. Liang, Y. Du, Y. Wang, A. Ma, S. Huang, Z. Ma, Intumescent fire-retardant coatings for ancient wooden architectures with ideal electromagnetic interference shielding, *Adv. Compos. Hybrid Mater.* 4 (4) (2021) 979–988.
- [49] W. Wu, Y. Ni, L. Chen, T. Fu, X. Wang, Y. Wang, Trinity effect of potassium sulfonate-benzimidazole towards self-intumescent flame-retarded polyester with low fire hazards, *Chem. Eng. J.* 429 (2022), 132121.
- [50] H. Lv, Y. Du, H. Zhang, Y. Zheng, Z. Yan, N. Dong, Advances in Mannich-type reactions based on the classification of compounds with activated α -H, *Chem. Select* 8 (21) (2023), e202300173.
- [51] M. Pu, H. Guo, Z. Qian, X. Li, Q. Shen, Application of the Mannich reaction in the structural modification of natural products, *J. Enzym. Inhib. Med. Ch.* 38 (1) (2023) 2235095.
- [52] I. Bagheri, L. Mohammadi, V. Zadsirjan, M.M. Heravi, Organocatalyzed asymmetric Mannich reaction: an update, *Chem. Select* 6 (5) (2021) 1008–1066.
- [53] C. Wan, G. Zhang, F. Zhang, A novel guanidine ammonium phosphate for preparation of a reactive durable flame retardant for cotton fabric, *Cellulose* 27 (6) (2020) 3469–3483.
- [54] F. Xu, L. Zhong, Y. Xu, C. Zhang, P. Wang, F. Zhang, G. Zhang, Synthesis of three novel amino acids-based flame retardants with multiple reactive groups for cotton fabrics, *Cellulose* 26 (12) (2019) 7537–7552.
- [55] T. Gou, X. Wu, Q. Zhao, S. Chang, P. Wang, Novel phosphorus/nitrogen-rich oligomer with numerous reactive groups for durable flame-retardant cotton fabric, *Cellulose* 28 (11) (2021) 7405–7419.
- [56] M. Mathlouthi, A.M. Seuvre, J.L. Koenig, FT-IR and laser-Raman spectra of adenine and adenosine, *Carbohydr. Res.* 1 (131) (1984) 15.
- [57] S. Li, L. Zhong, S. Huang, D. Wang, F. Zhang, G. Zhang, A reactive fluorine-free, efficient superhydrophobic and flame-retardant finishing agent for cotton fabrics, *Cellulose* 26 (10) (2019) 6333–6347.

- [58] F. Fang, D. Xiao, X. Zhang, Y. Meng, C. Cheng, C. Bao, X. Ding, H. Cao, X. Tian, Construction of intumescent flame retardant and antimicrobial coating on cotton fabric via layer-by-layer assembly technology, *Surf. Coat. Tech.* 276 (2015) 726–734.
- [59] C. Feng, M. Liang, Y. Zhang, J. Jiang, J. Huang, H. Liu, Synergistic effect of lanthanum oxide on the flame retardant properties and mechanism of an intumescent flame retardant PLA composites, *J. Anal. Appl. Pyrol.* 122 (2016) 241–248.
- [60] F. Xu, L. Zhong, C. Zhang, P. Wang, F. Zhang, G. Zhang, Novel high-efficiency casein-based P-N-containing flame retardants with multiple reactive groups for cotton fabrics, *ACS Sustain. Chem. Eng.* 7 (16) (2019) 13999–14008.
- [61] Z. Xu, N. Deng, L. Yan, Flame retardancy and smoke suppression properties of transparent intumescent fire-retardant coatings reinforced with layered double hydroxides, *J. Coat. Technol. Res.* 17 (1) (2020) 157–169.
- [62] Z. Xu, D. Liu, L. Yan, X. Xie, Synergistic effect of sepiolite and polyphosphate ester on the fire protection and smoke suppression properties of an amino transparent fire-retardant coating, *Prog. Org. Coat.* 141 (2020), 105572.
- [63] A. Satdive, S. Mestry, P. Borse, S. Mhaske, Phosphorus- and silicon-containing amino curing agent for epoxy resin, *Iran. Polym. J.* 29 (5) (2020) 433–443.
- [64] M. Patel, S. Mestry, S.P. Khuntia, S. Mhaske, Gallic acid-derived phosphorus-based flame-retardant multifunctional crosslinking agent for PU coating, *J. Coat. Technol. Res.* 17 (1) (2020) 293–303.
- [65] Q. Yang, J. Wang, X. Chen, S. Yang, S. Huo, Q. Chen, P. Guo, X. Wang, F. Liu, W. Chen, P. Song, H. Wang, A phosphorus-containing tertiary amine hardener enabled flame retardant, heat resistant and mechanically strong yet tough epoxy resins, *Chem. Eng. J.* 468 (2023), 143811.
- [66] Q. Zhang, J. Wang, S. Yang, J. Cheng, G. Ding, Y. Hu, S. Huo, Synthesis of a P/N/S-based flame retardant and its flame retardant effect on epoxy resin, *Fire Saf. J.* 113 (2020), 102994.
- [67] C. Jo, Y. Jang, D. Mun, C. Yu, C. Choe, S. Ri, Preparation of acrylic emulsion coating with melamine polyphosphate, pentaerythritol and titanium dioxide for flame retardant cotton/polyethylene terephthalate blend fabrics, *Polym. Degrad. Stabil.* 214 (2023), 110366.
- [68] Q. Chen, L. Liu, A. Zhang, W. Wang, Z. Wang, J. Zhang, J. Feng, S. Huo, X. Zeng, P. Song, An iron phenylphosphinate@graphene oxide nanohybrid enabled flame-retardant, mechanically reinforced, and thermally conductive epoxy nanocomposites, *Chem. Eng. J.* 454 (2023), 140424.
- [69] S. Zhu, Xu, preparation of flame-retardant rigid polyurethane foams by combining modified melamine-formaldehyde resin and phosphorus flame retardants, *ACS Omega* 5 (17) (2020) 9658–9667.
- [70] T. Gao, F. Wang, Y. Xu, C. Wei, S. Zhu, W. Yang, H. Lu, Luteolin-based epoxy resin with exceptional heat resistance, mechanical and flame retardant properties, *Chem. Eng. J.* 428 (2022), 131173.
- [71] Q. Zhao, M. Zhang, S. Gao, Z. Pan, Y. Xue, P. Jia, C. Bo, Z. Luo, F. Song, Y. Zhou, A mussel-inspired high bio-content thermosetting polyimine polymer with excellent adhesion, flame retardancy, room-temperature self-healing and diverse recyclability, *J. Mater. Chem. A* 10 (2022) 11363–11374.

Article

Phenol Liquefaction of Waste Sawdust Pretreated by Sodium Hydroxide: Optimization of Parameters Using Response Surface Methodology

Shihao Lv, Xiaoli Lin, Zhenzhong Gao, Xianfeng Hou, Haiyang Zhou * and Jin Sun * 

College of Materials and Energy, South China Agricultural University, Guangzhou 510642, China

* Correspondence: hyzhou@scau.edu.cn (H.Z.); sunjin@scau.edu.cn (J.S.)

Abstract: In this study, a two-step method was used to realize the liquefaction of waste sawdust under atmospheric pressure, and to achieve a high liquefaction rate. Specifically, waste sawdust was pretreated with NaOH, followed by liquefaction using phenol. The relative optimum condition for alkali–heat pretreatment was a 1:1 mass ratio of NaOH to sawdust at 140 °C. The reaction parameters including the mass ratio of phenol to pretreated sawdust, liquefaction temperature, and liquefaction time were optimized by response surface methodology. The optimal conditions for phenol liquefaction of pretreated sawdust were a 4.21 mass ratio of phenol to sawdust, a liquefaction temperature of 173.58 °C, and a liquefaction time of 2.24 h, resulting in corresponding liquefied residues of 6.35%. The liquefaction rate reached 93.65%. Finally, scanning electron microscopy (SEM), Fourier transform infrared spectroscopy (FT-IR), and X-ray diffraction (XRD) were used to analyze untreated waste sawdust, pretreated sawdust, liquefied residues, and liquefied liquid. SEM results showed that the alkali–heat pretreatment and liquefaction reactions destroyed the intact, dense, and homogeneous sample structures. FT-IR results showed that liquefied residues contain aromatic compounds with different substituents, including mainly lignin and its derivatives, while the liquefied liquid contains a large number of aromatic phenolic compounds. XRD showed that alkali–heat pretreatment and phenol liquefaction destroyed most of the crystalline regions, greatly reduced the crystallinity and changed the crystal type of cellulose in the sawdust.

Keywords: waste sawdust; alkali–heat pretreatment; liquefaction; response surface methodology; residual content



Citation: Lv, S.; Lin, X.; Gao, Z.; Hou, X.; Zhou, H.; Sun, J. Phenol Liquefaction of Waste Sawdust Pretreated by Sodium Hydroxide: Optimization of Parameters Using Response Surface Methodology. *Molecules* **2022**, *27*, 7880. <https://doi.org/10.3390/molecules27227880>

Academic Editors: Mohamad Nasir Mohamad Ibrahim, Patricia Graciela Vázquez and Mohd. Hazwan Hussin

Received: 15 October 2022

Accepted: 11 November 2022

Published: 15 November 2022

Publisher's Note: MDPI stays neutral with regard to jurisdictional claims in published maps and institutional affiliations.



Copyright: © 2022 by the authors. Licensee MDPI, Basel, Switzerland. This article is an open access article distributed under the terms and conditions of the Creative Commons Attribution (CC BY) license (<https://creativecommons.org/licenses/by/4.0/>).

1. Introduction

Fossil energy is an important raw material utilized for the production of chemical products [1]. However, the utilization of fossil energy generates a number of greenhouse gases including sulfur oxide, nitrogen oxide, carbon oxide and carbon dioxide, causing air pollution and climate change [2]. Therefore, in order to alleviate energy crises and environmental pollution, researchers need to urgently search for cheap, clean and renewable energy resources [3]. As a natural renewable material with a huge storage capacity, lignocellulosic biomass has attracted increased research attention. It has a rich variety, including crop waste, wood processing residues, and wood product recycling waste, which is considered to be one of the most promising and sustainable alternatives to petroleum for the production of energy, materials and chemicals in the future [4,5].

Several treatment methods such as pyrolysis, liquefaction and gasification have been used to process lignocellulosic biomass to produce biofuels and other valuable chemicals [6,7]. Among them, liquefaction is an effective method for the integrated utilization of lignocellulosic biomass. Liquefaction technologies can be divided into two broad categories, hydrothermal liquefaction and solvent liquefaction [8]. Hydrothermal liquefaction is often carried out under harsh conditions, including high temperatures (200 °C to 400 °C), high pressures (5 MPa to 20 MPa), and a closed environment. Compared with hydrothermal

liquefaction, solvent liquefaction can be carried out under mild reaction conditions and is an effective method for the integrated utilization of biomass [9]. Solvent liquefaction usually uses polyols or phenols to liquefy biomass at atmospheric pressure and relatively low temperature. Most often, acid is used as the catalyst and phenol as the solvent in solvent liquefaction, which reflects a high biological conversion rate [10]. The liquefied products are rich in phenolic compounds, which can be used to prepare phenolic resin adhesives after condensation with formaldehyde [11]. However, the liquefied products contain unreacted solvents and acidic catalysts that require recycling or alkali neutralization before preparing adhesives [12].

Further, during the liquefaction, the cellulose and hemicellulose of lignocellulosic biomass are wrapped in highly polymerized polyphenolic structured lignin, which makes it difficult to transform, thus hindering the high-value utilization of lignocellulosic biomass. Targeted pretreatment of lignocellulosic biomass before liquefaction can change the chemical structure and composition of lignocellulose, soften the raw materials, and induce depolymerization and chain breaks [13]. More importantly, the alkaline or acidic conditions of the pretreatment stage can be utilized to meet economic and environmental criteria during the liquefaction, and the pretreated lignocellulosic biomass exhibits better liquefaction performance [14].

Response surface methodology (RSM) is highly effective for the optimal design of a regression model, which is used to resolve problems related to nonlinear data processing [15]. By fitting the regression and plotting the model, the effect of the variables and their interactions on the response variables can be easily evaluated, and the optimal value of the response and the corresponding experimental conditions can be determined. The model obtained by RSM is continuous and can be analyzed continuously for each experimental level during the search for the optimizing experimental conditions, so we can better understand the experimental process [16]. In addition, RSM allows process optimization in a limited number of experimental runs, thus significantly reducing experimental time and costs [17].

In this study, a two-step process was used to achieve the effective liquefaction of waste sawdust. The first step entailed the pretreatment of waste sawdust with hot alkali under atmospheric pressure. In the second step, the pretreated sawdust was liquefied using phenol as the liquefying agent. The effects of the mass ratio of sawdust to NaOH on the liquefaction were studied. Based on RSM, the effects of the three experimental variables, namely the mass ratio of phenol to pretreated sawdust, liquefaction temperature, and liquefaction time, and their interactions on the liquefaction effect of waste sawdust were systematically investigated. At the same time, the specific residual content model was established using the design software, which was analyzed in detail to determine the optimal liquefaction conditions. The validity of the model was verified by repeated experiments. Finally, the untreated waste sawdust, pretreated sawdust, liquefied residues and liquefied liquid were characterized and analyzed by scanning electron microscopy (SEM), Fourier transform infrared (FT-IR) spectroscopy, and X-ray diffraction (XRD) to facilitate the high-value utilization of waste sawdust.

2. Results and Discussion

2.1. Alkali–Heat Pretreatment—Screening and Optimization Tests

The effects of the mass ratio of sawdust to NaOH at 140 °C on the liquefied residue yield were studied (Figure 1). It could be seen that the mass ratio of sawdust to NaOH had a significant effect on the liquefied residue yield. The liquefied residue yield decreased initially and then increased as the sawdust to NaOH mass ratio increased. The liquefied residue yield was 12.5% at a mass ratio of 1:1.5. The liquefied residue yield of sawdust without alkali–heat pretreatment under the same liquefaction conditions was 80.4%, which was really high, indicating that the alkali–heat treatment destroyed the internal structure of sawdust, which was conducive to liquefaction. In a certain range, the liquefied residue yield decreased with the reduction in the sawdust to NaOH mass ratio. This was explained by as

the amount of NaOH increased, additional wood components were decomposed. Under alkali–heat pretreatment, the carbohydrates are degraded via the peeling reaction of the reducing end groups. Since hemicellulose has a substantially lower molecular weight than cellulose, it is also degraded via hydrolysis in hot alkali, increasing the number of reducing end groups and enhancing the erosion of polymer chains [18,19]. In addition, the presence of NaOH separated the bonds between lignin and carbohydrates, and disrupted the ether bonds between lignin polymers, resulting in the depolymerization and degradation of lignin [20,21]. However, when the mass ratio of sawdust to NaOH was 1:2, the yield of the liquefied residue was slightly increased, indicating that the high proportion of NaOH enhanced the repolymerization of degradation products or inhibited the depolymerization of lignocellulose [22].

At a sawdust to NaOH mass ratio of 1:1, the yield of liquefied residue was relatively low. However, when the mass ratio decreased to 1:1.5, the yield of liquefied residue changed slowly. In terms of energy conservation, a satisfactory liquefied residue yield was obtained at a sawdust to NaOH mass ratio of 1:1. Meanwhile, it should be noted that some of the adsorbed NaOH crystal on sawdust during the pretreatment was dissolved during the subsequent liquefaction, which induced cellulose swelling and increased the porosity and specific surface area of the sawdust, thus increasing the accessibility of phenol to sawdust and promoting the degradation of the sawdust [23–25]. According to the literature, the liquefied residue of sawdust has a significant impact on the performance of the subsequent fabrication of bio-based phenolic resins [26]. Therefore, it is important to optimize the pretreatment conditions and thus reduce the residual content of liquefaction.

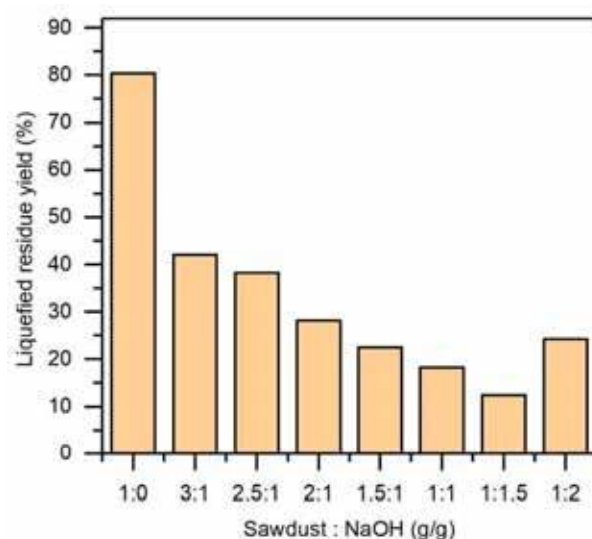


Figure 1. The effect of alkali–heat pretreatment on the liquefied residue yield. The phenol liquefaction temperature was 150 °C, the mass ratio of phenol to pretreated sawdust was 5:1, and the liquefaction time was 2 h.

2.2. Optimization of Phenol Liquefaction of Waste Sawdust

2.2.1. Model Fitting

The results of the whole experimental runs are summarized in Table 1. In general, the residual content after phenol liquefaction of waste sawdust was relatively low. Under different liquefaction conditions, the residual content varied from 6.82% to 17.13%, suggesting that phenol liquefaction is an effective and feasible biomass conversion method. The liquefied products can further react with formaldehyde to produce valuable biobased wood adhesive [27]. The lowest residual content was observed in a phenol-to-pretreated sawdust mass ratio of 4.21, a liquefaction temperature of 173.58 °C, and a liquefaction time of 2.24 h. The fitting quadratic multiple regression equation after the exclusion of the

insignificant terms for the residual content of waste sawdust is determined based on these data, as shown in Equation (1).

$$R = 162.74864 - 24.02153A - 1.03750B - 14.186057C - 0.134375BC + 2.15511A^2 + 0.003566B^2 + 7.64545C^2 \quad (1)$$

where R is the residual content (%), A denotes the mass ratio of phenol to pretreated sawdust (P/S), B refers to the liquefaction temperature (°C), and C is the liquefaction time (h).

Table 1. Liquefaction variables and levels.

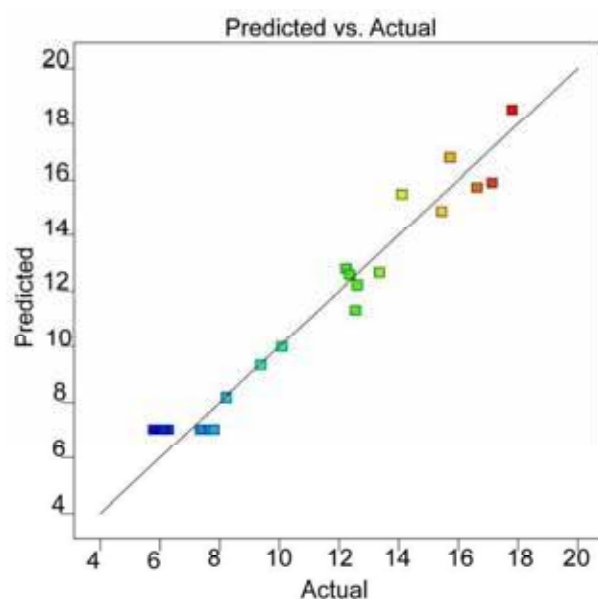
Factors				
Order	Mass Ratio of Phenol to Pretreated Sawdust, P/S	Liquefaction Temperature, T (°C)	Liquefaction Time, t (h)	Residual Content, R (%)
1	3	140	1.5	17.13
2	5	140	1.5	12.55
3	3	180	1.5	15.44
4	5	180	1.5	12.61
5	3	140	2.5	16.62
6	5	140	2.5	13.36
7	3	180	2.5	9.38
8	5	180	2.5	8.22
9	2	160	2	17.8
10	6	160	2	12.23
11	4	120	2	14.11
12	4	200	2	10.09
13	4	160	1	15.72
14	4	160	3	12.36
15	4	160	2	7.58
16	4	160	2	7.35
17	4	160	2	7.81
18	4	160	2	6.28
19	4	160	2	5.78
20	4	160	2	6.12

In order to further verify the adequacy of the quadratic model, an analysis of variance (ANOVA) was carried out and the results are shown in Table 2. *p*-values less than 0.05 indicate the model variables are statistically significant, and the smaller the *p*-value, the more significant the corresponding coefficient and contribution to the response variable [17]. In this study, the *p*-value of the model was less than 0.0001 and the adjusted *R*² value was 0.9189. This indicated that the response regression model was highly significant and sufficient for the response variables tested. Further, the “lack of fit *f*-value” of 2.43 implied that the lack of fit was insignificant relative to the pure error. There was a 17.65% chance of a lack of fit *f*-value due to noise. The insignificant lack of fit was good, which indicated that the proposed model fitted the data well. Based on the *p*-values, it can be seen that the variables of A, B, C, the interaction term of BC, and the quadratic terms of A², B², C² were significant, indicating that the variables of the reaction were interactive and complex. The significant effect of every single variable on the residual content decreased as follows: A > B > C. The significant effect of interacting variables on residual content decreased in the order of BC > AB > AC. The magnitude of the *f*-value reflects the importance of each test variable on the index, and the larger *f*-value indicates the greater importance of the test index [28]. The importance of the influence of the test variables on residual content was as follows: A > B > C, which was identical to the significant effect of every single factor on residual content. In addition, the *R*² of the selected model was 0.9573, and the fitting degree was more than 95%, indicating that the model effectively reflected the changes in response values.

Table 2. Results of the analysis of variance for residual content.

Source	Sum of Squares	df	Mean Square	F Value	p Value	
Model	284.38	9	31.60	24.91	<0.0001	significant
A	32.98	1	32.98	26.00	0.0005	
B	30.39	1	30.39	23.96	0.0006	
C	17.79	1	17.79	14.02	0.0038	
AB	1.85	1	1.85	1.46	0.2546	
AC	1.12	1	1.12	0.8811	0.3700	
BC	14.45	1	14.45	11.39	0.0071	
A ²	116.78	1	116.78	92.07	<0.0001	
B ²	51.15	1	51.15	40.33	<0.0001	
C ²	91.85	1	91.85	72.42	<0.0001	
Residual	12.68	10	1.27			not significant
Lack of fit	8.98	5	1.80	2.43	0.1765	
Pure error	3.70	5	0.7404			
Cor total	297.06	19				

The comparison between the actual residual content obtained in the experiment and the predicted residual content based on the quadratic model is shown in Figure 2. Generally, each experimental data point should be approximately close to the regression line of the prediction data, which suggests that the estimated effect is true and effective [29]. In this study, the 20 groups of actual experimental values were distributed near the predicted value, which implied a strong correlation between the experimental responses and predicted responses.

**Figure 2.** Comparison between the predicted (straight line) and actual response values (points) obtained from the model for the response of residual content.

2.2.2. Main Response Surface Plots and Optimization

The three-dimensional response surface plots and contour plots were used to delineate the effect of independent variables and their interactions on residual content based on the obtained regression equation. The response surface plots of residual content were a function of two specific variables, while the other variable remained at a fixed value. The curve shapes of all response surfaces were upward concave, and all the center and edge points were within the studied range, which indicated that there was an optimal response for the content of liquefied residues.

The effect of the P/S ratio and the liquefaction temperature on the residual content is shown in Figure 3a,b. It can be seen that P/S and liquefaction temperature significantly affected the residual content. In a specific range, the residual content decreased with the

increase in P/S and liquefaction temperature and then increased with the further increased P/S and temperature after reaching the optimal critical point (P/S and temperature of 4.21 and 173.58 °C, respectively). Similar phenomena were observed in other woody materials [30]. The increase in P/S in the range of 2 to 4.21 reduced the residual content, indicating that the P/S values in this range facilitated the liquefaction of sawdust. However, when the P/S increased to a higher value, it negatively affected the sawdust liquefaction. These results suggest that lower P/S values lead to the recondensation of the low-molecular-weight compounds into insoluble residues [31]. An insufficient amount of phenol in the reaction system increases the viscosity of the liquefied products [32]. The P/S value of 4.21 is reasonable to ensure minimum residual content of waste sawdust for adequate liquefaction.

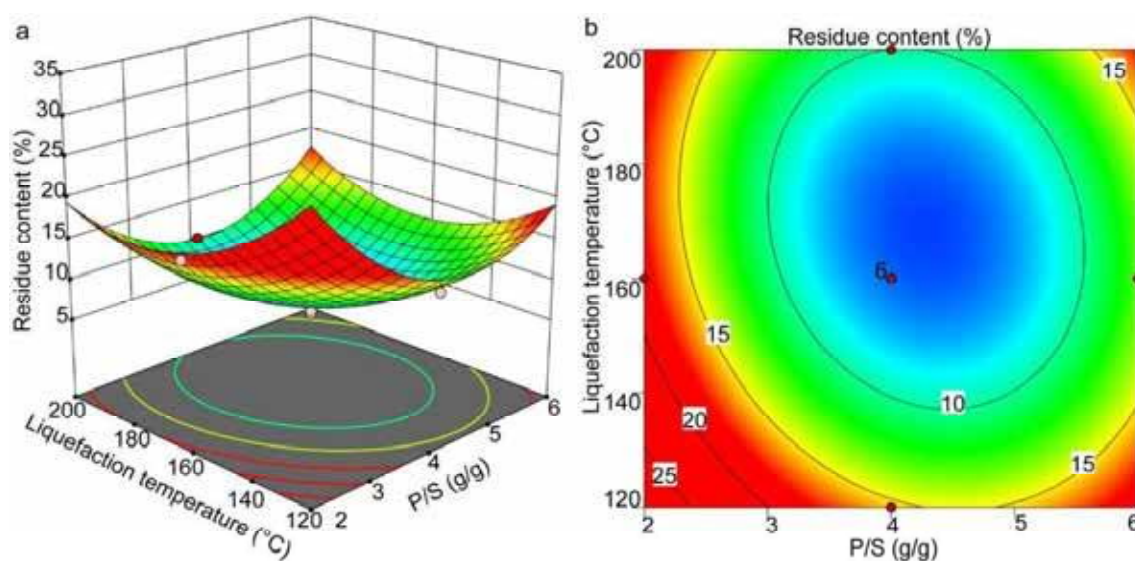


Figure 3. The response surface (a) and contour plots (b) showing the effects of P/S and liquefaction temperature on the residual content.

Further, the effect of liquefaction temperature on the residual content showed a similar trend compared with the P/S value. With the increase in reaction temperature, the residual content decreased first and then increased above 173.58 °C which is explained by the incomplete bond cleavage of different components of waste sawdust at lower temperatures due to less violent reaction conditions. In addition, reactions, such as hydrolyzation and depolymerization, resulting in smaller molecules could not be completed [33]. As the temperature increases, the glycosidic bonds break, leading to dehydration and decarboxylation, resulting in the cleavage of large molecules into smaller fragments [34], and a decrease in the residual content. However, with the further increase in temperature (>173.58 °C), the residual content increased gradually. This was mainly because of the unstable components in the liquefied product at high temperatures [35], and a series of complex reactions resulting in the formation of a large number of liquefied residues.

The comprehensive effects of the P/S ratio and liquefaction time on the residual content at a constant temperature are depicted in Figure 4a,b. It can be observed that the critical transition point was established when the P/S value was 4.21 and the liquefaction time was 2.24 h. With the increase in liquefaction time from 1 h to 2.24 h, the residual content gradually decreased to less than 5.6%. However, the residual content increased if the liquefaction time continued to extend. In the initial stage of the reaction, the degradation reaction played a dominant role, which decreased the residual content [32]; the residual content decreased. With the further extension of the reaction time, the polycondensation reaction and the degradation reaction among the liquefaction products gradually reach the balance until they took the dominant role, which led to the increase in the residue content [36].

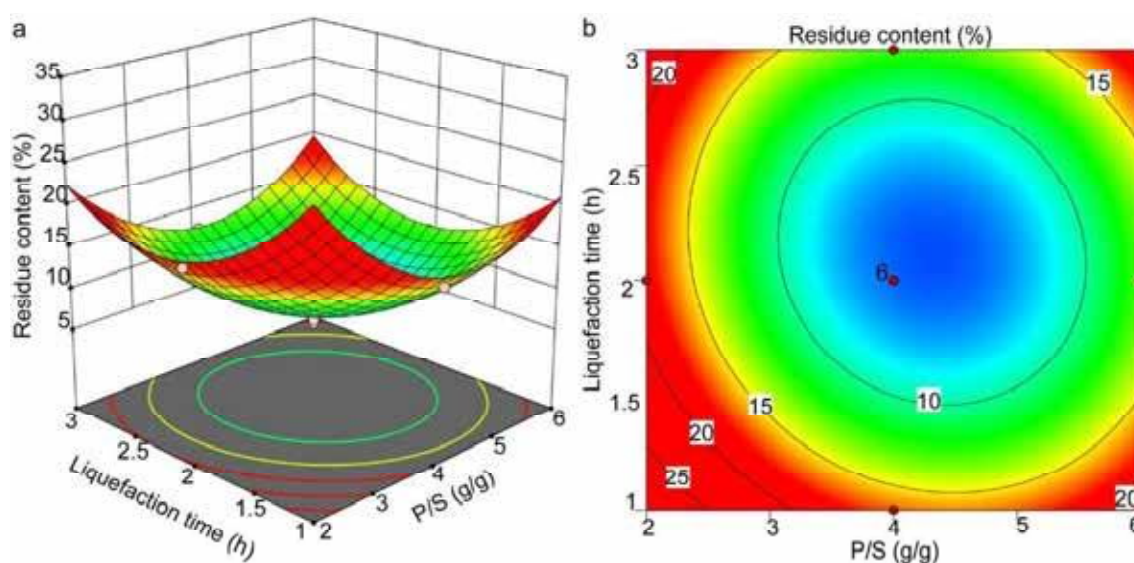


Figure 4. The response surface (a) and contour plots (b) showing the effects of P/S and liquefaction time on the residual content.

Figure 5a,b show the effects of liquefaction time and liquefaction temperature on the residual content at a constant P/S value. It can be seen that the effect of liquefaction time was closely related to the liquefaction temperature. Specifically, the variation in residual content over time was more pronounced at higher temperatures than at lower temperatures. At a constant liquefaction temperature (greater than 173.58 °C), when the liquefaction time increased from 1 h to 2.24 h, the residual content decreased significantly. Further extension of time to 2.6 h or longer resulted in an almost constant residual content or a slight increase. Similarly, compared with the shorter reaction times, the change in residual content with temperature was more significant under the longer reaction times. At a constant reaction time (greater than 2.24 h), the residual content decreased significantly with the temperature increase from 100 °C to 180 °C, followed by equilibrium and then a slight increase. This also confirmed that heating at 173.58 °C for 2.24 h facilitated waste sawdust liquefaction.

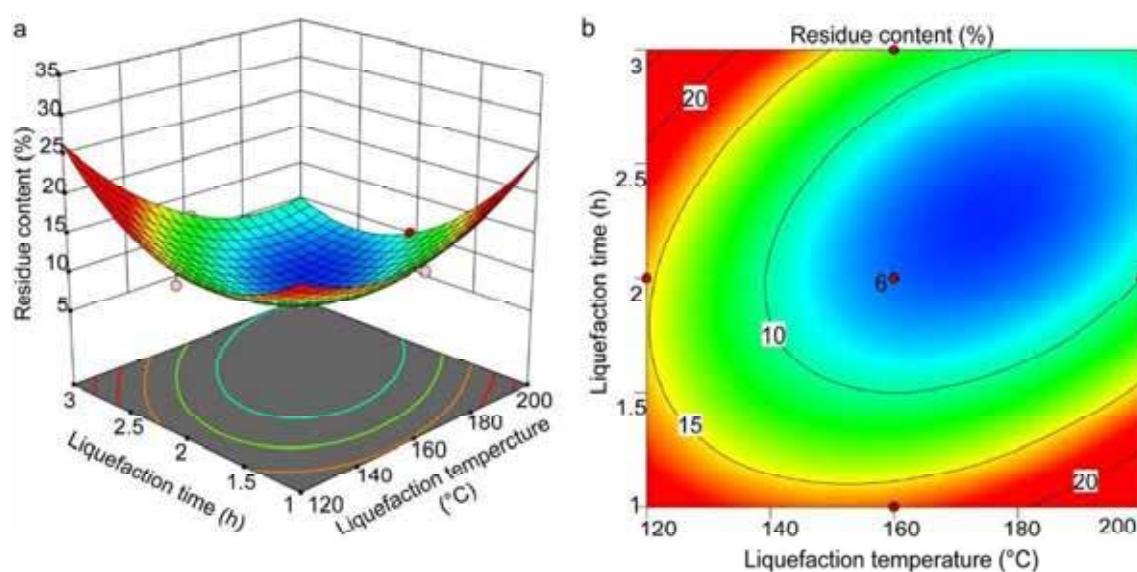


Figure 5. The response surface (a) and contour plots (b) showing the effects of liquefaction temperature and liquefaction time on the residual content.

To demonstrate the accuracy and reliability of the optimal liquefaction conditions determined from the fitted model, the experiment was repeated three times using the same method based on the predicted optimal point and the average value was calculated. The actual residual content obtained experimentally was 6.35%, while the residual content predicted based on Equation (1) was 6.15%. The results show that the experimental value agrees well with the model prediction, with an error of only 3.25%. It is thus clear that RSM can be used to optimize the process of waste sawdust phenol liquefaction. The optimal liquefaction occurred at a P/S ratio of 4.21, liquefaction temperature of 173.58 °C, and liquefaction time of 2.24 h.

2.3. SEM Analysis

SEM was used to assess the structural and morphological changes of sawdust after treatment (Figure 6). The surface of untreated sawdust was continuous and smooth, and the fibrous structure was relatively complete (Figure 6a), in which lignin was the encrusting material connecting the fibers and hemicellulose was the filling material distributed in the microfibrils of the cell wall [37]. The pretreated sawdust (Figure 6b) revealed many microfibril aggregates with a rougher and more wrinkled surface due to the activation of lignocellulose with alkali, resulting in partial structural degradation [38]. Further, the rough surface of pretreated sawdust increased the specific surface area, which increased the accessibility of phenol during the subsequent liquefaction. Following phenol liquefaction, the structure of the pretreated sawdust was severely damaged, with a lower degree of polymerization and loose and irregular texture (Figure 6c,d), due to the surface coke generated by the condensed lignin and cellulose [39].

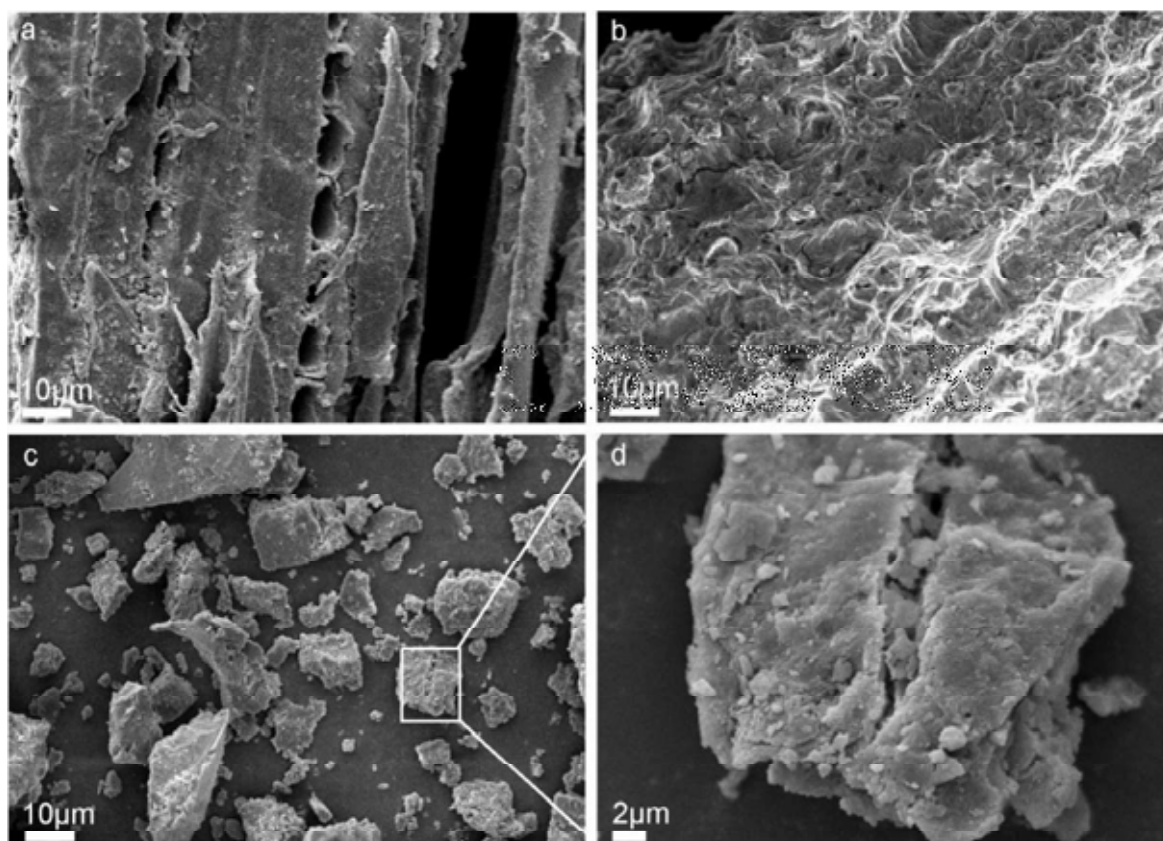


Figure 6. SEM micrographs of untreated sawdust (a), alkali-heat pretreated sawdust (b) liquefied residues (c,d).

2.4. FT-IR Analysis

The functional groups present in the untreated sawdust, pretreated sawdust, liquefied residues, and liquefied liquid were investigated by FT-IR. For untreated sawdust (Figure 7a), the broad peak at around 3400 cm^{-1} indicated O–H stretching vibrations [40]. The peak at 2925 cm^{-1} corresponded to the stretching vibration of C–H. The peaks between 1400 cm^{-1} and 1600 cm^{-1} are attributed to the aromatic skeleton in lignin [41]. Several peaks from 600 cm^{-1} to 900 cm^{-1} represent the characteristic peaks of aromatic monomers. Compared with untreated sawdust, the peak intensity of pretreated sawdust at 2925 cm^{-1} was significantly weakened, which suggested that pretreatment peels off most of the methylene groups in the aliphatic acid methylene group [42]. In addition, the weakening of the peaks at 1750 cm^{-1} , 1240 cm^{-1} , 1152 cm^{-1} and 1030 cm^{-1} indicates the breakage of cellulose glycosidic bonds and hemicellulose chains, suggesting that large amounts of hemicellulose and part of cellulose were degraded by hydrolysis and peeling reactions during the pretreatment [43]. Compared with untreated sawdust, the peaks between 1400 cm^{-1} and 1600 cm^{-1} and from 600 cm^{-1} to 900 cm^{-1} were enhanced, indicating that pretreatment promoted the decomposition of lignin into aromatic monomers and increased the formation of low-molecular-weight oligomers. It was noteworthy that the new peak of pretreated sawdust around 1332 cm^{-1} might correspond to the characteristic peak of NaOH.

After the liquefaction reaction, the disappearance of the peak at 1750 cm^{-1} for the liquefied residues (Figure 7b) indicated that the hemicellulose was further decomposed during the liquefaction. The strong peak of C–O at 1030 cm^{-1} associated with liquefied residues demonstrated the presence of a large amount of lignin and its derivatives remaining in the liquefied residues [39]. A strong peak at 1080 cm^{-1} attributed to the C–O peak in cellulose, indicated the presence of unliquefied cellulose in the liquefied residues. The peak enhancement at 1600 cm^{-1} and 1480 cm^{-1} indicated the presence of large amounts of aromatic compounds and their derivatives from lignin in liquefied liquid (Figure 7c). Similar phenomena were reported in previous studies [44,45]. The peak of the liquefied liquid around 1240 cm^{-1} may be due to the C–O stretching of the phenol or ester [46]. In addition, other peaks in the range of 600 cm^{-1} to 1000 cm^{-1} in the spectra of the liquefied liquid were attributed to C–H bending vibrations of aromatic hydrocarbons. The enhancement of these peaks can also be explained by the presence of a large number of phenolic compounds in the liquefied liquid.

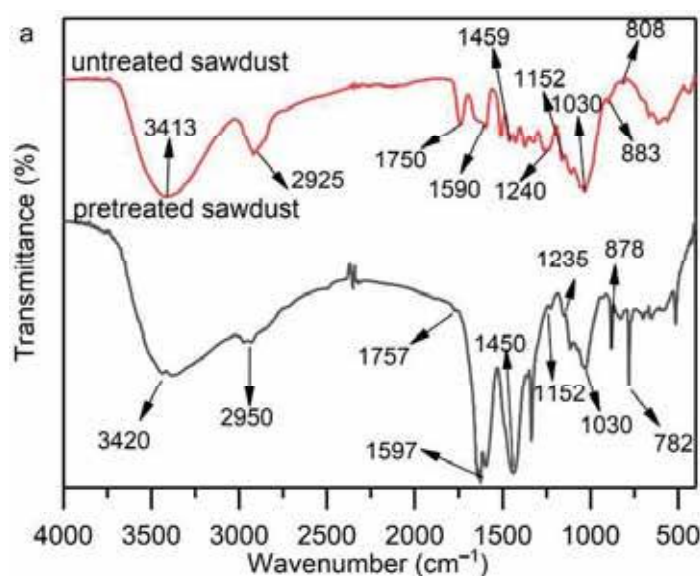


Figure 7. Cont.

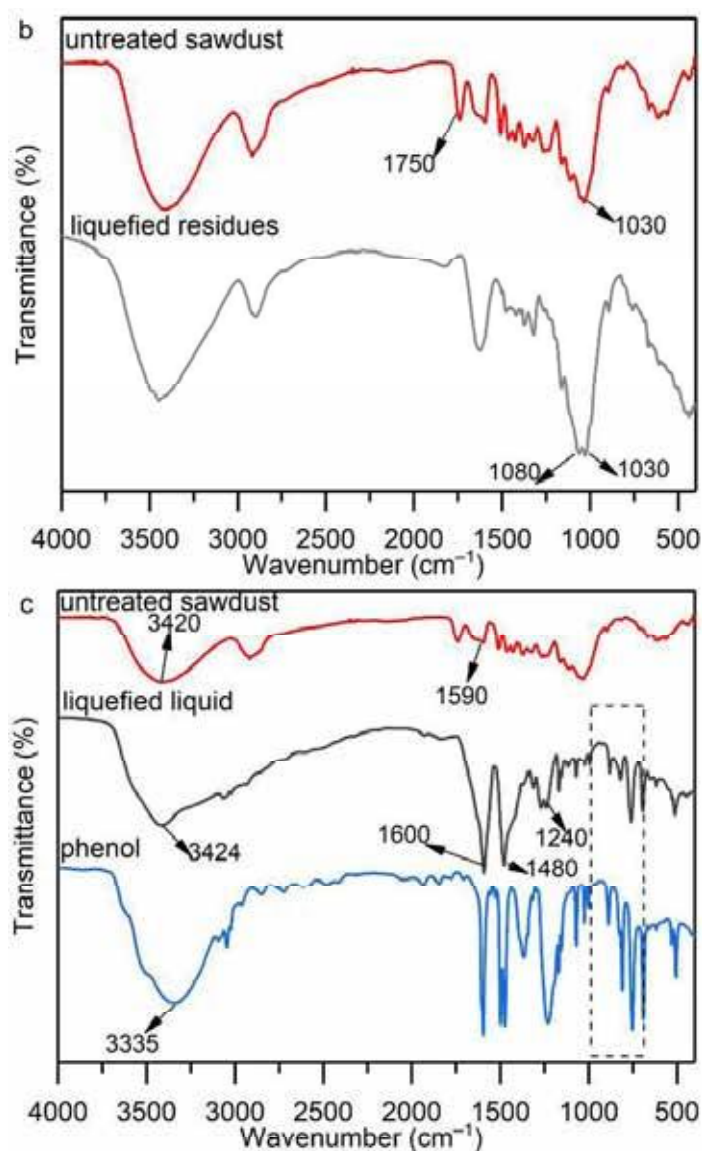


Figure 7. FT-IR spectra of untreated sawdust and pretreated sawdust (a), untreated sawdust and liquefied residues (b), untreated sawdust, liquefied liquid and phenol (c).

2.5. XRD Analysis

Waste sawdust showed two characteristic peaks of type I lignocellulose at 16.1° and 22.5°, which correspond to the lattice planes of (101) and (002), respectively [47]. The two peaks were both shifted after alkali–heat pretreatment due to the transformation of some cellulose crystals [48]. The Crystallinity Index (I_{Cr}) of the pretreated samples (18.21%) was reduced by 59.11% compared with untreated natural waste sawdust (44.53%) because a large number of hydrogen bonds between and within the cellulose were destroyed, resulting in the disruption of the crystal structure [49]. Besides, several small peaks between 28° and 50° resulted from the NaOH crystals rearranged in the hierarchical sawdust structures [50].

The XRD spectra of the liquefied residues exhibit many diffraction peaks (Figure 8), indicating that the liquefied residues contained several crystalline substances, which were difficult to liquefy. This was consistent with the results of previous studies [51]. The liquefied residues showed two peaks of type II cellulose at positions 20° and 22°, suggesting the synergistic effect of alkali–heat pretreatment and phenol liquefaction, resulting in altered cellulose crystals. Type II cellulose is stabler and less susceptible to liquefaction, which also explains its presence in the liquefied residues. A sharp peak at 26.5° was due to the

formation of carbonaceous structures, such as graphite, during liquefaction. The peak at about 32.2° was attributed to oxidized lignin [52], which corresponded to the results of the FT-IR analysis.

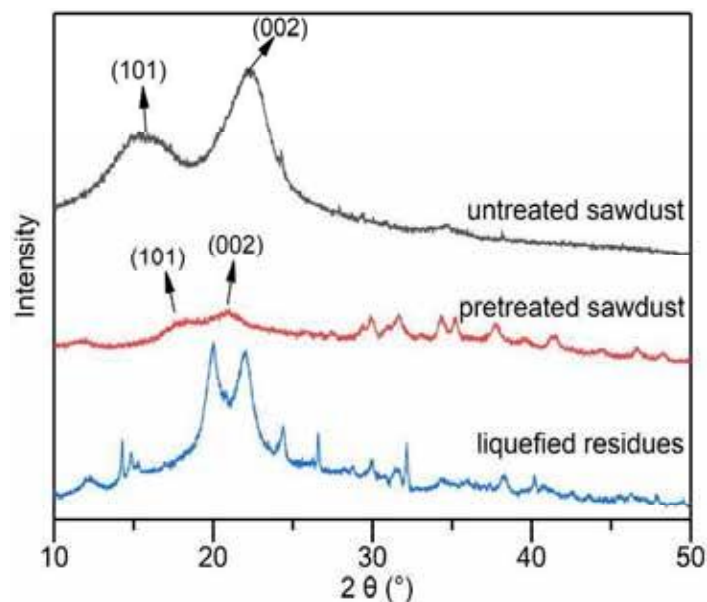


Figure 8. X-ray diffraction of untreated sawdust, alkali–heat pretreated sawdust and liquefied residues.

3. Materials and Methods

3.1. Materials

The waste sawdust with a size of 20 mesh was generously provided by the carpentry factory located at the South China Agricultural University. The chemical and elemental composition of the sawdust is shown in Table 3. Phenol (99%) and NaOH were purchased from Aladdin Reagent Company, Shanghai, China.

Table 3. Element and chemical composition of sawdust and the values were given on a dry basis.

Polymer Mass Fraction (%)			Element Mass Fraction (%)					Ash (%)
Cellulose	Hemicellulose	Klason Lignin	C	H	O	S	N	
42.11	24.32	28.06	46.77	5.97	46.52	0.00	1.01	1.6

3.2. Pretreatment

The sawdust was dried to absolute dryness in a drying oven at $103^\circ\text{C} \pm 2^\circ\text{C}$. The pretreatment was performed in a glass beaker (150 mL) with tinfoil, and heated in an oven. Briefly, 5 g dry sawdust, 25 g distilled water and some NaOH were loaded into the reaction vessel and mixed thoroughly. The mass ratios of dry sawdust to NaOH were 3:1, 2.5:1, 2:1, 1.5:1, 1:1, 1:1.5, and 1:2. The beaker was then transferred to a drying oven and heated to a fixed temperature (140°C) until the distilled water was dried (about 280 min). At the end of the pretreatment, the beaker was stored in a glass desiccator for subsequent liquefaction experiments. The overall flow chart of the two step-liquefaction is presented in Figure 9.

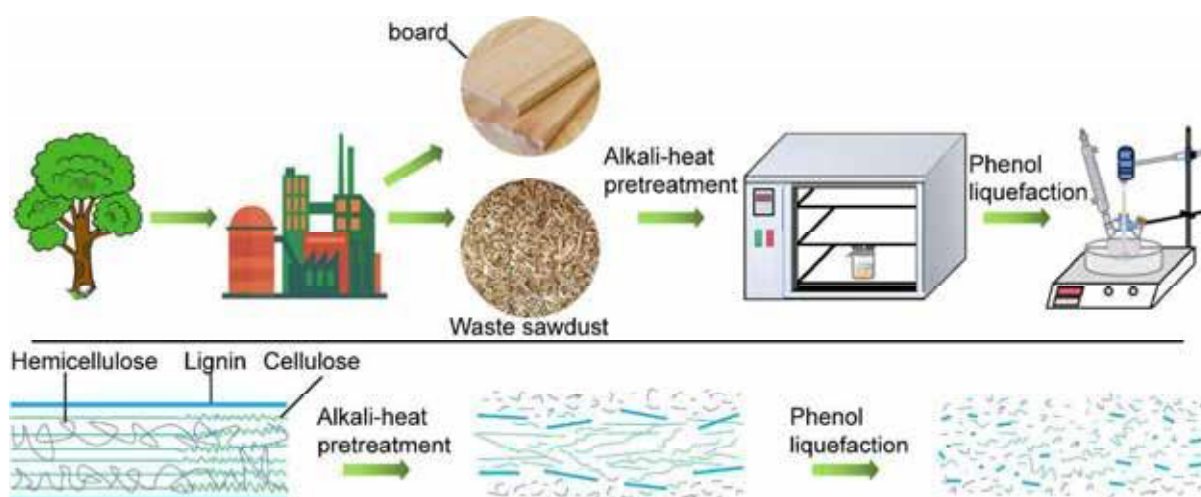


Figure 9. Overall flow chart of two step liquefaction of waste sawdust.

3.3. Phenol Liquefaction

The pretreated sawdust and phenol were loaded into a reactor equipped with a stirrer and a condenser. The whole assembly was immersed into an oil bath preheated to a given liquefaction temperature for a certain reaction time under continuous stirring. Then, the resulting reaction mixture was diluted and dissolved in hot distilled water (50 mL). The insoluble residues were separated by filtration with a G2 glass filter (30–50 μm) under vacuum (0.095 MPa). The filtrate was subjected to rotary evaporation under a vacuum at 70 $^{\circ}\text{C}$ to remove water. The residues were dried in an oven at 103 $^{\circ}\text{C} \pm 2$ $^{\circ}\text{C}$ to constant weight. All experiments were performed in triplicates and the average value was taken. All product yields were calculated using the following equations.

$$\text{Liquefied residue yield (wt \%)} = \frac{\text{Weight of Liquefaction Residue}}{\text{Weight of Sawdust}} \times 100 \quad (2)$$

$$\text{Liquefaction yield (wt \%)} = (1 - \text{Liquefied residue yield}) \times 100 \quad (3)$$

3.4. Experimental Design and Process Optimization Using Response Surface Methodology (RSM)

To investigate the effect of independent variables on the response value (residual content) and optimize the liquefaction conditions, experiments with three key variables and five levels were designed using the Box–Behnken design. The Design-Expert 12.0.3.0 software was used to design experiments, perform the statistical analysis, and create the regression model. Based on extensive pre-experiments, the independent variables that significantly influenced the residual content and the right levels were selected. The three independent variables were the mass ratio of phenol to pretreated sawdust (A), liquefaction temperature (B), and liquefaction time (C). The range of each value was chosen in the range of 2 to 6, 120 to 200 $^{\circ}\text{C}$, and 1 to 3 h, as shown in Table 4. The experimental design included a total of 20 experiments, corresponding to eight factor points, six axial points, and six center point replications to ensure the accuracy of the experiment.

Table 4. Liquefaction variables and levels.

Variables	Level					
	Code	−2	−1	0	1	2
Mass ratio of phenol to pretreated sawdust, P/S	A	2	3	4	5	6
Liquefaction temperature, T ($^{\circ}\text{C}$)	B	120	140	160	180	200
Liquefaction time, t (h)	C	1	1.5	2	2.5	3

What is more, the complete design matrix and actual residue are shown in Table 1, and the experimental data were analyzed using Design Expert 12.0.3.0. The test data were fitted to the following second order polynomial equation, as shown in Equation (4). The analysis of variance (ANOVA) and significance test was carried out for the residual content under different conditions to evaluate the quality of the model fitting. All these experiments were carried out in random order.

$$Y = \beta_0 + \sum_{i=1}^n \beta_i X_i + \sum_{i=1}^n \beta_{ii} X_i^2 + \sum_{i=1}^n \sum_{j=i+1}^n \beta_{ij} X_i X_j \quad (4)$$

where Y is the response function (residue content), β_0 is the model intercept, β_i , β_{ii} and β_{ij} represent coefficients of linear, quadratic, and interaction terms, respectively.

3.5. Characterization

3.5.1. Chemical and Elemental Composition Analysis

The chemical composition of sawdust was performed according to the Van Soest method [53]. Briefly, the neutral detergent fiber (NDF), acid detergent fiber (ADF), and acid detergent lignin (ADL) were prepared in turn by detergent waste sawdust sequentially with neutral detergent reagent, acid detergent reagent and 72% H_2SO_4 . Another amount of dry sawdust was put in a muffle furnace at 600 °C for 6 h, and the ash content was calculated by the weight difference. The difference values between ADF and NDF, ADF and ADL, ADL and ash were considered as contents of hemicellulose, cellulose and Klason lignin, respectively [49]. The elemental analysis of sawdust was performed with an Elemental Analyzer (Vario EL cube, Elementar, Hanau, Germany). The chemical and elemental composition of the sawdust was analyzed three times and the average values were taken separately.

3.5.2. Scanning Electron Microscope (SEM) Analysis

The morphology of untreated sawdust, alkali-heat pretreated sawdust and liquefied residues were analyzed via SEM (EVO MA 15, ZEISS, Oberkochen, Germany). The working voltage was 10 kV.

3.5.3. Fourier Transform Infrared Spectroscopy (FT-IR) Analysis

FT-IR instrument (Vertex 70, Bruker, MA, USA) was used to analyze the functional groups in the samples (untreated sawdust, alkali-heat pretreated sawdust, liquefied residues and liquefied liquid). The sample was diluted nicely in KBr. The sample was scanned 32 times in the range of 400 cm^{-1} to 4000 cm^{-1} at a resolution of 4 cm^{-1} . Background spectra were recorded before every sampling.

3.5.4. X-ray Diffraction (XRD) Analysis

Samples ground to powder (100 mesh) were analyzed by X-ray diffraction (xrd-6000, Shimadzu, Kyoto, Japan) with an $AlK\alpha$ radiation source at 40 kV. The scanning range was 5 to 50° with a step of 0.02° at a scanning rate of 10°/min.

4. Conclusions

In this study, a facile method was used to liquefy waste sawdust via a two-step method at a significant liquefaction rate. The alkali-heat pretreatment was optimized by a temperature of 140 °C and a 1:1 mass ratio of sawdust to NaOH, resulting in a 4.2-fold higher liquefaction rate than that of untreated sawdust. Based on the response model established by RSM, it was found that the P/S ratio was the most important variable affecting the liquefaction yield. A P/S ratio of 4.21, a liquefaction temperature of 173.58 °C, and a liquefaction time of 2.24 h were the optimal conditions for phenol liquefaction of pretreated sawdust, resulting in corresponding liquefied residue yield of 6.35%. Thus,

the liquefaction rate reached 93.65%. Based on SEM, FTIR, and XRD analyses, alkali–heat pretreatment is essential for subsequent phenol liquefaction.

Author Contributions: Conceptualization, J.S. and H.Z.; methodology, J.S. and S.L.; software, J.S. and S.L.; data curation, J.S., S.L., H.Z. and X.L.; validation, J.S. and S.L.; investigation, J.S., Z.G., S.L. and X.H.; formal Analysis, J.S. and S.L.; writing—original draft, J.S., S.L. and X.L.; writing—review and editing, J.S., S.L. and H.Z.; resources, J.S. and H.Z.; supervision, J.S., H.Z. and Z.G.; funding acquisition, J.S. and Z.G.; All authors have read and agreed to the published version of the manuscript.

Funding: This research was supported by the Science and Technology Program of Guangzhou (Project No. 202103000011).

Institutional Review Board Statement: Not applicable.

Informed Consent Statement: Not applicable.

Data Availability Statement: Not applicable.

Acknowledgments: The authors would like to acknowledge the Science and Technology Program of Guangzhou (Project No. 202103000011) for supporting this work. The authors also thank the support of the College of Materials and Energy, South China Agricultural University.

Conflicts of Interest: The authors declare no competing interest.

References

- Guo, J.Y.; Yu, B. When fossil fuels run out, what then? *World Environ.* **2019**, *5*, 46–48.
- Moriarty, P.; Honnery, D. Energy efficiency or conservation for mitigating climate change? *Energies* **2019**, *12*, 3543.
- Holeček, J.L.; Geli, H.; Sawalhah, M.N.; Valdez, R. A global assessment: Can renewable energy replace fossil fuels by 2050? *Sustainability* **2022**, *14*, 4792.
- Heal, G. Economic aspects of the energy transition. *Environ. Resour Econ.* **2022**, *83*, 5–21. [\[CrossRef\]](#)
- Zhang, Z.C.; Song, Y.D. Research Progress in Biotechnology for Comprehensive Utilization of Lignocellulosic Materials. *Guangdong Agric. Sci.* **2021**, *48*, 150–159.
- Kosmela, P.; Kazimierski, P.; Formela, K.; Haponiuk, J.; Piszczek, U. Liquefaction of macroalgae enteromorpha biomass for the preparation of biopolyols by using crude glycerol. *J. Ind. Eng. Chem.* **2017**, *56*, 399–406.
- Goncalves, D.; Orišková, S.; Matos, S.; Machado, H.; Vieira, S.; Bastos, D.; Gaspar, D.; Paiva, R.; Bordado, J.C.; Rodrigues, A.; et al. Thermochemical liquefaction as a cleaner and efficient route for valuing pinewood residues from forest fires. *Molecules* **2021**, *26*, 7156.
- Athanasios, D.; Stella, B. Hydrothermal liquefaction of various biomass and waste feedstocks for biocrude production: A state of the art review. *Renew. Sust. Energy Rev.* **2017**, *68*, 113–125.
- Gin, A.W.; Hassan, H.; Ahmad, M.A.; Hameed, B.H.; Din, A. Recent progress on catalytic co-pyrolysis of plastic waste and lignocellulosic biomass to liquid fuel: The influence of technical and reaction kinetic parameters. *Arab. J. Chem.* **2021**, *14*, 103035. [\[CrossRef\]](#)
- Feng, S.; Yuan, Z.; Leitch, M.; Shui, H.; Xu, C.C. Effects of bark extraction before liquefaction and liquid oil fractionation after liquefaction on bark-based phenol formaldehyde resoles. *Ind. Crop. Prod.* **2016**, *84*, 330–336.
- Cheng, S.N.; Yuan, Z.S.; Mathew, L.; Mark, A.; Xu, C.C. Highly efficient de-polymerization of organosolv lignin using a catalytic hydrothermal process and production of phenolic resins/adhesives with the depolymerized lignin as a substitute for phenol at a high substitution ratio. *Ind. Crop. Prod.* **2013**, *44*, 315–322. [\[CrossRef\]](#)
- Maree, C.; Görgens, J.F.; Tyhoda, L. Lignin phenol formaldehyde resins synthesised using South African spent pulping liquor. *Waste Biomass Valori.* **2022**, *13*, 3489–3507.
- Kumari, D.; Singh, R. Pretreatment of lignocellulosic wastes for biofuel production: A critical review. *Renew. Sust. Energy Rev.* **2018**, *90*, 877–891.
- Mafe, O.; Davies, S.M.; Hancock, J.; Du, C. Development of an estimation model for the evaluation of the energy requirement of dilute acid pretreatments of biomass. *Biomass. Bioenerg.* **2015**, *72*, 28–38.
- Kandasamy, S.; Zhang, B.; He, Z.; Chen, H.; Krishnamoorthi, M. Effect of low-temperature catalytic hydrothermal liquefaction of spirulina platensis. *Energy* **2020**, *190*, 116236. [\[CrossRef\]](#)
- Hassan, S.N.A.M.; Ishak, M.A.M.; Ismail, K. Optimizing the physical parameters to achieve maximum products from co-liquefaction using response surface methodology. *Fuel* **2017**, *207*, 102–108.
- Mazaheri, H.; Lee, K.T.; Bhatia, S.; Mohamed, A.R. Subcritical water liquefaction of oil palm fruit press fiber in the presence of sodium hydroxide: An optimisation study using response surface methodology. *Bioresour. Technol.* **2010**, *101*, 9335–9341. [\[CrossRef\]](#) [\[PubMed\]](#)
- Knill, C.J.; Kennedy, J.F. Degradation of cellulose under alkaline conditions. *Carbohydr. Polym.* **2003**, *51*, 281–300. [\[CrossRef\]](#)

19. Sintamarean, I.M.; Grigoras, I.F.; Jensen, C.U.; Toor, S.S.; Pedersen, T.H.; Rosendahl, L.A. Two-stage alkaline hydrothermal liquefaction of wood to biocrude in a continuous bench-scale system. *Biomass Convers. Biorefinery* **2017**, *7*, 425–435. [\[CrossRef\]](#)
20. Kim, J.S.; Lee, Y.Y.; Kim, T.H. A review on alkaline pretreatment technology for bioconversion of lignocellulosic biomass. *Bioresour. Technol.* **2016**, *199*, 42–48.
21. Xin, L.; Yong, F. Research progress in pretreatment techniques for lignocellulosic materials. *Guangzhou Chem. Industry* **2014**, *42*, 16–18.
22. Grigoras, I.F.; Stroe, R.E.; Sintamarean, I.M.; Rosendahl, A.L. Effect of biomass pretreatment on the product distribution and composition resulting from the hydrothermal liquefaction of short rotation coppice willow. *Bioresour. Technol.* **2017**, *231*, 116–123. [\[PubMed\]](#)
23. Grace, T.M.; Malcolm, E.W. *Pulp and Paper Manufacture: Volume 5 Alkaline Pulping*, 3rd ed.; Joint Textbook Committee of the Paper Industry: Montreal, QC, Canada, 1989; p. 45.
24. Maldas, D.; Shiraishi, N. Liquefaction of biomass in the presence of phenol and H₂O using alkalies and salts as the catalyst. *Biomass. Bioenerg.* **1997**, *12*, 273–279. [\[CrossRef\]](#)
25. Maldas, D.; Shiraishi, N.; Harada, Y. Phenolic resol resin adhesives prepared from alkali-catalyzed liquefied phenolated wood and used to bond hardwood. *J. Adhes. Sci. Technol.* **1997**, *11*, 305–316. [\[CrossRef\]](#)
26. Tran, M.H.; Lee, E. Development and optimization of solvothermal liquefaction of marine macroalgae *Saccharina japonica* biomass for biopolyol and biopolyurethane production. *J. Ind. Eng. Chem.* **2020**, *81*, 167–177. [\[CrossRef\]](#)
27. Bansode, A.; Barde, M.; Asafu-Adjaye, O.; Patil, V.; Hinkle, J.; Via, B.K.; Adhikari, S.; Adamczyk, A.J.; Farag, R.; Elder, T.; et al. Synthesis of Biobased Novolac Phenol-Formaldehyde Wood Adhesives from Biorefinery-Derived Lignocellulosic Biomass. *ACS. Sustain. Chem. Eng.* **2021**, *9*, 10990–11002. [\[CrossRef\]](#)
28. Wang, S.J.; Hou, X.F.; Huang, Y.S. Effect of Alkaline Ionic Liquid TBAH Pretreatment on Structure and Enzymatic Properties of Eucalypt. *Chem. Ind. For. Prod.* **2022**, *42*, 57–63.
29. Zhu, Z.; Rosendahl, L.; Toor, S.S.; Chen, G. Optimizing the conditions for hydrothermal liquefaction of barley straw for bio-crude oil production using response surface methodology. *Sci. Total. Environ.* **2018**, *630*, 560–569.
30. Wei, X.; Jie, D. Optimization to hydrothermal liquefaction of low lipid content microalgae *spirulina* sp. using response surface methodology. *J. Chem.* **2018**, *2018*, 2041812.
31. Li, G.; Hse, C.; Qin, T. Wood liquefaction with phenol by microwave heating and FTIR evaluation. *J. For. Res.* **2015**, *26*, 1043–1048.
32. Li, R.; Xu, W.; Wang, C.; Zhang, S.; Song, W. Optimization for the liquefaction of moso bamboo in phenol using response surface methodology. *Wood Fiber Sci.* **2018**, *50*, 220–227.
33. Hadhoum, L.; Loubar, K.; Paraschiv, M.; Burnens, G.; Awad, S.; Tazerout, M. Optimization of oleaginous seeds liquefaction using response surface methodology. *Biomass Convers. Bior.* **2021**, *11*, 2655–2667.
34. Zhou, R.; Zhou, R.; Wang, S.; Lan, Z.; Zhang, X.; Yin, Y.; Ye, L. Fast liquefaction of bamboo shoot shell with liquid-phase microplasma assisted technology. *Bioresour. Technol.* **2016**, *218*, 1275–1278. [\[CrossRef\]](#) [\[PubMed\]](#)
35. Singh, R.; Balagurumurthy, B.; Prakash, A.; Bhaskar, T. Catalytic hydrothermal liquefaction of water hyacinth. *Bioresour. Technol.* **2015**, *178*, 157–165. [\[PubMed\]](#)
36. Hadhoum, L.; Burnens, G.; Loubar, K.; Balistrou, M.; Tazerout, M. Bio-oil recovery from olive mill wastewater in sub-/supercritical alcohol-water system. *Fuel* **2019**, *252*, 360–370.
37. Zhao, L.; Zhou, J.H.; Sui, Z.J.; Zhou, X.G. Hydrogenolysis of sorbitol to glycols over carbon nanofiber supported ruthenium catalyst. *Chem. Eng. Sci.* **2010**, *65*, 30–35.
38. Mafu, L.D.; Neomagus, H.W.J.P.; Everson, R.C.; Carrier, M.; Strydom, C.A.; Bunt, J.R. Structural and chemical modifications of typical South African biomasses during torrefaction. *Bioresour. Technol.* **2016**, *202*, 192–197. [\[CrossRef\]](#)
39. Ma, Y.; Tan, W.H.; Feng, G.D.; Xu, J.M.; Wang, K.; Ying, H.; Jiang, J.C. Liquefaction of Bamboo Powder in Ethanol-phenol under High Pressure and Product Characterization. *Chem. Ind. For. Prod.* **2016**, *36*, 105–112.
40. Wang, W.X.; Zhang, L.; Li, A. Response relationship of hydrothermal humification products of waste biomass with acid-base property of medium. *J. Dalian Univ. Technol.* **2022**, *62*, 9–17.
41. Zhao, J.; Xiuwen, W.; Hu, J.; Liu, Q.; Shen, D.; Xiao, R. Thermal degradation of softwood lignin and hardwood lignin by TG-FTIR and Py-GC/MS. *Polym. Degrad. Stabil.* **2014**, *108*, 133–138.
42. Biswas, B.; Singh, R.; Kumar, J.; Khan, A.A.; Krishna, B.B.; Bhaskar, T. Slow pyrolysis of prot, alkali and dealkaline lignins for production of chemicals. *Bioresour. Technol.* **2016**, *213*, 319–326. [\[CrossRef\]](#) [\[PubMed\]](#)
43. Biswas, B.; Kumar, A.; Krishna, B.B.; Bhaskar, T. Effects of solid base catalysts on depolymerization of alkali lignin for the production of phenolic monomer compounds. *Renew. Energ.* **2021**, *175*, 270–280. [\[CrossRef\]](#)
44. Sun, P.; Heng, M.; Sun, S.; Chen, J. Direct liquefaction of paulownia in hot compressed water: Influence of catalysts. *Energy* **2010**, *35*, 5421–5429.
45. Xu, E.; Sun, J.; Zhu, X.; Wang, X.; Gao, Z. Liquefaction of coconut fibers in alkaline hot-compressed water. *Energ. Source. Part A* **2016**, *38*, 1750–1755. [\[CrossRef\]](#)
46. Zuluaga, R.; Putaux, J.L.; Cruz, J.; Velez, J.; Mondragon, I.; Ganan, P. Cellulose microfibrils from banana rachis: Effect of alkaline treatments on structural and morphological features. *Carbohydr. Polym.* **2009**, *76*, 51–59. [\[CrossRef\]](#)
47. Liu, M.; Wang, H.; Han, J.; Niu, Y. Enhanced hydrogenolysis conversion of cellulose to C₂–C₃ polyols via alkaline pretreatment. *Carbohydr. Polym.* **2012**, *89*, 607–612. [\[CrossRef\]](#)

48. Eronen, P.; Österberg, M.; Jskelinen, A.S. Effect of alkaline treatment on cellulose supramolecular structure studied with combined confocal Raman spectroscopy and atomic force microscopy. *Cellulose* **2009**, *16*, 167–178. [[CrossRef](#)]
49. Wang, Z.; Hou, X.; Sun, J.; Li, M.; Chen, Z.; Gao, Z. Comparison of ultrasound-assisted ionic liquid and alkaline pretreatment of Eucalyptus for enhancing enzymatic saccharification. *Bioresour. Technol.* **2018**, *254*, 145–150. [[CrossRef](#)]
50. Warwicker, J.O.; Wright, A.C. Function of sheets of cellulose chains in swelling reactions on cellulose. *J. Appl. Polym. Sci.* **1967**, *11*, 659–671.
51. Ahmadzadeh, A.; Zakaria, S. Preparation of novolak resin by liquefaction of oil palm empty fruit bunches (EFB) and characterization of EFB residue. *Polym. Plast. Technol. Eng.* **2009**, *48*, 10–16.
52. Bakarudin, S.B.; Zakaria, S.; Chia, C.H.; Jani, S.M. Liquefied residue of kenaf core wood produced at different phenol-kenaf ratio. *Sains Malays.* **2012**, *41*, 225–231.
53. Van Soest, P.J. Use of detergents in the analysis of fibrous feeds. II. A rapid method for the determination of fiber and lignin. *J. Assoc. Off. Agric. Chem.* **1963**, *46*, 829–835.



广东省技术发明奖 证书

为表彰 2023 年度广东省技术
发明奖获得者，特颁发此证书。

项目名称: 多元复合协同增效制造高性能功能
化木塑复合材料关键技术

奖励等级: 一等奖

获奖者: 周海洋(华南农业大学)

粤府证【2024】0734 号
项目编号:F011-1-01-R10



荣誉证书

周海洋同志参加完成的

绿色低碳谷壳再生木关键技术研究及应用项目，荣获二〇二三年中国物流与采购联合会科技进步二等奖，特此证明。

证书号：CFLP2023020201908



证书号第6534728号



发明专利证书

发 明 名 称：一种含有三维网络结构天然纤维复合材料的制造方法

发 明 人：王清文;郝笑龙;欧荣贤;周海洋;孙理超;唐伟;刘珍珍
李文娟;樊奇;刘涛

专 利 号：ZL 2022 1 0352315.7

专 利 申 请 日：2022年04月05日

专 利 权 人：华南农业大学

地 址：510642 广东省广州市天河区五山路483号

授权公告日：2023年12月05日

授权公告号：CN 114656658 B

国家知识产权局依照中华人民共和国专利法进行审查，决定授予专利权，颁发发明专利证书并在专利登记簿上予以登记。专利权自授权公告之日起生效。专利权期限为二十年，自申请日起算。

专利证书记载专利权登记时的法律状况。专利权的转移、质押、无效、终止、恢复和专利权人的姓名或名称、国籍、地址变更等事项记载在专利登记簿上。



局长

申长雨

申长雨

2023年12月05日

证书号 第6534728号

专利权人应当依照专利法及其实施细则规定缴纳年费。本专利的年费应当在每年04月05日前缴纳。
未按照规定缴纳年费的，专利权自应当缴纳年费期满之日起终止。

申请日时本专利记载的申请人、发明人信息如下：

申请人：

华南农业大学

发明人：

王清文;郝笑龙;欧荣贤;周海洋;孙理超;唐伟;刘珍珍;李文娟;樊奇;刘涛

证书号第 5574302 号



发明专利证书

发明名称：一种超高木质纤维含量木塑粒料及复合材料的制造方法

发明人：王清文;郝笑龙;欧荣贤;周海洋;孙理超;刘涛;徐俊杰
唐伟;易欣

专利号：ZL 2022 1 0292411.7

专利申请日：2022 年 03 月 24 日

专利权人：华南农业大学

地址：510642 广东省广州市天河区五山路 483 号

授权公告日：2022 年 11 月 11 日

授权公告号：CN 114605849 B

国家知识产权局依照中华人民共和国专利法进行审查，决定授予专利权，颁发发明专利证书并在专利登记簿上予以登记。专利权自授权公告之日起生效。专利权期限为二十年，自申请日起算。

专利证书记载专利权登记时的法律状况。专利权的转移、质押、无效、终止、恢复和专利权人的姓名或名称、国籍、地址变更等事项记载在专利登记簿上。



局长
申长雨

申长雨



第 1 页 (共 2 页)

其他事项参见续页

证书号 第 5574302 号

专利权人应当依照专利法及其实施细则规定缴纳年费。本专利的年费应当在每年 03 月 24 日前缴纳。未按照规定缴纳年费的,专利权自应当缴纳年费期满之日起终止。

申请日时本专利记载的申请人、发明人信息如下:

申请人:

华南农业大学

发明人:

王清文;郝笑龙;欧荣贤;周海洋;孙理超;刘涛;徐俊杰;唐伟;易欣

证书号第3072855号



发明专利证书

发明名称：一种胶合夹芯结构木塑复合材料、制品及其制造方法

发明人：王清文；郝笑龙；易欣；周海洋；孙理超；欧荣贤

专利号：ZL 2016 1 0948245.6

专利申请日：2016年10月27日

专利权人：华南农业大学

地址：510642 广东省广州市天河区五山路483号

授权公告日：2018年09月14日

授权公告号：CN 106499170 B

本发明经过本局依照中华人民共和国专利法进行审查，决定授予专利权，颁发本证书并在专利登记簿上予以登记。专利权自授权公告之日起生效。

本专利的专利权期限为二十年，自申请日起算。专利权人应当依照专利法及其实施细则规定缴纳年费。本专利的年费应当在每年10月27日前缴纳。未按照规定缴纳年费的，专利权自应当缴纳年费期满之日起终止。

专利证书记载专利权登记时的法律状况。专利权的转移、质押、无效、终止、恢复和专利权人的姓名或名称、国籍、地址变更等事项记载在专利登记簿上。



局长
申长雨

申长雨



ICS 79.020

CCS C 2019

团体标准

T/TSNR002-2023

木材产品碳足迹核算技术规范

Technical Specification for Carbon Footprint Assessment of

Woodproducts

(发布稿)

2023-11-2 发布

2023-11-2 实施

天津市自然资源学会 发布

目录

前 言	1
引 言	2
1 适用范围.....	3
2 规范性引用文件.....	3
3 术语和定义.....	3
4 原则.....	5
5 产品碳足迹评价.....	5
6 木材产品碳足迹评价报告.....	21
附录 A 产品描述信息清单	22
附录 B 排放因子缺省值	23
附录 C 含碳率	29
附录 D 木材产品使用寿命	40
附录 E 记录表格	41
参考文献	43

前 言

本团体标准按照GB/T 1.1—2020《标准化工作导则 第1部分：标准化文件的结构和起草规则》的规定起草。

本团体标准由宇相碳测认证（天津）有限公司提出。

本团体标准由天津市自然资源学会归口。

本团体标准起草单位：宇相碳测认证(天津)有限公司

南开大学

中国木材保护工业协会

华南农业大学

内蒙古建筑职业技术学院

江苏零界科技集团有限公司

崇左广林迪芬新材料科技有限公司

佛山市顺德区锡山家居科技有限公司

云南濒科委司法鉴定中心

江苏瀚之源环保科技有限公司

山东京博木基材料有限公司

江苏万航木业有限公司

四川尚林新型建筑材料有限公司

天津南开碳索技术服务有限公司

本团体标准主要起草人：胡智弢、肖佳、韩玉杰、唐景春、欧荣贤、郝笑龙、王清文、刘帅、孙理超、张炜、易欣、周海洋、李鹏、翁晓萌、纪晨琛、郝晓峰、李伟、隋永丰、魏忠华、李骛、潘礼成、黄剑飞、王宗和、黄良华、姜吉彪、顾学良、柯海涛、高赏举、马硕、崔通军、卢艳、徐婉秦

本团体标准为首次发布。

引言

人类活动引起的气候变化已成为各国政府、社会所面临的重大危机之一，且其对人类和自然系统产生着重人影响。为应对气候变化，国际、区域、国家和地区正在制定和实施各种行动计划，旨在降低地球大气中温室气体的浓度。这些温室气体行动计划依赖于对温室气体排放和/或清除的评价、监测、报告和核证。

我国林业资源丰富，但一直以来，对森林碳汇贡献的评估主要着眼于森林生态系统中的生物量和土壤碳储量上，而忽略了森林采伐后形成的木材产品，其中的碳并未立即全部排放，而是转移储存在木材产品中，可以将碳保存较长的时间，减缓碳排放，形成了巨大的木材产品碳库。2011年在南非德班召开的联合国气候变化大会缔约方第17次会议上，各国一致同意将木材产品碳储量纳入森林减排范畴。

本文件给出木材产品碳足迹评价的要求，提高了木材产品碳足迹评价和通报的透明性和一致性；帮助更好地了解木材产品碳足迹，以识别温室气体减排的机会；促进企业制定与实施贯穿木材产品整个生命周期的温室气体管理策略和计划。

木材产品碳足迹核算技术规范

1 适用范围

本评价方法及要求规定了木材产品温室气体排放评价的基本规则和要求，包括产品术语和定义、产品描述、产品碳足迹评价范围及计算方法；同时规定了木材产品碳足迹评价报告所应遵守的规则。

本评价方法及要求适用于木材产品。

2 规范性引用文件

下列文件对于本文件的应用是必不可少的。凡是注明日期的引用文件，仅所注日期的版本适用于本文件。凡是不注日期的引用文件，其最新版本(包括所有的修改单)适用于本文件。

PAS 2050 商品和服务的生命周期温室气体排放评价规范

ISO 14067 温室气体 产品碳足迹 关于量化和通报的要求和指南

GB 50005 木结构设计标准

GB/T 29894 木材鉴别方法通则

LY/T 2407 森林资源资产评估技术规范

LY/T 3182 森林生态旅游地木(竹)材产品使用技术要求

GB/T 15787 原木检验术语

GB/T 11917 制材工艺术语

GB/T 24044 环境管理 生命周期评价 要求与指南

企业温室气体排放核算与报告指南 发电设施

3 术语和定义

3.1 产品碳足迹 carbon footprint of a product (CFP)

特定产品在其整个生命周期内各种温室气体排放，温室气体包括二氧化碳(CO₂)、甲烷(CH₄)、氧化亚氮(N₂O)、氢氟碳化合物(HFCs)、全氟化合物(PFCs)、六氟化硫(SF₆)和三氟化氮(NF₃)等。

3.2 二氧化碳当量 carbon dioxide equivalent CO₂ equivalent CO₂e

在辐射强度上与某种温室气体质量相当的二氧化碳质量。

注：二氧化碳当量等于给定温室气体的质量乘以它的全球变暖潜势值。

3.3 碳储量 carbon storage

产品库中某种木材产品的储碳数量。

3.4 含碳率 carbon content rate

木材产品中碳质量占产品质量比率。

3.5 原木 log

原条经过横截造材所形成的圆形木段。

【来源：GB/T 15787-2017, 定义2.1.2】

3.6 锯材 sawn timber

原木经制材加工得到的产品。

【来源：GB/T 11917-2009, 定义2.6】

3.7 木材产品 wood products

木材产品指以木材为主要或部分组成单元制成的各类产品，包含原木、锯材、集成材、胶合板、刨花板、木塑复合材料、重组材等。

3.8 功能单位 functional unit

用来作为基准单位的量化的产品系统性能。

【来源：ISO14067-2018, 定义3.1.3.7】

3.9 系统边界 system boundary

通过一组准则确定哪些单元过程属于产品系统的一部分。

【来源：ISO14067-2018, 定义3.1.3.1】

3.10 活动数据 activity data

导致温室气体排放的生产或消费活动量的表征值，例如各种化石燃料消耗量、化石燃料低位发热量、购入使用电量等。

【来源：企业温室气体排放核算与报告指南 发电设施，定义3.6】

3.11 排放因子 emission factor

表征单位生产或消费活动量的温室气体排放系数，例如每单位化石燃料燃烧所产生的二氧化碳排放量、每单位购入使用电量所对应的二氧化碳排放量等。

【来源：企业温室气体排放核算与报告指南 发电设施，定义表3.7】

3.12 初级数据 primary data

通过直接测量或基于直接测量值计算得到的过程或活动的量化值。

【来源：ISO14067-2018, 定义3.1.6.1】

组织自身采集的、用来计算产品碳足迹的数据（包括根据既定情景收集的数据），也称现场数据。企业现场数据包括木材产品生产过程的原料消耗、能源消耗及运输等清单数据。初级数据能更好地反映出系统的特定本质或效率，以及该系统相关的温室气体排放，因此通常比次级数据更好。

3.13 次级数据 secondary data

不符合原始数据要求的数据。

【来源：ISO14067-2018, 定义3.1.6.3】

计算产品碳足迹的过程中，通过公用数据、参考文献和其他产品生命周期研究获取的数据，也称为背景数据。包括辅料生产及能源生产的清单数据，以及原辅料运输所需的清单数据。

3.14 取舍准则 cut-off criteria

对单元过程或产品系统相关的物质和能量流，根据其数量或环境影响重要程度作出是否被排除在研究范围之外的规定。

【来源：GB/T 24044-2008，定义 3.18】

4 原则

4.1 量化与评价原则

4.1.1 科学性

量化与评价以自然科学、社会科学为基础，注重数据详实、准确，采集样本具有代表性。

4.1.2 先进性

应重点考虑产品生命周期的资源、能源、环境及产品绿色属性，选取影响大、关注度高的关键工艺环节作为评价关注点。

4.1.3 规范性

量化与评价程序应覆盖所界定的产品系统范围，采用适宜的评估方法，确保结果的准确性和有效性。

4.1.4 适用性

应发布充分适用的温室气体信息，以确保对结果做出恰当的解释。

4.2 量化与评价内容

木材产品碳足迹量化与评价，指通过量化产品生命周期或选定过程中的所有温室气体排放和消除量，计算产品对全球变暖的潜在影响，用二氧化碳当量表示。

5 产品碳足迹评价

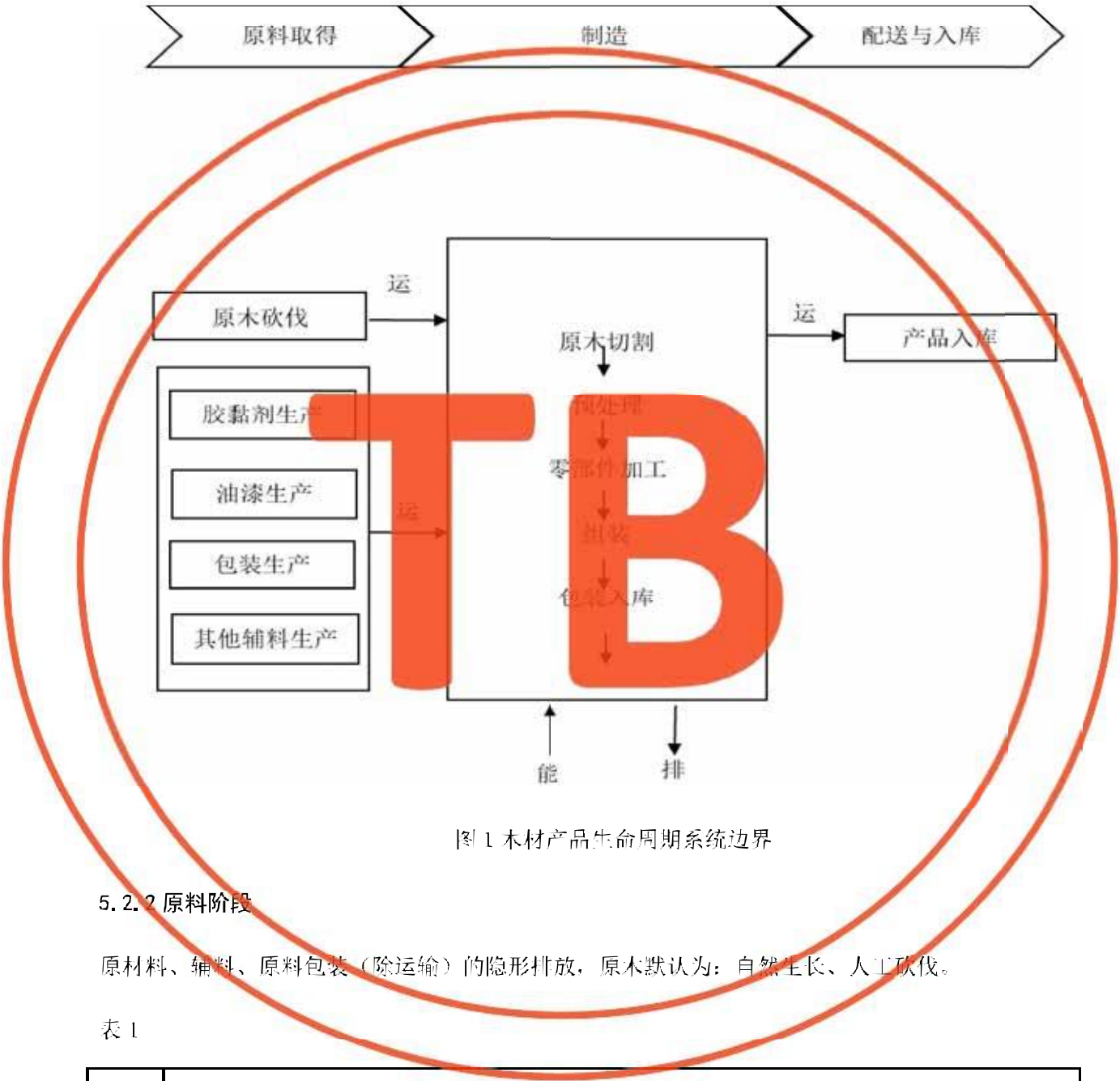
5.1 功能单位

选取 1 件（个）或者 1m³ 产品作为评价功能单位。

5.2 系统边界

5.2.1 系统边界设定

本技术规范界定的木材产品生命周期系统边界（如图 1 所示），从木材产品的原辅料生产、运输、产品生产，到产品至入库为止。产品碳足迹评估是计测从伐后原木运输、产品生产到产品入库过程中所有排放源的二氧化碳排放当量减去产品中转移的碳储量。



5.2.2 原料阶段

原材料、辅料、原料包装（除运输）的隐形排放，原木默认为：自然生长、人工砍伐。

表 1

序号	项目
A1	原材料（非原木，如木板材）（隐性排放）
A2	辅料：胶黏剂、油漆、五金件等
A3	原料包装：包装纸箱、泡沫纸、瓦楞纸等

5.2.3 生产阶段

生产阶段移动源计入运输阶段计算

表 2

序号	项目	备注
B1	加工过程中消耗电力（间接排放）	输入
B2	加工过程中消耗的能源（间接排放）：天然气、柴油、燃料油、液化石油气等	输入
B3	加工过程中消耗的资源包含：生产用水、冷却用水、生活用水等	输入
B4	产出废弃物：生物质不计入，参见 PAS 2050	产出：废弃物
B5	固定源：有组织废气（数据来源：定期检测报告等）	产出：排放
B6	厂区内逸散源（冷却、冰箱、冰柜、空调、工业冷水机、车等相应设备设施中填充的制冷剂，灭火器、化粪池等逸散源）	产出：排放
B7	无组织废气、废水（数据来源：定期检测报告等）	产出：排放
B8	生产工艺的直接排放：如注胶、喷漆等	产出：排放

5.2.4 运输阶段

表 3

序号	项目
C1	原料运输过程中消耗的柴油和石油等化石能源
C2	辅料运输过程中消耗的柴油和石油等化石能源
C3	原料包装运输过程中消耗的柴油和石油等化石能源
C4	厂区内移动源设备运输过程中消耗的柴油和石油等化石能源
C5	废弃物运输过程中消耗的柴油和石油等化石能源
C6	产品贮存运输过程中消耗的柴油和石油等化石能源

5.2.5 碳储量

表 4

序号	项目
D1	转移储存在产品中的碳储量

5.3 取舍准则

本标准确定的取舍准则为：产品生命周期内温室气体排放贡献估测值小于 1% 的物质和能量流可以被舍去。应遵循：

- (1) 能源的所有输入均列出；
- (2) 原辅料的所有输入均列出；
- (3) 与产品相关的所有运输所产生的排放均列出；
- (4) 辅助材料质量小于原料总消耗 0.01% 的项目输入可忽略；
- (5) 道路与厂房的基础设施、厂区内人员及生活设施的消耗和排放，人为操作或产品放置无实质性温室气体排放的均忽略。

5.4 数据收集

表 5

序号	数据类型	对象	基础数据	数据来源
1	石化能源	运输过程中使用的汽油、柴油	单位重量百公里油耗，运输量，运输距离，汽油和柴油碳排放因子	企业提供运输量、单位重量百公里数油耗，汽油和柴油碳排放因子(引用 Simapro 的 EcoInvent 数据库、中国产品全生命周期温室气体排放系数库等)
2	电能能源	加工过程中机器消耗的电能	抄表数据	电力碳排放因子（2012 年中国区域电网平均二氧化碳排放因子）应根据主管部门的最新发布数据进行取值。
3	附加物隐	加工过程添加	附加物的量和碳排	通过实际调查获得 1 件或 1m ³ 木材产品

	含碳	的胶黏剂、油漆，包装使用的纸箱等	放因子	附加物胶黏剂、油漆、包装箱的使用量，附加物的碳排放因子(引用 Simapro 的 Ecoinvent 数据库、中国产品全生命周期温室气体排放系数库等)
4	生物质能源	木材加工过程中产生的木废料燃料	碳转移率，含碳率，废木料燃烧比例，锅炉的燃烧效率，用于木材产品生产的比例	通过木材产品加工过程利用率计算废木料量，废木料燃烧比例通过调查获得，锅炉的燃烧效率根据经验值获得，木材含碳率（附录 C）
5	生物碳储量	木材产品转移储存的碳储量	生产过程碳转移率，制品干重，含碳率	1 件或 1m ³ 木材产品的碳储量、木材含碳率（附录 C）

注：数据源优先选择次序为：

- (a) 当地树种或树种组的数据；
- (b) 省级树种或树种组的数据(如省级温室气体清单)；
- (c) 国家级树种或树种组的数据(如国家温室气体清单)；
- (d) 文献值；
- (e) 缺省值。

5.5 数据分配

产品生产工序中存在一个单元过程同时产出两种或多种产品，而投入的原材料和能源又没有分开的情况，也会存在输入渠道有多种，而输出只有一种的情况。在这些情况下，不能直接得到清单计算所需的数据必须根据一定的关系对这些过程的数据进行分配。

清单是建立在输入与输出的物质平衡的基础上，分配关系需反映出这种输入与输出的基本关系与特性。分配的主要原则如下：

- (1) 须识别与其它产品系统公用的过程，并按分配程序加以处理；
- (2) 单位过程中分配前与分配后的输入与输出的总和必须相等；
- (3) 如果存在若干个可采用的分配程序，须对使用的分配方法及其选取原因进行说明；
- (4) 多重输出：分配是依据被研究的系统所提供的产品、功能或经济关联性发生变化后，资源消耗和碳排放量发生的变化来进行；
- (5) 多重输入：分配基于实际的关系。如生产过程中的排放物会受到输入的废物流的变化影响。处理数据分配问题一般按以下程序进行：
- (a) 尽量避免或减少出现分配。如：①将原来收集数据时划分的单元过程再进一步分解，以便将那些与系统功能无关的单元排除在外；②扩展产品系统边界，把原来排除在系统之外的一些单元包括进来；
- (b) 使用能反映其物理关系的方式来进行分配，如产品的重量、数量、体积、面积、热值等比例关系；
- (c) 当物理关系不能确定或不能用作分配依据时，用其经济关系来进行分配，如产品产值或利润比例关系等。但此种方法的不确定性较高，一般情况不推荐采用经济分配方法。

5.6 数据质量要求

5.6.1 时间范围

应收集最近连续生产3个月到1年的平均水平数据；优先使用最近连续生产1年的平均水平数据。

5.6.2 地理范围

应收集实际生产地理区域的数据。

5.6.3 技术范围

应收集实际生产工艺技术或技术组合的数据。

5.6.4 完整性

应收集涵盖产品系统边界范围的数据。

5.6.5 重现性

应保证独立从业人员可以重现产品碳排放的核算结果。

5.6.6 数据来源

应对数据的获得方式和来源均予以说明。

5.7 产品碳足迹计算

5.7.1 原料阶段

5.7.1.1 原材料隐含碳排放

原材料（非原木，如木板材）的隐性碳排放计算公式如下：

$$A_1 = \sum_i^n P_i \times EF_i \quad (1)$$

式中：

A_1 表示原材料隐含碳排放，单位 $\text{kgCO}_2/\text{件}$ 或 kgCO_2/m^3 ；

P_i 表示生产 1 件或 1m^3 原材料消耗量，单位 $\text{kg}/\text{件}$ 或 kg/m^3 ；

EF_i 表示原材料的碳排放因子，单位 kgCO_2/kg ；

i 为具体原材料种类。

若生产企业直接购买木板材中间产品开始木材产品的生产加工，如缺少中间产品碳排放数据等情况，可以采用附录 B 表 1 推荐值。

5.7.1.2 辅料碳排放

生产加工过程中，需使用胶黏剂、油漆、五金件等附加物。辅料隐含碳排放计算公式如下：

$$A_2 = \sum_i^n P_i \times EF_i \quad (2)$$

式中：

A_2 表示辅料隐含碳排放，单位 $\text{kgCO}_2/\text{件}$ 或 kgCO_2/m^3 ；

P_i 表示生产 1 件或 1m^3 原材料消耗量，单位 $\text{kg}/\text{件}$ 或 kg/m^3 ；

EF_i 表示辅料的碳排放因子，单位 kgCO_2/kg ；

i 为具体辅料种类。

加工过程常见辅料排放因子见附录 B 表 2。

5.7.1.3 原料包装碳排放

生产加工过程中，需使用包装时需用包装纸箱、瓦楞纸箱、珍珠棉等材料的碳排放计算公式如下：

$$A_2 = \sum_i^n P_i \times EF_i \quad (3)$$

式中：

A_2 表示原料包装隐含碳排放，单位 $\text{kgCO}_2/\text{件}$ 或 kgCO_2/m^3 ；

P_i 表示生产 1 件或 1m^3 原材料消耗量，单位 $\text{kg}/\text{件}$ 或 kg/m^3 ；

EF_i 表示原料包装的碳排放因子，单位 kgCO_2/kg ；

i 为具体原料包装种类。

加工过程常见原料包装排放因子见附录 B 表 2。

5.7.1.4 原料阶段排放

原料阶段排放量计算公式如下：

$$A = A_1 + A_2 + A_3 \quad (4)$$

式中：

A 为木材产品原料阶段碳排放，单位 $\text{kgCO}_2/\text{件}$ 或 kgCO_2/m^3 。

5.7.2 生产阶段

生产阶段移动源计入运输阶段计算。

5.7.2.1 加工过程中消耗的电力能源（间接排放）

木材产品加工过程各工序用电设备消耗电力产生的二氧化碳排放计算公式如（5）所示：

$$B_1 = \sum_i^n A_i \times EF_i$$

(5)

式中：

B_1 表示加工过程能电力消耗产生的碳排放，单位 $\text{kgCO}_2/\text{件}$ 或 kgCO_2/m^3 ；

A_i 表示 1 件木材产品生产消耗的电量，单位 $\text{kW}\cdot\text{h}/\text{件}$ 或 $\text{kW}\cdot\text{h}/\text{m}^3$ ；

EF_i 表示电力的碳排放因子，单位 $\text{kgCO}_2/\text{kW}\cdot\text{h}$ 。

5.7.2.2 加工过程中消耗的能源（间接排放）

加工过程中消耗的天然气、柴油、燃料油、液化石油气等化石燃料燃烧产生的 CO_2 ，但不包括生物质燃料燃烧产生的 CO_2 排放。其中，化石燃料燃烧排放计算如下：

$$B_2 = \sum_{i=1}^n FC_i \times NCV_i \times CC_i \times OF_i \times \frac{44}{12} / 1000$$

(6)

式中：

B_2 加工过程中消耗的能源产生的 CO_2 ，单位 $\text{kgCO}_2/\text{件}$ 或 kgCO_2/m^3 ；

i 为能源的种类；

FC_i 生产 1 件或 m^3 用品第 i 种能源的消耗量，单位为 $\text{kg}/\text{件}$ 或 kg/m^3 ；

NCV_i 第 i 种化石燃料的平均低位发热量，单位 GJ/t ($\text{GJ}/\text{万 Nm}^3$)，优先采用企业自测值，如缺失，可采用附录 B 表 3；

CC_i 第 i 种能源的单位热值含碳量，单位 tC/GJ ，可采用附录 B 表 3；

OF_i 第 i 种能源的碳氧化率，单位%，可采用附录 B 表 3；

44/12 二氧化碳与碳的分子量之比。

5.7.2.3 加工过程中消耗的资源碳排放

木材产品加工过程各工序所有资源（生产用水、冷却用水、生活用水等）产生的二氧化碳排放计算公式如（7）所示：

$$B_3 = \sum_{i=1}^n B_i \times EF_i$$

(7)

式中：

B_3 表示加工过程资源（生产用水、冷却用水、生活用水等）消耗产生的碳排放，单位 $\text{kgCO}_2/\text{件}$ 或 kgCO_2/m^3 ；

B_i 表示 1 件木材产品生产消耗的第 i 种资源（生产用水、冷却用水、生活用水等）的用量，单位 $\text{kg}/\text{件}$ 或 kg/m^3 ；

EF_i 表示第 i 种资源（生产用水、冷却用水、生活用水等）的碳排放因子，单位 kgCO_2/kg 。

常见资源排放因子见附录 B 表 5。

5.7.2.4 产出废弃物：生物质不计入，参见 PAS 2050。

木废料燃烧的生物质能源碳排放计测

在碳足迹调查过程中发现，企业利用木材产品生产中的一些废料如废木条、废木料等作为锅炉、蒸汽等的能源使用，废木料燃烧产生了部分 CO_2 的排放。但根据 PAS 2050，由于树木在生长过程吸收了 CO_2 ，此类燃烧排放只是把生长中所吸收的 CO_2 返回，在评估中需测算废木料燃烧的碳排放量，但并不计入木材产品碳足迹评估范围。

废木料燃烧的碳排放公式为

$$B_4 = P_i \times a \times b \times e \times K \times \frac{44}{12} \quad (8)$$

式中：

P_i 为木材产品生产过程中废料用于锅炉燃烧产生的 CO_2 排放当量；

P_i 为废木料干重；

K 为含碳率；

a 为废木料用于燃烧的比例；

b 为废木料锅炉燃烧效率；

e 为用于木地板加工的热能系数；

44/12 为 CO_2 和 C 比。

注：此数据仅为了解用，不计入碳足迹评估范围。

5.7.2.5 固定源：有组织废气碳排放

木材产品加工过程固定污染源（有组织废气）产生的二氧化碳排放计算公式如（9）所示：

$$B_5 = \sum_i^n B_i \times GWP \quad (9)$$

式中：

B_5 表示加工过程固定污染源（有组织废气）产生的二氧化碳排放，单位 $\text{kgCO}_2/\text{件}$ 或 kgCO_2/m^3 ；

B_i 表示 1 件木材产品生产固定污染源（有组织废气）消耗的第 i 种温室气体排放量，单位 $\text{kgCO}_2/\text{件}$ 或 kgCO_2/m^3 ；

GWP 表示在特定时间（100 年）内，某种温室气体（GHG）相对于二氧化碳辐射强度（气候变化）的影响程度的因子，见附录 B 表 6。

5.7.2.6 厂区内逸散源碳排放

木材产品加工过程厂区内逸散源（冰箱、冰柜、空调、工业冷水机、车等相应设备设施中填充的制冷剂，灭火器、化粪池等逸散源）产生的二氧化碳排放计算公式如（10）所示：

$$B_6 = \sum_i^n B_i \times EF_i \quad (10)$$

式中：

B_6 表示加工过程厂区内逸散源产生的碳排放，单位 $\text{kgCO}_2/\text{件}$ 或 kgCO_2/m^3 ；

B_i 表示 1 件木材产品生产厂区内的第 i 种逸散源的排放量，单位 $\text{kg}/\text{件}$ 或 kg/m^3 ；

EF_i 表示第 i 种逸散源的碳排放因子，单位 kgCO_2/kg ，见附录 B 表 7。

5.7.2.7 无组织废气、废水碳排放

木材产品加工过程无组织废气、废水处理产生的二氧化碳排放计算公式如（11）所示：

$$B_7 = \sum_i^n B_i \times GWP \quad (11)$$

式中：

B_f 表示加工过程无组织废气、废水处理产生的二氧化碳排放，单位 $\text{kgCO}_2/\text{件}$ 或 kgCO_2/m^3 ；

B_i 表示 1 件木材产品生产无组织废气、废水处理产生消耗的第 i 种温室气体排放量，单位 $\text{kgCO}_2/\text{件}$ 或 kgCO_2/m^3 ；

GWP 表示在特定时间 (100 年) 内，某种温室气体 (GHG) 相对于二氧化碳辐射强度（气候变化）的影响程度的因子，见附录 B 表 6。

5.7.2.8 生产工艺的直接排放：如注胶、喷漆等

生产阶段排放量

$$B=B_1+\cdots+B_6$$

(12)

式中：

B 为木材产品生产阶段碳足迹，单位 $\text{kgCO}_2/\text{件}$ 或 kgCO_2/m^3 。

5.7.3 运输阶段

C1	原料运输过程中消耗的柴油和石油等化石能源
C2	辅料运输过程中消耗的柴油和石油等化石能源
C3	原料包装运输过程中消耗的柴油和石油等化石能源
C4	厂区内移动源设备运输过程中消耗的柴油和石油等化石能源
C5	废弃物运输过程中消耗的柴油和石油等化石能源
C6	产品贮存运输过程中消耗的柴油和石油等化石能源

运输过程化石能源消耗将产生直接排放。包括伐后木材及胶黏剂、包装等原辅材料和产品的运输，主要是柴油、汽油能源燃烧产生的排放。

5.7.3.1 原料运输过程中碳排放

原料运输过程消耗的柴油和石油等化石能源（直接排放）碳排放计算公式如下：

$$C_1 = \sum_{i=1}^n D_i \times M_i \times EF_i$$

(13)

式中：

C_1 表示运输过程碳排放，单位为 $\text{kgCO}_2/\text{件}$ 或 kgCO_2/m^3 ；

D_i 表示运输距离，单位为 km ；

M_i 表示运输的物料质量，单位 kg ；

EF_i 表示运输过程碳排放因子，单位为 $\text{kgCO}_2/\text{t}\cdot\text{km}$ ；

运输过程排放因子可参考附录 B 表 4。

5.7.3.2 辅料运输过程中碳排放

辅料运输过程消耗的柴油和石油等化石能源（直接排放）碳排放计算公式如下：

$$C_2 = \sum_i^n D_i \times M_i \times EF_i \quad (14)$$

式中：

C_2 表示运输过程碳排放，单位为 $\text{kgCO}_2/\text{件}$ 或 kgCO_2/m^3 ；

D_i 表示运输距离，单位为 km ；

M_i 表示运输的辅料质量，单位 kg ；

EF_i 表示运输过程碳排放因子，单位为 $\text{kgCO}_2/\text{t}\cdot\text{km}$ ；

运输过程排放因子可参考附录 B 表 4。

5.7.3.3 原料包装运输过程中碳排放

原料包装运输过程消耗的柴油和石油等化石能源（直接排放）碳排放计算公式如下：

$$C_3 = \sum_i^n D_i \times M_i \times EF_i \quad (15)$$

式中：

C_3 表示运输过程碳排放，单位为 $\text{kgCO}_2/\text{件}$ 或 kgCO_2/m^3 ；

D_i 表示运输距离，单位为 km；

M_i 表示运输的原料包装质量，单位 kg；

EF_i 表示运输过程碳排放因子，单位为 $\text{kgCO}_2/\text{t}\cdot\text{km}$ 。

运输过程排放因子可参考附录 B 表 4。

5.7.3.4 厂区内移动源设备碳排放

厂区内移动源设备消耗的柴油和石油等化石能源（直接排放）碳排放计算公式如下：

$$C_4 = \sum_i^n D_i \times M_i \times EF_i \quad (16)$$

式中：

C_4 表示运输过程碳排放，单位为 $\text{kgCO}_2/\text{件}$ 或 kgCO_2/m^3 ；

D_i 表示运输距离，单位为 km；

M_i 表示运输的物料质量，单位 kg；

EF_i 表示运输过程碳排放因子，单位为 $\text{kgCO}_2/\text{t}\cdot\text{km}$ 。

运输过程排放因子可参考附录 B 表 4。

5.7.3.5 废弃物运输过程碳排放

废弃物运输过程中消耗的柴油和石油等化石能源（直接排放）碳排放计算公式如下：

$$C_5 = \sum_i^n D_i \times M_i \times EF_i \quad (17)$$

式中：

C_5 表示运输过程碳排放，单位为 $\text{kgCO}_2/\text{件}$ 或 kgCO_2/m^3 ；

D_i 表示运输距离，单位为 km；

M_i 表示运输的废弃物质量，单位 kg；

EF_i 表示运输过程碳排放因子，单位为 $\text{kgCO}_2/\text{t}\cdot\text{km}$ 。

运输过程排放因子可参考附录 B 表 4。

5.7.3.6 产品贮存运输过程碳排放

产品贮存运输过程中消耗的柴油和石油等化石能源（直接排放）碳排放计算公式如下：

$$C_6 = \sum_i^n D_i \times M_i \times EF_i \quad (18)$$

式中：

C_6 表示运输过程碳排放，单位为 $\text{kgCO}_2/\text{件}$ 或 kgCO_2/m^3 ；

D_i 表示运输距离，单位为 km ；

M_i 表示运输的物料质量，单位 kg ；

EF_i 表示运输过程碳排放因子，单位为 $\text{kgCO}_2/\text{t}\cdot\text{km}$ 。

运输过程排放因子可参考附录 B 表 4。

如 5.7.3 运输阶段中能确定柴油和石油等化石能源的消耗量，也可按公式（6）进行计算。

运输阶段排放量：

$$C = C_1 + \dots + C_6 \quad (19)$$

式中：

C 为木材产品运输阶段碳足迹，单位为 $\text{kgCO}_2/\text{件}$ 或 kgCO_2/m^3 。

5.7.4 碳储存

当木材产品包含生物碳并保留一年以上时，碳储存的影响根据产品中转移固定的碳储量乘以加权系数（以木材产品理论寿命计）进行计算，并以负的二氧化碳当量值纳入产品生命周期碳足迹排放评价，具体计算公式如下：

$$D_1 = \frac{M \times 0.76 \times T_0}{100} \quad (20)$$

式中:

D1 为木材产品理论寿命内存储的碳储量效益, 单位为 $\text{kgCO}_2/\text{件}$ 或 kgCO_2/m^3 ;

M 为 1 件或 1m^3 木材产品中存储的 CO_2 量, 单位为 $\text{kgCO}_2/\text{件}$ 或 kgCO_2/m^3 ;

T_0 为某个产品形成后, 其全部碳存储效益存在的年数;

$$\frac{0.76 \times T_0}{100}$$

为碳存储的加权系数(此加权系数适用于其全部碳存储效益存续 2—25 年, 此后没有碳存储效益)。

$$M = m \times c \times \frac{44}{12}$$

(21)

式中:

m 为 1 件或 1m^3 木材产品的重量, 单位为 $\text{kg}/\text{件}$ 或 kg/m^3 ;

c 为木材产品的含碳率, 单位为 kgC/kg ;

44/12 为 CO_2 与碳转换系数。

注: 如果企业无法检测木材产品的含碳率, 可按附录 C 执行。

5.7.5 木材产品碳足迹

$$P = A + B + C - D$$

(22)

式中:

P 为木材产品碳足迹, 单位 $\text{kgCO}_2/\text{件}$ 或 kgCO_2/m^3 。

6 木材产品碳足迹评价报告

木材产品足迹评价报告，包括但不限于下列内容：

- 生产企业/组织的描述；
- 产品描述；
- 评价范围；
- 报告覆盖的时间段；
- 功能单位；
- 系统边界；
- 数据收集清单及情况说明；
- 产品碳足迹计算过程按 5.7 计算方法计算；
- 附加的信息（如质量和能源管理体系或制度信息进行描述）
- 采用先进生产工艺或节能减排技术前后产品碳排放比较说明，或者与同类产品的碳排放比较说明。

附录 A

(资料性)

产品描述信息清单

产品描述应使用户能够明确的识别产品型号等信息。木材产品描述的具体信息如下表：

产品描述种类	具体信息
厂商名称	制造商
产品名称	名称
产品规格	规格(长×宽×高 cm)及重量(kg)
附加物含量	胶黏剂含量(kg/件)
	油漆含量(kg/件)
	五金件含量(kg/件)
	其他附加物含量(kg/件)
包装	材质、重量(kg/件)
其他	产品简单示意图
	产品主要技术参数
	产品满足相关质量标准的证明文件 产品所获取的其他标志等

附录 B

(资料性)

排放因子缺省值

B.1 表 1 常见中间产品缺省值

序号	项目	碳排放值	单位
1	原木	0.15	kgCO ₂ e/kg
2	原木	264.13	kgCO ₂ e/m ³
3	锯材	1637	kgCO ₂ e/m ³
4	胶合木	246	kgCO ₂ e/m ³
5	胶合板	312.08	kgCO ₂ e/m ³

数据来源：[2]

附表中各数据均基于规范发布时期的最新数值，不排除随着时间推移数据会发生变化的可能，待政府主管部门发布更新官方数据后宜采用最新官方发布数据。

B.2 表 2 常见原辅材料排放因子缺省值

序号	辅助材料品种	排放因子	单位
1	聚氨酯粘合剂	5.06	kgCO ₂ e/kg
2	油漆	0.88	kgCO ₂ e/kg
3	植物油	5.16	kgCO ₂ e/kg
4	金属件	2.44	kgCO ₂ e/kg
5	瓦楞纸箱	1.605	kgCO ₂ e/kg

6	包装膜（低密度聚乙烯）	3.11	kgCO ₂ e/kg
7	聚苯乙烯泡沫	8.43	kgCO ₂ e/kg
8	包装纸	141.56	gCO ₂ e/kg
9	普通塑料薄膜	2.57	kgCO ₂ e/kg
10	透明胶带	2.765	kgCO ₂ e/kg
11	石蜡	1.92	tCO ₂ e/t
12	无纺布	3.82	kgCO ₂ e/kg
13	柔性泡沫塑料（聚氨酯）	5.38	kgCO ₂ e/kg

数据来源：[2] [3]

附表中各数据均基于规范发布时期的最新数值，不排除随着时间推移数据会发生变化的可能，待政府主管部门发布更新官方数据后宜采用最新官方发布数据。

B.3 表3 常见化石燃料特性参数缺省值

燃料品种	低位发热量 (GJ/t, GJ/10 ⁴ Nm ³)	单位热值含碳量 (tC/GJ, tC/10 ⁴ Nm ³)	碳氧化率 (%)
无烟煤	24.515	27.49×10 ⁻³	94
烟煤	23.204	26.18×10 ⁻³	93
汽油	44.80	18.90×10 ⁻³	98
柴油	43.33	20.20×10 ⁻³	98
液化天然气	41.868	15.30×10 ⁻³	99
天然气	389.31	15.30×10 ⁻³	99

数据来源：[4]

附表中各数据均基于规范发布时期的最新数值，不排除随着时间推移数据会发生变化的可能，待政府主管部门发布更新官方数据后宜采用最新官方发布数据。

B.4 表 4 运输碳排放因子表

序号	运输方式	排放因子	单位
1	微型货车运输	0.12	kgCO ₂ e/ (t • km)
2	中型货车运输	0.041	kgCO ₂ e/ (t • km)
3	重型货车运输	0.049	kgCO ₂ e/ (t • km)
4	小型飞机货运	1.467	kgCO ₂ e/ (t • km)
5	中型飞机货运	1.146	kgCO ₂ e/ (t • km)
6	大型飞机货运	0.096	kgCO ₂ e/ (t • km)
7	铁路货运	0.028	kgCO ₂ e/km
8	杂货船货运	0.019	kgCO ₂ e/ (t • km)
9	集装箱船货运	0.01	kgCO ₂ e/ (t • km)

数据来源： [2]

附表中各数据均基于规范发布时期的最新数值，不排除随着时间推移数据会发生变化的可能，待政府主管部门发布更新官方数据后宜采用最新官方发布数据。

B.5 表 5 常见资源排放因子缺省值

序号	资源	排放因子	单位
1	城市用水 供水系统-地表水取水能耗（城市远程输水，距离 15-50km） 天津	0.15	kgCO ₂ e/m ³
2	城市用水 供水系统-地下水抽提能耗（提升高度 35-78m） 天津	0.31	kgCO ₂ e/m ³
3	城市用水 供水系统-脱盐产水能耗-多级闪蒸法 MAF（电耗） 天津	3.45	kgCO ₂ e/m ³
4	城市用水 供水系统-脱盐产水能耗-多效蒸馏法 MED（电耗） 天津	5.75	kgCO ₂ e/m ³
5	城市用水 供水系统-脱盐产水能耗-压气蒸馏法 MVC（电耗） 天津	11.5	kgCO ₂ e/m ³
6	城市用水 供水系统-脱盐产水能耗-电渗析法（电耗） 天津	18	kgCO ₂ e/m ³

7	城市用水	4.55	kgCO ₂ e/m ³
	供水系统-脱盐产水能耗-反渗透法 RO（电耗）		
8	城市用水	0.82	kgCO ₂ e/m ³
	供水系统-再生水生产能耗		

数据来源：[2]

附表中各数据均基于规范发布时期的最新数值，不排除随着时间推移数据会发生变化的可能，待政府主管部门发布更新官方数据后宜采用最新官方发布数据。

B.6 表 6 温室气体的 GWP

序号	气体名称	分子式	GWP（100 年）
1	二氧化碳	CO ₂	1
2	甲烷	CH ₄	27.9
3	氧化亚氮	N ₂ O	273
4	六氟化硫	SF ₆	25200
5	三氟化氮	NF ₃	17400
6	氢氟碳化物	HFCs	详见 IPCC
7	全氟碳化物	PFCs	详见 IPCC

数据来源：[5]

附表中各数据均基于规范发布时期的最新数值，不排除随着时间推移数据会发生变化的可能，待政府主管部门发布更新官方数据后宜采用最新官方发布数据。

B7 表 7 常见逸散排放因子缺省值

序号	资源	排放因子	单位
1	制冷剂	15897.73	kgCO ₂ e/kg
2	化粪池	0.3	kgCO ₂ e/kg
3	CO ₂ 灭火器	0.04	kgCO ₂ e/kg

数据来源：[2] [6]

附表中各数据均基于规范发布时期的最新数值，不排除随着时间推移数据会发生变化的可能，待政府主管部门发布更新官方数据后宜采用最新官方发布数据。

TB

附录 C

(规范性)

含碳率

一、中国主要造林树种的含碳率

中国主要造林树种的含碳率

种树名	各器官碳含率							数据来源
	干	树皮	枝	叶	地上平均	根	全株	
灌木(北京)a	0.4924			0.4595	0.4760	0.4813	0.4777	北京
10种灌木(华北)b	0.4882			0.4937	0.4909	0.4872	0.4897	华北
14种灌木(小陇山)c			0.4700	0.4302	0.4501	0.4335	0.4446	甘肃小陇山
白桦	0.5552	0.4625	0.5646	0.5159	0.5071	0.4834	0.5031	北京
白桦	0.4380	0.4380	0.4199	0.4066	0.4157	0.4201		大兴安岭
白桦	0.4732	0.5332	0.4900	0.5135	0.5025	0.4826	0.4985	甘肃小陇山
白桦	0.4890	0.5689	0.5046	0.5068	0.4934	0.5173	0.5125	华北
白蜡	0.5010	0.4550	0.4920	0.5160		0.4740	0.4880	北京
白柳	0.4669	0.4466	0.4573	0.4160		0.4672		新疆额尔齐斯河
柏木	0.5372	0.4832	0.4932	0.4861		0.5444	0.5088	四川
碧桃	0.5540		0.4600	0.4830		0.4420	0.4850	北京

侧柏	0.5429	0.4783	0.5551	0.5192	0.5109	0.5074	0.5104	北京
侧柏	0.5134	0.4952	0.4963	0.4915	0.5085	0.4991	0.5010	华北
侧柏	0.5270	0.4420	0.4750	0.5600		0.4510	0.4910	北京
擦木	0.5265		0.5122	0.4981		0.5364		浙江
柴松	0.5238			0.5413		0.4773	0.5068	黄土高原子午岭
怪柳							0.4145	海河流域
臭椿							0.4550	海河流域
垂柳	0.5410	0.4620	0.4870	0.4540		0.4790	0.4650	北京
刺槐	0.5012	0.4276	0.5269	0.4649	0.4703	0.4323	0.4640	北京
刺槐	0.4559		0.4518	0.4531		0.4314	0.4474	贵阳
刺槐							0.4175	海河流域
大叶白蜡	0.4400		0.4300			0.4400		北京东灵山
大叶榆子木	0.4694	0.4728	0.4638	0.4470	0.4520	0.4425	0.4501	甘肃小陇山
大叶女贞	0.4652		0.4595	0.4435		0.4423	0.4538	贵阳
丁香	0.4950		0.4890	0.4810		0.4690	0.4840	北京
冬瓜杨	0.4570		0.4890	0.5050		0.4460		贡嘎山
杜英	0.4598		0.4459	0.4494		0.4385	0.4473	贵阳

杜仲	0.4691		0.4584		0.4456	0.4452	0.4538	贵阳
椴树	0.4902	0.4517	0.4655	0.4824	0.4894	0.4732	0.4764	华北
额河杂交杨	0.4748	0.4447	0.4741	0.4151		0.4836		额尔齐斯河
二色胡枝子			0.4653	0.4771		0.4719	0.4714	黄土高原子午岭
枫香	0.4849		0.5016	0.4644		0.4713		浙江
国槐	0.5650	0.4980	0.4990	0.4680		0.4810	0.5020	北京
国外松林	0.5490	0.5420	0.5580	0.5590		0.5180	0.5450	江苏句容
旱柳							0.4560	海河流域
红桦	0.4810	0.4929	0.4880	0.5081	0.4925	0.4745	0.4889	甘肃小陇山
红皮云杉	0.5009	0.5157	0.4963	0.5205	0.5257	0.5084	0.5118	华北
红叶小檗	0.6050			0.5150		0.4930	0.5380	北京
猴樟	0.4615		0.4532	0.4456		0.4413	0.4543	贵阳
胡桃楸	0.5068	0.4467	0.5057	0.4403	0.4595	0.4108	0.4514	北京
虎榛子			0.5064	0.4948		0.4974	0.4995	黄土高原子午岭
虎榛子			0.4861	0.4601		0.4583	0.4682	黄土高原子午岭
华北落叶松	0.5356	0.5175	0.5557	0.5044	0.5248	0.5018	0.5210	北京
华北落叶松	0.4971	0.5276	0.5100	0.5107	0.5337	0.5114	0.5158	华北

华北落叶松	0.4752	0.4819	0.5032	0.4665		0.4065		秦岭火地塘
华山松	0.4927	0.4889	0.4881	0.5190	0.4970	0.4932	0.4962	甘肃小陇山
华山松	0.4955	0.4886	0.4902	0.5198	0.4985	0.4988	0.4986	秦岭
华山松	0.5513	0.5357	0.5243	0.5387		0.5456	0.5391	四川
华山松	0.4832	0.4337	0.5037	0.5135		0.4759		秦岭火地塘
黄刺玫			0.4791	0.4675		0.4782	0.4749	黄土高原子午岭
黄皮树	0.4678		0.4585	0.4465		0.4418	0.4546	贵阳
黄杨	0.4550			0.5210		0.4490	0.4750	北京
桧柏	0.5450	0.4970	0.4870	0.5620		0.5100	0.5110	北京
火炬松	0.5372		0.4935	0.5118		0.5036		浙江
火炬松	0.5244	0.5160	0.5281	0.5442		0.5234	0.5272	北京东灵山
棘皮桦	0.4800		0.5200			0.4500		海河流域
加杨							0.4532	黄土高原子午岭
莢蒾			0.4959	0.4792		0.4823	0.4858	北京
金银木	0.4890		0.4790	0.4700		0.4820	0.4800	海河流域
卷柏属							0.2833	浙江
楷木	0.4877		0.4903	0.5151		0.4584		新疆额尔齐斯河

冷杉	0.4941	0.4362	0.4806	0.4242		0.4640		四川
冷杉林	0.4780		0.4870	0.5290		0.4780		贡嘎山
栋林	0.5120	0.5230	0.4860	0.5210		0.4520	0.4990	江苏句容
连翘	0.5060		0.5000	0.5060		0.4770	0.4970	北京
辽东栎	0.4767	0.4492	0.4556	0.4804	0.4655	0.4540	0.4632	甘肃小陇山
辽东栎	0.4792	0.4641	0.4826	0.4767	0.4725	0.4757	0.4750	华北
辽东栎	0.4500		0.4100			0.4100		北京东灵山
柳杉	0.5550	0.5131	0.5320	0.5025		0.5620	0.5331	四川
栎树	0.5080	0.4340	0.4790	0.5000		0.4630	0.4770	北京
栎树	0.4699		0.4581	0.4418		0.4418	0.4538	贵阳
落叶松	0.5377	0.5341	0.5145	0.5027		0.5314	0.5341	四川
马尾松	0.5312		0.5121	0.5249		0.5123		浙江
马尾松	0.5117	0.5037	0.5144	0.5114		0.5464	0.5175	四川
马尾松	0.5578	0.5670	0.5470	0.5557		0.5287		干烟洲
马尾松(4年生)	0.5034	0.4898	0.5206	0.5573		0.4895	0.5121	福建光泽县
马尾松(10年生)	0.4950	0.4903	0.4750	0.4975		0.4715	0.4859	福建光泽县
生马尾松(18年生)	0.4846	0.5218	0.5048	0.5589		0.4746	0.5089	福建光泽县

马尾松 (41 年生)	0.5200	0.4857	0.5227	0.5460		0.4731	0.5095	福建光泽县
马尾松幼 龄林	0.5026	0.4956	0.4895	0.4825		0.4965	0.4969	福建顺昌
马尾松中 龄林	0.5263	0.5176	0.5126	0.5103		0.5256	0.5231	福建顺昌
马尾松成 熟林	0.5329	0.5226	0.5068	0.5019		0.5233	0.5259	福建顺昌
马尾松老 龄	0.5227	0.4919	0.4825	0.5177		0.4735	0.4977	福建光泽县
毛竹	0.5030		0.4961	0.4683		0.5210		浙江
蒙椴	0.4500		0.4300			0.43	437000	北京东灵山
蒙古栎	0.5275	0.4250	0.5265	0.4877	0.4798	0.4814	0.4801	北京
蒙古栎	0.4225	0.3834	0.3962	0.3893	0.3979			大兴安岭
木荷	0.4820		0.4645	0.5127		0.4700		浙江
木荷	0.5079	0.5057	0.5125	0.5275		0.5073		千烟洲
木麻黄幼 龄林木	0.4650	0.4540	0.4680	0.4792		0.4860		福建惠安
麻黄中龄 林木	0.4950	0.4870	0.4990	0.5047		0.5170		福建惠安
麻黄成熟 林	0.4850	0.4800	0.4880	0.5097		0.5110		福建惠安
南酸枣	0.4685		0.4586	0.4435		0.4485		贵阳
楠木幼龄 林	0.4943	0.5062	0.4773	0.4252		0.4789	0.4564	福建尤溪
楠木中龄 林	0.5056	0.5232	0.5040	0.4350		0.5053	0.4859	福建尤溪福 建

楠木成熟林	0.5248	0.5182	0.4961	0.4421		0.5065	0.5044	福建尤溪
欧洲黑杨	0.4835	0.4550	0.4636	0.4040		0.4746	0.5145	新疆额尔齐斯河
秦岭冷杉	0.4920	0.4722	0.4757	0.5295	0.4924	0.4839		甘肃小陇山
青冈	0.4702		0.4534	0.4921		0.4786	0.4907	浙江祁连山自然
青海云杉	0.5034	0.5000	0.5086	0.5696		0.5489		保护区黄土高原
忍冬			0.5062	0.4661		0.4637	0.5243	子午岭
日本落叶松	0.4853	0.5034	0.4919	0.5027	0.4958	0.4982	0.4787	甘肃小陇山
锐齿栎	0.4772	0.4578	0.4610	0.4813	0.4693	0.4492	0.4963	甘肃小陇山
锐齿栎	0.4885	0.4732	0.4876	0.5121	0.4904	0.4682	0.4653	秦岭
锐齿栎	0.4697	0.4791	0.4661	0.4382		0.4857	0.4860	火地塘
色木槭	0.4700		0.4500			0.4300		北京东灵山
山杜英	0.4916		0.5009	0.5031		0.5043		浙江
山杨	0.5188	0.5136	0.5434	0.4757	0.4977	0.4508	0.4824	北京
山杨	0.4844	0.4870	0.4866	0.4960	0.4861	0.4885	0.4880	华北
山杨						0.4719	0.4570	黄土高原子午岭
山楂			0.4556	0.4433		0.4719	0.4570	黄土高原子午岭
杉木	0.5234	0.5425	0.5164	0.5128		0.4722		浙江

杉木	0.5465	0.5435	0.5280	0.5116		0.5266	0.5280	四川
杉木	0.5419	0.4729	0.4972	0.5426		0.5178		千烟洲
杉木(10年)	0.4729	0.4764	0.4994	0.4811		0.4740	0.4756	湖南会同
杉木(14年)	0.4764	0.4740	0.5330	0.5093		0.4785	0.4807	湖南会同
杉木林	0.4740	0.5325		0.5190		0.5100	0.5100	江苏句容
湿地松	0.5325		0.5174	0.5237		0.5054		浙江
湿地松	0.5321	0.4879	0.5368	0.5436		0.4928	0.5190	四川
湿地松	0.5423	0.5607	0.5382	0.5548		0.53297		千烟洲
栓皮栎	0.4710	0.4934	0.4590	0.4974	0.4802	0.4566	0.4755	甘肃小陇山
水曲柳	0.4802	0.4519	0.4644	0.4521	0.4622	0.4751	0.4647	甘肃小陇山
水杉	0.5280	0.4918	0.5334	0.5084		0.4799	0.5083	四川
丝兰	0.4300					0.4180	0.4390	北京
思茅松 (中幼林)	0.4848	0.4749	0.4813	0.4727		0.4680		云南
棠梨			0.4670	0.4590		0.5000	0.4750	云南
五角枫	0.4809	0.4472	0.4622	0.4864	0.4692	0.4679	0.4689	北京
香樟	0.4698		0.4568	0.4425		0.4405	0.4535	甘肃小陇山
橡胶树	0.4586	0.4569	0.4640	0.4736		0.4570		贵阳

小叶杨							0.4860	海南西部
兴安落叶松	0.4431	0.4295	0.3860	0.4351	0.4234			大兴安岭
杏							0.4950	海河流域
悬铃木	0.4940	0.4830	0.4370	0.4710		0.4490	0.4670	北京
构子			0.4552	0.4743		0.4443	0.4579	黄土高原子午岭
杨树	0.4270	0.4364	0.4574	0.4482		0.4587	0.4507	黄淮海
杨树(5年生)	0.4558	0.4559		0.4231	0.4458		0.4458	洞庭湖
杨树(5年生)	0.4426	0.4621		0.4539	0.4528		0.4565	渭南
杨树(10年生)	0.4574	0.4536		0.4250	0.4453		0.4489	洞庭湖
杨树(10年生)	0.4640	0.4561		0.4594	0.4598		0.4607	渭南
杨树(15年生)	0.4580	0.4561		0.4360	0.4460		0.4512	洞庭湖
杨树(20年生)	0.4567	0.4498		0.4420	0.4487		0.4523	洞庭湖
杨树(20年生)	0.4612	0.4555		0.4580	0.4582		0.4593	渭南
杨树(25年生)	0.4542	0.4431		0.4317	0.4363		0.4450	渭南
杨树(30年生)	0.4780	0.4056		0.4477	0.4438		0.4467	渭南
杨树(农田林网8年生)	0.5163		0.5337	0.5628		0.4351		山东郓城
杨树(农田林网16年生)	0.4969		0.5295	0.5493		0.4630		山东郓城

杨树(杨农间作)	0.5267	0.5100	0.5050	0.4850		0.4900		江苏宿迁
野樱桃			0.4698	0.4387		0.4743	0.4609	黄土高原子午岭
银白杨	0.4873	0.4666	0.4828	0.4262		0.4578		新疆额尔齐斯河
银灰杨	0.4770	0.4617	0.4757	0.3941		0.4371		新疆额尔齐斯河
银杏	0.5100	0.4420	0.4400	0.5200		0.4370	0.4460	北京
银杏	0.4685		0.4618	0.4465		0.4438	0.4547	贵阳
油松	0.5610	0.4808	0.5728	0.5621	0.5295	0.5639	0.5038	北京
油松	0.4935	0.5258	0.4996	0.5241	0.5108	0.4817	0.5049	甘肃小陇山
油松	0.4958	0.5311	0.5019	0.5158	0.5080	0.5112	0.5105	华北
油松	0.5530	0.5300	0.5240	0.5620		0.5120	0.5360	北京
油松	0.4967	0.5298		0.5264	0.5174	0.4916	0.5122	秦岭
油松	0.5244	0.5381		0.5708		0.5198	0.5397	四川
油松							0.5038	海河流域
油松	0.4995	0.4925	0.5080	0.5145		0.4425		秦岭火地塘
榆叶梅	0.4870		0.4910	0.4840		0.5120	0.4930	北京
月季	0.5370		0.4650			0.4370	0.4800	北京
云南松	0.5299	0.5067	0.5237	0.5389		0.5314	0.5261	四川

云杉	0.4909	0.4806	0.4981	0.5112	0.4952	0.4724	0.4906	甘肃小陇山
云杉	0.5324	0.4760	0.5161	0.5107		0.5060	0.5082	四川
樟子松	0.4515	0.4057	0.3839	0.4068	0.4120			大兴安岭
珍珠梅	0.5240		0.4930	0.5040		0.4700	0.4980	北京
竹子	0.5070		0.4740	0.4840		0.3830	0.4620	北京
紫薇	0.4692		0.4558	0.4496		0.4428	0.4508	贵阳
紫叶李	0.4900		0.4970	0.5040		0.4710	0.4900	北京
杂木林 (北京)	0.5038	0.4484	0.5322	0.4852	0.4833	0.4777	0.4824	北京

注：数据来源于 [1]

二、立木的不同器官含碳系数

立木的不同器官含碳系数							
名称	全树	地上	地下	树干	树皮	树枝	树叶
油松	0.5165 (±0.0057)	0.5184 (±0.0057)	0.5093 (±0.0066)	0.5104 (±0.0068)	0.5247 (±0.0127)	0.5229 (±0.0094)	0.5380 (±0.0184)
湿地松	0.4736 (±0.0156)	0.4756 (±0.0138)	0.4664 (±0.0182)	0.4744(±0.0178)	0.4612 (±0.0248)	0.4868 (±0.0143)	0.4810 (±0.0154)
云南松	0.5084 (±0.0137)	0.5106 (±0.0130)	0.4947 (±0.0218)	0.5007(±0.0144)	0.5178 (±0.0136)	0.5219 (±0.0160)	0.5346 (±0.0253)
马尾松	0.5252 (±0.0094)	0.5254 (±0.0096)	0.5082 (±0.0291)	0.5186 (±0.0115)	0.4994 (±0.0098)	0.5174 (±0.0474)	0.5755 (±0.0230)
杉木	0.4990 (±0.0120)	0.5003 (±0.0115)	0.4880 (±0.01795)	0.5014 (±0.0115)	0.4999 (±0.0198)	0.4947 (±0.0140)	0.5033 (±0.0159)
落叶松	0.4893 (±0.0264)	0.4895 (±0.0292)	0.4884 (±0.0331)	0.4826 (±0.0292)	0.5021 (±0.0319)	0.4990 (±0.0326)	0.4963 (±0.0285)
云杉	0.4900 (±0.0656)	0.4905 (±0.0553)	0.4880 (±0.0336)	0.4850 (±0.0670)	0.4854 (±0.0414)	0.4952 (±0.0422)	0.5006 (±0.0454)
冷杉	0.4962 (±0.0267)	0.4957 (±0.0263)	0.4985 (±0.0275)	0.4928 (±0.0255)	0.4919 (±0.0298)	0.4923 (±0.0347)	0.5178 (±0.0325)
柳杉	0.5137 (±0.0270)	0.5154 (±0.0208)	0.5091 (±0.0052)	0.5089 (±0.0420)	0.5183 (±0.0033)	0.5160 (±0.0360)	0.5382 (±0.0630)
栎树	0.4802 (±0.0430)	0.4827 (±0.0444)	0.4718 (±0.0395)	0.4839 (±0.0390)	0.4801 (±0.0620)	0.4805 (±0.0525)	0.4923 (±0.0653)
桦树	0.4872 (±0.0273)	0.4897 (±0.0290)	0.4779 (±0.0298)	0.4848 (±0.0280)	0.5054 (±0.0428)	0.4870 (±0.0379)	0.5038 (±0.0383)
木荷	0.4706 (±0.0216)	0.4712 (±0.0182)	0.4667 (±0.0232)	0.4683 (±0.0191)	0.4738 (±0.0239)	0.4712 (±0.0186)	0.4879 (±0.0234)
枫香	0.4668 (±0.0119)	0.4690 (±0.0136)	0.4604 (±0.0166)	0.4737 (±0.0145)	0.4487 (±0.0228)	0.4694 (±0.0158)	0.4583 (±0.0230)

注：括号中的数值为标准差。

注：数据来源于立木生物量模型及碳计量参数系列行业标准。

附录 D
(资料性)

木材产品使用寿命

类别	使用年限	示例
1	5 年	临时性建筑结构
2	25 年	易于替换的结构构件
3	50 年	普通房屋和构筑物
4	产品设计文件	其他木材产品

注：数据来源于GB 50005-2017木结构设计标准。

TB

附录 E

(资料性)
记录表格

E.1 表 1 产品碳足迹基本资料

产品碳足迹基本资料

负责部门:							联系人姓名:	
邮编:							联系方式:	
数据的时空边界:								
公司基本信息								
公司名称:								
公司地址:								
公司简介: 注:包括营业执照、产区分图及组织架构图								
产品基本信息								
目标产品名称							产品图片(——)	
目标产品单位								
目标产品介绍								
目标产品制造产地/制造厂区								
目标产品于核算期间生产数量	产品名称	总产量(选项)	单位	事件产品总量(不含损耗)	事件产品产量(选项)	测量值	计算值	推估值
						测量值、计算值和推估值,三选一在下表进行勾选“√”		

E.2 表 2 产品碳足迹原料阶段

产品碳足迹原料阶段

负责部门:							联系人姓名:								
邮编:							联系方式:								
数据的时空边界:															
1. 原材料使用情形 (行数不孝可增加)															
1.1 原料(直接材料) (目标产品之原料使用情形)															
原料名称 (中/英文)	材质	型号和规格	工艺	单一目标产品用量	单位	测量值 测量值、计算值和推估值,三选一在下表进行勾选“√”	计算值	推估值	用途说明	数据来源说明	供货商	供货商地址	供货商运输至生产厂区距离(km)	车型	燃料类型
1.2 辅料(间接材料) (目标产品之辅料使用情形)															
辅料名称 (中/英文)	材质	型号和规格	工艺	单一目标产品用量	单位	测量值 测量值、计算值和推估值,三选一在下表进行勾选“√”	计算值	推估值	用途说明	数据来源说明	供货商	供货商地址	供货商运输至生产厂区距离(km)	车型	燃料类型
2. 包装材料使用情形 (目标产品之包装材料使用情形) 原料包装															
包装材料名称 (中/英文)	材质	型号和规格	工艺	单一目标产品用量	单位	测量值 测量值、计算值和推估值,三选一在下表进行勾选“√”	计算值	推估值	用途说明	数据来源说明	供货商	供货商地址	供货商运输至生产厂区距离(km)	车型	燃料类型

E.3 表 3 产品碳足迹生产阶段

产品碳足迹生产阶段													
负责部门:				负责人姓名:									
日期:				联系方式:									
数据的时间边界:													
1. 产品生产说明 (说明产品生产工艺流程, 如有生产工艺图可自附附!)													
2. 生产资源消耗输入 (行数和列数自行增加)													
说明: 能源使用情形 (包含电网用量/清洁能源使用)													
名称	全厂总用量 (选填)	单一目标产品用量	单位	量测值	计算值	推估值	数据来源说明	备注					
				量测值, 计算值和推估值, 三选一在下表进行勾选“√”									
【注】1. 能源包含: 电力、天然气、柴油、燃料油、液化石油气一等; 2. 水源包含: 生产用水、冷却用水、生活用水一等。													
3. 生产产出废弃物 (行数和列数自行增加)													
说明: 废弃物产生情形 (包含废弃物产生种类)													
废弃物名称	全厂产出量 (选填)	单一目标产品产出量	单位	量测值	计算值	推估值	处理方式	数据源说明	回收/处理单位	回收/处理单位地址	生产厂/设施转运至回收/处理单位距离 (km)	运输工具	燃料类型
				量测值, 计算值和推估值, 三选一在下表进行勾选“√”									
4. 生产排放情形													
过程	排放种类	全厂排放量 (选填)	单一目标产品排放量	单位	量测值	计算值	推估值	数据来源说明					
					量测值, 计算值和推估值, 三选一在下表进行勾选“√”								

E.4 表 4 产品碳足迹配送阶段

产品碳足迹配送阶段															
负责部门:				负责人姓名:											
日期:				联系方式:											
数据的时间边界:															
1. 产品配送情形															
运输起点		运输终点 (仓库)		运输距离 (km)		运输工具		燃料类型		备注					
2. 包装材料使用情形 (目标产品之包装材料使用情形) 成品包装															
包装材料名称 (中/英文)	材质	型号和规格	工艺	单一目标产品用量	单位	量测值	计算值	推估值	用途说明	数据来源说明	供货商	供货商地址	供货商运输至生产厂区距离 (km)	车型	燃料类型
						量测值, 计算值和推估值, 三选一在下表进行勾选“√”									

参考文献

- [1] 田勇燕, 秦飞, 言华, 郭伟红, 关庆伟³。江苏省徐州市林政资源管理站, 江苏徐州 221009; 2. 江苏省徐州市市政园林局, 江苏徐州 221018; 南京林业大学森林资源与环境学院, 江苏南京 210037
- [2] 中国产品全生命周期温室气体排放系数库。
- [3] simapro 的 Ecoinvent 数据库。
- [4] 工业其他行业企业温室气体排放核算方法与报告指南(试行)
- [5] GWP 采用 2021 年 IPCC 第六次评估报告(AR6) 数据。
- [6] 中国石化加油站碳中和核算指南(试行)。
- [7] LY/T 2260 • 立木生物量模型及碳计量参数—油松。
- [8] LY/T 2261 • 立木生物量模型及碳计量参数—湿地松。
- [9] LY/T 2262 • 立木生物量模型及碳计量参数—云南松。
- [10] LY/T 2263 • 立木生物量模型及碳计量参数—马尾松。
- [11] LY/T 2264 • 立木生物量模型及碳计量参数—杉木。
- [12] LY/T 2654 • 立木生物量模型及碳计量参数—落叶松。
- [13] LY/T 2655 • 立木生物量模型及碳计量参数—云杉。
- [14] LY/T 2656 • 立木生物量模型及碳计量参数—冷杉。
- [15] LY/T 2657 • 立木生物量模型及碳计量参数—柳杉。
- [16] LY/T 2658 • 立木生物量模型及碳计量参数—栎树。
- [17] LY/T 2659 • 立木生物量模型及碳计量参数—桦树。
- [18] LY/T 2660 • 立木生物量模型及碳计量参数—木荷。
- [19] LY/T 2661 • 立木生物量模型及碳计量参数—枫香。



荣誉证书

温冬贤、江梦虹、苏浩岚、吴芷漩、王铭浩 同学

在广东第十届大学生材料创新大赛高分子材料分赛区中荣获

二等奖

特发此证，以资鼓励。

作品名：基于硼酸锌原位矿化的木材多功能化研究
指导老师：欧荣贤、周海洋

主办单位：
广东省材料研究学会



合作单位：
广东省本科高校材料类专业教学指导委员会
(南方科技大学代章)



承办单位：
广东工业大学材料与能源学院



二〇二〇年十二月十九日



荣誉证书

温冬贤、江梦虹、苏浩岚、吴芷漩、王铭浩同学
在广东省第十届大学生材料创新大赛中，荣获总决赛

三等奖

特发此证，以资鼓励。

作品名：基于硼酸锌原位矿化的木材多功能化研究
指导老师：欧荣贤、周海洋

主办单位：
广东省材料研究学会



合作单位：
广东省本科高校材料类专业教学指导委员会



承办单位：
广东工业大学材料与能源学院



二〇二〇年十二月二十日



获奖证书

华南农业大学

多功能材料制造者

你队参赛作品《
在“孙武故里，美丽广饶”第九届中国大学生高分子材料创新创业大赛中，荣获**三等奖**》。

队伍成员：温冬贤，江梦虹，苏浩岚，王铭浩，吴芷璇

指导老师：欧荣贤，周海洋

特发此证，以资鼓励。

中国石油和化学工业联合会

中国化工教育协会

广饶县人民政府

橡胶谷集团有限公司

二〇二一年十一月十九日

